

Physical properties of double perovskites



Vom Fachbereich Material- und Geowissenschaften
der Technischen Universität Darmstadt



zur Erlangung des akademischen Grades des
Doktors der Naturwissenschaften (Dr. rer. nat.)
genehmigte Dissertation

von

Dipl.-Ing. Narendrakumar Narayanan,
aus Colombo, Sri Lanka

Referent: Prof. Dr. rer. nat. Lambert Alff
Koreferent: Priv.-Doz. Dr. rer. nat. Helmut Ehrenberg

Tag der Einreichung: 10. September 2010
Tag der mündlichen Prüfung: 24. September 2010

Darmstadt 2010

D17

Die vorliegende Arbeit wurde zwischen Oktober 2007 und August 2010 unter der Leitung von Priv.-Doz. Dr. rer. nat. Helmut Ehrenberg und unter der Betreuung von Dr. Daria Mikhailova im Institut für komplexe Materialien am IFW Dresden und im Fachgebiet Strukturforchung des Fachbereiches Material- und Geowissenschaften der Technischen Universität Darmstadt durchgeführt.

Danksagung

An dieser Stelle möchte ich mich ganz herzlich bedanken bei

Prof. Dr.-Ing. Dr. h. c. Hartmut Fuess für das Ermöglichen dieser Arbeit.

Priv.-Doz. Dr. rer. nat. Helmut Ehrenberg für die freundliche Aufnahme in seine Arbeitsgruppe, für die gesamte Betreuung und für das entgegengebrachte Vertrauen.

Prof. Dr. rer. nat. Lambert Alff für die Bereitschaft zum Referenten dieser Arbeit.

Dr. Daria Mikhailova für die exzellente Betreuung und für die immer positiven Impulse.

Univ. Prof. Dr. phil. Karlheinz Schwarz für die freundliche Aufnahme in seine Arbeitsgruppe für zwei Monate und für seine Bereitschaft als externer Prüfer zu fungieren.

Ao. Univ. Prof. Dr. techn. Peter Blaha und Dr. Robert Laskowski für die exzellente Betreuung während meines Aufenthalts in Wien.

Prof. Dr.-Ing. Jürgen Eckert für die freundliche Aufnahme in sein Institut.

Dr. Anatoliy Senyshyn für die Neutronenpulverdiffraktometrie.

Dr. Dmytro Trots, mit dessen Hilfe ich die Messungen am Synchrotron durchgeführt habe.

Dr.-Ing. Björn Schwarz für zahlreiche Diskussionen und Hilfe bezüglich der Magnetisierungsmesstechnik und für die konstruktiven Diskussionen über Quantenmechanik und Philosophie.

Dr. Natasha Kuratieva für die Indizierung der Einkristalle.

Ulrike Nitzsche für die Hilfe bezüglich des Computerclusters am IFW Dresden.

Der ganzen Arbeitsgruppe für das angenehme Arbeitsklima.

Meiner Familie, die mich mein Leben lang unterstützen und immer für mich da sind.

Contents

1. Introduction and aim of the work	1
2. Theoretical background	5
2.1 The many-body problem and the density functional theory (DFT)	5
2.1.1 The many-body Hamiltonian	5
2.1.2 Born-Oppenheimer approximation	5
2.1.3 Jellium solid	6
2.1.4 Hartree-approximation and Hartree-Fock-approximation	6
2.1.5 Exchange and correlation holes	8
2.1.6 Thomas-Fermi-Dirac approximation	9
2.1.7 Density functional theory	9
2.1.7.1 Hohenberg-Kohn theorems	9
2.1.7.2 Kohn-Sham equations	10
2.1.7.3 The exchange-correlation functional	13
2.1.7.4 Bandstructure methods	15
2.1.7.5 Basis set	17
2.1.7.6 Linearized augmented plane waves method (LAPW) and the augmented plane wave plus local orbital method (APW+lo)	17
2.1.7.7 Scalar relativistic approximation and the inclusion of the spin-orbit coupling (SOC) in a second variational step	23
2.1.7.8 Non-collinear magnetism (NCM) and its implementation in WIENNCM	26
2.1.7.9 Highly correlated electron systems and concepts beyond the LSDA/GGA approximation: LSDA/GGA+U approximation	30
2.1.7.9.1 Theoretical background	30
2.1.7.9.2 LSDA/GGA+U correction term ΔV	34
2.1.7.9.3 Fluctuation form of LSDA/GGA+U: Around the mean field method (AMF)	35
2.1.7.9.4 The fully localized limit (FLL)	36
2.2 Double perovskites	37
2.3 Determination of the oxidation state (valence state) of the ions in Oxides	42
2.3.1 Introduction	42

2.3.2 Bond valence sum (BVS)	42
2.3.3 Bader charges	43
2.4 Electronic conduction in insulators	44
2.5 Magnetic interactions in double perovskites	46
3. Experimental methods	54
3.1 Powder diffraction methods	54
3.1.1 Introduction	54
3.1.2 Laboratory x-ray	58
3.1.3 Synchrotron powder diffraction	58
3.1.4 Neutron diffraction	59
3.1.5 Rietveld refinement	59
3.2 MPMS: Magnetic Property Measurement System	64
3.2.1 Theoretical background and basics of the instrument	64
3.2.2 Experimental procedure	69
3.3 PPMS: Physical Property Measurement System	70
3.3.1 Introduction	70
3.3.2 Resistivity option and the van der Pauw method	71
3.3.3 Heat capacity option	75
3.3.3.1 Introduction	75
3.3.3.2 Theoretical models used in the relaxation method	77
3.3.3.2.1 The simple model (single τ model)	77
3.3.3.2.2 Two τ model	77
3.3.3.3 Experimental procedure	78
3.B DFT calculation procedure	81
4. Synthesis of the compounds	84
4.1 Polycrystalline samples	84
4.2 Single crystals of $\text{La}_2\text{CoIrO}_6$	85
5. Results and discussion	86
5.1 Crystal structures of $\text{La}_{2-x}\text{Sr}_x\text{CoIrO}_6$	86
5.1.1 Room temperature crystal structures	86
5.1.2 Temperature dependence of crystal structures	92

5.2 Temperature and field dependence of magnetizations	96
5.3 Magnetic structures of $\text{La}_{2-x}\text{Sr}_x\text{CoIrO}_6$	99
5.4 Specific heat capacity	110
5.5 Transport properties of $\text{La}_{2-x}\text{Sr}_x\text{CoIrO}_6$	112
5.6 Characterization of $\text{La}_2\text{CoIrO}_6$ single crystals	117
5.7 Electronic structures	122
5.7.1 Collinear calculations	122
5.7.2 Non collinear calculations (NCM calculations)	129
5.8 The $\text{La}_{2-x}\text{Ca}_x\text{CoIrO}_6$ ($0 \leq x \leq 0.75$) system	135
5.8.1 Crystal structures at room temperature and at 4K	135
5.8.2 Magnetic properties of $\text{La}_{2-x}\text{Ca}_x\text{CoIrO}_6$	138
5.8.3 Transport properties of $\text{La}_{2-x}\text{Ca}_x\text{CoIrO}_6$	142
6. Summary	145
7. Outlook	147
8. Appendix	148
Appendix 1: X-ray and neutron diffraction patterns with calculated intensities	148
Appendix 2: Atomic positions at room temperature	157
Appendix 3: Self-consistent procedure (SCF) flow chart and important input files for WIEN2K and WIENNCM for $\text{La}_2\text{CoIrO}_6$	160
9. Bibliography	166

1. Introduction and aim of the work

In recent years double perovskites $A_2BB'O_6$ (A = alkali metal, alkaline earth metal or lanthanides) with transition metals at the BB' sites have been extensively studied due to their interesting physical properties such as colossal magnetoresistance, higher Curie-temperatures, metal-insulator transitions, different magnetic orderings and structural and magnetic phase transitions. Especially the double perovskites with Curie temperatures above room temperature are of practical relevance in spintronic applications. Concerning the 3d/5d BB' combination, most of the research was focussed on $B'=W, Re$ and Os based double perovskites with ferromagnetic ordering temperatures T_C above room temperature [1-6]. Less attention was diverted towards the Ir-based ones, although the ability of Ir to exist in different oxidation states and the effects of electron correlation and spin-orbit coupling on the spatially more extended 5d-orbitals should result in a rich variety of physical properties and elucidate the structure-property relationships in this interesting class of compounds. Examples for interesting properties in oxide systems containing Ir are the bandwidth controlled metal-insulator transition in the Ruddlesden-Popper series $Sr_{n+1}Ir_nO_{3n+1}$ going from $n=2$ to $n=1$ and unusual magnetic and transport properties in $BaIrO_3$ with not even 30% saturation of the magnetic moment of Ir at even 30 Tesla. In the former the metal-insulator transition is a result of an enhancement of the electron correlation triggered by the $J_{1/2}$ - $J_{3/2}$ 5 d band splitting due to strong spin-orbit coupling. Concerning the Ir based double perovskites, the compounds $La_2B'IrO_6$, $B = Mg, Mn, Co, Ni$ and Cu were first synthesized in 1965 [7-8]. At that time the research was mainly focussed on the synthesis of these compounds. Much later crystal structures and magnetic properties were determined for $B=Mn, Co, Ni$ and Zn , and band structure calculations were performed for $B=Mn, Co$ and Fe within the LDA and these compounds were predicted to be metallic [9-11]. At room temperature the double perovskites with $B=Co, Ni$ and Zn adopt a monoclinic $P2_1/n$ superstructure, while the underlying space group of La_2MnIrO_6 was not determined. A high degree of cation disorder, i.e. an occupation of the B-site with B' and vice versa, was also reported for the compounds $La_2B'IrO_6$ with $B=Mn$ and Fe due to the small differences in charge and ionic radii between the B and $B'=Ir$ ions [10, 12]. Ferromagnetic behaviour is reported for La_2MnIrO_6 , based on magnetization measurements and confirmed by band structure calculations. A more complicated behaviour was found for $B=Co, Ni$ and Fe : The magnetic ground states of these compounds exhibit both ferromagnetic and antiferromagnetic components, so that non-collinear magnetism (NCM)

was concluded, again supported by calculations, which gave larger calculated magnetic moments for B=Co and Fe in a collinear framework than the observed ones [10-11, 13].

Cobalt in oxides on the other hand is interesting due to the fact that within a certain oxidation state depending on the compound it may exhibit different orbital occupancies thus appear in different spin states such as high spin (HS) (HS-Co³⁺ in the trigonal prisms of Ca₃Co₂O₆ [14]), low spin (LS) (LiCoO₂ [15]) or even intermediate spin (IS) (LaCoO₃ [16]) configuration. In some compounds it shows phenomena such as charge ordering as in La_{1.5}Sr_{0.5}CoO₄ (checkerboard HS-Co²⁺/LS-Co³⁺ charge order) [17] and/or orbital ordering as in LaCoO₃ [18]. In Co-containing double perovskites Co is combined with 4d/5d transition metals. In most cases they are antiferromagnets with relatively low Neel temperatures and insulators with small band gaps. Table 1.1 summarises the important properties of some of the Co-based double perovskites with 4d/5d transition metals.

Table 1.1: Space group, Neel temperature (T_N) and transport property of a few Co based double perovskites.

compound	Space group	T _N (K)	Transport properties
LaSrCoNbO ₆ [19]	<i>P2₁/n</i>	16	
Sr ₂ CoMoO ₆ [20]	<i>I4/m</i>	37	insulator
La ₂ CoRuO ₆ [21]	<i>P2₁/n</i>	25	insulator
Sr ₂ CoWO ₆ [22]	<i>I4/m</i>	32	insulator
Sr ₂ CoReO ₆ [23]	<i>I4/m</i>	65	insulator

Therefore, combining Co and Ir in a rocksalt type arrangement promises interesting physical properties, that can be tuned by changing the underlying electronic structure. In double perovskites this could be done through several ways. Before going into detail it is worthy to take a look at the available information on this selected system. As already mentioned while describing Ir based double perovskites, one of the end members of the system La₂CoIrO₆ crystallizes in the *P2₁/n* space group, undergoes NCM below 100 K and band structure calculations within LDA predict it to be metallic. Other compounds of this system are yet to be synthesized or investigated. Coming back to the influencing of the electronic structure, a well established method is the partial substitution of cations that has been successfully applied to several double perovskite systems to influence the physical properties [23-24]. In this work only on A-site substitution of La by Sr (Ca) is considered, which has mainly two effects on

the resulting structures and properties: On one hand the La:Sr ratio determines the averaged ionic size on the A-site and hereby the symmetry of the underlying crystal structure. This influences the bond angles, which in turn determines the overlap of the wavefunctions of the atoms and therefore the exchange paths. An interesting aspect in this context, which will be investigated in the present work, is how the non-collinear magnetic ordering could be effected by the substitution of La by Sr in this system. On the other hand the replacement of trivalent La by bivalent Sr increases the formal oxidation states on the B- and B'-sites (from +6 to +8). It is interesting to investigate whether the individual increase in the oxidation states of B and B' are continuous or any anomalies (abrupt changes) exist. The increase of the oxidation states also means a lower number of d-electrons, and therefore less repulsion between these d-electrons, which could result in an insulator to metal transition, assuming $\text{La}_2\text{CoIrO}_6$ to be an insulator, in contrary to the prediction by earlier band structure calculations within LDA, which is known to describe correlated electron systems not sufficiently (section 2.1.7.9), to be metallic. Therefore, resistivity measurements and band structure calculations with additional terms describing the electron-electron interaction (repulsion between the electrons), the so called U, will be carried out in the present work and the density of states (DOS) at the Fermi-level will be compared with the LDA/GGA results. Summarizing the above possibilities the $\text{La}_{2-x}\text{Sr}_x\text{CoIrO}_6$ system offers two degrees of freedom, which are correlated with each other. As a comparison the $\text{La}_{2-x}\text{Ca}_x\text{CoIrO}_6$ ($0 \leq x \leq 0.75$) system is also investigated, which has the following unique feature. Due to similar ionic radii of La^{3+} and Ca^{2+} the size degree of freedom can be switched off, resulting only in the band filling degree of freedom. In addition, however, the cation site disorder $\text{Co} \leftrightarrow \text{Ir}$ on the B- and B'-sites (y) and a possible oxygen deficiency δ will also affect the physical properties and have to be considered carefully as two additional relevant parameters in the system $\text{La}_{2-x}\text{Sr}_x(\text{Co}_{1-y}\text{Ir}_y)(\text{Ir}_{1-y}\text{Co}_y)\text{O}_{6-\delta}$. Concerning the oxygen deficiency the main results, obtained for $\text{Sr}_2\text{CoIrO}_{6-\delta}$ in another work, would be compared in the discussion section with the results of the most related oxygen deficiency system $\text{Sr}_2\text{CoMoO}_{6-\delta}$ [20]. It is also not uncommon for systems with NCM ordering to undergo spin-reorientation transitions depending on an external magnetic field in combination with the temperature thus reaching metamagnetic states [6]. As $\text{La}_2\text{CoIrO}_6$ is known to undergo NCM ordering below 100 K, this aspect will also be investigated in terms of magnetization measurements on single crystals, as they are ideal to investigate anisotropies and total energy calculations within non-collinear arrangement of the magnetic moments in dependence of the tilting angle of the magnetic moments (especially of Co), in order to find

energy minima that may correspond to metamagnetic states reached by spin-reorientation transitions.

In the present work $\text{La}_{2-x}\text{Sr}_x\text{CoIrO}_6$ polycrystalline samples are synthesized for five different compositions $x=0,0.5,1,1.5$ and 2 and $\text{La}_2\text{CoIrO}_6$ single crystals are grown and their physical properties are investigated experimentally by diffraction methods (laboratory x-ray, synchrotron and neutron powder diffraction), magnetization measurements using a Superconducting Quantum Interference Device (SQUID) integrated in a MPMS, resistivity measurements in the van der Pauw setup (PPMS) and heat capacity measurements (PPMS) and theoretically by density functional theory calculations within both collinear and non collinear framework using the WIEN2K and WIENNCM code. As a comparison $\text{La}_{2-x}\text{Ca}_x\text{CoIrO}_6$ polycrystalline samples are synthesized for two different compositions $x=0.5$ and 0.75 (other than $x=0$) and their physical properties are investigated by diffraction methods, magnetization measurements and resistivity measurements.

2. Theoretical background

2.1 The many-body problem and the density functional theory (DFT)

2.1.1 The many-body Hamiltonian

A solid constitutes of heavy positively charged nuclei und lighter negatively charged electrons. This is a quantum many-body problem and in case of a certain number of nuclei the internal electromagnetic interaction between the particles in the system could be described by the following expression:

$$\hat{H} = -\frac{\hbar^2}{2} \sum_i \frac{\nabla_{\vec{R}_i}^2}{M_i} - \frac{\hbar^2}{2} \sum_i \frac{\nabla_{\vec{r}_i}^2}{m_i} - \frac{1}{4\pi \epsilon_0} \sum_{i,j} \frac{e^2 Z_i}{|\vec{R}_i - \vec{r}_j|} + \frac{1}{8\pi \epsilon_0} \sum_{i,j} \frac{e^2}{|\vec{r}_i - \vec{r}_j|} + \frac{1}{8\pi \epsilon_0} \sum_{i,j} \frac{e^2 Z_i Z_j}{|\vec{R}_i - \vec{R}_j|} \quad (2.1)$$

The electrons at r_i have the mass m and the nuclei at R_i have the mass M . The first two terms denote the kinetic energy operators for the nucleus and electrons respectively. The last three terms denote the Coulomb interaction between the nucleus and an electron (attractive), between electrons and between nuclei (repulsive). This problem cannot be solved exactly for “realistic” many particle systems (solving on the order of 3×10^{23} coupled differential equations), thus several approximations are needed to tackle this challenge.

2.1.2 Born-Oppenheimer approximation

Even the lightest of the nuclei, the proton weighs around 1800 times more than the electron, thus the nuclei move much slower than the electrons. As a consequence the electrons could be treated as if they are moving in the field of fixed nuclei. In most cases this is a good approximation (although cases exist where this approximation is critical or even breaks down [25]). Therefore, the nuclei act as a source of positive charge und thus become external to the negative interacting particles, moving in this potential. As a consequence the first term in the above expression becomes zero and the last term is reduced to a constant. The above expression is altogether reduced to the kinetic energy of the electron gas (\hat{T}), the potential

energy due to electron-electron interaction (\hat{V}) and the potential energy of the electrons in the external field of the positive charges (\hat{V}_{ext}).

$$\hat{H} = \hat{T} + \hat{V} + \hat{V}_{\text{ext}} \quad (2.2)$$

It is interesting to note that in the above expression, the first two terms do not depend on the particular kind of the many electron system, as they only describe the kinetic energy and the interaction between the electrons and thus they are universal. System specific information such as the particular kind of nuclei or their positions, are entirely included in the term \hat{V}_{ext} .

The electron-electron interaction \hat{V} still prevents solving this problem exactly, as it hinders the single particle description. Many interesting effects could not be described if this term would be neglected.

2.1.3 Jellium solid

Solids exist in various forms: From noble gas solids to metals with covalent and ionic solids in between. All of these forms of solids have in common that their form and most of the properties are determined by the valence electrons. As a first simplification the core of the atoms, which has little influence on most of the properties is treated as a source of positive charge that neutralizes the negative charge of the valence electrons. A further simplification is that the charge that is concentrated in the core region, is smeared out uniformly, thus the solid becomes translational invariant (the valence electrons become a homogeneous gas). All the properties that differentiate two solids (that have particular kind of nuclei or their positions) are lost. The only parameter which is retained is the overall electron density. This is the jellium model and it is the most basic model to understand the effects of interacting electrons on the behaviour of solids and facilitates the inclusion of such interaction effects in various approximative many body models and methods [26].

2.1.4 Hartree-approximation and Hartree-Fock-approximation

The interaction potential \hat{V} seen by an electron depends on the positions of all the other electrons. The idea behind the Hartree-Approximation [27] is that this interaction potential would be replaced by a function that depends only on the individual position of this electron,

thus the problem would lead to a set of single particle differential equations, with the assumption of a product total wave function, which could be solved self-consistently (Rayleigh-Ritz variational principle). Practically this is done by freezing the positions of other electrons, assuming a set of wave functions for electronic states that are occupied and calculating the contribution of them to the interaction potential of a particular electron self consistently using electrostatics.

$$\hat{V} = \frac{1}{8\pi\pi_0} \sum_{i,j} \frac{e^2}{|\vec{r}_i - \vec{r}_j|} \rightarrow \hat{V}_H = \frac{1}{4\pi\pi_0} \sum_i V_i(\vec{r}_i), \quad V_i(\vec{r}_i) = \sum_{\substack{j \neq i \\ j \text{ occupied}}} \int \frac{e^2 |\psi_j(\vec{r}_j)|^2}{|\vec{r}_i - \vec{r}_j|} d\vec{r}_j \quad (2.3)$$

In other words each electron would move in an electrostatic field due to the charge distribution of all the other electrons. Applying this approximation to the jellium solid with plane waves as wave functions, would lead to a mutual cancellation of the interaction term and the positive background. This is the famous Sommerfeld-model. Conceptual disadvantage of this approximation is that it does not include the anti-symmetrisation of the total wave function for fermions and thus neglecting exchange effects. Pauli-principle is only guaranteed by the restricted occupation of the electronic states.

An improvement of this model was achieved by the inclusion of the Pauli-principle by taking an anti-symmetric total wave function, thus including exchange effects. This is known as the Hartree-Fock-approximation [28]. The total wave function could be written as a Slater determinant:

$$\Psi(\vec{r}_1, \dots, \vec{r}_N) = \frac{1}{\sqrt{N!}} \begin{vmatrix} \psi_\alpha(\vec{r}_1) & \psi_\alpha(\vec{r}_2) & \psi_\alpha(\vec{r}_3) & \dots \\ \psi_\beta(\vec{r}_1) & \psi_\beta(\vec{r}_2) & \psi_\beta(\vec{r}_3) & \dots \\ \psi_\gamma(\vec{r}_1) & \psi_\gamma(\vec{r}_2) & \psi_\gamma(\vec{r}_3) & \dots \\ \cdot & \cdot & \cdot & \cdot \end{vmatrix}, \quad (2.4)$$

N: index of the single-electron states

The self consistent procedure is the same as in the Hartree-approximation, by varying each of the single-electron states. However the anti-symmetric nature of the total wave function introduces a new non local potential to the Hamiltonian, namely the exchange potential V_{ex} . With this the differential equation becomes a more complicated integro-differential equation.

$$\hat{H} = \hat{T}_0 + \hat{V} + V_H + \sum_{\alpha} \int V_{\text{ex}}(\vec{r}, \vec{r}') d\vec{r}', \quad V_{\text{ex}} = -\frac{e^2}{|\vec{r} - \vec{r}'|} \sum_{\substack{\beta \neq \alpha \\ \beta \text{ occupied}}} \psi_{\beta}(\vec{r}) \psi_{\beta}^*(\vec{r}') \quad (2.5)$$

The exchange term brings a charge-depletion in the vicinity of an electron with the same spin thus Pauli-principle is fulfilled and thus contributes to the reduction of the repulsive electrostatic energy of an electron with the same spin. For a detailed and obvious description of the exchange interactions see section 2.5. As for V_H within the Hartree-approximation many approximations in form of a local exchange potential for V_{ex} exist, including the $\rho^{2/3}$ dependency of V_{ex} suggested by J. C. Slater for plane waves [29]. Conceptual disadvantage of the conventional Hartree-Fock approximation could be seen by applying this to the jellium solid. The outcome is a zero DOS at the Fermi-level, which could not be found experimentally for metals. The missing ingredient in this approximation is the contribution from electron correlation. Nowadays correlation contribution is included in its subsequent improvements such as the configurational interaction method (CI) [30]. But its application is limited to smaller systems, which is the practical disadvantage of this method.

2.1.5 Exchange and correlation holes

Consider a jellium solid. For a moment neglecting the Coulomb repulsion and only considering exchange between electrons, a particular electron would be surrounded by a hole in the electron density through exchange screening that contains only half of an electron charge, since the electron density of the opposite spin is unchanged. This is called the exchange hole. But the electron has a negative charge and the other electrons would correlate their motion in order to screen out the repulsive electric field of this electron thus creating a hole in the electron density around this electron that contains an equal and opposite charge. This is called the correlation hole. Both the effects have more or less the same net result, but considering typical densities encountered in solids the coulomb effect is as equal to or larger than the exchange effect and as a consequence the electrons do not get close enough for the Pauli exclusion principle to be effective. Moreover the interaction between the electrons is no longer the bare coulomb interaction because of screening effects. Therefore the inclusion of the exchange through Pauli-principle is not a good starting point.

2.1.6 Thomas-Fermi-Dirac approximation

The Thomas-Fermi [31-32] approximation proposed in 1927 is the precursor for the modern day density functional theory. Although it is not accurate enough for the present electronic structure calculations, it introduces the functional formalism of the energy depending on the density. In this approximation the kinetic term of the electrons is approximated as an explicit functional of the electron density and they were idealized as non-interacting in a homogeneous gas with the electron density is equal to the local density at any given point. In the original formalism the electron-electron interaction contains only the Hartree term thus neglecting exchange and correlation terms, the former been included by P. Dirac as a local approximation [33]. The ground state density and energy could be found by utilizing the Rayleigh-Ritz variational principle, where the constraint being the total number of electrons. The disadvantage of this theory is that it does not reveal the correct atomic shell structures and binding of molecules.

2.1.7 Density functional theory

2.1.7.1 Hohenberg-Kohn theorems

Density functional theory is an approach to the many-electron problem in which the electron density as in the case of Thomas-Fermi-Dirac approximation, rather than the electron wave function as in the case of Hartree-Fock approximation, plays the central role [34]. The backbone of this method is the two theorems presented by P. Hohenberg and W. Kohn in 1964 [35].

Theorem 1: There is a one-to-one correspondence between the ground state electron density $\rho(\vec{r})$ of a many-electron system and the external potential V_{ext} . An immediate consequence is that the ground state expectation value of any observable \hat{O} is a unique functional of the exact ground state electron density:

$$\langle \Psi | \hat{O} | \Psi \rangle = O[\rho] \quad (2.6)$$

This means that the Schrödinger equation yields a unique many particle ground state wave function for a given many electron system that has a unique external potential, which is defined by eq. 2.2. The electron density could be easily found from this unique wave function, thus the above one to one correspondence is valid.

Theorem 2: For the observable \hat{O} being the Hamiltonian \hat{H} , the ground state total energy functional $E_{V_{\text{ext}}}[\rho]$ can be written in the following form:

$$\begin{aligned} H[\rho] = E_{V_{\text{ext}}}[\rho] &= \underbrace{\langle \Psi | \hat{T} + \hat{V} | \Psi \rangle}_{F_{\text{HK}}[\rho]} + \langle \Psi | \hat{V}_{\text{ext}} | \Psi \rangle \\ &= F_{\text{HK}}[\rho] + \int \rho(\vec{r}) V_{\text{ext}}(\vec{r}) d\vec{r} \end{aligned} \quad (2.7)$$

The Hohenberg-Kohn density functional $F_{\text{HK}}[\rho]$ in the above expression is universal for any many body systems. $E_{V_{\text{ext}}}[\rho]$ reaches its minimal for the ground state density corresponding to V_{ext} .

Although an explicit expression for $F_{\text{HK}}[\rho]$ is unknown, the universality of it for any many electron systems could be seen from the fact it does not contain any information on the nuclei or its positions. Suppose the ground state density $\rho(\vec{r})$ is known, the second term in eq. could be calculated exactly for a given external potential V_{ext} and thus the existence of a $F_{\text{HK}}[\rho]$ is guaranteed. The second theorem also allows us to use the Rayleigh-Ritz variational principle to find the ground state density. Out of the infinite number of possible densities, the ground state density corresponding to the external potential $V_{\text{ext}}(\vec{r})$, is the one that minimizes $E_{V_{\text{ext}}}[\rho]$. Calculation procedure for the ground state density and approximations for $F_{\text{HK}}[\rho]$ are discussed in the following chapters.

2.1.7.2 Kohn-Sham equations

The Kohn-Sham equations serve as a practical procedure to calculate the ground state density [36]. In the following the Hohenberg-Kohn density functional would be rewritten. As seen in the above sections the exchange energy is the contribution to the energy that exists in the Hartree-Fock approximation but not in the Hartree approximation. The correlation energy is the contribution to the energy that exists in the exact solution but not in the Hartree-Fock approximation.

$$E_{\text{exact}} = T + V \quad (2.8)$$

$$E_{\text{H}} = T_0 + V_{\text{H}} \quad (2.9)$$

$$E_{\text{HF}} = T_0 + \underbrace{V_{\text{H}} + V_{\text{ex}}}_V \quad (2.10)$$

$$\rightarrow V_{\text{C}} = T - T_0 \quad (2.11)$$

Thus the Hohenberg-Kohn density functional becomes:

$$F_{\text{HK}}[\rho] = T_0 + V_{\text{H}} + \underbrace{V_{\text{ex}} + V_{\text{C}}}_{V_{\text{XC}}} \quad (2.12)$$

And the ground state total energy functional becomes:

$$E_{\text{V}_{\text{ext}}}[\rho] = T_0[\rho] + V_{\text{H}}[\rho] + V_{\text{XC}}[\rho] + V_{\text{ext}}[\rho] \quad (2.13)$$

This expression could be seen as energy functional of non interacting electron gas now subjected to two external potentials, namely the nucleus-electron and the exchange-correlation potentials. Instead of using the second Hohenberg-Kohn theorem, Schrödinger like single particle equations could be solved now in order to find ρ . The corresponding Hamiltonian, the so called Kohn-Sham Hamiltonian could be written as:

$$\hat{H}_{\text{KS}} = \hat{T}_0 + \hat{V}_{\text{H}} + \hat{V}_{\text{XC}} + \hat{V}_{\text{ext}} = -\frac{\hbar^2}{2m} \nabla_i^2 + \frac{e^2}{4\pi \epsilon_0} \int \frac{\rho(\vec{r}')}{|\vec{r} - \vec{r}'|} d\vec{r}' + \frac{\delta V_{\text{XC}}[\rho]}{\delta \rho} + V_{\text{ext}} \quad (2.14)$$

Thus the Kohn-Sham equation becomes:

$$\hat{H} \phi_i(\vec{r}) = \epsilon_i \phi_i(\vec{r}) \quad (2.15)$$

Where, $\phi_i(\vec{r})$ are the N lowest energy solutions of the Kohn-Sham equation. The ground state density becomes:

$$\rho(\vec{r}) = \sum_{i=1}^N \varphi_i^*(\vec{r})\varphi_i(\vec{r}) \quad (2.16)$$

Both V_H and V_{XC} depend on ρ which depend on $\varphi_i(\vec{r})$ that in turn is being searched by the Kohn-Sham equation. The iterative problem has to be solved self-consistently. A starting density would be guessed and usually it would be a linear combination of the atomic densities. This procedure is continued until a given convergence criterium would be fulfilled. Fig. 2.1 illustrates this self-consistent procedure and a more sophisticated flow chart, which illustrates this procedure as implemented in the software code WIEN2K and WIENNCM, is shown in appendix 3.

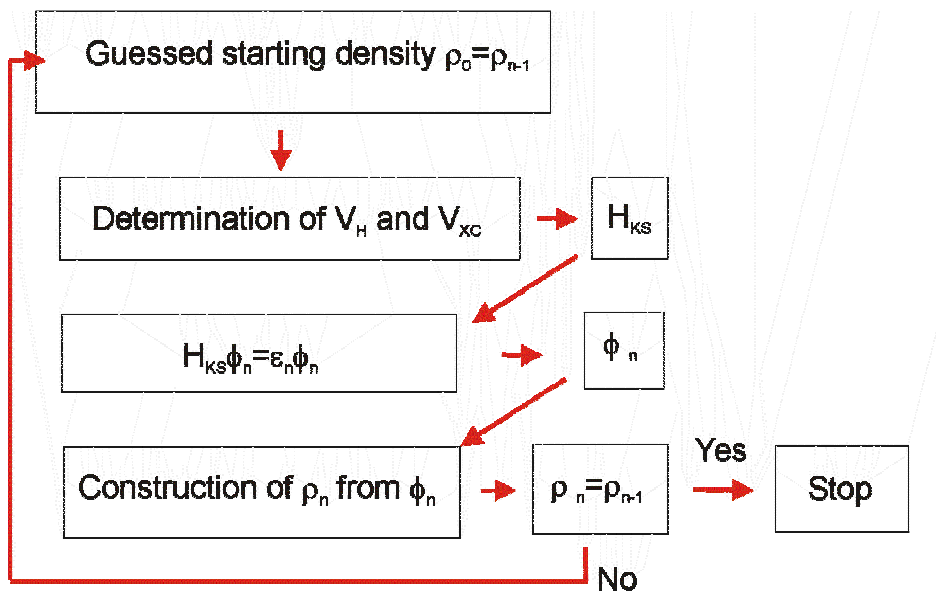


Fig. 2.1: Example of a procedure to solve the Kohn-Sham equations self-consistently.

Alternatively the ground state density could also be expressed in terms of the occupation numbers n_i and hereby the factor two considers the orbital occupancy with two different spins.

$$\rho(\vec{r}) = 2 \sum_i n_i \varphi_i^*(\vec{r})\varphi_i(\vec{r}) \quad (2.17)$$

$$n_i = \begin{cases} 1 & \text{for } \varepsilon_i \leq \varepsilon_F \\ 0..1 & \text{for } \varepsilon_i = \varepsilon_F \\ 0 & \text{for } \varepsilon_i \geq \varepsilon_F \end{cases}$$

The variation of the ground state total energy functional respect to the occupation numbers gives the orbital energies and this is known as Janak's theorem [37], which would become a major problem describing strong correlated electron system, which will be seen in section 2.1.7.9.

$$\frac{\partial E}{\partial n_i} = \varepsilon_i \quad (2.18)$$

2.1.5 Exchange and correlation holes

Apart from the Born-Oppenheimer approximation, the Kohn-Sham scheme is exact. But the exact expression for the exchange-correlation functional V_{XC} is not known and approximations should be introduced to this functional. The widely used approximation is the so called local density approximation (LDA), that is defined as follows:

$$V_{XC}^{LDA} = \int \rho(\vec{r}) \varepsilon_{xc}(\rho(\vec{r})) d\vec{r} \quad (2.19)$$

The exchange correlation energy density function $\varepsilon_{xc}(\rho)$ is calculated for the jellium solid in the following way. The different energies could be calculated analytically for the non interacting case. For interacting case this could only be done numerically. Subtracting the non interacting kinetic term and the Hartree term results in a numerical solution for ε_{xc} . This is calculated for several densities and thus the function $\varepsilon_{xc}(\rho)$ is obtained that could be applied to a material of interest in the following way. The material would be divided into infinitesimally small volumes (volume element) of constant ρ . The contribution from the densities corresponding to each of these volumes to the exchange-correlation energy would be taken from $\varepsilon_{xc}(\rho)$ of the homogeneous electron gas. The above expression for LDA could be generalized for spin-polarized (LSDA) cases as follows:

$$V_{XC}^{LSDA} = \int \rho(\vec{r}) \varepsilon_{xc}(\rho_{\uparrow}(\vec{r}), \rho_{\downarrow}(\vec{r})) d\vec{r} \quad (2.20)$$

In the following, concerning the local density approximation, only the local spin density approximation (LSDA) would be addressed, as the latter is the version of local density approximation, which is used for a part of the calculations, carried out in this work. The

LSDA approximation is expected to perform well for systems with slowly varying electron density such as in bulk metals, but it performs well for other systems also. In the following the success and limitations of LSDA are summarized.

It overestimates the cohesive energy in solids and the binding energy of molecules that results in an underestimation of bond lengths. However if strong bonds are involved as in the case of ionic, covalent or metallic compounds, LSDA reproduces the bond lengths, bond angles and vibrational frequencies within a few percentage of the experimental values. In case of weakly bound systems containing van der Waals or hydrogen bonds, the above limitation is severe. Chemical trends of atomic quantities such as ionization potentials, depending on atomic number are also usually correctly reproduced. Electronic densities at the core region, where they are quite localized, are rather poorly described because of the self-interaction present in the Hamiltonian. Electronic densities in the valence region are much better described but ϵ_{xc} decays exponentially instead of the correct long range $-e^2/r$ behaviour into the vacuum region, affecting the ionization energies and in case of negatively charged ions, in many instances this rapid decay predicts them to be unstable. But the most important failure, that plays a key role in the present work, is the underestimation or in many cases even a non prediction (predicted to be metallic) of the band gap at the Fermi-level in the electron density of states in contrast to the experimental finding in semiconductors or insulating behaviour in highly correlated materials. This problematic will be discussed rigorously in the LSDA/GGA+U section.

An improvement of LSDA would be to consider not only the dependence of ϵ_{xc} on the local density of this particular volume element, but also on the densities of the neighbouring volume elements as well (or in other words the gradient). This approximation is known as the generalized gradient approximation (GGA).

$$V_{xc}^{GGA} = \int \rho(\vec{r}) \epsilon_{xc}(\rho_{\uparrow}(\vec{r}), \rho_{\downarrow}(\vec{r}), |\nabla \rho_{\uparrow}(\vec{r})|, |\nabla \rho_{\downarrow}(\vec{r})|, \dots) d\vec{r} \quad (2.21)$$

In contrast to LSDA, which is uniquely defined, the definition of gradient has certain amount of freedom, in many cases even experimentally obtained parameters are included in order to fit the functional. As a result many versions of GGA's are available today. But in this work the parameter free Perdew-Burke-Ernzerhof (PBE) version of the GGA is exclusively used [38]. Comparing with LSDA, generally GGA improves the binding energies, bond lengths

and angles even for weakly bound systems. But in some cases it also overestimates them slightly as in the case of the lattice constants of noble metals (Ag, Au, Pt). But even after the inclusion of the gradient the band gap problem remains the same and as it will be discussed in section 2.1.7.9, new concepts beyond the LSDA are needed to tackle this problem. But first the implementation of density functional theory within the Kohn-Sham theory will be discussed in the next section.

2.1.7.4 Bandstructure methods

For a crystalline solid, bandstructure methods are utilized for the implementation of the density functional theory within the single particle description using the Kohn-Sham theory. The band theory for (periodic) crystalline solid is based on the translational invariance of the lattice potential $V(\vec{r})$.

$$V(\vec{r} + \vec{T}) = V(\vec{r}), \quad (2.22)$$

\vec{T} : Lattice vector

The consequence is that the total wave function is constrained to be the basis function of the irreducible representation of the translation group of the crystal and hence eigenfunctions of the translation operator τ and the Schrödinger equation.

$$\tau(\vec{T})\varphi_{\vec{k}}(\vec{r}) = \varphi_{\vec{k}}(\vec{r} + \vec{T}) = e^{i\vec{k}\vec{T}}\varphi_{\vec{k}}(\vec{r}) \quad (2.23)$$

$$\hat{H}\varphi_{\vec{k}}(\vec{r}) = E(\vec{k})\varphi_{\vec{k}}(\vec{r}) \quad (2.24)$$

These eigenfunctions are called the Bloch-functions and the index \vec{k} the wavevector (quantum number). The problem of solving the electronic structure of the (periodic) crystalline solid is therefore reduced to the unit cell of the crystal of volume Ω in the first instance. The manifold $E(\vec{k})$ is the bandstructure of the solid. The manifold $E(\vec{k})$ and $\varphi_{\vec{k}}(\vec{r})$ both have the translation symmetry of the reciprocal space (k space) and therefore \vec{k} could be restricted to a primitive cell in the reciprocal space, called the Brillouin-zone (BZ) of volume $(2\pi)^3/\Omega$, any \vec{k} outside the BZ could be mapped back to it with a fixed translation

vector \vec{G} analogous to \vec{T} in real space. The restricted band structure (or bands) $E_i(\vec{k})$ and the eigenfunctions $\varphi_{i,\vec{k}}(\vec{r})$ are given a further index, so called band index i . In this context the Kohn-Sham equation should be solved for infinite number of \vec{k} in the BZ in order to describe the electronic structure of the crystal perfectly, which is not possible in reality. But symmetry of the crystal reduces the BZ to a irreducible BZ wedge and this wedge would be sampled by a proper k-mesh with a finite number of k points (\vec{k}) whereas the remaining values in the wedge would be recovered by interpolation. The plot of the eigenvalues as a function of \vec{k} gives a set of energy bands, each corresponding to a different orbital state. Important information about the electronic properties of the crystal could be obtained from the position, form (dispersion) and interaction (hybridization) of a band with other bands. Usually the plot of the eigenvalues as a function of \vec{k} is carried out in high symmetry directions of the reciprocal space of the particular crystal.

An important quantity derived from the manifold $E(\vec{k})$ to compare with experimental data (especially transport properties) is the density of states (DOS) $D(E)$. This is the number of possible solutions of the Kohn-Sham equations (number of states) at a particular energy and it is obtained by integrating over the whole k space (BZ).

$$D(E) = \frac{\Omega}{(2\pi)^3} \sum_i \int_{\text{BZ}} d\vec{k} \delta(E - E_i(\vec{k})) \quad (2.25)$$

The Fermi-energy, which separates the unoccupied states from the occupied states, could be obtained from the following constraint:

$$n_T = \int_{-\infty}^{E_F} D(E) dE \quad (2.26)$$

, n_T : total number of electrons in the BZ

There are many methods to perform Brillouin zone integration to determine the DOS in numerical calculations. WIEN2k defaultly uses the so called improved tetrahedron method [39]. Hereby the irreducible BZ (IBZ) wedge is split into smaller parallelepipeds topologically like cubes, which are subsequently each split once again into six tetrahedral with equal

volume. The eigenvalues and the eigenfunctions are solved at the four vertices of each tetrahedron and linearly interpolated elsewhere. The integration over each tetrahedron can be calculated from a weighted sum over the irreducible k points. The resultant plot gives the occupation of each band in the bandstructure. In certain cases also a temperature broadening is employed.

2.1.7.5 Basis set

The different DFT computational codes, that are used to solve the band structure problem, differ in the choice of the basis set expansion of the Kohn-Sham eigenfunctions and the type of the approximation that is used. These factors determine the accuracy of the calculation and especially the choice of the basis set type determines the size of the matrix that has to be diagonalized. Traditionally two different types of basis sets are used. They are the plane waves, which is best suited for regions with free electron like states (delocalized electrons) and the atomic functions that are best suited for regions near the ionic cores, where the wave functions oscillate rapidly (localized electrons). Usually pseudo potentials are combined with plane waves in order to reduce the number of them. As transition metal oxides are usually both localized and delocalized, they are hard to treat with either of the types. The following solvers are widely used in DFT computations, which utilize the above mentioned types of basis sets in different ways: FP-LAPW/APW+lo, FP-LMTO [40], KKR [41], PP-PW [42] and FPLO [43]. In the following the FP-LAPW/APW+lo method would be briefly addressed as WIEN2K and WIENNCM are based on this DFT solver.

2.1.7.6 Linearized augmented plane waves method (LAPW) and the augmented plane wave plus local orbital method (APW+lo)

The augmented plane method (APW), the predecessor method of LAPW was introduced by Slater [44]. He combined the advantages of the basis sets discussed above. In this method the volume of the crystal is divided into two parts (Fig. 2.2 left).

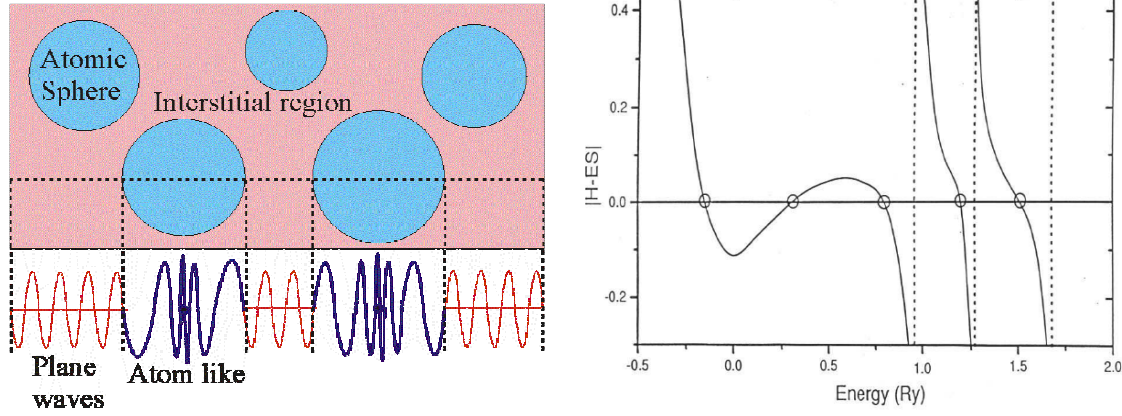


Fig. 2.2: Volume divided into spheres and interstitials (left) and solutions to APW [45] (right).

A non overlapping spherical region (atomic sphere) with a radius R is defined around each ion in the crystal, where R depends on the character of the particular ion and its nearest neighbours. Within this atomic sphere, solutions (eigenfunctions) of the Schrödinger equation in a spherical potential (atom like), which consists of a combination of the product of radial functions $u_l(\vec{r})$ and spherical harmonics $Y_{lm}(\vec{r})$, are used as basis set.

$$\varphi(\vec{r}) = \sum_{l,m} A_{lm} Y_{lm}(\vec{r}) u_l(\vec{r}) \quad (2.27), \quad A_{lm} : \text{coefficients of the linear combination}$$

The radial functions $u_l(\vec{r})$ being the solutions of the radial part of the Schrödinger equation:

$$\left[-\frac{d^2}{dr^2} + \frac{l(l+1)}{r^2} + V(r) - E_l \right] r u_l(r) = 0 \quad (2.28)$$

Outside the atomic sphere radius R , in the interstitial region, solutions of the Schrödinger equation in a constant potential, the plane waves are used as basis set.

$$\varphi_{\vec{k}}(\vec{r}) = \frac{1}{\Omega^{\frac{1}{2}}} \sum_{\vec{G}} C_{\vec{G}} e^{i(\vec{k}+\vec{G})\vec{r}} \quad (2.29)$$

, Ω : cell volume, \vec{G} : reciprocal lattice vector, $C_{\vec{G}}$: PW coefficients

An augmented plane wave (APW) is a plane wave in the interstitial region matched continuously to the atomic like basis functions at the surface of the atomic sphere. The plane wave is expanded in a set of spherical harmonics Y_{lm} and a coefficient matching of the Y_{lm} is carried out, thus the coefficients of the linear combination of atomic like functions A_{lm} could be determined in terms of the plane wave coefficients $C_{\vec{G}}$ and E_1 (energy corresponding to the numerical solution u_1) which are the variational parameters of the APW method.

$$\frac{1}{\Omega^{\frac{1}{2}}} e^{i(\vec{k}+\vec{G})\vec{r}} = \frac{4\pi}{\Omega^{\frac{1}{2}}} e^{i(\vec{k}+\vec{G})\vec{r}} \sum_{lm} i^l j_l(|\vec{k}+\vec{G}|\vec{r}) Y_{lm}^*(\vec{k}+\vec{G}) Y_{lm}(\vec{r}) \quad (2.30)$$

$$A_{lm} = \frac{4\pi i^l}{\Omega^{\frac{1}{2}} u_1(\vec{r})} \sum_{\vec{G}} C_{\vec{G}} j_l(|\vec{k}+\vec{G}|\vec{r}) Y_{lm}^*(\vec{k}+\vec{G}) \quad (2.31)$$

, j: Bessel function of order l

From the expression 2.31 it is clear that an infinite number of lm terms are involved and therefore an infinite number of A_{lm} are required for the matching, which is not realistic computationally thus the sum has to be truncated at some l_{max} . This could be selected from the following consideration. For a given l_{max} , the maximum number of nodes Y_{lm} can have along one great circle is $2l$ (for a fixed ϕ) of an atomic sphere. Converted into nodes per unit length, this would be $l/\pi R$. If a plane wave has to be matched at the surface it should have at least a similar number of nodes. The number of nodes that a plane wave with the shortest period of $2\pi/G_{max}$ has is $2/(2\pi/G_{max})$ (2 nodes per period). A truncation criterion for both l_{max} and G_{max} could be obtained by the requirement that the number of nodes should be identical. This yields $l_{max}=RG_{max}$ (in the WIEN2K/WIENNCM code known as RK_{max}) and it is one of the important inputs in APW and its modified methods. For a given G_{max} a good l_{max} could be obtained with this criterion and with a finite l_{max} the matching at the surface is not exact but good enough. For comparison of different calculations the l_{max} should be identical. It is also clear from the above considerations that the atomic sphere R of different atoms are not allowed to be too different, as this would yield values for l_{max} that are too different from one another, preventing a good global l_{max} .

Although the basis function is continuous at the surface, there may be a difference in the slopes of the plane wave and the atomic like functions, resulting in a surface term in the kinetic energy, as this depends on the spatial derivative of the wave function. The main disadvantage of the APW method is that the solutions of the radial part of the Schrödinger equation u_l are dependent on the energy E_l at which the radial part is evaluated, whereas the plane waves are energy independent. Therefore a Kohn-Sham eigenfunction would only be correctly described by the u_l , that are evaluated at the eigenenergy ε_i of this eigenfunction. Therefore a different energy dependent set of APW basis functions must be evaluated for each considered energy. As the matrix elements depend on the choice of the basis-functions, the secular equation $|\mathbf{H}-E\mathbf{S}|=0$ (\mathbf{S} is the overlap matrix due to the non orthogonal property of the APW) becomes non linear in energy, thus the procedure of evaluating the determinant for different energies in order to find the Kohn-Sham eigenenergies, makes the APW method computationally time consuming (Fig. 2.2 right).

In order to heal the cumbersome procedure of APW, resulting from the energy dependence of basis-functions, Andersen proposed a linearized version of the APW called the LAPW [46]. In the LAPW method the energy dependence of each u_l is linearized by taking a linear combination of a solution u_l and its energy derivative $\dot{u} = \partial u_l / \partial E$ at a fixed linearisation energy E_0 (Taylor expansion).

$$u_l(E, \vec{r}) = u_l(E_0, \vec{r}) + (E - E_0) \frac{\partial u_l(\vec{r})}{\partial E} + O((E - E_0)^2) \quad (2.32)$$

The term $O((E - E_0)^2)$ denotes errors that are quadratic in the energy difference and it becomes smaller for E close to E_0 . Note that the use of a universal E_0 in the above equation is only for demonstration purpose. Moreover for each atom involved, separate fixed E_l would be used for l values 0, 1, 2 and 3 that are close to their eigenenergies, thus the error term could be neglected in eq. 2.32. For l values higher than 3 (beyond f states), a fixed value would be used. The basis set becomes:

$$\varphi(\vec{r}) = \begin{cases} \sum_{l,m} \left[A_{lm} u_l(\vec{r}, E_l) + B_{lm} \frac{\partial u_l(\vec{r}, E_l)}{\partial E} \right] Y_{lm}(\vec{r}) & \text{within the atomic sphere} \\ \frac{1}{\Omega^{\frac{1}{2}}} \sum_{\vec{G}} C_{\vec{G}} e^{i(\vec{k}+\vec{G})\vec{r}} & \text{in the interstitial region} \end{cases} \quad (2.33)$$

With this construction the secular equation becomes a general eigenvalue problem and all the eigenenergies could be found by diagonalizing the secular matrix only once. On the other hand considering the basis-functions, there are now two coefficients (A_{lm} and B_{lm}) within the atomic sphere, which must be determined. The A_{lm} are determined as in the APW method requiring that the atomic like basis-functions and plane waves should match at the surface of the atomic sphere, whereas the B_{lm} are determined, requiring that the slope of both the basis-functions are continuous at the surface, thus removing the possible kink in the basis-function at the surface and additionally removing the surface term in the kinetic energy.

The LAPW may still have a small deficiency. The electronic states are usually divided into core and valence states, which are described by core and valence basis-functions. The core functions are created using spherical potential and they become zero at the surface of the atomic sphere. Therefore core functions are not APWs but just atomic like functions inside the atomic sphere with no contribution to the eigenfunctions outside the sphere (in WIEN2K/WIENNCM they are treated fully relativistically). The valence states on the other hand are extended outside the atomic sphere and therefore obtained by the LAPW method. In this context the valence functions are orthogonal to the core functions. But there are other states, which do not fall completely into either category. They are the semi-core states (high lying core states). These states do not extend beyond the atomic sphere significantly nor are they fully inside the atomic sphere. A problem appears if for a particular atom, two states with different n but with the same l should be treated with LAPW. An example would be the bcc Fe. The valence states contain a non negligible amount of 4p character, 0.2Ry below E_F and at the same time 4.3Ry below E_F , the 3p state, that belong to the above discussed semi core state. Now the question would arise how to select the linearization energy $E_{l=1}$, close to 3p or 4p or in between. Any of the above selection would not be an optimal choice. To solve this dilemma another type of functions, the so called local orbitals (LO) are added (altogether known as LAPW+LO method) [47], as shown below.

$$\phi_{lm}^{LO}(\vec{r}) = \begin{cases} \left[A_{lm}^{LO} u_l(\vec{r}, E_1^1) + B_{lm}^{LO} \frac{\partial u_l(\vec{r}, E_1^1)}{\partial E} + C_{lm}^{LO} u_l(\vec{r}, E_1^2) \right] Y_{lm}(\vec{r}) & \text{within the atomic sphere} \\ 0 & \text{in the interstitial region} \end{cases} \quad (2.34)$$

It is constructed from u and $\partial u/\partial E$ of LAPW at one energy E_1^1 in the valence band region (eg. 4p of Fe) and from another u at another energy E_1^2 in the semi core region (eg. 3p of Fe). The coefficients are determined from the normalization condition and from the condition that the LO should vanish in value and slope at the surface of the atomic sphere and therefore not connected to the plane waves in the interstitial region. This increases the basis set slightly (therefore the computation time) but compared to the basis set of LAPW alone this increase is negligible (only one function per lm combination: 3 for p like functions and 5 for d like functions) and at the same time increases the accuracy.

As shown above, the main disadvantage of the APW method is the energy dependence of its basis functions and this is removed in the LAPW (LAPW+LO) but at the cost of a much larger basis set. Sjöstedt [48] introduced a method, where the basis-functions would be energy independent but at the same time the size of the basis set would remain as in the APW method, thus the advantages of the APW and LAPW+LO would be combined. Hereby the basis set is constructed from two types of functions. The first ones are the APWs but at fixed energies.

$$\varphi(\vec{r}) = \begin{cases} \sum_{l,m} A_{lm} u_l(\vec{r}, E_1) Y_{lm}(\vec{r}) & \text{within the atomic sphere} \\ \frac{1}{\Omega^2} \sum_{\vec{G}} C_{\vec{G}} e^{i(\vec{k}+\vec{G})\vec{r}} & \text{in the interstitial region} \end{cases} \quad (2.35)$$

But as discussed above within the APW scheme the eigenfunctions are badly described (energy dependence). Therefore the basis-functions within the atomic sphere are augmented with a second type of functions, the local orbitals, but in contrast to the LAPW+LO the same set of fixed energies E_1 are used as for APW and it is abbreviated as lo.

$$\varphi_{lm}^{lo}(\vec{r}) = \begin{cases} \left[A_{lm}^{lo} u_l(\vec{r}, E_1) + B_{lm}^{lo} \frac{\partial u_l(\vec{r}, E_1)}{\partial E} \right] Y_{lm}(\vec{r}) & \text{within the atomic sphere} \\ 0 & \text{in the interstitial region} \end{cases} \quad (2.36)$$

The coefficients are determined from the normalization condition and from the condition that the value of the LO should vanish at the surface of the atomic sphere but not its slope. Therefore both the APW and lo would be continuous at the surface, but their first derivative

may be discontinuous at the surface. This method is called the APW+lo method. As in the LAPW+LO method, where fixed energies are used in the APW+lo method, all the eigenenergies could be found by a single diagonalization. The APW+lo method has the same problem with semi core states as in the LAPW method and is cured by using local orbitals (now LO) as in the LAPW+LO. This extension is known as the APW+lo+LO. In the default set up of the input file case.in1 in WIEN2K/WIENNCM, a mixed basis set method is used. For the states with $l=0,1,2,3$ the APW+lo (and if necessary APW+lo+LO) is used, whereas for the higher l values the LAPW with a global linearization energy is used.

At this stage it is also important to mention the form of the Coulomb potential V (V_H+V_{ext}) which is used. For valence and semi-core states atom like functions are used within the sphere and a Fourier representation is used in the interstitial region.

$$V(\vec{r}) = \begin{cases} \sum_{l,m} V_{lm}(\vec{r}) Y_{lm}(\vec{r}) & \text{within the atomic sphere} \\ \sum_{\vec{G}} V_{\vec{G}} e^{i\vec{G}\vec{r}} & \text{in the interstitial region} \end{cases} \quad (2.37)$$

This is known as the full potential which is obtained from the total charge density ρ by solving the Poisson's equation and from this, after adding V_{XC} and T_0 contributions, the valence density ρ_{val} could be calculated from the eigen-functions. The core density ρ_{core} on the other hand is obtained from the muffin tin approximation of the full potential, only including the $l=0$ and $G=0$ contributions to V (spherical average within the atomic sphere and volume average in the interstitial region). The addition of ρ_{val} and ρ_{core} gives the total charge density ρ .

2.1.7.7 Scalar relativistic approximation and the inclusion of the spin-orbit coupling (SOC) in a second variational step

Up to now only the non relativistic contribution to the Hamiltonian is described. Relativistic effects such as spin-orbit coupling cannot be neglected for heavier atoms and become important for Co or Ir, which have partially filled d bands, giving rise to a net orbital moment, whose magnitude is determined by the crystalline field, which may lock the spin moment in a particular direction in real space. Other relativistic contributions to the Hamiltonian are the correction to the kinetic energy and the Darwin term. It is not intended to describe the

relativistic quantum mechanics in detail (see [49]) and therefore start with the Dirac equation in the Hamiltonian form:

$$H_D = c\vec{\alpha}\vec{p} + (\beta - 1)mc^2 + V(\vec{r}) \quad , \quad (2.38)$$

$\vec{\alpha} = \begin{pmatrix} \vec{\sigma} & 0 \\ 0 & \vec{\sigma} \end{pmatrix}$ 4×4 matrix, $\sigma_x, \sigma_y, \sigma_z$:Pauli matrices, $\vec{\beta} = \begin{pmatrix} I & 0 \\ 0 & -I \end{pmatrix}$ 4×4 matrix, V: Coulomb potential (only)

The eigenfunctions φ have four components and are usually written as two component functions Φ and χ , the former known as the large component (dominating component) and the latter as small components concerning the electron solutions.

$$\varphi = \begin{pmatrix} \Phi \\ \chi \end{pmatrix} \quad (2.39)$$

Insertion of φ to eq. 2.38 yields a couple of coupled equations, from which the equation for Φ could be extracted. For the present work the solutions of the Dirac equation in a spherical potential V is of importance, as this describes the wavefunctions within the atomic sphere. After some cumbersome manipulation the equation of Φ (χ can be constructed from Φ) for spherical V becomes:

$$\left[T + V - \frac{p^4}{8mc^2} - \frac{\hbar^2}{4m^2c^2} \frac{dV}{dr} \frac{\partial}{\partial \vec{r}} + \frac{1}{2m^2c^2} \frac{1}{r} \frac{dV}{dr} (\vec{l}\vec{s}) \right] \Phi = \varepsilon \Phi \quad (2.40)$$

The first two terms are the same as within the Schrödinger eq. The third term is a relativistic correction for T. The fourth is the so called Darwin term that describes the “Zitterbewegung” of the electrons. The last term results from the awaited spin-orbit coupling (SOC), resulting from the magnetic field that a moving electron feels out of an electrostatic potential. Because of SOC l and s are no more good quantum numbers but j and j_z are good quantum numbers together with a new quantum number $\kappa = \pm(j+1/2)$. From the sign of κ it could be seen whether j and s are parallel ($\kappa < 0$) or anti-parallel ($\kappa > 0$). Now φ can be written as follows:

$$\varphi = \begin{pmatrix} \Phi \\ \chi \end{pmatrix} = \begin{pmatrix} g(r)y_{j_z, l_\Phi} \\ f(r)y_{j_z, l_\chi} \end{pmatrix} \quad (2.41)$$

Each of Φ and χ are written as product of radial functions $g(r)$ and $f(r)$ and angular functions $y_{j_z, l_{\Lambda(B)}}$. The angular functions in turn are written as combinations of the product of spherical harmonics and (two component) spinors.

$$y_{j_z, l_{\Lambda(B)}} = \pm \sqrt{\frac{l + j_z + \frac{1}{2}}{2l + 1}} Y_l^{j_z - 1/2} \begin{pmatrix} 1 \\ 0 \end{pmatrix} + \sqrt{\frac{l - j_z + \frac{1}{2}}{2l + 1}} Y_l^{j_z + 1/2} \begin{pmatrix} 0 \\ 1 \end{pmatrix} \quad (2.42)$$

Inserting φ into eq. 2.38 yields once again a couple of coupled equations from which the equation for g could be separated and f (needed for proper normalization) could be calculated from this.

$$-\frac{\hbar^2}{2Mr^2} \frac{d}{dr} \left(r^2 \frac{dg}{dr} \right) + \left[V + \frac{\hbar^2}{2Mr^2} \frac{l(l+1)}{r^2} \right] g - \frac{\hbar^2}{4Mc^2} \frac{dV}{dr} \frac{dg}{dr} - \frac{\hbar^2}{4Mc^2} \frac{dV}{dr} \frac{1+\kappa}{r} g = \varepsilon g \quad (2.43)$$

$$f = \frac{\hbar}{2mc} \left(\frac{dg}{dr} + \frac{1+\kappa}{r} g \right) \quad (2.44)$$

$$M = m + \frac{\varepsilon - V}{2c^2}$$

In WIEN2K core states are treated fully relativistically and the following considerations are valid for valence states. If the term that depends on κ would be omitted, SOC would be eliminated and l and s become good quantum numbers which is an advantage. This form of approximation is known as scalar relativistic approximation and is the default option in WIEN2K for valence states. The large component $\tilde{\Phi}$ (\sim to denote the approximation) becomes a pure spin state ($\tilde{\chi}$ is mixed but not important).

$$\tilde{\Phi} = \tilde{g} Y_{lm} \chi_s \quad (2.45), \quad s = \uparrow, \downarrow, \chi_\uparrow = \begin{pmatrix} 1 \\ 0 \end{pmatrix}, \chi_\downarrow = \begin{pmatrix} 0 \\ 1 \end{pmatrix}$$

Therefore the scalar relativistic version could be used in place of the Schrödinger equation with the LAPW/APW+lo basis set with minor additional relativistic terms.

The correction to the contribution due to SOC would be added in a second step. As it is obvious $\tilde{\varphi}$ is not an eigenfunction of the Dirac equation and applying the Dirac equation to $\tilde{\varphi}$ yields:

$$H_D \tilde{\varphi} = \tilde{\varepsilon} \tilde{\varphi} + H_{\text{SOC}} \tilde{\varphi} \quad (2.46)$$

$$H_{\text{SOC}} = \frac{\hbar^2}{2Mc^2} \frac{dV}{dr} \frac{1}{r} \begin{pmatrix} \vec{\sigma} \cdot \vec{l} & 0 \\ 0 & 0 \end{pmatrix} = \frac{\hbar^2}{2Mc^2} \frac{dV}{dr} \frac{1}{r} \begin{pmatrix} l_z & (l_x - il_y) \\ (l_x + il_y) & -l_z \end{pmatrix} \quad (2.47)$$

H_{SOC} is the contribution due to SOC and is a measure of the extent to which $\tilde{\varphi}$ fails to be an eigenfunction of the Dirac equation. In order to include SOC, the starting point would be the LAPW/APW+lo basis set obtained by solving the coupled equations (and summing up). As s is a good quantum number, spin up and spin down states could be considered separately.

$$\varphi_{\text{ms}} = \begin{pmatrix} \tilde{g}_{ls} Y_{lm} \chi_s \\ -i \tilde{f}_{ls} Y_{lm} \chi_s \end{pmatrix} \quad (2.48), \quad s = \uparrow, \downarrow, \chi_{\uparrow} = \begin{pmatrix} 1 \\ 0 \end{pmatrix}, \chi_{\downarrow} = \begin{pmatrix} 0 \\ 1 \end{pmatrix}$$

From $\vec{\sigma} \cdot \vec{l}$ in H_{SOC} it is clear that this has non diagonal matrix elements that would couple spin up and spin down states, thus the obvious way would be to double the basis set size, which is of course difficult for larger systems. Instead of this in WIEN2k (following [50]) the basis set is obtained scalar relativistically in a first variational step and in a second variational step now including H_{SOC} the same basis set would be used to calculate the contributions from the non diagonal terms (as the diagonal terms are already calculated in the first step).

2.1.7.8 Non-collinear magnetism (NCM) and its implementation in WIENNCM

As the name suggests, NCM arises if the spins are ordered non-collinearly. Examples for such orderings are canted AFM, spiral, helical, conical or even more complicated ordering of the magnetic moments. Primarily NCM results from competing AFM and FM interactions, which are pronounced in frustrated lattices, such as two dimensional triangular, Kagome, three dimensional fcc and pyrochlore lattices. Another important factor in determining NCM is the

SOC, resulting in certain cases of magnetocrystalline anisotropy, which is a consequence of the strong coupling of the spin moments to the lattice in certain directions or in anisotropic Dzyaloshinski-Moriya interactions. An important feature of many compounds undergoing NCM is the spin-reorientation transition in an external magnetic field and the resulting metamagnetic states. NCM within the DFT is an ideal tool to theoretically investigate such phenomenon. In the following the implementation of NCM within the DFT is discussed.

Starting point would be the Dirac equation, in which for simplicity the part of the Hamiltonian that is applied to the smaller component of the eigenfunction is neglected. From the Dirac equation the so called Pauli equation is obtained. Furthermore in the previous sections the exchange-correlation field B_{XC} , which makes spin polarization possible, is not explicitly mentioned, included implicitly through the spin densities. For the present case this would be explicitly included. The external magnetic field B_{ext} is also important in the present work as for certain calculations the direction of the magnetization density should be fixed in some directions with this external field. Contributions from SOC and U are discussed later. The Hamiltonian becomes:

$$\hat{H}_P = \hat{T}_0 + \hat{V}_H + \hat{V}_{XC} + \hat{V}_{ext} + \mu_B \vec{\sigma} (\vec{B}_{XC} + \vec{B}_{ext}) \quad (2.49)$$

\vec{B}_{ext} : external magnetic field

Within the LDA \hat{V}_{XC} and \vec{B}_{XC} become:

$$\hat{V}_{XC} = \varepsilon_{XC}(\rho, m) + \rho \frac{\partial \varepsilon_{XC}(\rho, m)}{\partial \rho} \quad (2.50), \quad \vec{m} : \text{magnetization density}$$

$$\vec{B}_{XC} = \rho \frac{\partial \varepsilon_{XC}(\rho, m)}{\partial m} \vec{m} \quad (2.51), \quad \vec{B}_{XC} \parallel \vec{m}$$

In the collinear case all the magnetic moments are aligned in the same direction and the spin quantization axis could be selected along \vec{m} . Selecting the z axis in the spin space as the quantization axis, the Hamiltonian becomes diagonal in the spin space, thus the spin up and spin down channels are separately treated.

$$\vec{\sigma}(\vec{B}_{XC} + \vec{B}_{ext}) = \sigma_z (\vec{B}_{XC} + \vec{B}_{ext}) \quad (2.52)$$

$$\hat{H} = \begin{pmatrix} \hat{T}_0 + \hat{V}_H + \hat{V}_{XC} + \hat{V}_{ext} + \mu_B \vec{\sigma}(\vec{B}_{ext} + \vec{B}_{XC}) & 0 \\ 0 & \hat{T}_0 + \hat{V}_H + \hat{V}_{XC} + \hat{V}_{ext} - \mu_B \vec{\sigma}(\vec{B}_{ext} + \vec{B}_{XC}) \end{pmatrix} \quad (2.53)$$

In the non-collinear case \vec{m} varies in space and all three components of $\vec{\sigma}(\vec{B}_{XC} + \vec{B}_{ext})$ may contribute.

$$\vec{\sigma}(\vec{B}_{XC} + \vec{B}_{ext}) = \begin{pmatrix} B_z & (B_x - iB_y) \\ (B_x + iB_y) & -B_z \end{pmatrix} \quad (2.54)$$

$$\hat{H} = \begin{pmatrix} \hat{T}_0 + \hat{V}_H + \hat{V}_{XC} + \hat{V}_{ext} + \mu_B B_z & \mu_B (B_x - iB_y) \\ \mu_B (B_x + iB_y) & \hat{T}_0 + \hat{V}_H + \hat{V}_{XC} + \hat{V}_{ext} - \mu_B B_z \end{pmatrix} \quad (2.55)$$

The Hamiltonian is not diagonal in the spin space, thus the spin up and spin down channels are coupled via the non diagonal matrix elements and cannot be treated separately. The diagonalization should be performed in one step in the 2×2 spin space. As already mentioned in section 2.1.7.7, this requires spinors as basis function. In the interstitial region pure spinors are used as basis functions in the global spin frame (g , spin index σ). In this region the Hamiltonian contains only the terms listed in eq. 2.55. The symbols have their usual meaning as above.

$$\varphi_{\vec{G},\sigma}(\vec{r}) = e^{i(\vec{G}+\vec{k})\vec{r}} \chi_{\sigma}^g \quad (2.56)$$

Inside the atomic spheres combinations of pure spinors are used as basis function in a local coordinate frame (λ , spin index σ^λ), where each atomic sphere has its own local coordinate system and the quantization axis z is along the direction of the average magnetization. The expressions for LAPW, APW and LO within the spinor formulation are given below.

$$\varphi_{\sigma}^{LAPW}(\vec{r}) = \sum_{\sigma^\lambda} \sum_{l,m} \left[A_{lm}^{\sigma\sigma^\lambda} u_l^{\sigma^\lambda}(\vec{r}, E_1) + B_{lm}^{\sigma\sigma^\lambda} \frac{\partial u_l^{\sigma^\lambda}(\vec{r}, E_1)}{\partial E} \right] Y_{lm}(\vec{r}) \chi_{\sigma^\lambda} \quad (2.57)$$

$$\varphi_{\sigma}^{\text{APW}}(\vec{r}) = \sum_{\sigma^{\lambda}} \sum_{l,m} A_{lm}^{\sigma\sigma^{\lambda}} u_1^{\sigma^{\lambda}}(\vec{r}, E_1) Y_{lm}(\vec{r}) \chi_{\sigma^{\lambda}} \quad (2.58)$$

$$\varphi_{\sigma^{\lambda}}^{\text{LO}}(\vec{r}) = \left[A_{lm}^{\text{LO},\sigma^{\lambda}} u_1^{\sigma^{\lambda}}(\vec{r}, E_1^1) + B_{lm}^{\text{LO},\sigma^{\lambda}} \frac{\partial u_1^{\sigma^{\lambda}}(\vec{r}, E_1^1)}{\partial E} + C_{lm}^{\text{LO},\sigma^{\lambda}} u_1^{\sigma^{\lambda}}(\vec{r}, E_1^2) \right] Y_{lm}(\vec{r}) \chi_{\sigma^{\lambda}} \quad (2.59)$$

For LAPW/APW the coefficient matching of spherical harmonics to the plane waves corresponding to $\sigma=\uparrow,\downarrow$ is done in the global coordinate frame for $A_{lm}^{\sigma\sigma^{\lambda}}$ and $B_{lm}^{\sigma\sigma^{\lambda}}$, thus they depend on both global and local spin index σ and σ^{λ} respectively. The LO on the other hand vanishes at the surface of the atomic sphere, thus $A_{lm}^{\sigma^{\lambda}}$, $B_{lm}^{\sigma^{\lambda}}$ and $C_{lm}^{\sigma^{\lambda}}$ depend only on the local spin index σ^{λ} . Concerning the Hamiltonian inside the atomic sphere, the eq. 2.55 may have additional terms from SOC (section 2.1.7.7), orbital dependent potential such as U (section 2.1.7.9) and/or constraining external magnetic field B_c , defined as:

$$\hat{H}_c = \mu_B \vec{B}_c \sigma = \begin{pmatrix} 0 & \mu_B (B_{c,x} - iB_{c,y}) \\ \mu_B (B_{c,x} + iB_{c,y}) & 0 \end{pmatrix} \quad (2.60)$$

Such constraint fields are used in the present work to fix the magnetic moment of Cobalt in a certain fixed direction during the self consistency procedure. Note that in the NCM case the diagonalization is performed in the 2×2 spin space, thus for SOC a second variational step as in the collinear case is not needed. Concerning the spin density inside the atomic spheres, there are two further possibilities. In the atomic moment approximation (AMA), only the diagonal part of the potential would be used, ignoring the non diagonal part, resulting in the collinearity of the spin magnetization inside each atomic sphere, but different spheres may have different orientations. On the other hand in the full non collinearity mode (FULL), the non diagonal terms are also used, resulting in a variation of the spin magnetization also inside the atomic spheres. Exclusively the latter option is used in the present work.

2.1.7.9 Highly correlated electron systems and concepts beyond the LSDA/GGA approximation: LSDA/GGA+U approximation

2.1.7.9.1 Theoretical background

In the following highly correlated electron systems are considered, which typically contain partially filled localized d or f orbitals. Table 2.1 shows some transition metal monoxides with experimentally found band gaps and calculated band gaps (or behaviour at Fermi-level) within the LSDA/GGA approximation. Additionally partial DOS of NiO and MnO are shown in fig. 2.3 (a) and (b).

Table 2.1: Experimental and calculated (fundamental) band gaps within LSDA and GGA. The values are taken from [51].

	Experimental band gap (eV)	Calculated band gap (eV)	
		LSDA	GGA (PBE)
NiO	4.0 - 4.3	0.4	0.9
MnO	3.9	0.8	0.9
CoO	2.5	0.0	0.0
FeO	2.4	0.0	0.0

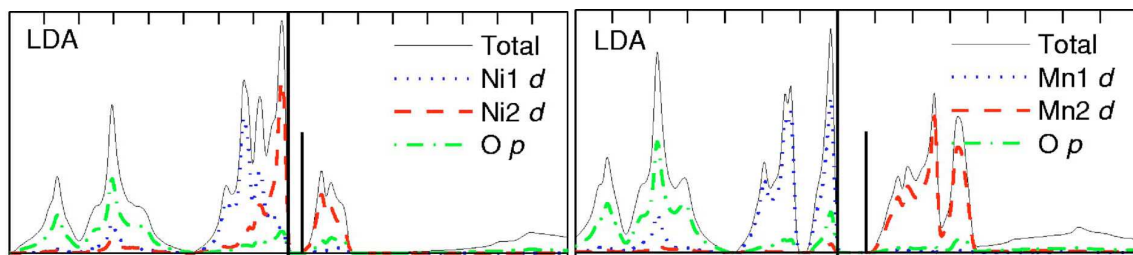


Fig. 2.3: DOS within the LDA for (a) NiO and (b) MnO [51].

Comparing Table. 2.1 with the DOS in fig. 2.3 (a)-2.3 (b), it is evident that in case of NiO and MnO the calculated band gaps are underestimated almost an order of magnitude within the LSDA/GGA approximation. In case of CoO and FeO the LSDA/GGA totally fails to reproduce even the behaviour of the DOS qualitatively at the Fermi level, predicting them to be metallic (table 2.1). The qualitative insulating behaviours of NiO and MnO within LSDA/GGA, are even coincident cases. In the former, the crystal field splits the completely filled down spin t_{2g} d bands of Ni from the empty e_g d bands of Ni, that is above the Fermi

level and in the latter the exchange interaction described by the first Hund's rule completely shifts the empty up spin d bands of Mn against the completely filled down spin d bands of Mn (fig. 2.3(a)-fig. 2.3(b)). In both of the above cases, the band gap is obtained as a result that the number of d electrons is such as they completely fill the lower d bands, creating a gap in the DOS that is too small in comparison with the one which is determined by photoelectron spectroscopy measurements. A similar development is also known to be happening in semiconductors, where LSDA/GGA predicts a much smaller band gap than the experimentally observed one. However the behaviour of LSDA/GGA in case of highly correlated materials should be viewed differently from the conventional semiconductors, as regarding the former LSDA/GGA in most cases predict the crystal and magnetic structures fairly well but fail to predict the behaviour of their DOS at the Fermi level. To find the reason why LSDA/GGA failed to describe the electronic structure of strongly correlated materials, a gedankenexperiment, which was suggested by Sir Neville Mott would be recalled in the following. The band theory, which is based on the non-interacting or weakly interacting electrons, explains the difference between metals and insulators in the following way. For a metal the Fermi level lies inside the highest occupied band and for an insulator in the band gap. As shown above, this does not hold for transition metal oxides. In the following a hydrogen-like lattice system (each atom has only one electron) at $T=0$ would be considered, where the atoms occupy lattice sites. Initially the inter-atomic distance is thought to be so small, that the electron wave functions overlap and form a band. Now the inter-atomic distance would be continuously increased. It could be observed that the electronic states of vanishing width crossing the Fermi level, but retaining the metallic character. At an infinitive inter atomic distance the system would become insulating as the electronic states around the Fermi level would produce an extremely localized charge distribution around the atoms. In this extreme limit, the hopping of the electron between the atomic sites is thus prevented. The realization of an insulating state "only" at infinitive inter-atomic distance is the result of the inadequacy based on the description of the band theory. The solution of this problem lies in the electron-electron interaction, which is neglected so far in this gedankenexperiment and treated by several authors in different ways [52-54]. Therefore two factors should be considered here, namely the kinetic energy of the electrons, which is manifested by the bandwidth W and the energy that has to be paid as an electron approaches regions where other electron are localized (ionic cores), which is manifested by the Coulomb (repulsion) interaction parameter U . In strongly correlated materials some of the electrons are supposed to spend their time in regions of ionic cores, where they feel strong Coulomb repulsion and

therefore affects their motion. In simple metals, where the electron-electron scattering is negligible, the electrons spend infinitively small time in these regions. If the kinetic energy is the dominant contribution, then the electrons can overcome this on-site Coulomb repulsion, delocalize themselves and thus minimize their kinetic energy. The band width W can be seen as a measure of this effect. On the other hand if the bands in which the electrons move are localized due to high effective mass, the kinetic energy becomes low and therefore it cannot overcompensate the on-site Coulomb repulsion thus the electrons localize in some regions (correlation dominates) and the system becomes insulating (Mott-Hubbard type insulators). Typically the world of strongly correlated materials starts on the verge of $W/U \leq 1$. Now it is evident why band structure methods are not the best approach to observe such behaviour, as they manifest the one electron theory and correlation as seen in the above sections is a many body phenomena. Within the LSDA/GGA the exchange-correlation contribution is also treated in a mean-field way as the values are taken from calculations that are carried out for homogeneous electron gas, that are not accurate enough to describe correlation effects. Therefore model-Hamiltonians have manifested themselves as theoretical methods to investigate such Mott-Hubbard insulators and highly correlated systems, where the band width and electron correlation are explicitly included and this allows one to investigate the behaviour of the systems in different regimes of the competing factors. The Anderson impurity model [55] and the Hubbard model [54] are examples of such model-Hamiltonians, where the delocalisation is described by the hopping amplitudes t_{ij} and the on-site Coulomb repulsion by U . Unfortunately these models do not include the effects coming from the position of the nuclei in the crystal structure or from different kinds of atoms. Therefore numerically accurate results could not be obtained because of these above simplifications. Furthermore these models are also strongly parameter dependent (U , t_{ij}). In the past two decades there were a lot of efforts to combine the ab initio calculation scheme with the model-Hamiltonian concept in order to obtain a maximum efficient way of treating strongly correlated materials. One such concept resulted in the LSDA/GGA+ U method, which is used in the present work in two different flavours. This method is successfully applied for a number of systems containing highly correlated electrons, however at the same time it is also controversially discussed as it contains the input parameter U (also the parameter J , derived from the Hund's rules), which in some cases should be varied at a particular range in order to obtain the correct magnitude of the band gap. Nevertheless the use of LSDA/GGA+ U is justified to the fact that it represents the static limit of the so called "dynamical mean field theory" (DMFT) [56]. As it is mentioned in the previous sections, the main concept behind

the LSDA/GGA+U is that to somehow correct the LSDA/GGA approximation, thus to go beyond the description of the electron-electron interaction within the homogeneous electron gas approximation. In the following the correction of LSDA/GGA through the inclusion of U is discussed.

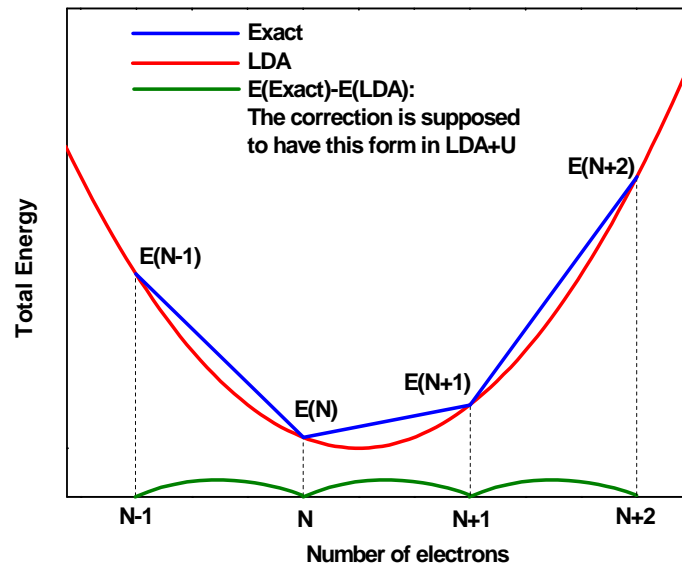


Fig. 2.4: The total energy as a function of the number of electrons N for “exact” and LDA cases. The difference of these energies is plotted in the bottom part of the figure. Note that the minimum of $E(N)$ at N for the “exact” case results from the consideration by Perdew [57] that the ordinate of the segment is the difference between the ionization potential I and the electron affinity. The difference between the smallest first I (3.89 eV for Cs) and the biggest A (3.62 eV for Cl) in the periodic table is positive.

Perdew [57-59] considered the following problem. An atom in contact with a reservoir of electrons (eg. other atoms containing electrons), can only exchange integer number of them with the reservoir. Fractional occupancies of the orbitals arise only in open systems, as a time average of states with orbitals occupied with integer number of electrons. In quantum mechanics, an open system with a fluctuating number of particles are not described by a pure state but by a statistical mixture or ensemble, which is defined by a set of pure states and their respective probabilities. The total energy E and the average number of particles (electrons) in the system n could be written as follows.

$$E = (1 - \omega)E_N + \omega E_{N+1} \quad (2.61)$$

$$n = (1 - \omega)N + \omega(N + 1) = N + \omega \quad (2.62)$$

In this context, E_N and E_{N+1} represent the total energies of the state of the system containing N and $N+1$ electrons, respectively, whereas $0 \leq \omega \leq 1$ is the statistical weight of the state containing $N+1$ electrons, thus the total energy of this open system is a series of straight line segments, that are joined at integer values of N and the slopes of these straight line segments correspond to the eigenvalues of the orbitals that are being filled (in the time averaged sense). These straight line segments fulfil in fact the continuity at the integer values of N but not differentiable as shown in fig. 2.4. This results in a discontinuity in the functional derivative at integer values of N (exchange-correlation potential). Gunnarsson and Schönhammer [60] showed that this above discontinuity in the functional derivative could give large contributions to the band gap at least for the finite linear chain of atoms. But this behaviour of $E(N)$ is not well reproduced by LDA approximation, which creates unphysical total energy minima at fractional occupancies. This problem is more evident if the inter atomic distance is increased to the dissociation limit. This would mean that the system would dissociate into parts with fractional electron occupancies, which is of course a paradox (eg: Separated LiH within the LDA [57]). But constraining the orbital occupancy to integer values in LDA reproduces the energy difference between different states quite well (the LDA curve touches the segments at integer values). The alternative method of compensating this deficiency, without constraining the orbital occupation is to analyse the form of the difference between “exact” and LDA cases and try to add a correction term in the form of this difference to the as correlated considered orbitals. The definition of a correction term should be based on this fact. In the following two different flavours of LSDA+U will be presented, which are based on this idea.

2.1.7.9.2 LSDA/GGA+U correction term ΔV

The LSDA+U functional is usually coded in the so called rotationally invariant way, that is, it does not depend on the choice of the basis set [619]. The LSDA+U functionals, that are used in the present work could be written as a sum of two different terms.

$$\Delta V = V_I - V_{DC} \quad (2.63)$$

The first term includes the direct (on-site) Coulomb repulsion U as in a model Hamiltonian approach and the spin dependent Hund's exchange contribution J , where m and σ denote the orbital and spin index and n orbital occupation. The role of J is that, electrons of same spin would feel around J reduced Coulomb repulsion as they are already constrained by the Pauli principle, whereas electrons with opposite spin would feel the whole U . This term is the same for both of the functionals that are considered here.

$$V_1 = \frac{1}{2} \sum_{m\sigma \neq m'\sigma'} (U_{mm'} - J_{mm'} \delta_{\sigma\sigma'}) n_{m\sigma} n_{m'\sigma'} \quad (2.64)$$

The second term V_{DC} is the so called double counting correction term, which is included in a mean field way, in order to compensate the Coulomb contribution already included within the LSDA, thus this not be included twice. This term differs from functional to functional and in many cases has a big influence on the self consistent solution. Apart from V_{DC} the input parameters U and J and the projection method used to determine the occupation numbers would also influence the self consistent solution. Selection of U and J values are seen critically as in many cases they should be manually varied in a certain range in order to obtain the preferred solution (width of the band gaps). Approximate values for U and J could be obtained from the so called constrained LSDA calculations [62] and these values are used for calculations in the present work.

2.1.7.9.3 Fluctuation form of LSDA/GGA+U: around the mean field method (AMF)

This method was introduced by Anisimov et al. [63] for the non spin-polarized case and it was later expanded to the spin polarized case by Czyzyk et al. [64].

$$\Delta V^{AMF} = \frac{1}{2} \sum_{m\sigma \neq m'\sigma'} (U_{mm'} - J_{mm'} \delta_{\sigma\sigma'}) (n_{m\sigma} - \bar{n}_\sigma) (n_{m'\sigma'} - \bar{n}_{\sigma'}) \quad (2.65), \quad \bar{n}_\sigma = \frac{N_\sigma}{(2l+1)}$$

Hereby \bar{n}_σ describes the average occupation and N_σ the number of electrons of a single spin sort of the correlated orbitals. The energy difference (energy correlation) comes from the angular fluctuations away from the spin-dependent average value. Therefore the above expression becomes zero if all the orbitals of a spin sort of a shell are equally occupied. This

is the case for half filled completely spin-polarized 4f shell of Gd, where AMF has no contribution at all.

2.1.7.9.4 The fully localized limit (FLL)

In order to describe systems like 4f of Gd, where $n_{m\sigma} = \bar{n}_\sigma$, Czyzyk et al [64] introduced a new functional called the atomic limit (AL), which is widely known since then as the fully localized limit (FLL). A J=0 version of this functional was already introduced by Anisimov et al [65]. The new feature of this functional could be seen from eq. 2.65 of AMF, where the term corresponding to mean field (average occupation \bar{n}_σ) was subtracted to compensate for the onsite Coulomb interaction considered already in LSDA (double counting term). Instead of this mean field, in the FLL the total energy contribution of an open shell of a localized atom containing degenerate orbitals (N_σ electrons per spin sort) within the Hartree-Fock approximation is subtracted. This double counting term could be written as follows:

$$V_{DC} = \frac{1}{2} \left[UN(N-1) - J \sum_{\sigma} N_{\sigma} (N_{\sigma} - 1) \right] \quad (2.66)$$

Thus the resulting correction term ΔV^{FLL} becomes:

$$\Delta V^{FLL} = \frac{(U-J)}{2} \sum_{m\sigma} n_{m\sigma} (1 - n_{m\sigma}) \quad (2.67)$$

This is a non negative term (as $U \gg J$), vanishes at integer values of $n_{m\sigma}$ and has the form of an inverted parabola. By recalling fig. 2.4, it is evident that this term resembles the form of $E(\text{LSDA}) - E(\text{exact})$ which is needed to cure the deficiency of LSDA and thus the effect of LSDA/GGA+U is more obvious in the FLL case. The orbital energies could be obtained by applying Janak's theorem (including LSDA) [37]:

$$\varepsilon_{m\sigma} = \varepsilon_{m\sigma}^{\text{LSDA}} + (U-J) \left(\frac{1}{2} - n_{m\sigma} \right) \quad (2.68)$$

The correction part of the orbital energy consists of straight line segments, discontinuous at integer values and thus preferring complete occupation of the orbital. For a completely

occupied orbital ($n_{m\sigma}=1$) the orbital energy is shifted around $-(U-J)/2$ and for an unoccupied orbital it is shifted around $+(U-J)/2$, making it possible to obtain a gap in the density of states around the Fermi-level (Mott-Hubbard gap). In realistic calculations however hybridization and/or spin-orbit coupling always compete with $n_{m\sigma}=1$ and results in fractional occupancies.

2.2 Double perovskites

In order to understand the structure of a double perovskite, it is necessary to understand the structure of a perovskite, the former being in this context an ordered superstructure variant of the latter. Perovskites have the stoichiometry ABX_3 , where A being usually the larger and B the smaller cation and X being any anion, but in most cases oxygen and thus representing an oxide with perovskite structure. Imagining a cube, the A site cation would occupy the corners and the B site cation the center, which is surrounded by six anions, that occupy the face centers in an octahedral arrangement (corner shared BO_6 octahedra). The A site cation on the other hand is surrounded by twelve oxygen anions in a cubo-octahedral arrangement. The symmetry of this ideal perovskite is described by the space group $Pm\bar{3}m$ and $SrTiO_3$ being the aristotype. But most of the perovskites deviate from this structure and crystallize in a structure with lower symmetry (distorted structure) due to one or more of the following three effects, where the first effect is the most common one.

- (1) Octahedral tilting
- (2) Distortion of bond lengths in BO_6 octahedra
- (3) Displacement of the B site cation

All three effects occur in order to obtain a compromise between the bonding requirements of the A and B site cations and result in a structure with minimum energy, thus the size and the electronic structure of the cations determine the distortion of the structure. An empirical parameter that describes the distortion of the ideal cubic structure is the tolerance factor f introduced by Goldschmidt for close packed hard spheres [66].

$$f = \frac{r_A + r_O}{\sqrt{2}(r_B + r_O)} \quad (2.69), \quad r_i: \text{radius of A, B and O}$$

For the ideal cubic structure $f=1$ and requires the B-O bond length to be a factor $1/\sqrt{2}$ less than the A-O bond length. For other structures f deviates from one and the more it deviates the more is the distortion from the ideal cubic structure. Values of f smaller than one indicate a too small A site cation compared to B site cation in this context, and vice versa. As already mentioned the most common effect is a tilting of the BO_6 octahedra, in order to obtain a compromise of the bond requirements, because of a too small A site cation in the cub-octahedral cage. Generally this tilting is assumed to be nearly rigid, so that it does not affect the bond lengths within the BO_6 octahedra significantly but the twelve A-O bond lengths need not to be equal. The different “nearly rigid” octahedral tilting systems in perovskites are described by the so called Glazer’s notation [67], where tiltings of the octahedra along the three orthogonal axes of the ideal cubic structure are indicated. The general case of unequal tilting along each of the orthogonal axis is denoted by $a^{+-0}b^{+-0}c^{+-0}$. Equal tilting magnitude would be denoted by equal letters. The superscript + describes the in plane tilting, where the octahedra in alternating layers rotate in the same direction, – describes the out of plane tilting, where the octahedra in alternating layers rotate in opposite directions and 0 describes no rotations at all.

A further class of perovskites is obtained by substituting the A or B sites with two or more cations. They may be ordered (partially ordered) or randomly distributed. A double perovskite is obtained if the B site is substituted with two cations (B and B') that are ordered (partially ordered). There are two different arrangements of the B site cations in the structure. They are the rock salt type which is by far the most common arrangement found in double perovskites (fig. 2.5) and the layered type of which only a few examples are known [68].

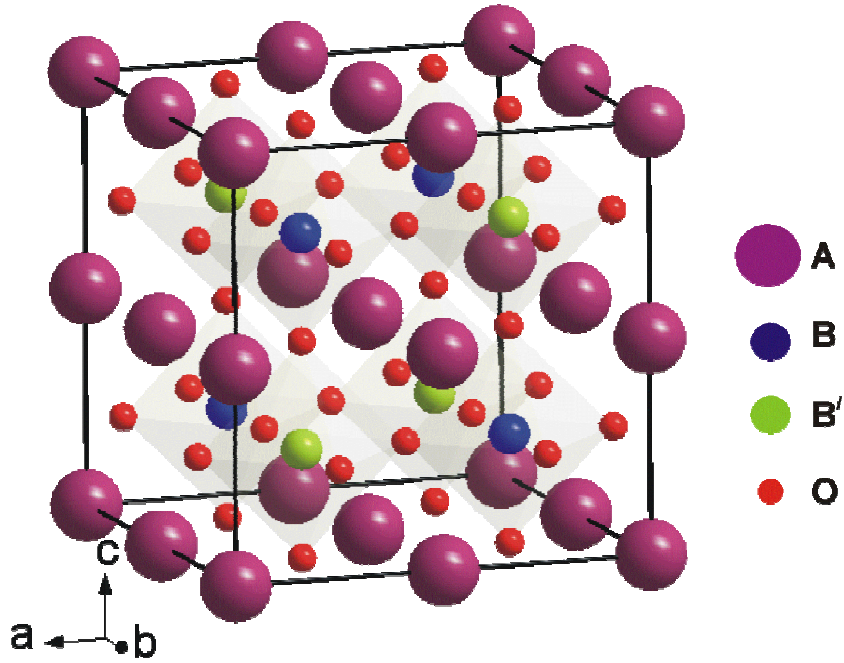


Fig 2.5: Unit cell of a double perovskite of the rock salt type.

Two factors determine the tendency towards ordering, namely the charge difference and the size difference between B and B' [68]. An empirical rule is that small differences in charge (charge difference less than 2) and size (ionic radii differ less than 0.2 Å) prefer the tendency towards a random arrangement, whereas the rock salt arrangement is preferred if the charge difference is two or more. The rarely found layered arrangement is preferred on the boundary of the charge difference of 2 with a difference in size less than 0.2 and in the following only the rock salt arrangement would be considered in this work. In reality most of the “ordered” double perovskites are actually partially ordered, as some amount of B and B'-site cations are intermixed (fig. 2.6 right). Therefore a new parameter is needed in contrast to the ideally ordered double perovskite to describe the degree of this disorder. This parameter is called the site disorder α defined by the following expression:

$$\alpha = \frac{R}{F} \quad (2.70), \quad R: \text{refined mixed occupancy, } F: \text{full occupancy} \quad A_2(B_{1-\alpha}B'_\alpha)(B'_{1-\alpha}B_\alpha)O_6$$

R can be refined in a Rietveld refinement procedure. Considering the above formula it is clear that a fully ordered structure would be obtained for $\alpha=0$ and a random arrangement would be obtained for $\alpha=0.5$.

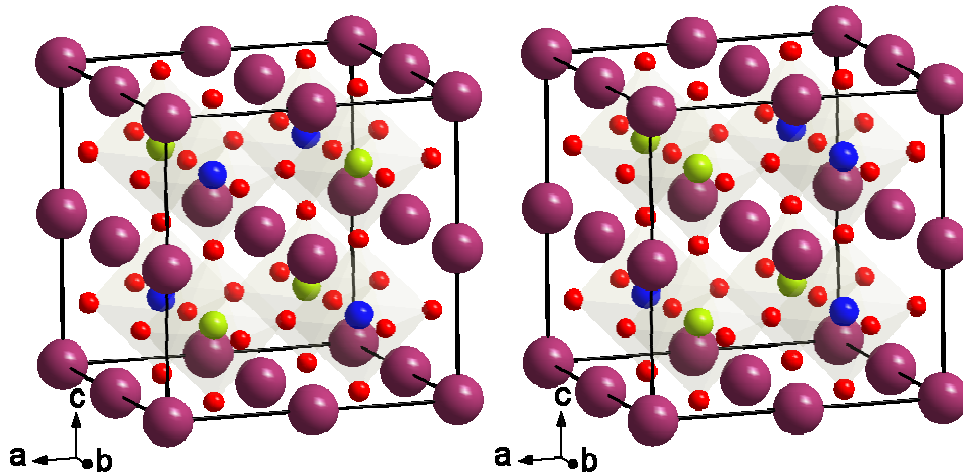


Fig 2.6: Unit cell of a double perovskite of the rock salt type with partial site disorder (right) and for a comparison an ordered double perovskite (left).

As there are now two distinct B sites, the ordering would lead to a change in the symmetry and the ideal cubic structure is now described by the space group $Fm\bar{3}m$ but with doubled cell parameter with respect to the perovskite structure. Distortions in the structure that lead to lower symmetries, arises from the same effects as described for simple perovskite, where the octahedral tilting being the most common one. Double perovskites (or perovskites) of lower symmetry structure may undergo a series of phase transitions (maybe more than one path) to attain higher symmetry by increasing the temperature and/or increasing the size of the A site cation, as the octahedral tilting would gradually become unimportant. In order to investigate such transitions it is important to know in which space groups a double perovskite crystallizes. A group theoretical analysis by Howard et al [69] (also [70]) resulted in 12 possible space groups for double perovskites considering the deviation from the cubic structure only due to octahedral tiltings. These are classified by group-subgroup relationships and the Landau theory is used to analyse whether the phase transition between the space groups should be first or be second order (Fig. 2.7).

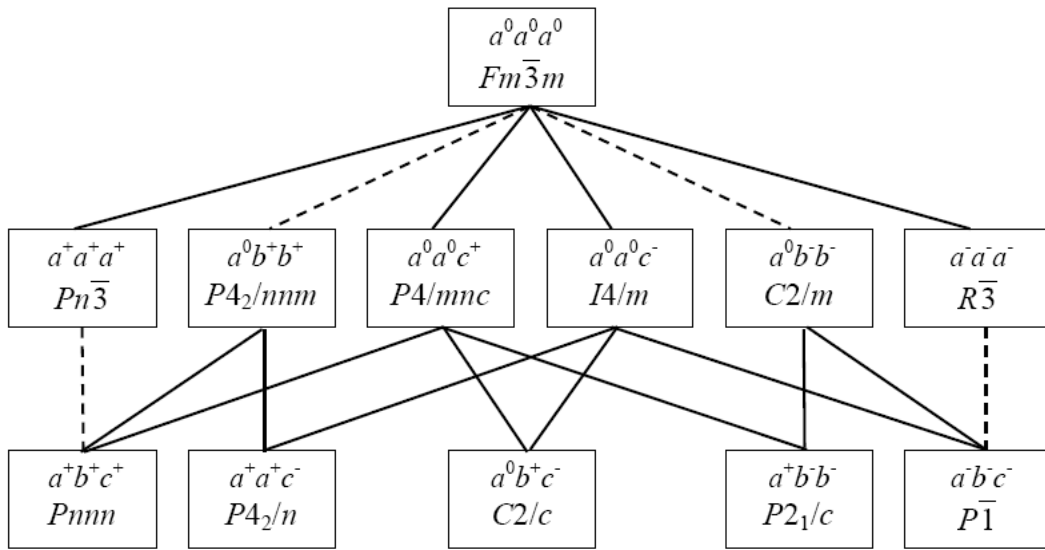


Fig. 2.7: Classification of the 12 possible space groups derived from octahedral tilting in double perovskites [69].

At this point it is also important to sketch the main differences between both orders of structural phase transitions. A phase transition of first order is characterized by a discontinuity in one or more of the first derivatives of the appropriate thermodynamic potential, such as the entropy S and volume V , leading to latent heat or volume jumps. In a crystalline solid concerning structural phase transitions this means primary bonds would be broken and there would be nucleation and growth of a new phase within the primary phase, thus both phases coexist. In this case the group-subgroup relation need not be valid. In contrast a phase transition second order is characterized by a discontinuity in one or more of the second derivatives of the appropriate thermodynamic potential, whereas the first derivatives are continuous, thus no (negligible) latent heat or volume jumps occur. In a crystalline solid concerning structural phase transitions this means that primary bonds would retain and a change in the surrounding of the individual atoms would take place in the whole crystal simultaneously, making the transition continuous. For such a transition, a group-subgroup relation between the involved phases must exist.

Finally the tolerance factor is rewritten for the double perovskites with A-site substitution ($A_2-xA_xBB'O_6$) [71] and their range for different crystal structures are given in table 2.4 [72].

$$f = \frac{\left[\left(1 - \frac{1}{2}x \right) r_A + \frac{1}{2}x r_{A'} \right] + r_o}{\sqrt{2} \left[\frac{(r_B + r_{B'})}{2} + r_o \right]} \quad (2.71), \quad r_i: \text{radius of A, A', B, B' and O}$$

Table 2.4: Correlation between the tolerance factor and the underlying crystal structures of double perovskites.

Tolerance factor f	Crystal structure
$f > 1.05$	hexagonal
$1.05 > f > 1.00$	cubic
$1.00 > f > 0.97$	tetragonal
$f < 0.97$	monocline or orthorhombic

2.3 Determination of the oxidation state (valence state) of the ions in oxides

2.3.1 Introduction

Physical properties are directly dependent on the (valence) charge distribution in a crystal. Therefore the trend of the valence state (oxidation state) within the present system investigated is of high importance. In the present work two methods are employed in order to determine the charge distribution, in other words the oxidation state of the ions involved and its trend within the system. They are the bond valence sum (BVS) and the Bader charges, which needs converged charge densities from DFT calculations. In section 5.7.1 additionally to the above mentioned methods the occupation of the different d bands are obtained by integrating the charge densities within the atomic spheres.

2.3.2 Bond valence sum (BVS)

This method was historically derived from the Pauling's rules for crystal chemistry and developed by I. D. Brown [73]. Within this approximation to a certain extent the bond length is a unique function of the bond valence (strength). The strength of a bond between two atoms

i and j v_{ij} is defined such that the sum of all the strengths of a given atom i is equal to the valence of this atom.

$$V_i = \pm \sum_j v_{ij} \quad (2.72)$$

The valence is negative for an anion and positive for a cation. For most inorganic crystals the valence is close to the formal oxidation state. The most commonly used empirical expression for the bond strength v_{ij} depending on the bond length is given by:

$$v_{ij} = e^{\left(\frac{r_0 - r_{ij}}{B}\right)} \quad (2.73)$$

r_{ij} : bond length between the two atoms, r_0 : reference bond length between the same atoms and B : constant, which is approximately equal to 0.37.

With these expressions the valence can be calculated from the experimentally determined bond lengths.

2.3.3 Bader charges

This method is based on the atoms in molecules (AiM) concept developed by Bader [74], which divides the space into regions using surfaces that run through minima in the charge density. The appropriate regions are chosen such that the gradient of the charge density at any location on the bordering surface has no component normal to the surface. A region within the boundary surfaces is called a Bader region. Integrating the charge density within the Bader region where a given atom's nucleus is located and adding electronic charges in "naturally associated neighboring regions" that do not include a nucleus, yield an estimate of the total excess charge on that atom. However it should be mentioned that this approach does not always give a quantitative assessment of the valence state, but it is quite useful for investigating trends within a certain system. The problem lies in the admixture of ionic and covalent bonds in the above mentioned compounds, which do not only involve the particular atoms of interest [75].

2.4 Electronic conduction in insulators

The temperature dependence of the resistivity is the primary consequence of the electron-phonon scattering. Metals and insulators show different behaviour in this context, depending on the electronic structure at the vicinity of the Fermi level. Whereas the resistivity of metals increases with rising temperature (linearly at moderate to high temperatures), the resistivity of insulators decreases at first, reaches a minimum and increases once again. The electron-phonon scattering is the dominating contribution to the resistivity at higher temperatures, as this scattering depends on the number of phonons, which increases with increasing temperature, describing the range, where the resistivity increases with temperature. Especially at lower temperatures phonons are increasingly frozen, thus the conduction is limited by other mechanisms that depend on the electronic structure. Usually in metals apart from the first scenario this may be limited by scattering of the conduction electrons on d electrons, impurities [76] or due to electron-electron interaction [77]. In all cases the excitation to the unoccupied states is continuous as there is no gap (or the energy due to the potential difference is enough to overcome this) between the occupied and the unoccupied states. In insulators, where most of the transition metal oxides would be categorized, the valence electrons are occupied in narrow bands, as a consequence of the high effective mass resulting from polaronic effects, a combination of an electron with its deformed lattice [78]. This effect is high in ionic crystals and decreases with an increase in covalency. Additionally strong onsite electron-electron interaction results in splitting of the bands in a lower and higher Hubbard band (section 2.1.7.9.4), which results in a band gap (In certain oxides, containing heavier elements even a relativistic splitting may trigger a band gap formation [79]). Electrons must be excited beyond this gap in order to reach the unoccupied states. The common conduction mechanism especially dominant at room temperature is the thermal activation band conduction (fig. 2.8 left). The thermal activation from the valence band to the unoccupied band usually obeys the Arrhenius law. The pre-exponential factor in this case may depend on T due to carrier mobility and density.

$$\rho = \rho_0 e^{\left(\frac{E_g}{2k_B T}\right)} \quad (2.74)$$

, ρ_0 : Pre-exponential factor and E_g : Band gap

However at lower temperatures, the thermal energy is not enough to excite the electron beyond the band gap and therefore the thermal activation band conduction is negligible. The electronic conduction in this range is dominated by the hopping mechanism. In this concept the electron hops between the localized states of different ions (sites) in the vicinity of the valence band. The localized states belong either to impurity ions or they are due to real crystal properties such as grain boundary due to polycrystalline nature of the sample or site disorder. The hopping mechanism is initiated by electron phonon interaction, in which the electrons gain or lose energy to make the transition thus the activation behaviour depends on the width of the localized states. Usually the hopping takes place to the nearest neighbour sites, but if the thermal energy is not enough for the hopping, it is favourable for the electron to hop further to find a site with a smaller barrier (potential difference). This type of hopping is known as the variable range hopping (VRH) (fig. 2.8 right) and this is introduced by N. Mott [80] to describe disordered semiconductors. The resistivity in this range is described by the following eq.

$$\rho = \rho_0 e^{\left(\frac{T_0}{k_B T}\right)^{d+1}} \quad (2.75)$$

ρ_0 : Pre-exponential factor

T_0 depends on the localization length of the electron and from the electron density of states, whereas d is the dimensionality of the hopping. The pre-exponential factor in this case depends on the phonon density. Note that the transition between the extreme idealized mechanisms discussed above is usually continuous especially in case of comparable size of the band gap and the width of the distribution of the localized states.

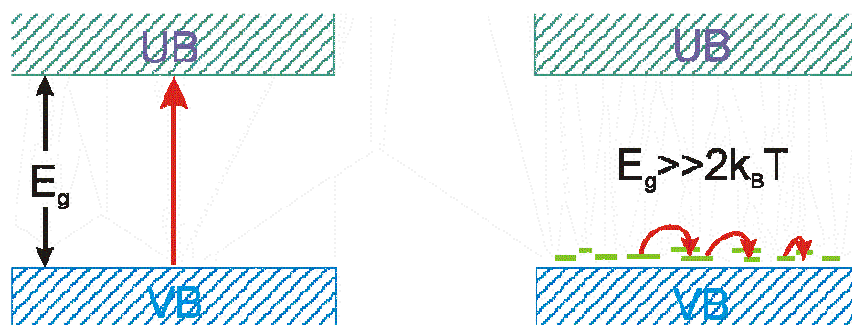


Fig. 2.8: Thermal activation band conduction (left) and variable range hopping (VRH) (right).

2.5 Magnetic interactions in double perovskites

At first an introduction to the collective magnetism would be given and the basics of magnetism are discussed elsewhere. Magnetic phenomenon, which exhibit long range or short range ordering of the magnetic moments, are known as collective magnetism. In case of the former depending on the interactions between neighbouring magnetic moments in a first instance, the ordering may be ferromagnetic (FM), anti-ferromagnetic (AFM) or ferrimagnetic. AFM and ferrimagnetic ordering may be even non-collinear (NCM) and/or canted (CM). The ordering may also be more complicated than this as in the case of helical or conical arrangement of the moments. An example for short range order is a spin glass. A simple model for FM and AFM and its transition to the paramagnetic state (Curie temperature for FM and Néel temperature for AFM) is given by the molecular field approximation introduced by Weiss, which treats the magnetic moment in an effective magnetic field (mean-field), created by the neighbouring moments. In the paramagnetic state (in a magnetic field) the temperature dependence of the magnetic properties could be described by the Curie-Weiss law.

$$\chi = \frac{C}{T - \theta} \quad (2.75)$$

, χ : magnetic susceptibility, C: Curie constant and θ : Curie-Weiss temperature

The molecular field theory in fact introduces an effective field, which interacts with the magnetic moment, but does not reveal the nature of the interaction between the spins. But as already mentioned in section 2.1.4, it is of quantum mechanical nature and it is the exchange interaction, which creates the ordering of the spins with a combination of electrostatic interaction and Pauli-principle. This is illustrated in the following for a system containing two electrons with spin in the non relativistic limit. Only the electrostatic interaction between the electrons is considered. The total wave-function φ_{tot} could be written as a product of the orbital function φ_{O} (linear combination of the individual orbital functions $\varphi_{\text{O}1}$, $\varphi_{\text{O}2}$ in order to dismiss the symmetry less state) and the spin function χ .

$$\varphi_{\text{tot}} = \varphi_{\text{O}}\chi \quad (2.76)$$

Although the electrostatic term of the Hamiltonian V_{ee} acts only on φ_O , there are two solutions to the equation depending on the linear combination of the individual φ_{O_i} . This depends on the antisymmetrization condition of φ_{tot} for fermions that requires for a particular spin configuration, only the linear combination of the orbital function would be selected, that together with χ antisymmetrize φ_{tot} . The energies could be written as:

$$E_T = E_C - J \text{ for the triplet state } \chi_T = \frac{1}{\sqrt{2}} \left(|\uparrow\downarrow\rangle + |\downarrow\uparrow\rangle \right) \left(|\uparrow\uparrow\rangle, |\downarrow\downarrow\rangle \right) \quad (2.77)$$

$$E_S = E_C + J \text{ for the singlet state } \chi_S = \frac{1}{\sqrt{2}} \left(|\uparrow\downarrow\rangle - |\downarrow\uparrow\rangle \right) \quad (2.78)$$

$$E_C = \int \varphi_1^*(r_1) \varphi_2^*(r_2) V_{ee} \varphi_2(r_2) \varphi_1(r_1) \quad (2.79) \quad \text{Coulomb integral}$$

$$J = \int \varphi_1^*(r_1) \varphi_2^*(r_2) V_{ee} \varphi_1(r_2) \varphi_2(r_1) \quad (2.80) \quad \text{Exchange integral}$$

$$2J = E_S - E_T$$

The state with the lowest energy depends on the sign of J. Until now the spin configuration is not explicitly involved in the Hamiltonian. To do this the considered Hamiltonian is rewritten in terms of the spins, so that the eigenvalues of the spin term re-establishes the eigenvalues of the original Hamiltonian.

$$\hat{H} = E_C - \frac{1}{2}J - 2J s_1 s_2 \rightarrow \begin{cases} E_S = E_C + J & \text{for the eigenvalue } -3/4 \\ E_T = E_C - J & \text{for the eigenvalue } 1/4 \end{cases} \quad (2.81)$$

Only the third term contains the spin configuration explicitly, which is needed to describe different spin arrangements and its generalization for an array of atoms with net spins obtains the Heisenberg operator which becomes (2.83) considering only the next neighbours

$$\hat{H} = -2 \sum_{i(\neq j)=1}^N J_{ij} s_i s_j \quad (2.82)$$

$$\hat{H} = -2J \sum_{i=1}^N s_i s_{i+1} \quad (2.83)$$

It seems that (2.83) describes some dipole-dipole interaction but in reality it is a consequence of electrostatic interaction and Pauli-principle for fermions. The above described model of

direct exchange is suited for the case where there is a direct overlap of the wave functions. But in solids particularly in transition metal oxides such as double perovskites the direct overlap of d orbitals are small and usually one or more p orbitals of the oxygen anion are between them, so the indirect exchange becomes the relevant mechanism. Additionally the magnetic ordering is coupled to correlation effects, depends on the electronic structure in the vicinity of Fermi-level thus it is prone to phenomenon such as metal-insulator transition. In double perovskites different types of indirect exchange interactions are present, depending on the crystal structure and electronic structure correlation.

The most common exchange interaction is the superexchange interaction present in insulating double perovskites (usually low symmetry) such as the system investigated in the present work, that exhibit AFM in different types, NCM or CM [81-82]. Ferromagnetic double perovskites with T_C above room temperature, being metallic or insulating are described by the so called kinetic driven exchange interaction (an enhanced form of double exchange) [5, 83] and recently the same exchange interaction is also predicted to be the dominant contributor in the AFM La rich part of $\text{La}_{2-x}\text{Sr}_x\text{FeMoO}_6$, where the parent compound $\text{Sr}_2\text{FeMoO}_6$ being a FM double perovskite with T_C above room temperature [84]. A major class consists of double perovskites, which usually have a non magnetic B site and a weak spin polarized B' site containing 5d transition metals or lanthanides, which occupy the edge shared tetrahedra of the fcc lattice of B' . This system is geometrically frustrated, due to the competing (weak) superexchange AFM and FM interactions in the edge-shared tetrahedra, which represents the three dimensional form of the triangular lattice [85]. It should be mentioned that the transition between the first type and the third type is continuous. The interactions are further complicated by spin-orbit coupling that couples the spin of the B and B' to the lattice in certain directions, paving way to anisotropic interactions such as Dzyaloshinski-Moriya interaction $s_i \times s_j$ and electron-electron interaction that splits the narrow d bands in lower and upper Hubbard bands. In the following superexchange in AFM double perovskites, which is the relevant interaction in this work, is described.

In the superexchange interaction the electrons hop from one site to another virtually (from one d orbital to another d orbital via p orbital of the oxygen) as the electronic structure of such materials are governed by strong onsite electron-electron repulsion. Therefore, any model Hamiltonian that characterizes such an interaction must contain principally two parameters, namely a kinetic hopping parameter and an electrostatic repulsion parameter. In the original

“one band” Hubbard model the hopping is characterized by a transfer parameter t and the onsite repulsion by the Hubbard U and the superexchange is described in the $U \gg t$ limit. But to describe the superexchange interactions in a double perovskite, the simple Hubbard model must be modified for each compound. Apart from t and onsite U , a U' for the repulsion of d electrons of different orbitals, crystal field splitting and Hund’s coupling J for the d electrons on the same site should be included. Recently such a “multi band” Hubbard model is constructed for the insulator Sr_2FeWO_6 and calculations are quite cumbersome [86]. This is one of the main reasons why DFT calculations are widely used even with U as they are globally applicable and comparison of the results are much easier. But one question remains. Is it possible from an obtained magnetic structure (from neutron diffraction) to deduce approximately the type of the superexchange (depending on the different orbitals involved) and its dominant path as there are different exchange paths (without evaluating the more complicated magnon spectrum)? These questions were answered by simple rules (GKA rules) introduced by Goodenough, Kanamori and Anderson independently long before the Hubbard model was introduced [87]. They are given below.

- (1) The 180° exchange between filled or empty orbitals is strong and anti-ferromagnetic
- (2) The 180° exchange between a filled and an empty orbital is weak and ferromagnetic.
- (3) The 90° exchange between filled orbitals is weak and ferromagnetic

Although these rules do not describe the interaction exactly in most real compounds, with some additional arguments and considerations they could still be applied. With these rules Goodenough created a table with different combinations of the number of d electrons in different orbital states such as LS and HS, and the experimental magnetic structure could be compared with the table. Now the possible AFM structures in double perovskites are described in terms of dominating exchange paths, which are based on [88]. As already mentioned the B and B' cations form an fcc lattice (Fig. 2.9), that may be distorted depending on the symmetry of the system. Fig. 2.10 shows such an fcc lattice and the different exchange paths present in this lattice. For a moment only one sublattice (B) is considered to be filled with both t_{2g} and e_g electrons and in B' the involved d orbital is assumed to be empty, as it would be seen in a moment, it is not a bad assumption even if d electrons are present in B' , in

case if they are occupied by for example 5 t_{2g} electrons (LS) as in the present work, they are mostly limited to the low lying t_{2g} orbitals.

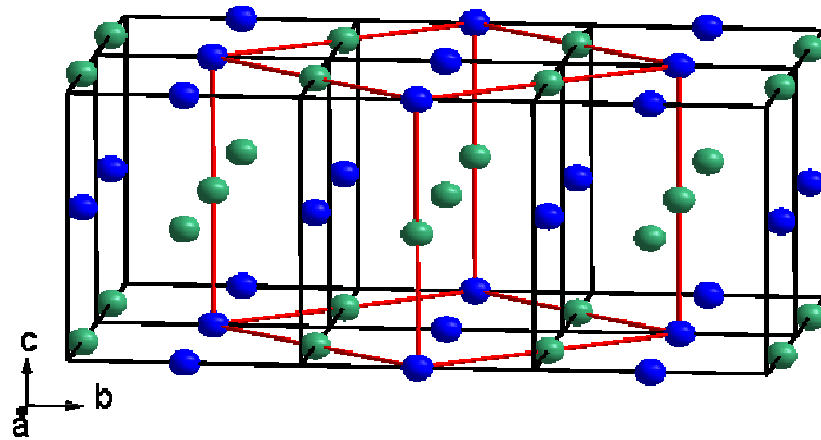


Fig. 2.9: Formation of a fcc lattice by B and B' cations (shown in red). Deviation from the cubic symmetry leads to distortion of the fcc lattice.

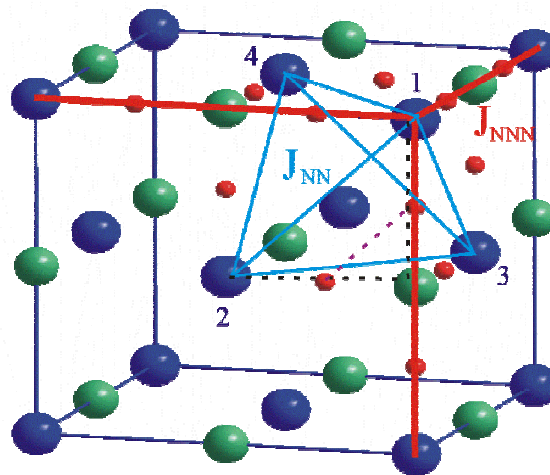


Fig. 2.10: Different exchange paths are shown on the fcc lattice formed by B.

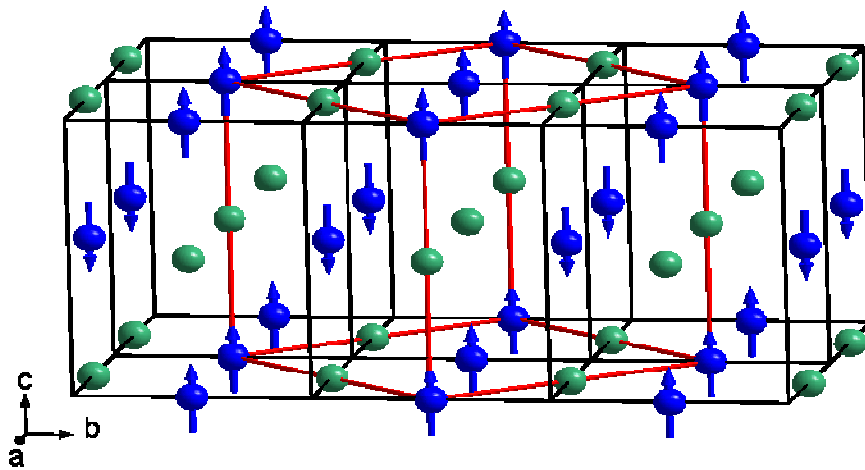


Fig. 2.11: Arrangement of the neighboring magnetic moments in the fcc lattice for a $k=(0,0,0)$ magnetic structure.

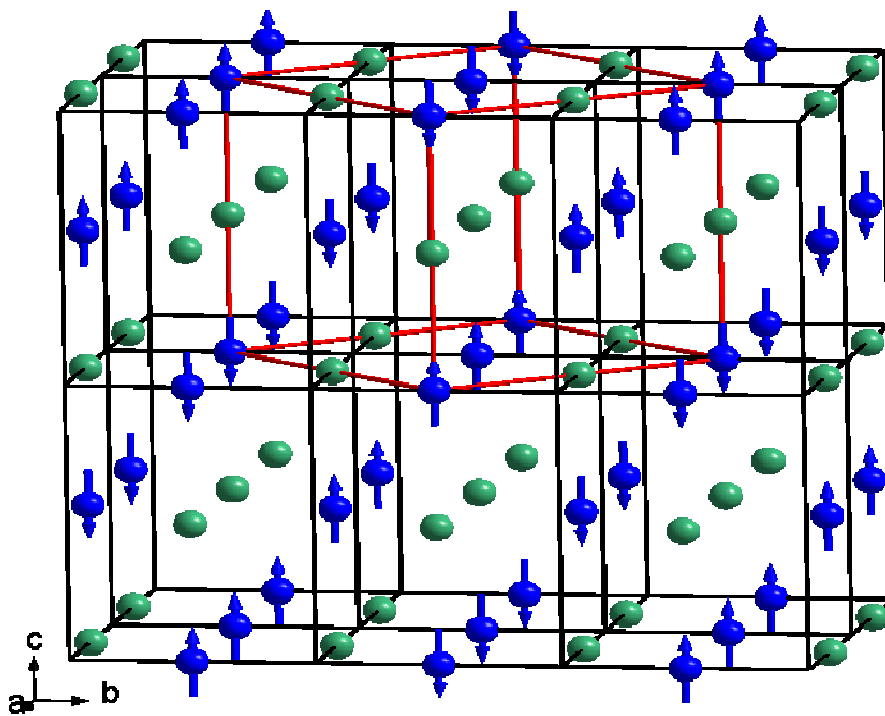


Fig. 2.12: Arrangement of the neighboring magnetic moments in the fcc lattice for a $k=(0,1/2,1/2)$ magnetic structure.

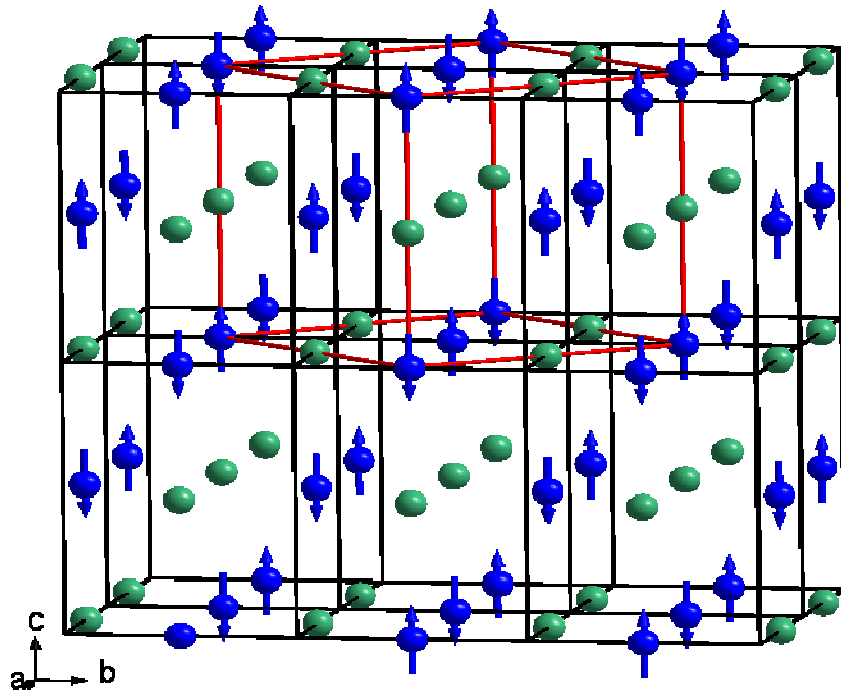


Fig. 2.13: Arrangement of the neighboring magnetic moments in the fcc lattice for a $k=(1/2,0,1/2)$ magnetic structure.

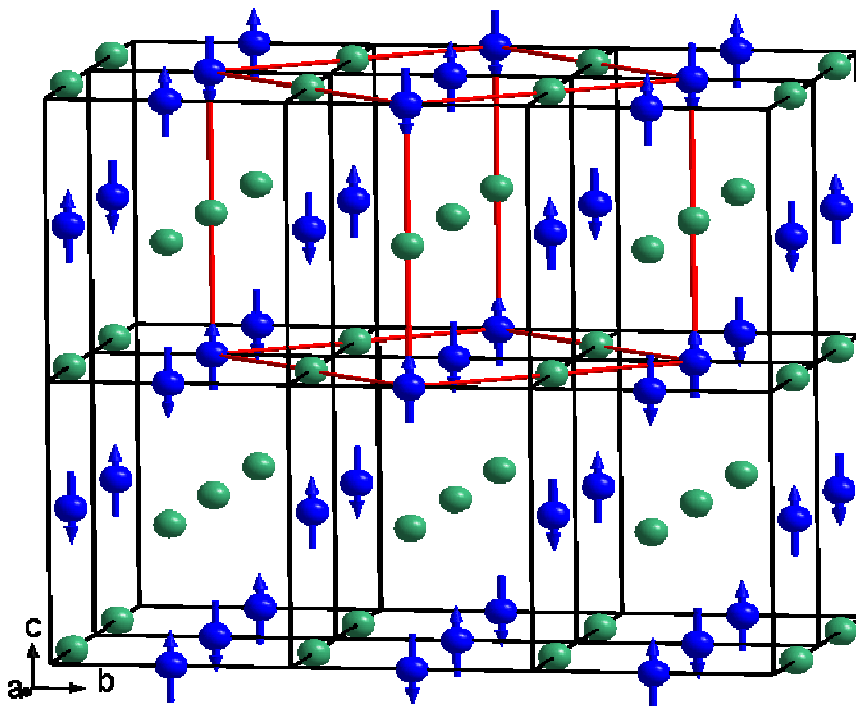


Fig. 2.14: Arrangement of the neighboring magnetic moments in the fcc lattice for a $k=(1/2,1/2,1/2)$ magnetic structure.

There are mainly two different dominant overlaps between the p orbitals of oxygen and the d orbitals of B and B'. The t_{2g} orbitals overlap with the p orbital of oxygen in the π ordering and

the e_g orbitals overlap with the p orbital of oxygen in the σ ordering. Considering the superexchange in the fcc lattice, there are two different exchange paths. Taking the B ion “1” as reference, as marked in fig. 2.10 they are the 180° (angle ideal for the cubic case) next nearest neighbour (NNN) interaction σ B-O-B'-O-B (between the e_g of B via the vacant e_g of B') that connects B “1” to the three B ions in the corners and the nearest neighbour (NN) interaction that connects B “1” to the three B ions 2, 3 and 4 on the face centres, that form a frustrated AFM tetrahedron. The $k=(0,1/2,1/2)$ and $k=(1/2,0,1/2)$ magnetic structures are shown in fig. 2.12 and fig. 2.13. As it could be seen, the 180° AFM NNN are fulfilled in all three directions for both the structures, thus they are the strongest interactions in these cases. The difference between them arises from the 90° AFM NN interactions between 1, 2, 3 and 4 along the B-O-B'-O-B path (black dashed line in fig. 2.10), that are not identical for low symmetry such as monoclinic cases. For the $k=(0,1/2,1/2)$ structure 1-4 NN dominates over 3-4 and visa versa for $k=(1/2,0,1/2)$. For high symmetry cases such as cubic, all the 90° NN interactions become similar, resulting in high geometric frustration, resulting in the $k=(1/2,1/2,1/2)$ structure [19]. At very large distortions of the crystal structure the deviation of the O-B'-O bond angle from 180° and 90° are quite large, thus these interactions are weak, on the other hand the exchange paths B-O-O-B (fig. 2.10) may become significant in this particular case. The $k=(0,0,0)$ structure results in such cases (fig. 2.11) [88]. Note that the $k=(0,0,0)$ AFM structure is actually a description of a more complicated magnetic interaction often containing a comparable ferromagnetic component.

3. Experimental methods

3.1 Powder diffraction methods

3.1.1 Introduction

The powder diffraction methods used in this work can be divided into three categories, namely the laboratory x-ray diffraction, the synchrotron diffraction and the neutron diffraction. Laboratory x-ray diffraction is used in this work primarily to find the optimum synthesis temperature of the investigated double perovskite, where the fraction of the impurity phases is minimal (high quality) and it is also used to roughly determine the crystal structure and therefore the space group of the compound at room temperature. The diffraction patterns obtained from this method are also used to perform multi-pattern refinements together with neutron diffraction patterns at room temperature. The laboratory x-ray powder diffraction is carried out in flat sample transmission mode, using a STOE STADIP diffractometer. To investigate the temperature and composition dependence of the crystal structure of the double perovskites synchrotron diffraction (HASYLAB/DESY) and neutron powder diffraction (SPODI FRMII) are combined. In many ways these two methods are complimentary and therefore ideally suited to describe the crystal structure of polycrystalline double perovskites. In this work neutron powder diffraction is also used to investigate the long range magnetic order in double perovskites and crystal structure features at lower temperatures. In the next paragraph the basic principles of diffraction are sketched and the characteristics of x-rays (synchrotron radiation) and neutron diffraction methods are compared. It is followed by the instrumentation information of laboratory x-ray, synchrotron and neutron diffraction.

Below the phenomenon of diffraction is addressed in terms of x-ray scattering and similar principles could be transferred later to neutron diffraction. X-rays are scattered by the electron density. This interaction may be inelastic as in the case of photoionization and Compton scattering or elastic known as the Thomson scattering. In the latter electrons oscillate like a Hertz dipole at the frequency of the incoming x-rays and thus becomes the source of dipole radiation with the wave length being conserved. It is the third type of scattering that is used for structural investigation and termed as diffraction. The scattering of the x-rays by the atom involves all its electrons (electron density) and described by the scattering amplitude of the x-rays by an atom, called the (uncorrected) atomic x-ray form factor f_x , that depend primarily on

the charge density ρ and the difference between the incidence and scattered directions $\vec{q} = \vec{k}_j - \vec{k}_i$. The intensity of the scattered x-rays is thus proportional to the square of f_x .

$$I(\vec{q}) \propto |f_x|^2, \quad f_x = \int \rho(\vec{r}) e^{i\vec{q}\vec{r}} d^3r \quad (3.1)$$

In the following the diffraction of x-rays at a periodic lattice of a crystal is considered and sketched in fig. 3.1.

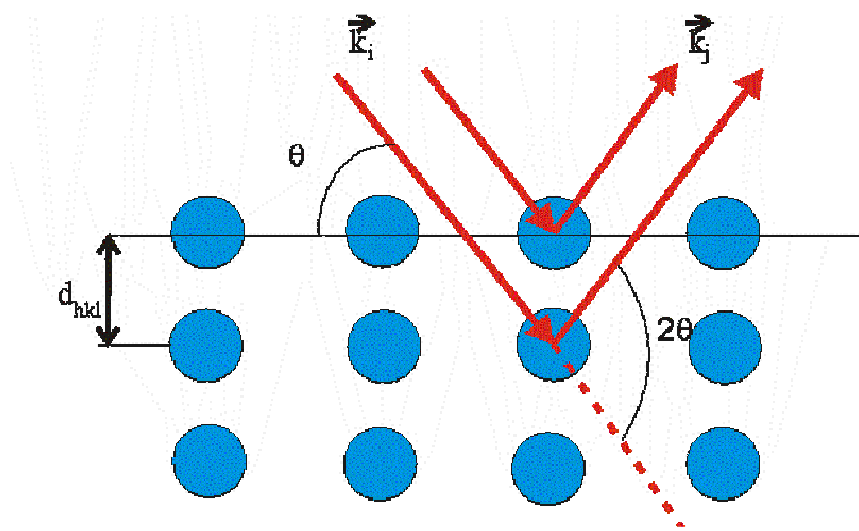


Fig. 3.1: Diffraction of x-rays at a periodic lattice of a crystal

In this case there isn't only one atom but an array of atoms in three directions and that paves way to interference effects between the scattered x-rays from different atoms. Bragg was the first to construct a condition for the constructive interference of x-rays (waves of the same phase) scattered from neighbouring parallel lattice planes at the separation distance d_{hkl} , that result in intense reflections at certain angles.

$$n\lambda = 2d_{hkl} \sin\theta \quad (3.2)$$

λ : wave length of x-rays, d_{hkl} : distance between parallel lattice planes, θ : angle of incidence and n : diffraction order.

The Bragg equation above describes the case, where the scattered x-rays, that interfere, come from the whole lattice (many unit cells). In this context the amplitudes of the Bragg reflections are proportional to a quantity known as structure factor F_k ($k=(hkl)$).

$$F_k = \sum_i f_i e^{2\pi i(hx_i + ky_i + lz_i)} \quad (3.3)$$

f_i : form factor of i th atom

This is the most important quantity in x-ray diffraction as it contains the atomic position coordinates. It is the deciding factor for relative intensities including systematic absence of reflexions thus conditions for systematic absence due to translation (centering, glide plane and screw axis) could be formulated. In refinement procedures usually the Debye-Waller factor, which contains the thermal displacement parameter is also included in this term.

The elastic scattering principles of x-rays can be transferred to neutrons as well, but the relevant interactions differ from the one in the x-ray case. Indeed there are two different contributions for the neutron case. Neutrons are scattered at the nucleus involving the strong force in contrary to electrons in the x-ray case. As the neutrons have a spin magnetic moment of $\frac{1}{2}$ there is a dipole interaction between the spin magnetic moment of the neutron and magnetic moment in the compound, resulting in a second contribution to the scattering in case of ions in the compound that have a net magnetic moment. As in the case of x-rays, neutron scattering at an atom can also be described by form factors, namely a nuclear form factor and a magnetic form factor.

In the following the synchrotron diffraction and the neutron diffraction are compared, leaving out the laboratory x-rays for a moment in this comparison, as synchrotron represents a superior form of the former. Firstly the resolution is compared. Typically synchrotron diffraction has a higher angular resolution than the neutron diffraction, due to the more monochromatic nature and the lower divergence, that in turn as a consequence of the high intensity available from the synchrotron source, which allows the x-rays to be highly focussed and monochromated, at the same time maintaining a high flux on the sample and allowing faster data collection. As a result of the higher resolution sharper peaks could be obtained and therefore splitting due to distortions of the crystals structures could be resolved. The mentioned high flux of synchrotron also improves the signal to noise ratio thus weaker peaks

could be seen. The variation of the resolution with the angle 2θ depends on the geometry of the diffractometer (on the instrumentation). Considering the 2θ dependence of the scattering power, in case of x-rays that interacts with the electrons, the form factor rapidly falls at higher angles. On the other hand for the interaction of neutrons with nucleus there are no major changes to the nucleus form factor up to higher angles, whereas the magnetic form factor changes even more rapidly than the x-ray case going towards higher angles. Another difference between them is that x-rays react with the electrons stronger than neutron with matter and therefore synchrotron needs smaller sample sizes and much shorter data collection time than neutrons ($m \geq 4g$). For the latter feature synchrotron measurements are preferred to investigate a larger number of samples in a short period of time and especially temperature dependence of the crystal structure of samples, where fine temperature intervals are desired. In the present work because of this feature the temperature dependence of the samples are investigated by synchrotron (20K steps) and only at special temperatures neutron diffraction is applied. At this point it seems that synchrotron is superior to neutron diffraction in structural investigations but as already mentioned they may give complimentary information as they both interact with matter differently especially concerning sensitivity for different elements. The interaction between the x-rays and the elements in a sample is proportional to the number of electron in an element, thus the scattering of x-rays at heavier elements is stronger than at lighter elements. On the other hand the interaction between neutrons and nucleus has no clear relationship with the isotopes as this depends on the short range strong nuclear force. This may result in significant difference in nuclear scattering between elements next to each other in the periodic system and even between isotopes of the same element thus neutron scattering is essential for structure investigations of compounds that contain two or more elements with similar atomic number. As the scattering strength for neutrons does not depend on the atomic number as in the case of x-rays, it is more sensitive to lighter elements in the presence of heavier elements. This is very important to oxides containing heavy elements as in the present case of double perovskites with Lanthanum at A-site, as in its presence x-ray diffraction is rather insensitive to oxygen and the intensity of the additional reflections due to octahedral tilting from the cubic structure depends primarily on the actual positions of oxygen.

3.1.2 Laboratory x-ray

The laboratory x-ray patterns are obtained using a STOE STADIP diffractometer, operated with Mo-K α_1 radiation (using a curved Ge(111) monochromator) in transmission mode and equipped with a linear position sensitive detector. Powder samples are placed within two thin foils and attached to the rotating disc. Diffraction patterns are collected in steps of 0.01° and from 3°-49.99° 2 θ angles. The refinement of the structural parameters is carried out using the program FULLPROF. A photograph of the diffractometer is shown in fig. 3.2.



Fig. 3.2: Image of a STOE STADIP diffractometer.

3.1.3 Synchrotron powder diffraction

The synchrotron powder diffraction patterns are obtained from the beamline B2 [89] situated at a bending magnet of the storage ring DORIS III at HASYLAB/DESY in Hamburg, Germany, in the Debye-Sherrer mode using capillary sample holder. The diffraction patterns are collected in steps of 0.004° and from 4°-49.99° 2 θ angles. For the detection of the scattered rays an on-site readable image-plate detector OBI [90] is utilized. For high temperature measurements (above room temperature), a STOE furnace equipped with a EURO THERM temperature controller is used, whereas for low temperature measurements a special cryostat [91]. With this beamline the temperature dependence of the crystal structure is investigated between 20K-1173K during heating in different temperature steps depending on the compound, see table 3.1. The wavelength of the synchrotron radiation is determined using the reference material LaB₆ and it is $\lambda = 0.49327(1)$ Å for high temperature measurements (above room temperature) and $\lambda = 0.50205(1)$ Å for low temperature measurements (below room temperature). The refinement of the structural parameters is

carried out using the program FULLPROF [92]. A detailed description of the beamline and the diffractometer setup is described elsewhere [89-90].

Table 3.1: Measurement details concerning the composition and temperature steps for $\text{La}_{2-x}\text{Sr}_x\text{CoIrO}_6$.

x	Below room temperature	Above room temperature
0	-	300-1173K in 100K steps and 440-560 in 40 K steps
0.5	-	273-1173K in 75K steps
1.0		
1.5	20 K-300K in 20 K steps	273-1173K in 75K steps
2.0		

3.1.4 Neutron diffraction

The neutron powder diffraction patterns are obtained from the “Forschungs-Neutronenquelle” FRM II at the structure powder diffractometer SPODI in Garching, in the Debye-Sherrer mode, in order to investigate the crystal and magnetic structures [93]. The diffraction patterns are collected in steps of 0.05° and from 2° - 151.95° 2θ angles. The scattered neutrons are detected using 80 He3 counters (2° angle range per counter). Low temperature diffraction patterns are obtained at 3, 50, 100 and 300K for $x=0, 0.5, 1.0, 1.5$ and 2.0 of $\text{La}_{2-x}\text{Sr}_x\text{CoIrO}_6$ and at 4 and 300K for $x=0.5$ and 0.75 of $\text{La}_{2-x}\text{Ca}_x\text{CoIrO}_6$ using a cryostat for cooling and additionally high temperature diffraction patterns are obtained only for $x=2$ of the LaSr system at 300, 500 and 900K using a furnace. The wavelengths for low and high temperature measurements are $1.548(1) \text{ \AA}$ and $1.546(1) \text{ \AA}$ respectively. The refinement of the structural parameters is carried out using the program FULLPROF.

3.1.5 Rietveld refinement

The Rietveld refinement is a least square fit approach to minimize the difference between the experimental diffraction pattern and the modelled one, in contrast to earlier structure determination approaches, where the peaks are assigned to individual reflections and the crystal structure is determined [94]. In powder diffraction it is common to have overlapped peaks, where the Rietveld refinement has the advantage compared with earlier approaches, it

does not rely on the splitting of the peaks as it rather refines a number of parameters in the model comparing with the experimental diffraction pattern to obtain an optimal least square fit. In this work the program FULLPROF is used to carry out Rietveld refinement. The function to be minimized in the Rietveld refinement is written as:

$$\chi^2 = \sum_{i=1}^n w_i (y_{oi} - y_{ci})^2 \quad (3.4)$$

y_{oi} : experimentally observed intensity at the data point i , y_{ci} : calculated intensity at the data point i and $w_i = 1/\sigma_i^2$, where σ_i^2 being the variance of y_{oi} .

In several cases as in the present work where parameters are refined simultaneously using more than one diffraction patterns (Lanthanum and Strontium sites are more weighted from XRD and Oxygen sites from NPD), known as multi-pattern refinement, the above function could be generalized as shown below.

$$\chi^2 = \sum_{\lambda=1}^N \omega_{\lambda} \left[\sum_{i=1}^n w_i (y_{oi} - y_{ci})^2 \right], \quad \sum_{\lambda=1}^N \omega_{\lambda} = 1 \quad (3.5)$$

The weight factors ω_{λ} are provided manually by the users and are internally normalized. The calculated intensity at i is formulated as follows.

$$y_{ic} = y_{ib} + \sum_p S_p \sum_k G_{ik}^p I_k \quad (3.6)$$

y_{ib} : background intensity at i , G_{ik}^p : normalized profile function, I_k : intensity of the k th Bragg reflexion contributing to the intensity at i S_p : scale factor of phase p and p : number of phases. The intensity I_k contains the following parameters.

$$I_k = L_k P_k A_k E_k Q_k |F_k|^2 \quad (3.7)$$

L_k : Lorentz factor, polarization factor and multiplicity factor together, P_k : preferred orientation factor, A_k : absorption correction, E_k : extinction correction, Q_k : geometry factor and F_k : structure factor.

The structure factor F_k contains the structural information of the sample and other factors describe the instrument and sample related corrections. The positions of the reflections are optimized by the refinement of the lattice parameters. The structure factor F_k contains the information about the atomic positions, occupation numbers (also mixed occupancies) and Debye-Waller factors B_j . While the Atomic positions and occupation numbers affect the intensities of the peak, the temperature factor reduces and contributes to the background, thus all three are strongly correlated parameters.

The normalized profile function G_{ik}^p contains information about real-structure effects in the sample such as particle size or strain effects and resolution parameters of the instrument and, therefore, is a convolution of instrument related and sample related functions. Usually they are described by a Gaussian function $G(x)$ (x denotes the diffraction angle in this case, but generally it may also denote energy or time of flight), a Lorentzian function $L(x)$ or a combination of both. A convolution of $G(x)$ and $L(x)$, known as the Voigt function $V(x)$, would be an ideal function to describe this, but numerically quite difficult to handle. Instead of this a linear combination of $G(x)$ and $L(x)$, known as the Pseudo-Voigt $PV(x)$ is used, which is numerically more easy to calculate.

$$G(x) = \frac{2}{H} \sqrt{\frac{\ln 2}{\pi}} e^{-\left(\frac{4 \ln 2}{H^2} x^2\right)} \quad \text{Gaussian function} \quad (3.8)$$

$$L(x) = \frac{2}{\pi H} \frac{1}{\left(1 + \frac{4}{H^2} x^2\right)} \quad \text{Lorentz function} \quad (3.9)$$

$$V(x) = G(x) \otimes L(x) = \int_{-\infty}^{+\infty} L(x-u)G(x)du = \frac{1}{\beta_G} \operatorname{Re} \left[\operatorname{erf} \left(\frac{\sqrt{\pi}}{\beta_G} |x| + i \frac{\beta_L}{\beta_G \sqrt{\pi}} \right) \right], \quad \text{Voigt function}$$

$$\operatorname{erf}(y) = \frac{2}{\sqrt{\pi}} \int_0^y e^{-t^2} dt, \quad \beta_G = \frac{H_G}{2} \sqrt{\frac{\pi}{\ln 2}}, \quad \beta_L = \pi \frac{H_L}{2} \quad (3.10)$$

$$PV(x) = \eta L(x) + (1-\eta)G(x), \quad 0 \leq \eta \leq 1 \quad \text{Pseudo-Voigt function} \quad (3.11)$$

Until now the meaning of H is not mentioned. It is the full width at half maximum (FWHM) of the profile function and depends on the diffraction angle 2θ . For the Voigt function therefore two different FWHM's H_G and H_L are used. All the refinements in the present work are done by using the Pseudo-Voigt function from the option Npr =7 in FULLPROF. Also in the Pseudo-Voigt function, that is selected for the refinement (Npr=7), two FWHM's are used and they are given by the following expressions.

$$H_G^2 = (U + D_{st}^2) \tan^2 \theta + V \tan \theta + W + \frac{I_G}{\cos^2 \theta} \quad (3.12)$$

$$H_L = X \tan \theta + \frac{[Y + F(SZ)]}{\cos \theta} \quad (3.13)$$

The parameters U, V and W characterize the resolution of the instrument, whereas D_{st} , I_G , X and $Y + F(SZ)$ characterize the Gaussian contribution to strain, size, the Lorentzian contribution to strain and size. The expression for H_G^2 is a modified form of the Cagliotti formula.

Although several options including polynomial fitting are available in FULLPROF, the background intensity y_{ib} at i is calculated in this work from the linear interpolation between the (N) selected background points.

FULLPROF also offers corrections to sample displacement in Debye-Sherrer geometry (Sycos) and to the displacement of the detector from the zero point (Zero), where the former is refined in diffraction patterns obtained from x-ray synchrotron diffraction (thin capillary) and the latter for the laboratory x-ray and neutron diffraction patterns.

After the parameters are refined, it is important to judge the quality of the refinement, especially for the case, where the refinement of the parameters are carried out for structure models with different space groups for the same compound. To do this there are several statistical measures for the quality of the fits (residuals) available and they are listed below.

$$R_p = \frac{\sum_i |y_{io} - y_{ic}|}{\sum_i y_{io}} \quad , \quad \text{profile R factor} \quad (3.14)$$

$$R_{wp} = \left[\frac{\sum_i w_i (y_{io} - y_{ic})^2}{\sum_i w_i y_{io}^2} \right]^{\frac{1}{2}}, \text{ weighted } R_p \quad (3.15)$$

$$R_B = \frac{\sum_k |I_{ko} - I_{kc}|}{\sum_k I_{ko}}, \text{ Bragg } R \text{ factor} \quad (3.16)$$

$$\text{GOF: } \tilde{\chi}^2 = \frac{\sum_i w_i (y_{io} - y_{ic})^2}{N - P}, \text{ goodness of fit} \quad (3.17)$$

N: Number of y_{io} 's, P: Number of refined parameters, I_{ko} : observed intensity of the k th Bragg reflexion and I_{kc} : calculated intensity of the k th Bragg reflexion.

Refinement would be carried out until the lowest possible value for these residuals is reached. As these residuals are greatly influenced by the signal to noise ratio of the diffraction pattern, the range of values for these factors differ depending on the types of radiation used (laboratory x-ray, synchrotron radiation or neutrons) thus these factors should only be used to compare different fits to the same diffraction pattern. Although these above mentioned residuals are employed, it is also important to visually compare the agreement between the calculated and the experimentally observed diffraction pattern. A difference plot may be useful in this context, especially to find systematic errors and to identify magnetic Bragg reflections in the pattern.

3.2 MPMS: Magnetic Property Measurement System

3.2.1 Theoretical background and basics of the instrument

The temperature and external magnetic field dependences of the magnetic properties of the compounds are measured using a magnetic property measurement system (MPMS) from Quantum Design from 1.8-350 K and up to 7 Tesla respectively. The main element of the MPMS is a superconducting quantum interference device magnetometer, known as SQUID magnetometer. It utilizes the Josephson-effect and the flux quantization in a superconducting ring. The Josephson-effect is a macroscopic quantum phenomenon, including a number of effects, related to the behaviour of an insulating contact (Josephson junction), which weakly couples two superconductors (wave functions ψ_1 and ψ_2), in a dc current, ac current, voltage or an external magnetic field. In the DC Josephson effect, a supercurrent is induced across the junction only due to the phase difference of the wave functions without voltage drop. This supercurrent is due to the tunnelling of the Cooper pairs, that should not exceed a particular critical value I_C . In case of exceeding I_C normal conducting quasi particles would also tunnel through the junction parallel to the Cooper pairs, resulting in a voltage drop, as a result the supercurrent shows oscillatory behaviour depending on the voltage drop. This is the AC Josephson effect. F. London showed considering the wave mechanics that the frozen magnetic flux in a superconducting ring should be quantized. Applying an external magnetic field to the ring would induce a supercurrent in the ring that would stabilize to a stationary state, as there is no resistivity. But this supercurrent and the induced local magnetic field can only have discrete values, as the stationary state demands the constructive interference of the macroscopic wave function (as in the case of the Bohr atomic model). This implies that the total flux, that consists of the local flux and the externally applied flux should also be quantized and be an integer number times the elementary flux quanta Φ_0 ($\Phi_0 = h/2e$). Coming back to the Josephson contact in an external magnetic field, it can be shown that current density oscillates along the direction which is perpendicular to both the external field and transport direction of the current. Integrating along this direction would give the supercurrent, that shows a damped oscillating behaviour depending on the flux penetrating the contact.

$$I = I_C \cdot \left| \frac{\sin\left(\pi \frac{\Phi}{\Phi_0}\right)}{\left(\pi \frac{\Phi}{\Phi_0}\right)} \right| \quad (3.18)$$

The Josephson junction could be used to measure the external magnetic field. But the resolution of such a junction is poor. This could be seen by looking at the sensitivity δ , keeping in mind that at the first minimum of $I_S(\Phi)$ curve, one elementary flux quantum Φ_0 has penetrated the contact with the area of A .

$$\delta \equiv \frac{I_s}{\Phi_0} = \frac{I_s}{B_0 A} \quad (3.19)$$

Increasing A of the contact would improve δ , but alternatively a superconducting ring with one or more Josephson contacts can be used to improve δ . The relevant area would be the one within the ring. The instruments that use such a superconducting ring with one or more Josephson contacts are called SQUIDs. The SQUID, which is used by the MPMS, consists of only one Josephson contact. The total flux for this case could be written as a sum of the external flux Φ_{ext} and the screening term as:

$$\frac{\Phi}{\Phi_0} = \frac{\Phi_{\text{ext}}}{\Phi_0} - \frac{\beta_L}{2\pi} \sin\left(2\pi \frac{\Phi}{\Phi_0}\right) \quad (3.20), \quad \beta_L = 2\pi \frac{LI_C}{\Phi_0}, \quad \beta_L: \text{screening parameter, } L: \text{inductivity}$$

The variation of Φ with Φ_{ext} is shown in fig. 3.3 (left) for different values of β_L .

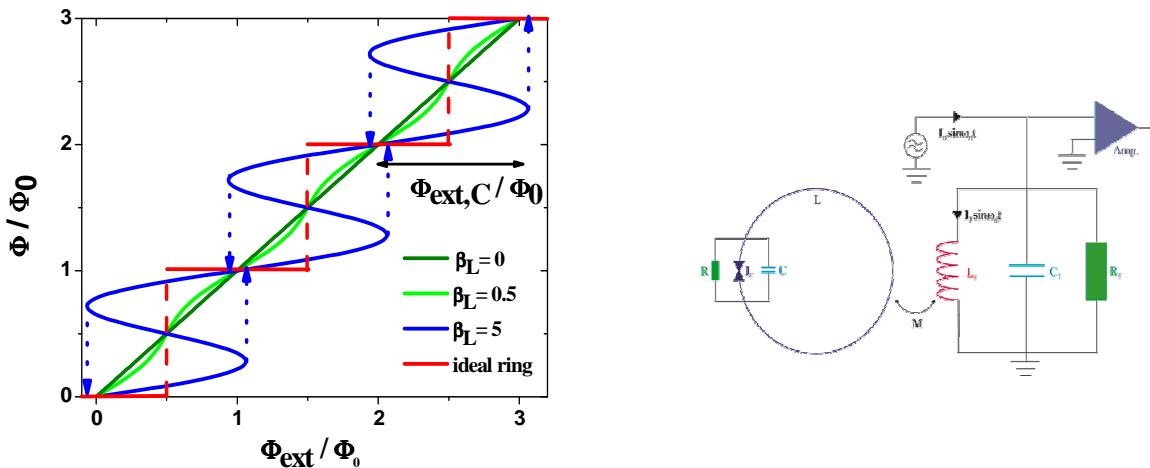


Fig. 3.3: Variation of Φ with Φ_{ext} (left) and the external tank circuit (right).

For $\beta_L > 1$, hysteresis behaviour is obtained and the most of the SQUIDs are operated in this regime. With increasing external flux Φ_{ext} , the total flux Φ increases only slowly as the supercurrent I_S would screen the external flux (only partially due to the insulating barrier). This screening would break down as soon as I_S reaches I_C (critical external flux $\Phi_{\text{ext},C}$) and the Josephson junction switches to the resistivity state thus an elementary flux quantum can penetrate into the ring and a new quantum state is obtained. If now Φ_{ext} would be reduced, the SQUID would remain in the new quantum state until $\Phi = \Phi_0 - \Phi_{\text{ext}}$, where I_S would again exceed I_C and returns to the initial state. This hysteresis behaviour is related to an energy loss at the Josephson junction. In following the practical operation of this type of SQUID is described. The SQUIDs with one Josephson contact are operated in the so called radiofrequency mode and also known as rf-SQUIDs. In this set up field energy would be made available from an external resonance circuit (fig. 3.3 right) and this energy would be used by the SQUID as soon as a flux quantum penetrates the ring. This resonance circuit is fed in with an alternating current $I_{\text{rf}} \sin(\omega_{\text{rf}} t)$ (frequency up to 1GHz) with the amplitude I_{rf} (actually $Q I_{\text{rf}}$ is the current in the circuit due to a quality factor Q of the circuit) and a frequency close to or with the resonance frequency ω_{rf} , which enables a continuous circulation through the hysteresis loop. During a measurement additionally to the penetration of the magnetic flux created by the radiofrequency, the magnetic flux from the sample Φ_S would also penetrate the SQUID. In the following only the cases $\Phi_S = n\Phi_0$ and $\Phi_S = (n+1/2)\Phi_0$ are discussed considering the fig. 3.4.

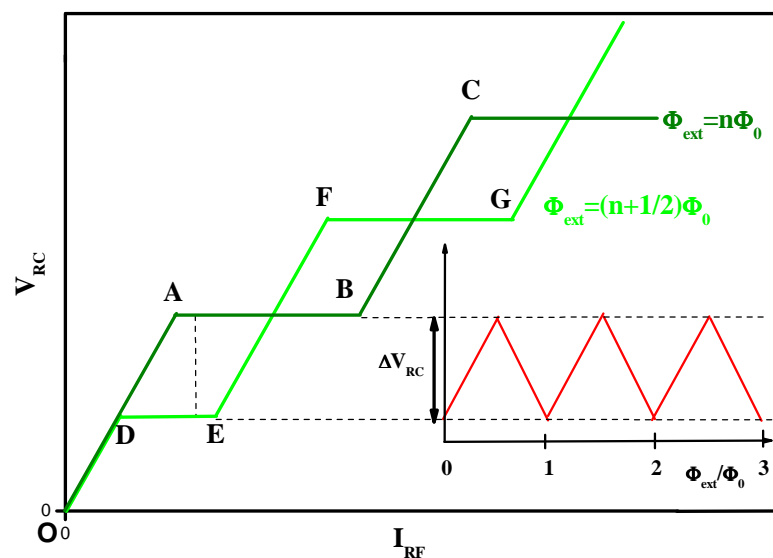


Fig. 3.4: I_{rf} dependence of the voltage at the resonance circuit.

In the first case it is assumed $n=0$ and therefore only the flux Φ_{rf} due to the alternating current in the circuit should be considered. With increasing amplitude of the alternating current I_{rf} the voltage at the resonance circuit V_{RC} increases as long as Φ_{rf} would be compensated by I_S at the ring. Reaching $I_S=I_C$, Φ_0 penetrates into the ring and as the sign of I_{rf} is reversed due to the alternating current and a hysteresis loop would be circulated (0-A). The dissipated energy is taken from the resonance circuit and as a result V_{RC} would crumble. The recovery of the V_{RC} takes many periods of I_{rf} and once again a hysteresis loop would be circulated, that result in the crumbling of V_{RC} , that is once again restored by many periods of I_{rf} . Increasing I_{rf} further would reduce the number of periods needed for the recovery of V_{RC} , but does not increase V_{RC} (A-B). The I_{rf} range of constant V_{RC} comes to an end as each period of I_{rf} induces a hysteresis loop. Increasing I_{rf} further would result in an increase of V_{RC} as now an excess energy is stored in the resonance circuit and crumbles once again as the energy is reached that induces the penetration of two Φ_0 (B-C). The behaviour of V_{RC} would be repeated depending on I_{rf} . In the second case once again $n=0$ is assumed and there is already $\frac{1}{2} \Phi_0$ in the ring and together with Φ_{rf} the penetration happens at a smaller I_{rf} than for the first case (0-D) and the behaviour of V_{RC} is the same as in the first case but only shifted due to the external $\frac{1}{2} \Phi_0$. The response of V_{RC} for all other values of Φ are between the extreme cases $\Phi_S=n\Phi_0$ and $\Phi_S=(n+1/2)\Phi_0$. Now varying Φ_S in a constant I_{rf} yields an oscillation of V_{RC} between the $\Phi_S=n\Phi_0$ and $\Phi_S=(n+1/2)\Phi_0$ cases with a period of Φ_0 thus an rf-SQUID is a non linear flux-voltage converter. For a high sensitivity, the amplitude of $V_{RC}(\Phi)$ oscillation should be as large as possible thus the rf-SQUID is operated in the plateau region. Such a construction of the rf-SQUID has one main short coming. Only Φ_S up to $\frac{1}{2} \Phi_0$ can be uniquely detected, as larger Φ would result in an ambiguous signal in the voltage characteristic curve due to the periodicity of V_{RC} in Φ . One way to detect larger magnetic field changes would be to make the area of the rf-SQUID smaller, but limited by the manufacturing process, this cannot be done arbitrarily. Instead of this the external magnetic field change is compensated by a coil and the rf-SQUID itself functions as a null detector [95]. This compensation “direct” current is proportional to the external magnetic field change. The resolution of the signal depends additionally only on the on the sensitivity of the rf-SQUID, namely on the gradient of the voltage-flux curve. Usually the maximum gradient range of the voltage-flux curve is utilized. The resolution of the SQUID in this range is between 10^{-2} - $10^{-4} \Phi_0$ [96].

However such a construction (magnetometer) is prone to other signals such as noise from the power line or earth magnetic field therefore another construction is used in the MPMS to

detect the signal. The MPMS uses a second derivative coil set (longitudinal set up, coil length 3cm) to detect the signal from the sample. This has an advantage of maximizing the magnetic field gradient of the signal from the sample and minimizing the above mentioned noises. The signal detected in the second derivative coil is coupled to the SQUID through a superconducting transformer. During the measurement the sample is moved inside the second derivative coil by a stepper motor (DC mode) or a servo motor (both DC and RSO mode) and the signal is converted into the SQUID voltage. From the amplitude of the voltage distribution the magnetic moment of the sample could be calculated. The set up with the servo motor in the RSO option is used for the measurements in this work [97]. In the RSO option the sample is moved rapidly and sinusoidally through the second derivative coils around the center of the coil, which is exclusively applied in the present work, or around the maximum gradient position of the voltage curve. The signal is recorded position sensitively. With this option a sensitivity of up to 3×10^{-9} emu can be reached and the effects of the noise from the superconducting magnets can be reduced. The second derivative coil set up and the detection system are shown in fig. 3.5.

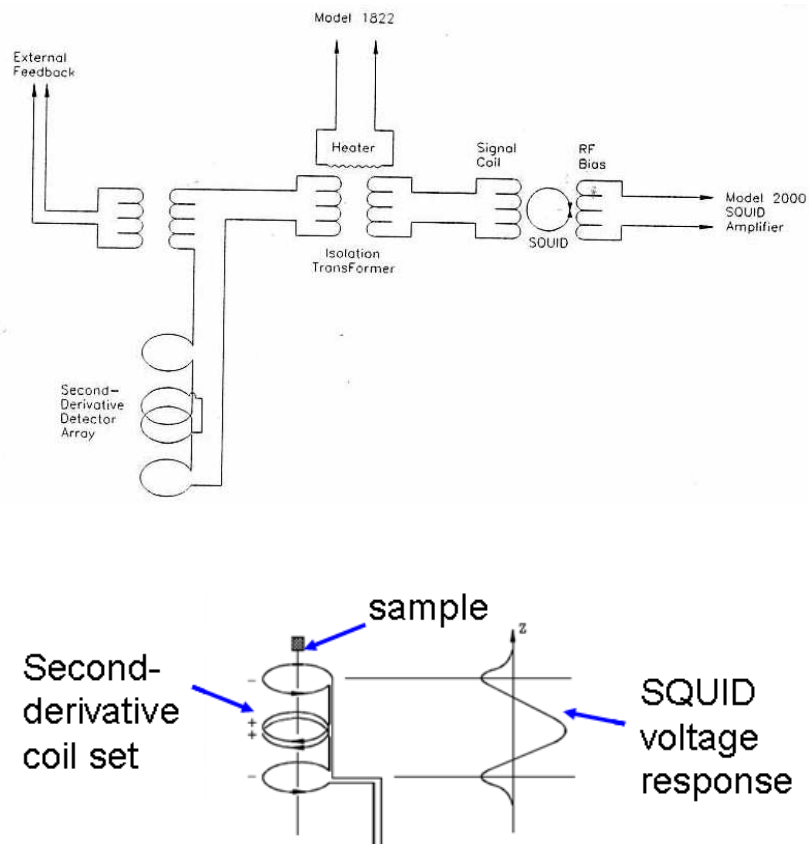


Fig. 3.5: The detection system [a127] (top) and the second derivative coil set up in an MPMS (bottom).

3.2.2 Experimental procedure

The temperature dependence of the magnetization is measured in the range 1.8-350 K and the field dependence of the magnetization is measured up to 7 Tesla using the RSO option. The oscillating amplitude around the center and the frequency of the oscillation are selected to be 4 cm and 1Hz respectively. Furthermore, three scans are done per measurement point each with two cycles of oscillation with the above mentioned frequency. Polycrystalline samples are ground, weighed and are put into a capsule. The capsule containing the powder are then fixed to a long plastic straw, which is mounted using a sample rod that in turn is moved by the servo motor.

For single crystal measurements special plastic sample holder platforms with different gradient surfaces are used (which are fixed to a straw as in the above case). As with φ and θ any macroscopic crystal surface (corresponding to some crystallographic direction) could be oriented in space, one of the angles is fixed by the choice of the sample holder with a certain gradient surface and the other angle is fixed by rotating the single crystal on the surface, thus the preferred lattice direction parallel to the external magnetic field could be fixed (fig. 3.6).

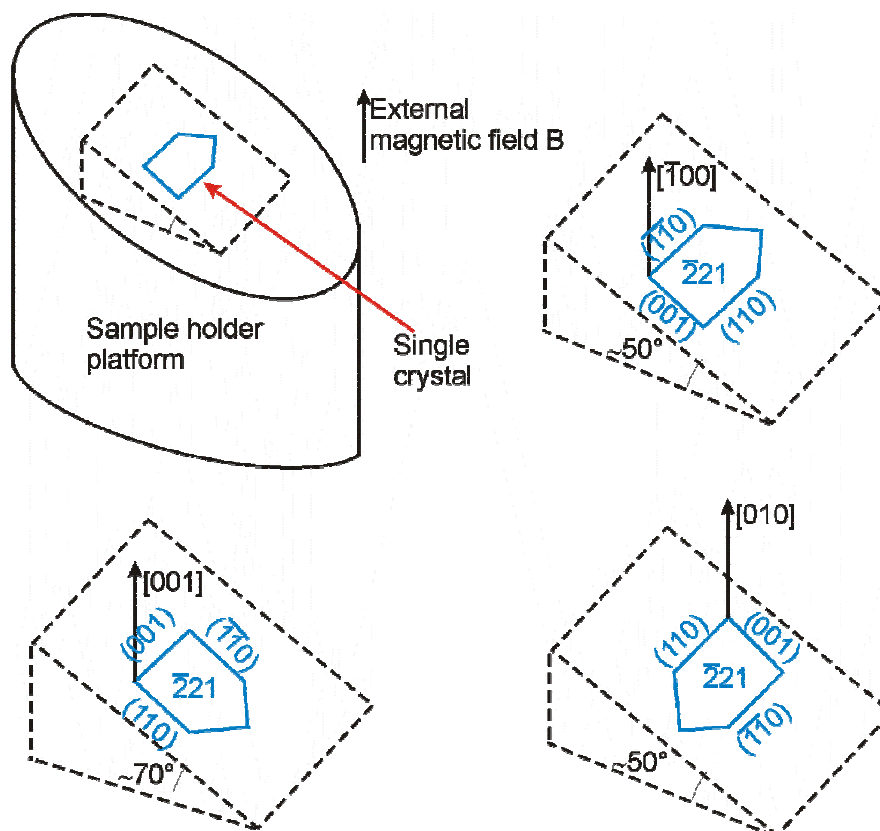


Fig. 3.6: Different orientations of the $\text{La}_2\text{CoIrO}_6$ single crystal on special sample holders.

3.3 PPMS: Physical Property Measurement System

3.3.1 Introduction

The resistivity and the heat capacity of the samples are measured using a Quantum Design Physical Properties Measurement System (PPMS). The PPMS is a cryogenic system incorporated with a 9 Tesla superconducting magnet, a precision current supply and a precision voltmeter, where different types of measurement options are available such as resistivity, heat capacity, AC transport, VSM, Hall voltage etc. These measurements can be done from 1.8-400 K and at external magnetic fields up to 9 Tesla. In case of VSM, an oven option is also available, that facilitates measurements up to 1000 K. A schematic diagram of the PPMS probe is shown in fig. 3.7. At the bottom of the sample chamber a twelve pin connector is prewired to the system electronics. A removable sample puck (sample is mounted into the puck), separate ones for each option, can be plugged and locked to the twelve pin connector with the connection to the hardware and software of the system. The temperature inside the sample chamber and the external magnetic field are controlled by the computer [99]. In the following the resistivity option and the heat capacity option are discussed.

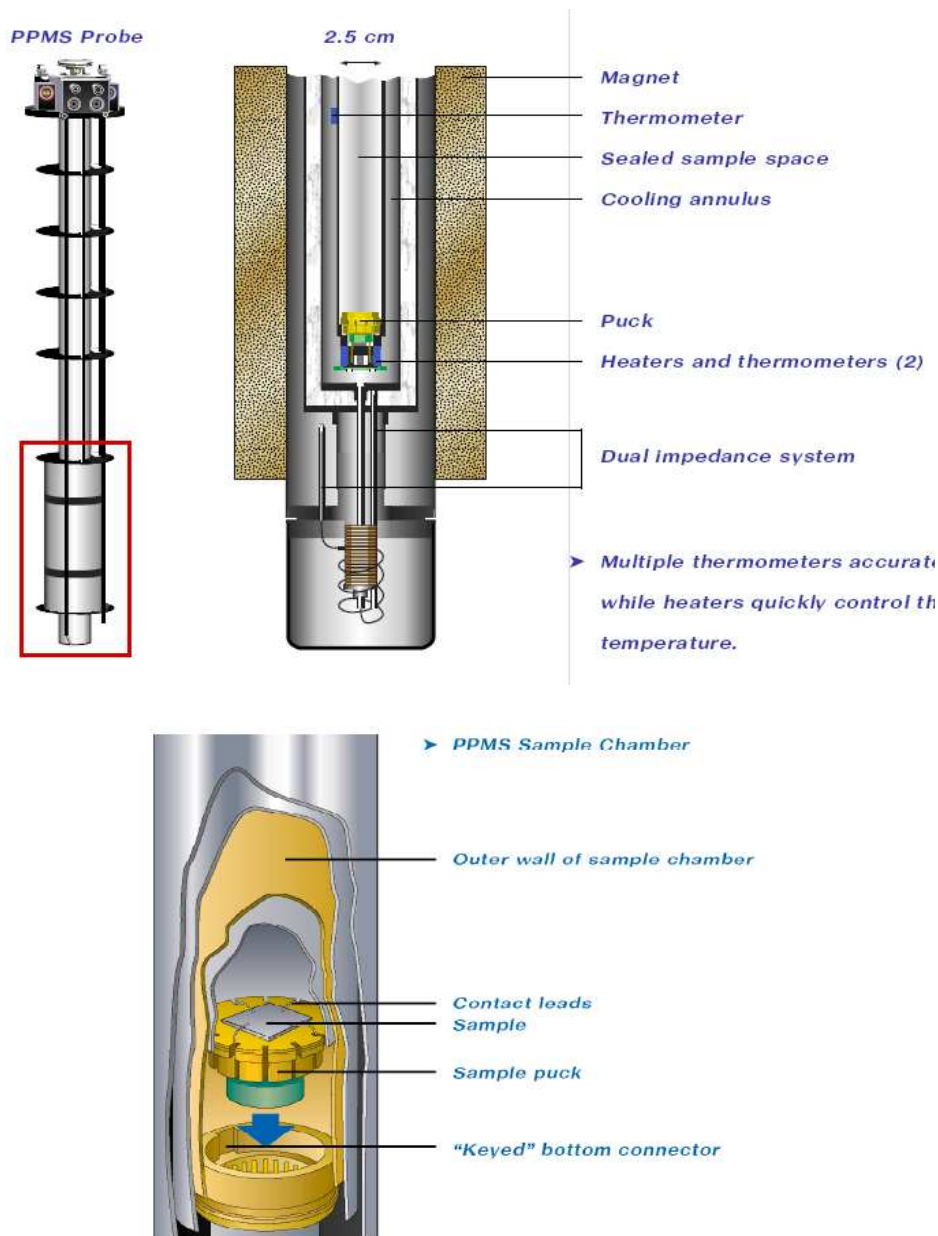


Fig. 3.7: PPMS probe [99]

3.3.2 Resistivity option and the van der Pauw method

The resistivity measurements are done using the resistivity option of the PPMS [100]. They are used to study the temperature and magnetic field dependence of the electronic transport properties of the compounds and to calculate the band gap in case of insulators by fitting the data to an adequate transport model. To measure the resistivity the van der Pauw four-point-method is utilized [101-102]. This method has the advantage that samples with arbitrary shape can be used, in contrary to the conventional four point method, where the geometry parameters are needed to calculate the resistivity. Van der Pauw showed that, for a sample of

arbitrary shape (but single connected) with homogeneous thickness and with four contacts (A,B,C,D) on it (fig. 3.8 left), the resistivity can be calculated using the following equation.

$$\rho = \frac{\pi d}{\ln 2} \left(\frac{R_{AB,CD} + R_{BC,DA}}{2} \right) f \left(\frac{R_{AB,CD}}{R_{BC,DA}} \right) \quad (3.21)$$

ρ : resistivity of the sample, d : thickness of the sample, $R_{AB,CD}$ ($R_{BC,DA}$): resistance if the current is sent between AB (BC) and the voltage is measured between CD (DA) and f is a function of the quotient of the resistances and its dependency is shown in fig. 3.8 on the right. If the quotient of the resistances is kept small, then f can be set to unity. Furthermore the contacts should be one magnitude smaller than the sample size.

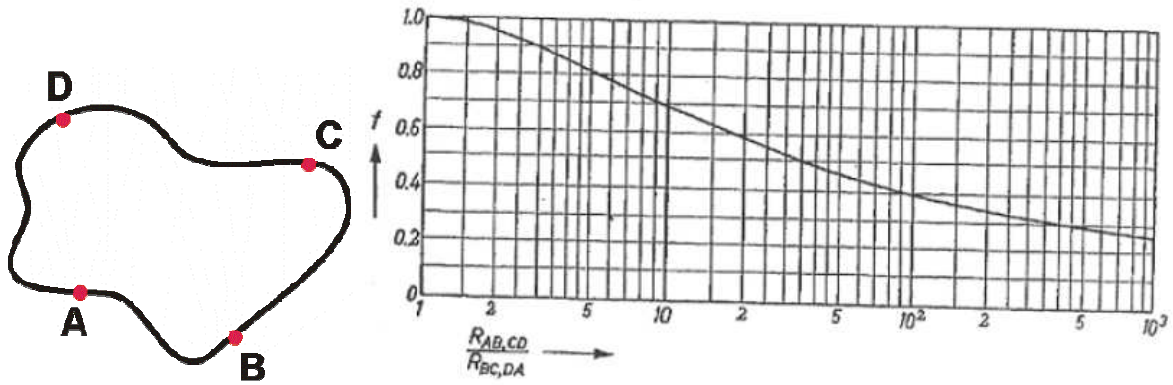


Fig. 3.8: Four contacts on the boundary of a arbitrary shaped object (left) and quotient of the resistances dependency of f [101].

In case of equidistant contacts on vertices of an imaginary square and a sample that approximately has four fold rotation axis perpendicular to the sample surface, it can be assumed the resistances $R_{AB,CD}$ and $R_{BC,DA}$ are very much similar, thus eq. 3.21 can be simplified as:

$$\rho = \frac{\pi d}{\ln 2} R_{AB,CD} \quad (3.22)$$

This is the equation used in this work. In the following the functional principle of the resistivity option in the PPMS is briefly discussed.

The samples are mounted on a special resistivity sample puck (fig. 3.9). The resistivity sample puck has four contacts (pads) each on three sides of the puck, a negative and a positive contact for current and voltage. Therefore, van der Pauw measurements are possible using this puck architecture. Each side with four contacts is connected to one of the user bridge board channels thus three samples can be measured simultaneously. But in this work only one sample is measured at the same time. For the measurements wires should be soldered to the pads and connected to the samples on the other end. This is cumbersome and may damage the pads. Instead of this a special press contact assembly (see fig 3.9) is developed, that connects the sample to the pads. There is however another problem concerning the contacts on the sample. The press contact assembly can be directly used without any further considerations for metallic samples but in the present work, the investigated compounds are polycrystalline oxides with rough surface, which paves the way for large contact resistivity. In order to tackle this problem electrically conductive two component silver epoxy Epo-Tek H20 is used on the contact points on the surface of the samples. Contacts are annealed in a furnace at 400°C. For all the investigated samples the contact resistivity reached a minimum for annealing periods around 7 minutes. In order to guarantee, that the sample has the temperature of the sample chamber, a good thermal contact between the sample and the puck is required but at the same time an electrical isolation is needed in order to avoid a short circuit. Therefore, a small weighing paper, coated with the grease Apiezon N is placed between the puck and the sample, thus guaranteeing a good thermal contact and at the same time avoiding a short circuit.

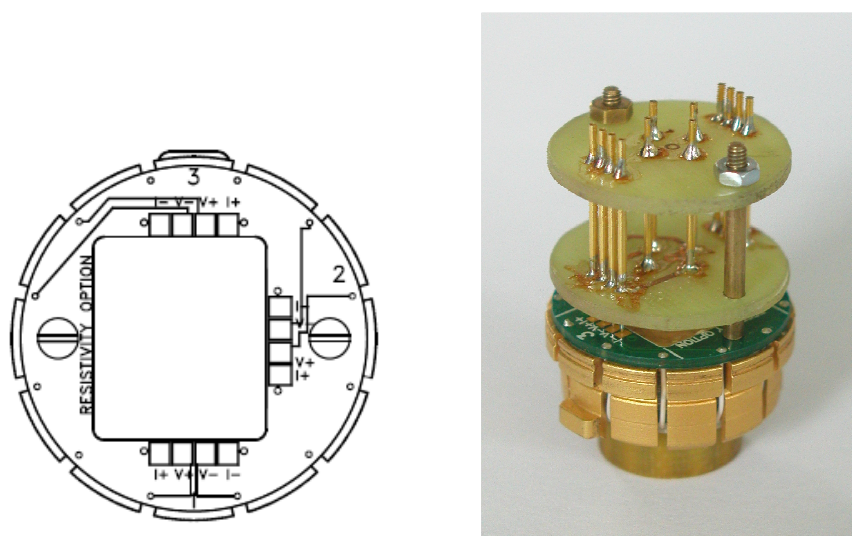


Fig. 3.9: Special resistivity sample puck [100] and a fixed special press contact assembly.

With the resistivity option, measurements can be done either in the AC or in the DC mode. In the DC mode the user bridge board applies a DC excitation to the sample and measures the voltage drop twice with the same polarity and averages them. The resistance is calculated from the DC excitation and the voltage drop and the resistivity is calculated using the eq. 3.22. In the AC mode the user bridge board applies a DC excitation to the sample and measures the voltage drop once and reverses the direction of the DC excitation current and measures once again (7.5 Hz square wave excitation) and the absolute value of the readings are averaged. The resistivity is calculated as mentioned in the first case. The AC mode has the advantage, that it eliminates errors due to a DC offset voltage. In the present work the AC mode is exclusively used. Regarding the measurement ranges, the resistivity option can measure resistances in the range from below one Ohm to more than one mega Ohms (up to 5 mega Ohms possible), which is in contrary to the ACT option in the PPMS that measures only in the nano Ohms to the kilo Ohms range. The current, voltage and the power are limited by the user bridge board. As the latter is the product of the first two parameters, the combinations of values are limited to a certain range and shown in fig. 3.10. The ranges for current, voltage and power are shown in table 3.2. The resistivity measurements of all samples of $\text{La}_{2-x}\text{Sr}_x\text{CoIrO}_6$ and $\text{La}_{2-x}\text{Ca}_x\text{CoIrO}_6$ are carried out below 300 K. For $x=0, 0.5$ and 1 of the LaSr system and $x=0.5$ and $x=75$ of the LaCa system the lowest temperature measured is limited by the large resistance (largest voltage limit and smallest current limit are exceeded), whereas for $x=1.5$ and 2 of the LaSr system resistance could be measured up to 2 K.

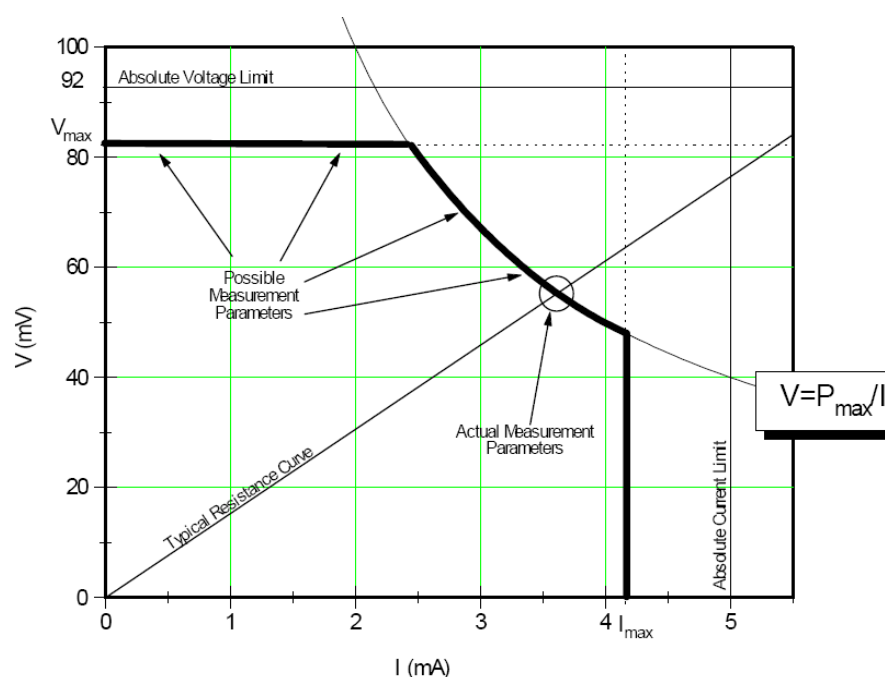


Fig. 3.10: I, V and P limitations of the operation of the resistivity option [100].

Table 3.2: The ranges for I, V and P.

Parameter	Range
Current I	$\pm 0.01\text{--}5000 \mu\text{A}$
Voltage V	$0.001\text{--}1000 \mu\text{W}$
Power P	$1\text{--}95 \text{ mV}$

3.3.3 Heat capacity option

3.3.3.1 Introduction

Heat capacity measurements are done using the heat capacity option of the PPMS [103]. They are used to study the change in the degrees of freedom of the physical properties and the interaction between them. In the present work these measurements are done in order to determine the temperature range of the magnetic ordering of the investigated compounds. The relaxation method is used to evaluate the heat capacity.

The heat capacity at constant pressure P is defined as:

$$C_P = \lim_{\delta Q \rightarrow 0} \left(\frac{\delta Q}{\Delta T} \right)_P \quad (3.23)$$

, δQ : Input heat energy, ΔT : Temperature change

The heat capacity option controls the application of the heat into the sample and its removal from the sample and monitors the temperature change during this process. A measurement includes a heating period with a constant heating power pumped to the sample for a defined period of time and cooling period with the same defined time interval, where no heating power would be pumped. During this time the difference in the sample temperature would be monitored and could be fitted to an adequate model for the heat capacity that considers either the thermal relaxation between the sample and the platform (simple model) or two relaxations, one between the sample and the platform and the other between the platform and the thermal bath (two τ model). These models are discussed in section 3.3.3.1. But at first the functional principle of the components of the heat capacity unit, which is the central part of

the calorimeter puck, is discussed. A schematic sketch of the heat capacity unit and the calorimeter puck are shown in fig. 3.11.

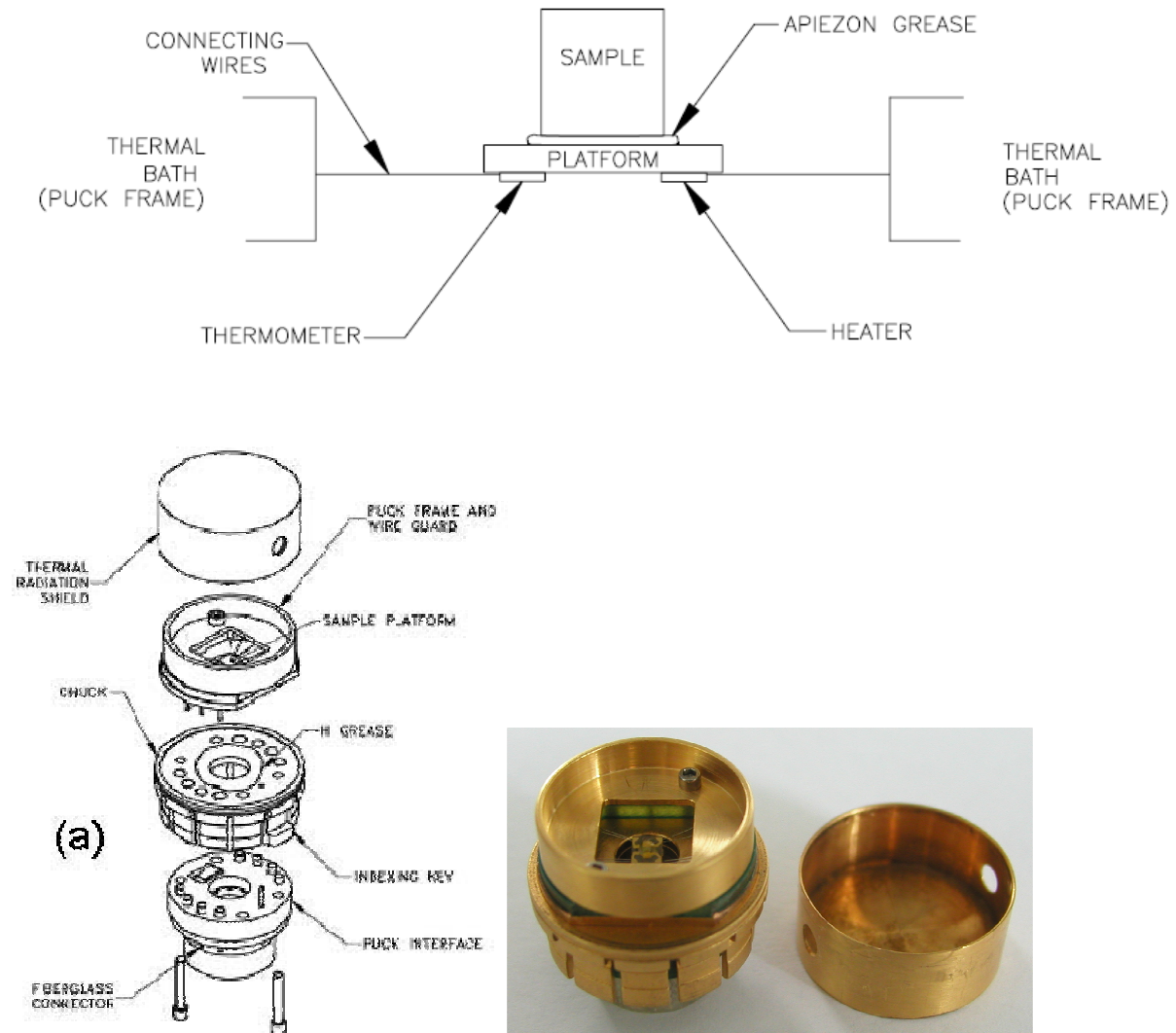


Fig. 3.11: Schematic sketch of the heat capacity unit [103] and the calorimeter puck.

The platform heater and the platform thermometers are integrated into the bottom part of the sample platform which is the calorimeter chip. The calorimeter puck contains also another thermometer, the puck thermometer, which cannot be seen in fig. 3.11. The platform temperature and thus the sample temperature are measured by the platform thermometer. The sample is mounted onto the platform using the Apiezon N grease layer as the contact between the sample and the calorimeter chip (platform). This grease is selected due to its good thermal conductivity and good adhesive properties. The eight small wires are primarily used for electrical connections to the platform thermometer and the platform heater. They also provide the thermal connection of the platform and structural stability of the platform. The PPMS

Cryopump High-Vacuum option provides a high vacuum (base pressure about 0.01 mTorr when high vacuum is activated). This enables a dominant thermal conductance between the platform and the thermal bath (puck frame) through the wires, giving a reproducible heat link to the bath with a corresponding time constant, large enough to allow reaching a good thermal equilibrium for the platform and the sample during the measurement.

3.3.3.2 Theoretical models used in the relaxation method

3.3.3.2.1 The simple model (single τ model)

If good thermal contact between the sample and the sample platform exist, then it could be assumed that the temperature of the sample and the sample platform are the same. The temperature of the platform T as a function of the time t obeys the following equation.

$$C_{\text{tot}} \frac{dT}{dt} = -K_w (T - T_b) + P(t) \quad (3.24),$$

C_{tot} : Total heat capacity of the sample and the sample platform, K_w : Thermal conductance of the wires, T_b : Temperature of the bath (puck frame) and $P(t)$: Heater power, which is a constant P_0 during heating and zero during cooling thus representing a step function. The solutions to the equation are exponential functions with the time constant $\tau = C_{\text{tot}}/K_w$. Inserting the measured platform temperature and the K_w (from calibration) to the solutions of eq. 3.24, C_{tot} can be obtained via τ . The software uses the simple model to measure the addenda (platform and grease) and generally to measure the heat capacity of most samples. In the latter case the heat capacity of the sample is obtained by subtracting the addenda contribution ($C_{\text{tot,Add}}$) from the sample measurement ($C_{\text{tot,S}}$). However if the thermal contact between the sample and the sample platform is poor, the software uses the more sophisticated two τ model.

3.3.3.2.2 Two τ model

This model is used if the thermal contact between the sample and the sample platform is poor (or if the sample is too big) and produces a temperature difference between the two. Therefore considering both the heat flow between the sample platform and the sample and as well as the

heat flow between the sample platform and the bath (puck frame), the temperatures of the platform T_p and of the sample T_s as a function of the time t obey the following equations.

$$C_{PI} \frac{dT_p}{dt} = P(t) - K_w (T_p(t) - T_b) + K_g (T_s(t) - T_p(t)) \quad (3.25)$$

$$C_S \frac{dT_s}{dt} = -K_g (T_s(t) - T_p(t)) \quad (3.26) ,$$

C_{PI} : Heat capacity of the platform and the grease, C_S : Heat capacity of the sample, K_w : Thermal conductance of the wires and K_g : Thermal conductance between the sample platform and the sample due to grease. Inserting the measured platform temperature with the two τ model, two time constants can be obtained.

$$\tau_1 = \frac{1}{\alpha + \beta} \quad (3.27)$$

$$\tau_2 = \frac{1}{\alpha - \beta} \quad (3.28)$$

$$\alpha = \frac{K_w}{2C_{PI}} + \frac{K_g}{2C_{PI}} + \frac{K_g}{2C_S} \quad (3.29)$$

$$\beta = \frac{\sqrt{(K_g C_S)^2 + 2K_g^2 C_{PI} C_S + (K_g C_{PI})^2 + (K_w C_S)^2 + 2K_g C_S^2 K_w - K_g K_w C_{PI} C_S}}{2C_{PI} C_S} \quad (3.30)$$

The heat capacity of the sample can be obtained via the two τ values by subtracting the addenda contribution, which is obtained from the simple model.

3.3.3.3 Experimental procedure

The determination of the heat capacity of the sample consists of three steps. They are the puck calibration, addenda measurement and the sample measurement. The puck calibration needed to be done only once for a puck unless the calibration files get erased or the components get damaged. The calibration procedure consists of the temperature dependent measuring the

conductivity of the wires, the resistivity of the puck thermometer, platform thermometer and platform heater and they are stored in a calibration file and used for solving the above equations. As the above parameters are also field dependent, especially non-negligible contributions below 20 K, these parameters are also calibrated at selected magnetic fields and stored in the same file. For other magnetic fields these values can be interpolated. Prior to each sample measurement an addenda measurement is carried out. For this purpose, a small amount of grease (Apiezon N) is applied onto the platform and the heat capacity of the grease together with the platform is measured (addenda). Such a heat capacity of an addenda measurement is shown in fig.3.12.

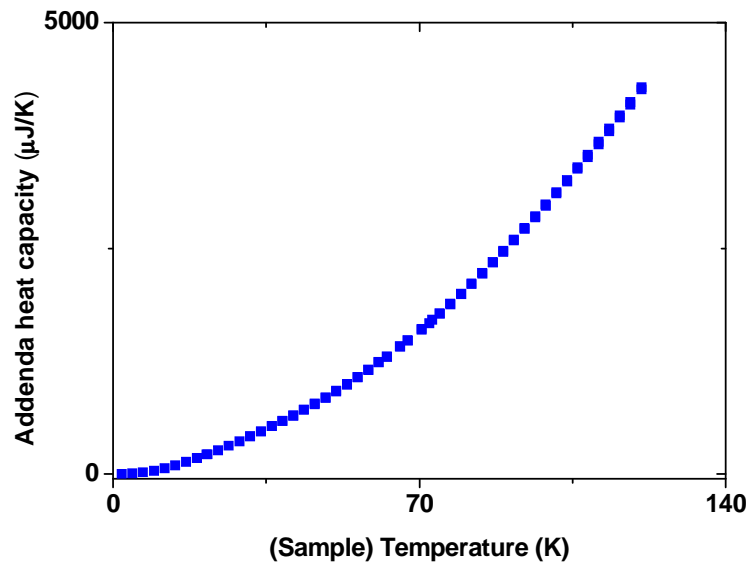


Fig. 3.12: Heat capacity of an addenda measurement.

Now in the final step the sample measurement is done. In the prior step the amount of grease should be selected depending on the size and geometry of the sample. It is also important that the flattest side of sample (should be polished in critical cases) be placed on the grease as inhomogenities in the surface of the sample would influence the thermal contact between the platform and sample which in turn would affect the accuracy of the measurement. Once the measurement is started, the determination of the heat capacity of the sample is automatically done by the software. In this work the temperature dependence of the heat capacity is measured from 2 K up to 250 K for $x=0, 0.5$ and 1.5 of $\text{La}_{2-x}\text{Sr}_x\text{CoIrO}_6$ (at around 280 K there is an anomaly in the addenda probably coming from the grease [a88]). In most cases 3 measurements are done per temperature point and the heat capacity is measured with 2% of temperature change.

After the heat capacity data are obtained, it is important to analyse their temperature dependence. In the present work finding anomalies at the magnetic ordering temperature is of primary interest or, in other words, the magnetic contribution to the heat capacity. In order to obtain the magnetic contribution, the phononic contribution should be subtracted from the total C_P (in case of insulating oxides the electronic contribution is negligible). Usually the C_P of a non-magnetic isostructural compound would be measured and it would be subtracted from the sample C_P . In the present work there is no possibility for such an option and therefore the phononic contribution should be approximated using an appropriate model. Usually the Debye model is used to approximate the phononic contribution. Within this model only the acoustic branches of the phononic spectrum would be considered and furthermore all of them are described by the same sound velocity. With these assumptions the Brillouin zone of the crystal is approximated by a sphere of the same volume in the reciprocal space and the formula for specific heat capacity C_P has the following form.

$$C_P = 9R \left(\frac{T}{\Theta_D} \right)^3 \int_0^{\frac{E_D}{k_B T}} \frac{e^x x^4}{(e^x - 1)^2} dx \quad (3.31),$$

Universal gas constant $R=8.314$ J/K mol, Θ_D : Debye temperature, Debye energy $E_D=k_B\Theta_D$ and k_B : Boltzmann's constant.

The integral in the above expression is the Debye integral and cannot be solved without special functions analytically.

Therefore the Debye integral is approximated by the Simpsons method with $n=4$.

$$C_P = \frac{3R}{8} \left(\frac{T}{\Theta_D} \right)^2 \left[\begin{aligned} & \frac{e^{\frac{\Theta_D}{T}} \left(\frac{\Theta_D}{T} \right)^4}{\left(e^{\frac{\Theta_D}{T}} - 1 \right)^2} + 2 \frac{e^{\frac{\Theta_D}{8T}} \left(\frac{\Theta_D}{8T} \right)^4}{\left(e^{\frac{\Theta_D}{8T}} - 1 \right)^2} + 2 \frac{e^{\frac{3\Theta_D}{8T}} \left(\frac{3\Theta_D}{8T} \right)^4}{\left(e^{\frac{3\Theta_D}{8T}} - 1 \right)^2} + 2 \frac{e^{\frac{5\Theta_D}{8T}} \left(\frac{5\Theta_D}{8T} \right)^4}{\left(e^{\frac{5\Theta_D}{8T}} - 1 \right)^2} \\ & + 2 \frac{e^{\frac{7\Theta_D}{8T}} \left(\frac{7\Theta_D}{8T} \right)^4}{\left(e^{\frac{7\Theta_D}{8T}} - 1 \right)^2} + 4 \frac{e^{\frac{\Theta_D}{4T}} \left(\frac{\Theta_D}{4T} \right)^4}{\left(e^{\frac{\Theta_D}{4T}} - 1 \right)^2} + 4 \frac{e^{\frac{\Theta_D}{2T}} \left(\frac{\Theta_D}{2T} \right)^4}{\left(e^{\frac{\Theta_D}{2T}} - 1 \right)^2} + 4 \frac{e^{\frac{3\Theta_D}{4T}} \left(\frac{3\Theta_D}{4T} \right)^4}{\left(e^{\frac{3\Theta_D}{4T}} - 1 \right)^2} \end{aligned} \right] \quad (3.32)$$

3.B DFT calculation procedure

First principles density functional theory (DFT) spin polarized electronic structure calculations are performed for $x=0, 1$ and 2 of $\text{La}_{2-x}\text{Sr}_x\text{CoIrO}_6$ (calculations are performed for $x=0.5$ and 1.5 in the FM configuration only to obtain the Bader charges) by the full-potential linearized augmented plane wave plus local orbital method as implemented in the WIEN2k code [105]. The following non-overlapping atomic spheres with radii R_{MT} (in a.u.) are used (Table 3B.1):

Table 3B.1: Non-overlapping atomic sphere radii (in a.u.), mesh of the special k points in the IBZ and the number of independent atoms corresponding to composition x and the different magnetic structures.

x	La	Sr	Co	Ir	O	Special k mesh	No. of independent atoms	magnetic structure
						$6 \times 6 \times 4$	6	FM
0	2.38		2.04	1.98	1.76	$6 \times 6 \times 4$	12	$k=(0,0,0)$, AFM
						$4 \times 2 \times 1$	80	$k=(0,1/2,1/2)$, AFM
0.5*	2.40	2.26	2.06	1.97	1.75	$5 \times 5 \times 3$	20	FM
1.0	2.40	2.27	2.02	1.96	1.73	$2 \times 4 \times 1$	80	$k=(1/2,0,1/2)$, AFM
						$4 \times 2 \times 1$	80	$k=(0,1/2,1/2)$, AFM
1.5 ($P2_1/n$)*	2.37	2.24	2.00	1.91	1.70	$5 \times 5 \times 3$	20	FM
1.5 ($I2/m$)*	2.50	2.32	1.89	1.91	1.68	$5 \times 5 \times 3$	16	FM
2.0 ($P2_1/n$)		2.38	1.91	1.92	1.69	$4 \times 2 \times 1$	80	$k=(0,1/2,1/2)$, AFM
								$k=(1/2,0,1/2)$, AFM
2.0 ($I2/m$)		2.38	1.91	1.94	1.70	$4 \times 2 \times 1$	80	$k=(0,1/2,1/2)$, AFM
								$k=(1/2,0,1/2)$, AFM

*Only for the calculation of Bader charges.

The value of $R_{\text{MT}}K_{\text{max}}$, where K_{max} corresponds to the largest plane wave vector, is set to 6.5 and spherical harmonics up to the 10th order were included in the expansion of the radial part of the wave function. The mesh of special k points in the irreducible Brillouin zone (IBZ) are selected as shown in table 3B.1. The numbers of independent atoms in the unit cell are also

given in table 3B.1. For the exchange-correlation energy functional the Perdew-Burke-Ernzerhof (PBE) version of the generalized gradient approximation (GGA) is used [38]. The spin-orbit-coupling (SOC quantization axis:z) was included in a second variational step with scalar relativistic orbitals as basis [106]. The structural parameters were taken from NPD at 3 K and are shown in Table II. To compensate the shortcomings of the LDA/GGA regarding the exchange-correlation effects a “U”, which describes the electron-electron interaction is added to the calculation in two different flavours FLL and AMF [64]. The convergence is reached as the difference in the charge fluctuation becomes less than 0.0001 of an electron. Additionally a relaxation of the internal atomic positions is carried out for x=0 in order to compare the total energies of the FM ($4 \times 4 \times 2$), $k=(0,0,0)$ AFM ($4 \times 4 \times 2$) and the $k=(0,1/2,1/2)$ AFM ($4 \times 2 \times 1$) structures. From the converged charge densities Bader charges are also calculated for all five compositions using the Bader’s AiM concept (using WIEN2k) [74]. For this calculation additionally to the charge densities of the experimentally found AFM structures of x=0,1 and 2, charge densities of the FM configuration of x=0.5 and 1.5 are used. However it should be mentioned, that this approach does not always give a quantitative assessment (see section 2.3.3) of the valence state but it is quite useful for investigating trends within a certain system [75]. The trend of the Bader charges is discussed in section IV A together with the bond valence sums (BVS).

Calculations for x=0 with a non collinear arrangement of the magnetic moments are performed by the WIENNCM code, which is based on the WIEN2k concept [107]. The basics of this type of calculations are discussed in section 2.1.7.8. The calculations are performed with the following arrangement of the magnetic moments.

-The AFM arranged moments of Co is tilted from the c direction towards b direction, creating an increasing ferromagnetic component in this direction.

-The AFM arranged moments of Co is tilted from the $[-1,0,2]$ direction towards b direction, creating an increasing ferromagnetic component in this direction.

The reason for the present selection of this particular direction for the tilting is discussed in section 5.7.2. Note that in all the non collinear calculations the magnetic moments of Ir are free to rotate and are not constrained, whereas the direction of the magnetic moments of Co are constrained to the above restrictions. Most of the options are retained from the WIEN2k

calculations and the only major change is the type of the Brillouin zone integration. For the non collinear calculations the temperature broadening method [108] is used with a broadening parameter of 0.005 Ry. The important input parameters are summarized in table 3B.

Table 3B.2: The direction of the FM component, non-overlapping atomic sphere radii in atomic units, mesh of the special k points in the IBZ and the number of independent atoms, corresponding to the different magnetic structures.

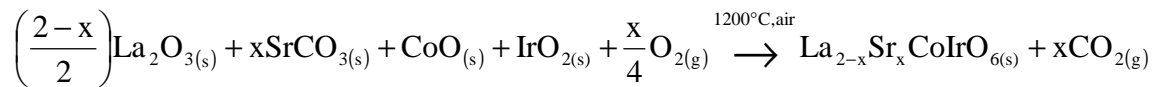
Direction of the AFM component of Co	Direction of the FM component	La	Co	Ir	O	Special k mesh	No. of independent atoms	magnetic structure
c [0,0,1]	b [0,1,0]	2.38	2.04	1.98	1.76	5×5×3	20	NCM
[-1,0,2]	b [0,1,0]	2.38	2.04	1.98	1.76	5×5×3	20	NCM

Furthermore all the important input files for both WIEN2k and WIENNCM are shown in appendix 3.

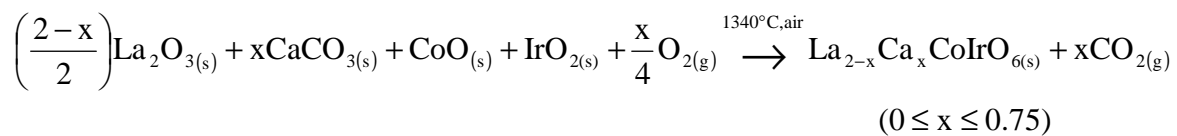
4. Synthesis of the compounds

4.1 Polycrystalline samples

Polycrystalline samples of $\text{La}_{2-x}\text{Sr}_x\text{CoIrO}_6$ are synthesized by solid state reaction for five different compositions $x=0, 0.5, 1, 1.5$ and 2 . Stoichiometric amounts of reactants La_2O_3 (Alfa Aesar, 99.99%), SrCO_3 (Alfa Aesar, 99.99%), CoO (Alfa Aesar, 99.99%) and IrO_2 (UMICORE, 99.698%) are ground together in an agate mortar, pressed into pellets, placed into corundum crucibles, heated to 1200°C in air within a muffle furnace, hold at this temperature for 24 hours and slowly cooled down to room temperature. Under these conditions of synthesis only negligible oxygen deficiency $\delta \approx 0$ is expected. Phase purity and crystal structures are determined at room temperature by X-ray powder diffraction in flat-sample transmission mode, using a STOE STADIP diffractometer, which is described in section 3.1.2. The reaction equation is shown in the following.



Polycrystalline samples of $\text{La}_{2-x}\text{Ca}_x\text{CoIrO}_6$ are also synthesized by the above method for two different compositions $x=0.5$ and 0.75 . For $x>0.75$ single phase samples are not obtained. For $x=0.5$ and 0.75 , pellets are heated to 1340°C in air within a muffle furnace, hold at this temperature for 24 hours and slowly cooled down to room temperature. The phase purity of $x<0.75$ is determined by X-ray power diffraction. The reaction equation is shown in the following.



Additionally BaO_2 is added instead of La_2O_3 in order to synthesize polycrystalline samples of $\text{Sr}_{2-x}\text{Ba}_x\text{CoIrO}_6$ ($x \leq 0.25$) in air. With this, it is intended to increase the average size of the A-site cation and thus influence the bandwidth of the d bands, in order to trigger a possible insulator to metal transition. But single phase samples are not obtained even after increasing the synthesis temperature to 1350°C .

4.2 Single crystals of $\text{La}_2\text{CoIrO}_6$

Single crystals of $\text{La}_2\text{CoIrO}_6$ are grown by the flux method [109-111]. The flux is a mixture of PbO and PbF_2 . This mixture is mixed with La_2O_3 , CoO and IrO_2 in the flux to sample ratio of 80:20, put in a platinum crucible, heated to 1000°C in air within a muffle furnace, hold at this temperature for 24 hours and slowly cooled to 500° for sixteen days. Single crystals are scratched from the flux masses and later polished. The largest obtained single crystal is approximately $3 \times 2 \times 1 \text{ mm}^3$, which is kept for neutron diffraction experiments in the future. Two single crystals with $2 \times 1 \times 1 \text{ mm}^3$ are selected for heat capacity and magnetization measurements (4.33 mg). The faces of one of the single crystal used for magnetization measurements, are indexed by single crystal diffraction in order to align specific crystal directions with respect to the external field

5. Results and discussion

5.1 Crystal structures of $\text{La}_{2-x}\text{Sr}_x\text{CoIrO}_6$

5.1.1 Room temperature crystal structures

Rietveld refinements of structural parameters are performed, based on x-ray and neutron diffraction data simultaneously, using the program FullProf [92]. As an example the diffraction patterns of $\text{Sr}_2\text{CoIrO}_6$ obtained from x-ray diffraction and neutron diffraction together with the calculated ones are shown in fig. 5.1 and fig. 5.2. From fig. 5.1 and fig. 5.2 it is evident that single phase samples (apart from a very small amount of IrO_2) are obtained for the mentioned compositions. The diffraction patterns with the calculated intensities of other compositions are shown in appendix 1.

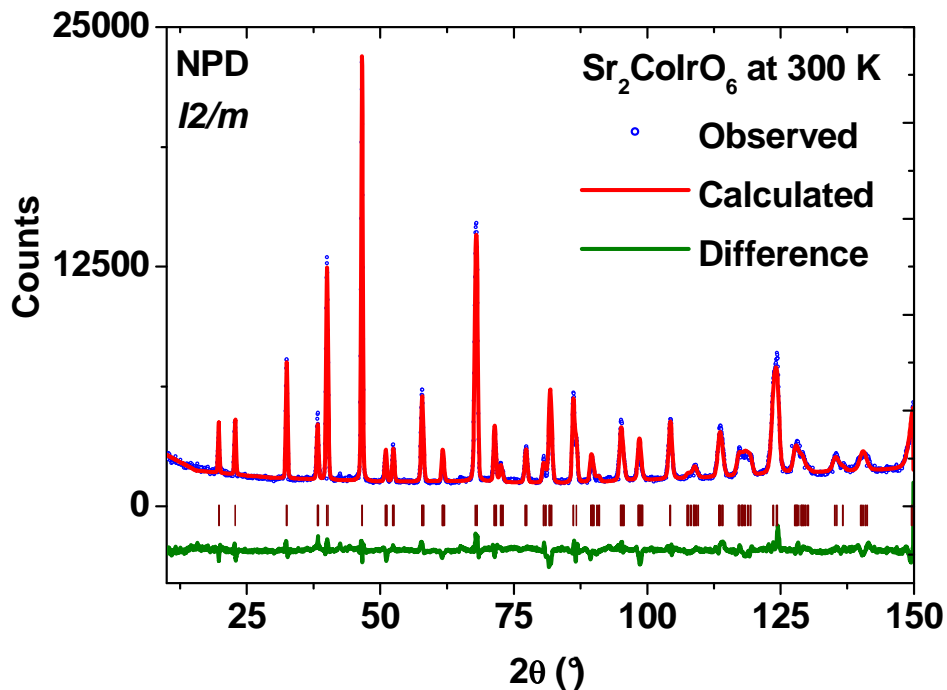


Fig. 5.1: Room temperature neutron powder diffraction (NPD) pattern of $\text{Sr}_2\text{CoIrO}_6$ with the calculated pattern.

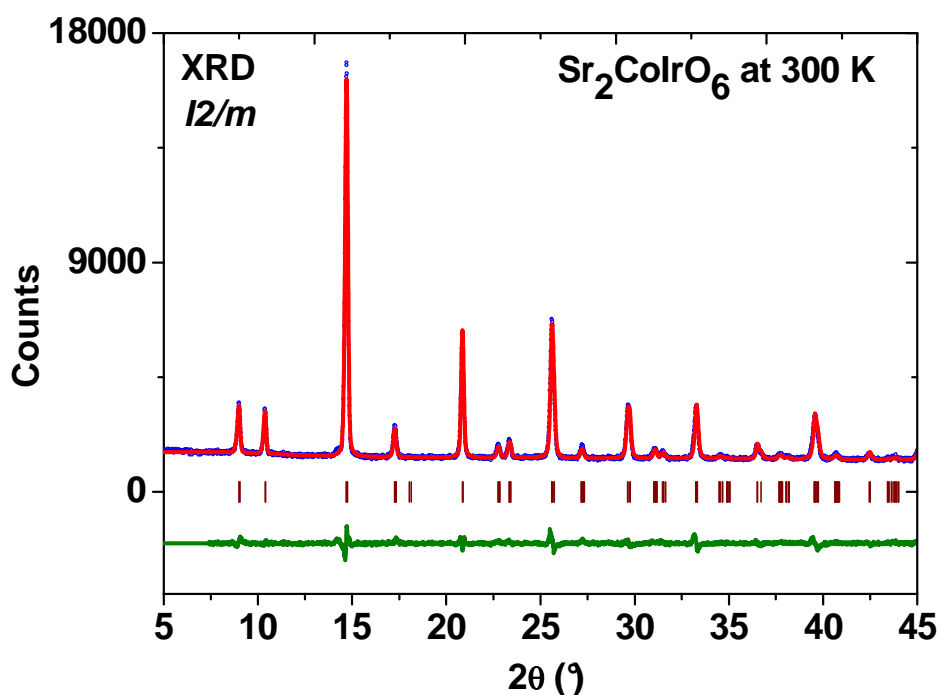


Fig. 5.2: Room temperature x-ray diffraction (XRD) pattern of $\text{Sr}_2\text{CoIrO}_6$ with the calculated pattern.

All members of the series crystallize with a monoclinic symmetry but in two different space groups. Compounds with the composition $x=0, 0.5$ and 1 crystallize in the space group $P2_1/n$. This agrees with the crystal structure reported earlier for $\text{La}_2\text{CoIrO}_6$ with $x=0$ [10]. $\text{Sr}_2\text{CoIrO}_6$ with $x=2$ crystallizes in the space group $I2/m$. For $x=1.5$ two monoclinic modifications with space groups $P2_1/n$ and $I2/m$ coexist at room temperature. The coexistence could be seen from broadening or even splitting of the nuclear reflexes. The (partial) splitting is clearly visible for the 040 Bragg reflection (together with 400 -224 and 224) and this is shown in fig. 5.3. As a comparison the range of the 040 reflex of $x=0$ in $P2_1/n$ and of $x=2$ in $I2/m$ are also shown in the same figure.

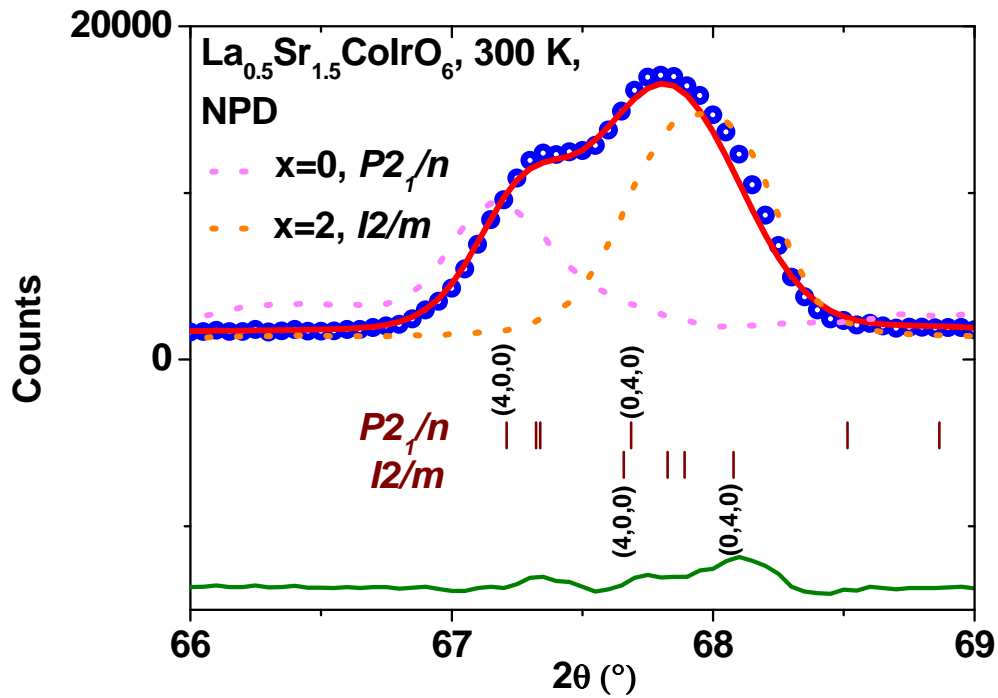


Fig. 5.3: Part of the NPD of $\text{La}_{0.5}\text{Sr}_{1.5}\text{CoIrO}_6$ with contains the 400 and 040 Bragg reflexes. The partial splitting of this peak is due to the coexistence of two monoclinic phases. As a comparison the peaks of $x=0$ and $x=2$, which contains the above mentioned reflexes are also shown.

Depending on composition the following phase transitions occur at room temperature with increasing Sr-content: $P2_1/n \leftrightarrow P2_1/n + I2/m \leftrightarrow I2/m$. The corresponding crystal structures are superstructures of the perovskite type as stated in section 2.2. The deviation from the ideal cubic perovskite structure is the distribution of Co and Ir on two distinct crystallographic sites (“double perovskite”) and rotations of the corner-sharing CoO_6 - and IrO_6 -octahedra, which break the cubic symmetry as already stated in section 2.2. The crystal structures of the two monoclinic phases with space groups $P2_1/n$ and $I2/m$ are shown in fig. 5.4.

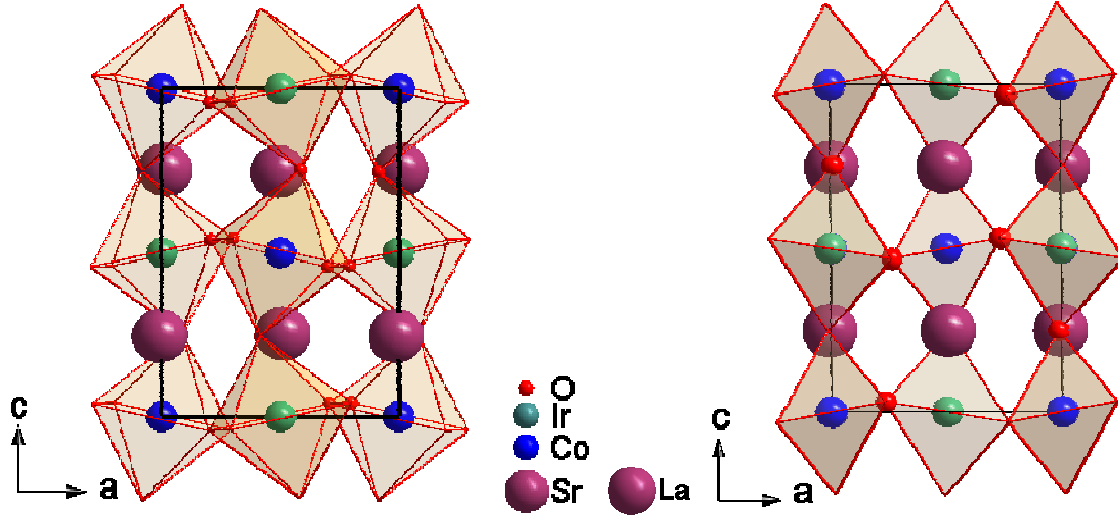


Fig. 5.4: Unit cells of the two monoclinic modifications in different space groups existing at room temperature: $P2_1/n$ ($a^- a^- c^+$) (left) and $I2/m$ ($a^0 b^- b^-$) (right).

Both structures differ with respect to the specific octahedra tilting system, described by Glazer's notation [112] and belong to the twelve possible space groups derived group theoretically by Howard et al. [69,70], by means of considering the deviation only due to the tilting of the octahedra. An empirical criterion for the prediction of the specifically distorted perovskite-type structure is based on the ionic radii according to the Goldschmidt tolerance factor f [71]. Monoclinic crystal structures are expected for $f < 0.97$ [72]. For all the compositions in this system f is clearly less than 0.97 and thus fulfils this empirical rule. The structural parameters together with the space groups and tolerance factors are listed in Table 5.1. The atomic coordinates of the five different compositions are given in appendix 2.

Table 5.1: Space groups and structural parameters of $\text{La}_{2-x}\text{Sr}_x\text{CoIrO}_6$ at room temperature.

x	Space group	f	a (Å)	b (Å)	c (Å)	β (°)
0	$P2_1/n$	0.8682	5.5819(1)	5.6576(1)	7.9078(2)	89.98(1)
0.5	$P2_1/n$	0.8868	5.6010(1)	5.6151(1)	7.9151(2)	89.982(5)
1.0	$P2_1/n$	0.9058	5.5988(1)	5.5750(1)	7.9029(2)	89.989(6)
1.5	$P2_1/n$	0.9253	5.5960(2)	5.5613(4)	7.9135(3)	89.98(1)
	$I2/m$		5.5633(3)	5.5329(2)	7.8479(5)	89.94(1)
2.0	$I2/m$	0.9452	5.5285(2)	5.5508(2)	7.8427(3)	90.297(3)

Possible changes of the oxidation states of Co and Ir due to the substitution of La by Sr should be reflected in the transition metal oxygen bond lengths along the series. The average bond lengths of Co-O and Ir-O were calculated using the software Diamond [113] and are shown in fig. 5.5 (a). The decreasing bond lengths with increasing Sr-content are an indication for a transition in the oxidation state of Co and Ir. Only minor changes in the Co-O bond length with Sr-content x are observed in space group $P2_1/n$, but a significantly shorter Co-O bond length is observed in the phase with space group $I2/m$. In contrast the Ir-O bond length becomes considerably shorter with increasing Sr-content within the stability range of the $P2_1/n$ phase. This is a strong indication that La-substitution by Sr results first (up to about $x=1.5$) in a higher oxidation state of Ir, whereas a higher oxidation state of Co is accompanied by the transition from the $P2_1/n$ phase into the $I2/m$ phase for high levels of substitution ($x \geq 1.5$). In order to interpret the above indications bond valence sums BVS for Co and Ir are calculated using the equation introduced by Brown et al and mentioned in section 2.3.2 [73]. The reference bond lengths $r_0(\text{M-O})$ are taken from [114] and the results are shown in Table 5.2. The values of the bond valence sums BVS confirms the observed trend of the bond lengths. Whereas regarding each compound, the bond valence sums for Co are similar for $r_0(\text{Co}^{2+}-\text{O}^{2-})$ and $r_0(\text{Co}^{3+}-\text{O}^{2-})$ cases, the sums for Ir are different for $r_0(\text{Ir}^{4+}-\text{O}^{2-})$ and $r_0(\text{Ir}^{5+}-\text{O}^{2-})$ cases. Nevertheless they show the same trend with increasing Sr-content. It is evident that there are only minor changes in the Co^{2+} state in the $P2_1/n$ space group that abruptly changes into a Co^{3+} state in the $I2/m$ space group for $x \geq 1.5$, whereas for Ir the transition $\text{Ir}^{4+} \rightarrow \text{Ir}^{5+}$ takes place gradually within the $P2_1/n$ space group and there are only minor changes in the $I2/m$ space group (for the reference bond length $r_0(\text{Ir}^{5+}-\text{O}^{2-})$ even a partial amount of Ir^{6+} is predicted for higher Sr-content, but it may be better approximated by Ir^{5+}). Therefore a partial transition in the oxidation states of Co and Ir from $\text{Co}^{2+}/\text{LS-Ir}^{4+} \rightarrow \text{HS-Co}^{3+}/\text{LS-Ir}^{5+}$ could be concluded. Almost the same trend can be observed in the composition dependence of the Bader charges, which are shown in Table 5.3. The only difference being the non-pronounced increase in the Bader charge of Co in the space group $I2/m$ for $x=1.5$. However, Rietveld refinements reveal a high degree of cation site disorder between B- and B'-sites. The site disorder increases from $y=5.4\%$ to 13.6% , indicating an increasing miscibility of Co and Ir ions (Fig. 5.5 (b)). The difference in ionic radii between Co^{2+} (0.745 Å) and Ir^{4+} (0.625 Å) is 0.12 Å, whereas between Co^{3+} (0.61 Å) and Ir^{5+} (0.57 Å) it is only 0.04 Å [115]. The increase of the site disorder for high values of x further supports the assumption of the proposed transition of the oxidation states. However, the rather short Co-O bond length in the $I2/m$

phase can partially result from the relative high admixture of Ir on the Co site and the higher weight of the shorter Ir-O bonds.

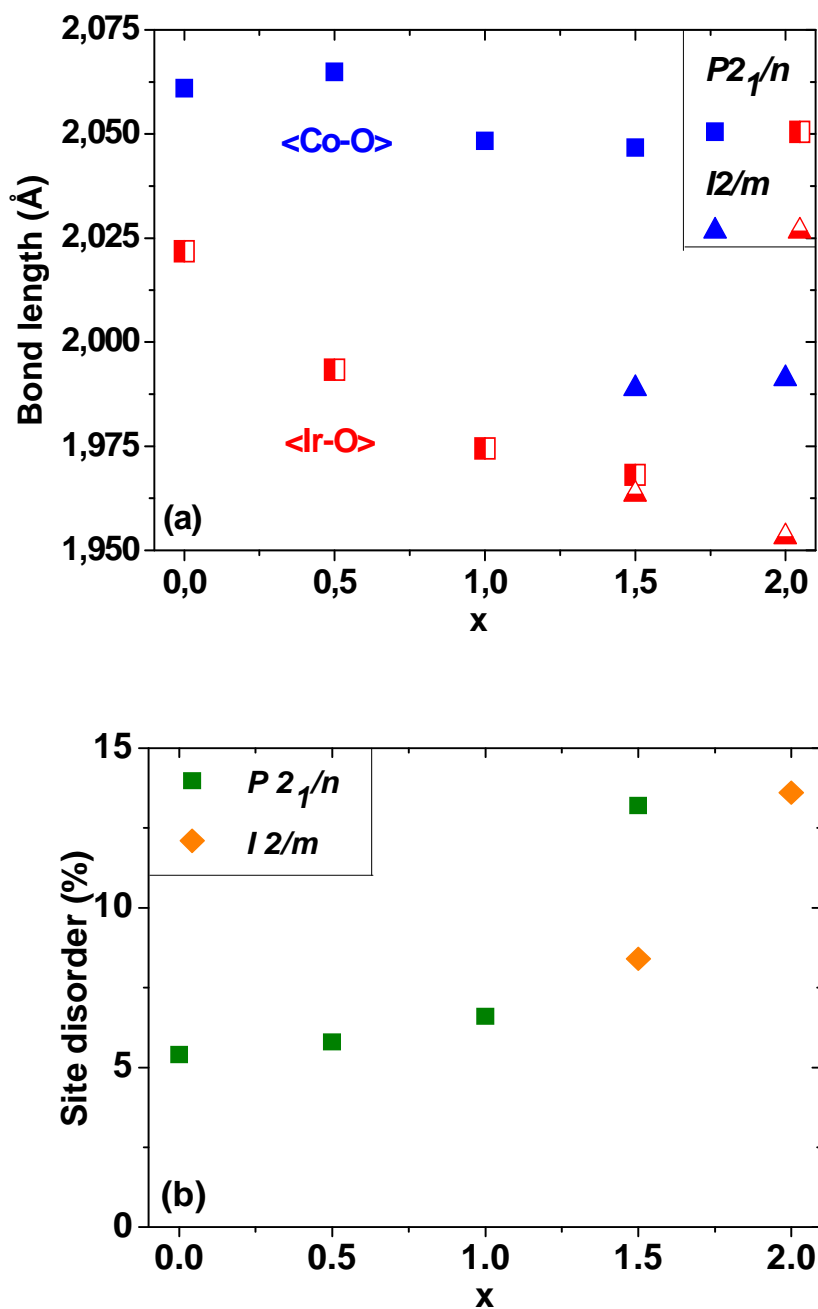


Fig. 5.5: (a) Composition dependence of Co-O and Ir-O bond lengths and (b) composition dependence of the site disorder.

Table 5.2: Bond valence sums calculated from Co-O and Ir-O at room temperature.

x	BVS [$r_0(\text{Co}^{2+}-\text{O}^{2-})$]	BVS [$r_0(\text{Co}^{3+}-\text{O}^{2-})$]	BVS [$r_0(\text{Ir}^{4+}-\text{O}^{2-})$]	BVS [$r_0(\text{Ir}^{5+}-\text{O}^{2-})$]
0	2.22	2.26	3.98	4.52
0.5	2.20	2.24	4.30	4.88
1.0	2.30	2.34	4.54	5.14
1.5 $P2_1/n$	2.26	2.30	4.76	5.38
$I2/m$	2.70	2.76	4.66	5.28
2.0	2.68	2.74	4.80	5.42

Table 5.3: Bader charges calculated from charge densities associated with the lattice parameters at 3K.

x	0	0.5	1.0	1.5 $P2_1/n$	1.5 $I2/m$	2.0 $P2_1/n$	2.0 $I2/m$
Co	1.37	1.37	1.42	1.42	1.47	1.72	1.69
Ir	1.69	1.82	1.91	1.98	1.98	1.98	2.01

5.1.2 Temperature dependence of crystal structures

Rietveld refinements were performed for all five compositions, based on diffraction patterns from 3 K to 1173 K. Sequences of phases with different crystal structures have been observed with respect to both composition x and temperature T as summarized in Fig. 5.6. The refined lattice parameters at 3 K together with their appropriate space groups are summarized in table 5.4.

Table 5.4. Space groups and structural parameters of $\text{La}_{2-x}\text{Sr}_x\text{CoIrO}_6$ at 3K.

x	Space group	a (Å)	b (Å)	c (Å)	β (°)
0	$P2_1/n$	5.5684(1)	5.6604(1)	7.8956(2)	89.96(1)
0.5	$P2_1/n$	5.5979(1)	5.6251(1)	7.9112(1)	90.004(5)
1.0	$P2_1/n$	5.6121(9)	5.6015(6)	7.9182(4)	89.96(1)
1.5	$P2_1/n$	5.5933(2)	5.5549(3)	7.9117(3)	89.98(1)
1.5	$I2/m$	5.5564(3)	5.5456(2)	7.8022(3)	90.24(1)
2.0	$P2_1/n$	5.5611(3)	5.5351(3)	7.7920(2)	89.70(1)
2.0	$I2/m$	5.5940(1)	5.5560(1)	7.7208(1)	89.93(1)

While the $P2_1/n$ phase for $\text{La}_2\text{CoIrO}_6$ ($x=0$) remains stable up to 1173 K, a substitution of 25% La by Sr ($x=0.5$) is sufficient for a temperature induced phase transition from the $P2_1/n$ phase into a two-phase coexistence region above 923 K. A further increase of the Sr-content reduces the transition temperature into the two-phase region, for $x=1$ down to 750 K and for higher Sr-contents down to the lowest temperatures. For $x=1.5$ and $x=2$ three successive phase transitions are observed during heating: from the two-phase region the primitive monoclinic phase disappears, for $x=2$ already at 260 K below room temperature. The phase

transition from $P2_1/n$ into $I2/m$ is of first order, with a broad coexistence range of both phases. This particular phase transition is discussed in detail later. At elevated temperature a further phase transition $I2/m \leftrightarrow I4/m$ takes place at around 973 K for $x=1.5$ and at around 625 K for $x=2$. This phase transition is of second order with no discontinuity in volume (Fig. 5.7). However, both Howard [69] and Gateshki [70] describe this phase transition to be of first order, whereas the only known double perovskite, which undergoes a second order phase transition $I2/m \leftrightarrow I4/m$ is Ba_2CaWO_6 [116]. This tetragonal body-centered phase has only a rather small stability window, and at higher temperatures a further phase transition of second order from $I4/m \leftrightarrow Fm-3m$ is observed at around 1073 K for $x=1.5$ and 700 K for $x=2$. The temperature dependences of lattice parameters are shown in Fig. 5.8(a)-5.8(c) for selected compounds over characteristic temperature ranges. From the phase diagram (fig. 5.6) it becomes evident that the symmetry of the crystal structure increases with increasing average size of the A-site cations at constant temperature, in agreement with other systems with double perovskite structure [72]. Depending on temperature and composition the following sequence of phase transitions is observed: $P2_1/n \leftrightarrow P2_1/n + I2/m \leftrightarrow I2/m \leftrightarrow I4/m \leftrightarrow Fm-3m$. This sequence of structural phase transitions was already reported for Sr_2MnTeO_6 , where the first order nature of the phase transition $P2_1/n \leftrightarrow I2/m$ was confirmed by the existence of a thermal hysteresis in DSC measurements [117]. However the coexistence region of the two monoclinic phases in case of Sr_2MnTeO_6 is only 50 K between 250 K and 300K, thus the coexistence does not extend to lower temperatures as in the case for $x=1.5$ and $x=2$. Such a coexistence of two monoclinic phases at lower temperatures is found in the double perovskite system $Ca_xSr_{2-x}FeReO_6$ for $1 \leq x \leq 2$ (some authors argue that the coexistence range is $0.8 \leq x \leq 2$ [3]). But in that case both of the monoclinic phases belong to the same space group $P2_1/n$ [118-119]. Furthermore the factors that influence this particular phase transition with coexistence of two monoclinic phases are also different for both of the systems. Whereas for $x=1.5$ of $La_{2-x}Sr_xCoIrO_6$ below room temperature, the phase coexistence (transition) is accompanied by a sudden increase in the oxidation state of Co in the $I2/m$ phase due to hole doping through A-site cation, the A-site cation in $Ca_xSr_{2-x}FeReO_6$ ($1 \leq x \leq 2$) has only the size degree of freedom, therefore the phase coexistence (transition) is accompanied by a charge transfer within the B- and B' sites induced by structural distortions [119]. The crystal structures corresponding to the different phases of Sr_2CoIrO_6 are shown in Fig. 5.9 for a view along the monoclinic b-axes.

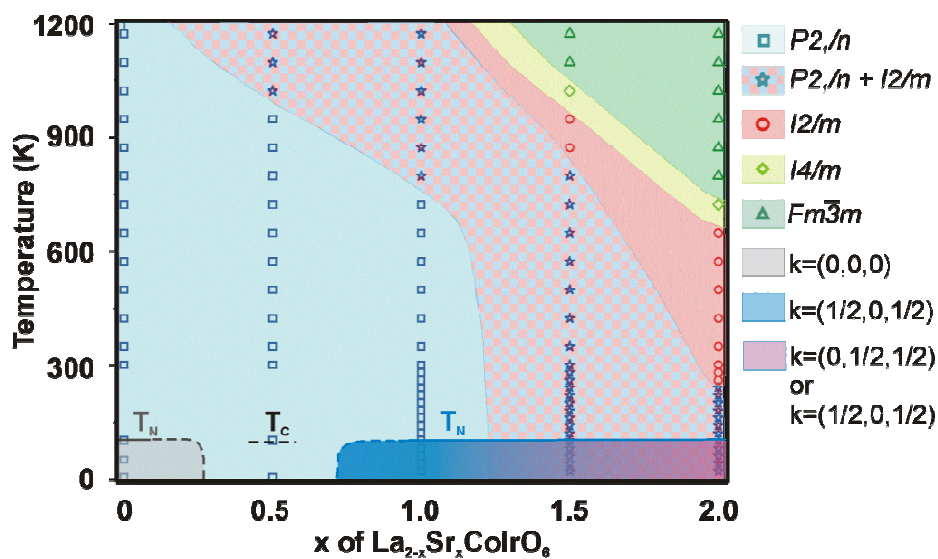


Fig. 5.6: Composition and temperature dependence in the phase diagram of $\text{La}_{2-x}\text{Sr}_x\text{CoIrO}_6$ together with the three different types of magnetic structures at low temperature. The symbols denote the experimentally obtained data.

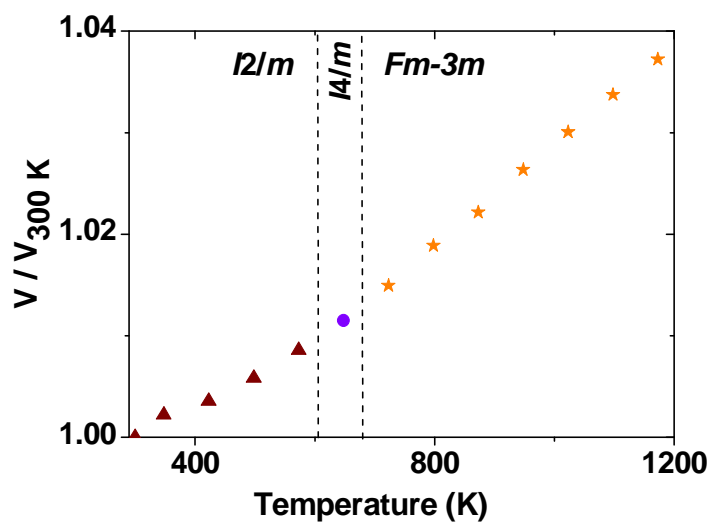


Fig. 5.7: Temperature dependence of the normalized volume of $\text{Sr}_2\text{CoIrO}_6$.

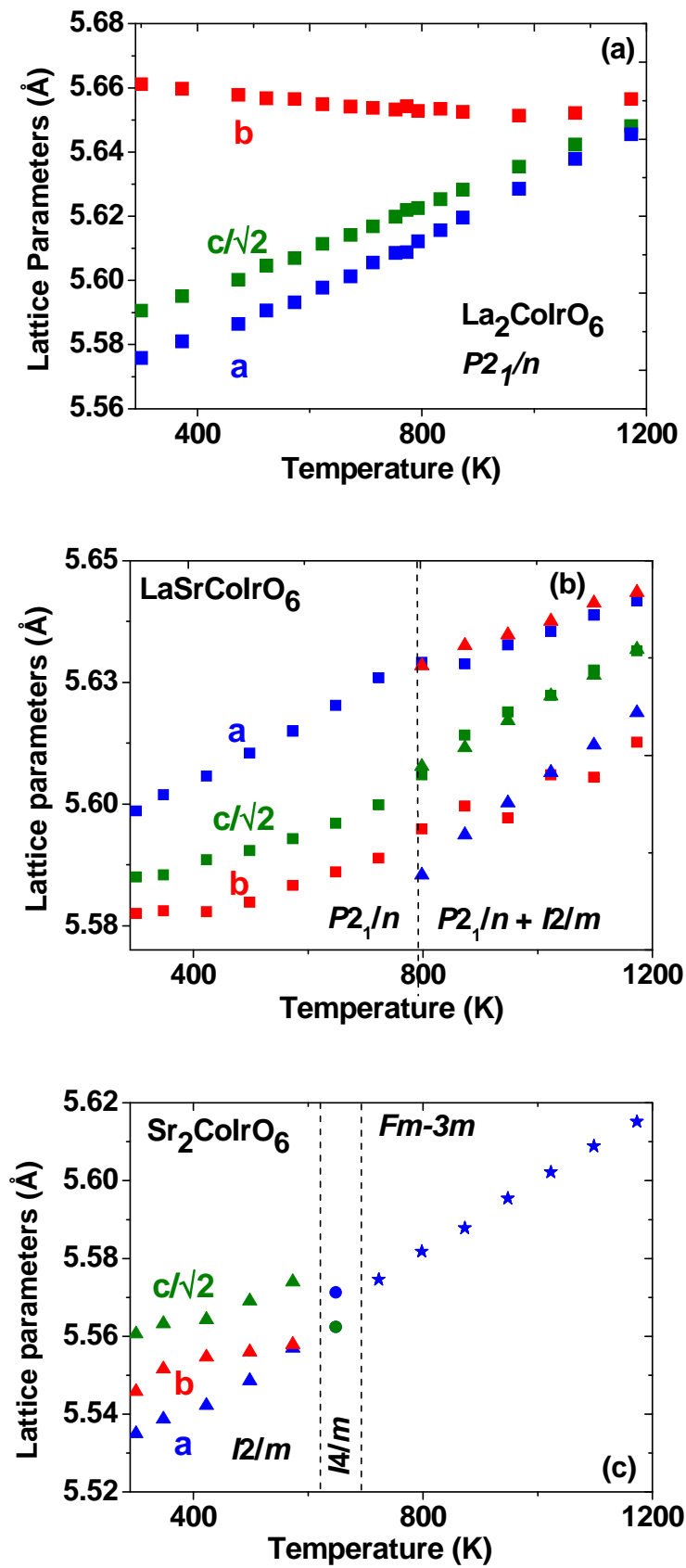


Fig.5.8: Temperature dependence of the lattice parameters for (a) $x=0$, (b) $x=1$ and (c) $x=2$.

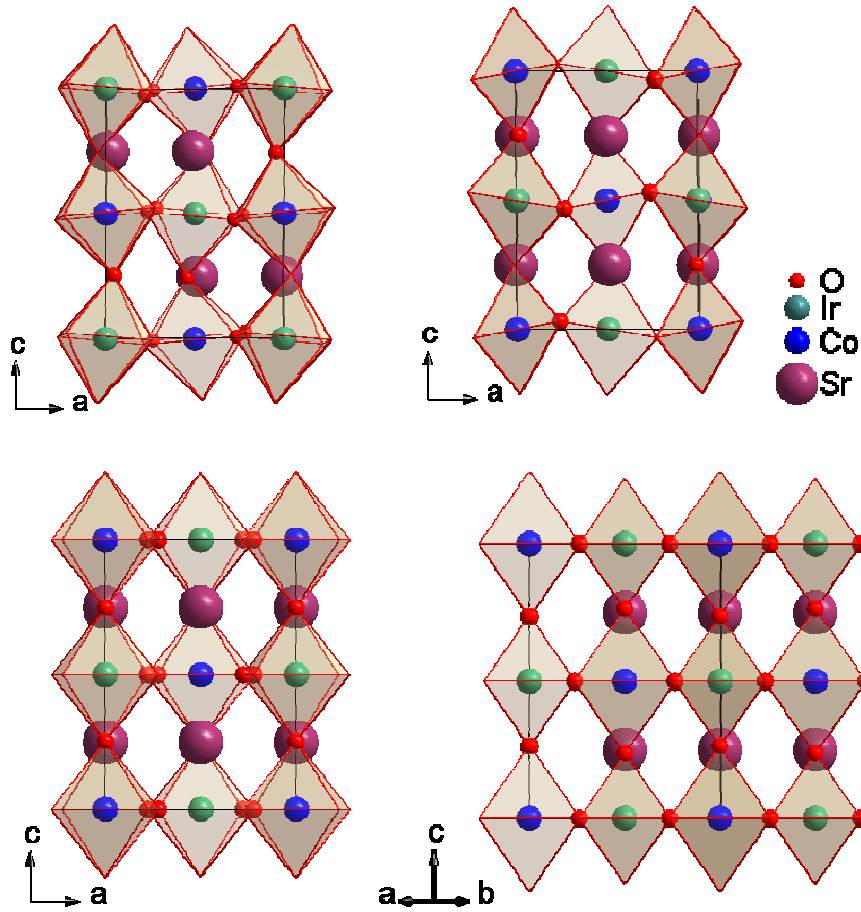


Fig 5.9: Unit cells of the modifications of $\text{Sr}_2\text{CoIrO}_6$ in different space groups: $P2_1/n$ ($a^- a^- c^+$) (top left), $I2/m$ ($a^0 b^- b^-$) (top right), $I4/m$ ($a^0 a^0 c^-$) (bottom left) and $Fm-3m$ ($a^0 a^0 a^0$) (bottom right).

5.2 Temperature and field dependence of magnetizations

The temperature dependence of magnetization of $\text{La}_{2-x}\text{Sr}_x\text{CoIrO}_6$ in an external field of 0.05 T reveals magnetic order below 100 K for all compositions, see Fig. 5.10, but the specific magnetization is reduced about almost two orders of magnitude with increasing substitution of La by Sr. The differences between magnetizations in field-cooled (FC) and zero-field cooled mode (ZFC) indicate the presence of ferromagnetic components, confirmed by the hysteresis loops in Fig. 5.11 (a), obtained at 1.8 K in external magnetic fields up to 7 Tesla. The spontaneous magnetization, determined by linear extrapolation of the high-field dependence of magnetization to zero field (Table 5.5), which is a measure for the available ferromagnetic component, is also reduced about almost two orders of magnitude with increasing substitution of La by Sr. The largest ferromagnetic component is observed for $\text{La}_2\text{CoIrO}_6$, and has a value around $0.7 \mu_B/\text{f.u.}$ As the spin polarization of iridium is expected

to be weak, cobalt may have significant contribution to the ferromagnetic component for $x=0$ and 0.5. But as this component is almost reduced to $0.03 \mu_B$ for $x=1$, it can be concluded that this small amount (for $x \geq 1$) results from iridium or even from impurities.

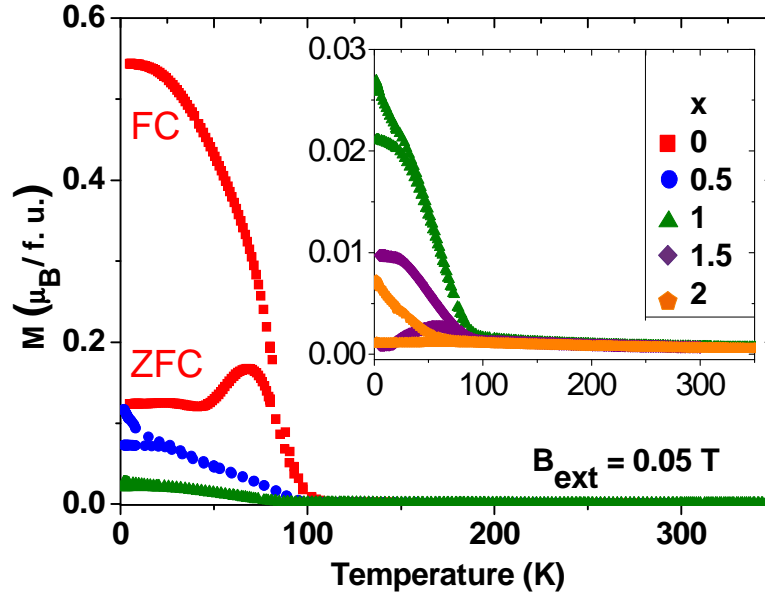


Fig. 5.10: Temperature dependence of magnetization for $\text{La}_{2-x}\text{Sr}_x\text{CoIrO}_6$

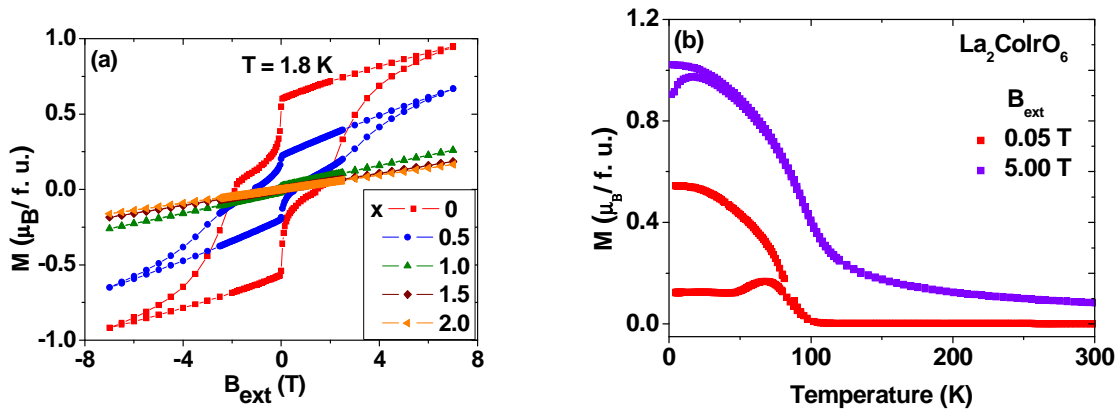


Fig. 5.11: (a) Field dependence of magnetization for $\text{La}_{2-x}\text{Sr}_x\text{CoIrO}_6$ and (b) Temperature dependence of magnetization for $\text{La}_2\text{CoIrO}_6$ at different external magnetic fields.

Curie-temperatures are determined using the linear extrapolation method and decrease from 90 K for $x=0-1.5$ to 70 K for $x = 2$ (Table 5.5). The paramagnetic Curie-Weiss temperatures θ , determined from the Curie-Weiss fits, are negative along the whole series, indicating dominant antiferromagnetic interactions, which become stronger with increasing Sr content (Table 5.5). The low values for the ferromagnetic components and the strong antiferromagnetic interactions indicate non-collinear magnetism (NCM) with ferro- and

antiferromagnetic components of the ordered magnetic moments (canted antiferromagnetism). Magnetizations are not saturated at 7 T, further supporting the proposed NCM for the whole series. Another characteristic feature of the hysteresis loops for $x = 0$ and $x=1$ is their shape, which might reflect an external-field induced magnetic phase transition as already found in many compounds with NCM due to magnetic anisotropy, which results in minima in the angle (of the magnetic moments) dependent energy curves (metamagnetic state) [120]. This can also be concluded from the different temperature dependence of the magnetization at different external fields below the ordering temperature shown in fig 5.11 (b). Regarding the double perovskites, investigations on such magnetic phase transitions are rare and known only for a few compounds such as $\text{Ca}_2\text{FeReO}_6$ [119], $\text{Sr}_2\text{NiReO}_6$ [121] and $\text{Sr}_2\text{RuGdO}_6$ [6], but the specific conditions for this transition are is different. For $\text{Ca}_2\text{FeReO}_6$, mainly a metal-insulator transition from metallic FM to an insulating FM (actually coexisting below the transition temperature) induces the spin-reorientation [122], where the insulating FM transits gradually to the metallic FM at higher external magnetic fields below the transition temperature [119]. For $\text{Sr}_2\text{NiReO}_6$ and $\text{Sr}_2\text{RuGdO}_6$ the external-field induced magnetic phase transition takes place in the AFM phase with a small ferromagnetic component. The field induced magnetic phase transition in $\text{La}_2\text{CoIrO}_6$ and $\text{La}_{1.5}\text{Sr}_{0.5}\text{CoIrO}_6$ can be therefore similar to $\text{Sr}_2\text{NiReO}_6$ and $\text{Sr}_2\text{RuGdO}_6$. The effective magnetic moments μ_{eff} were calculated from the Curie constants and are compared with the spin-only values of Co, based on the assumption of HS- Co^{2+} for $x=0$ and HS- Co^{3+} for $x=2$. The experimentally determined values for μ_{eff} are always larger than the calculated spin-only values especially for the Co^{2+} case (Table. 5.5), consistent with other double perovskites containing Co^{2+} [121]. This discrepancy indicates significant contributions to the paramagnetic moments from Ir and/or orbital momentum.

Table 5.5: Ferromagnetic Curie-temperature T_C , paramagnetic Curie-Weiss temperature θ , spontaneous magnetization M_S , experimentally determined and calculated effective magnetic moments μ_{eff} and $\mu_{\text{eff}}(\text{Co-spin only})$

x	$\mu_{\text{eff}} (\mu_B / \text{f. u.})$	$\mu_{\text{eff}}(\text{Co-spin only})$ ($\mu_B / \text{f. u.})$	Θ (K)	$M_S (\mu_B / \text{f. u.})$	T_C (K) (linear extrapolation)
0	4.7(1)	3.88 (Co^{2+})	-13.8(6)	0.7	95
0.5	5.0(1)		-55.1(8)	0.15	91
1	5.1(0)		-94.9(1)	0.03	89
1.5	5.0(0)		-103.0(5)	0.015	91
2	5.1(1)	4.90 (Co^{3+})	-138.8(0)	0.005	70

5.3 Magnetic structures of $\text{La}_{2-x}\text{Sr}_x\text{CoIrO}_6$

Magnetic superstructure Bragg reflections were observed in neutron powder diffraction (NPD) patterns recorded at temperatures below 100 K. In fig. 5.12 – fig. 5.18 the NPD patterns are shown for all the compositions at 3 K and at RT for comparison.

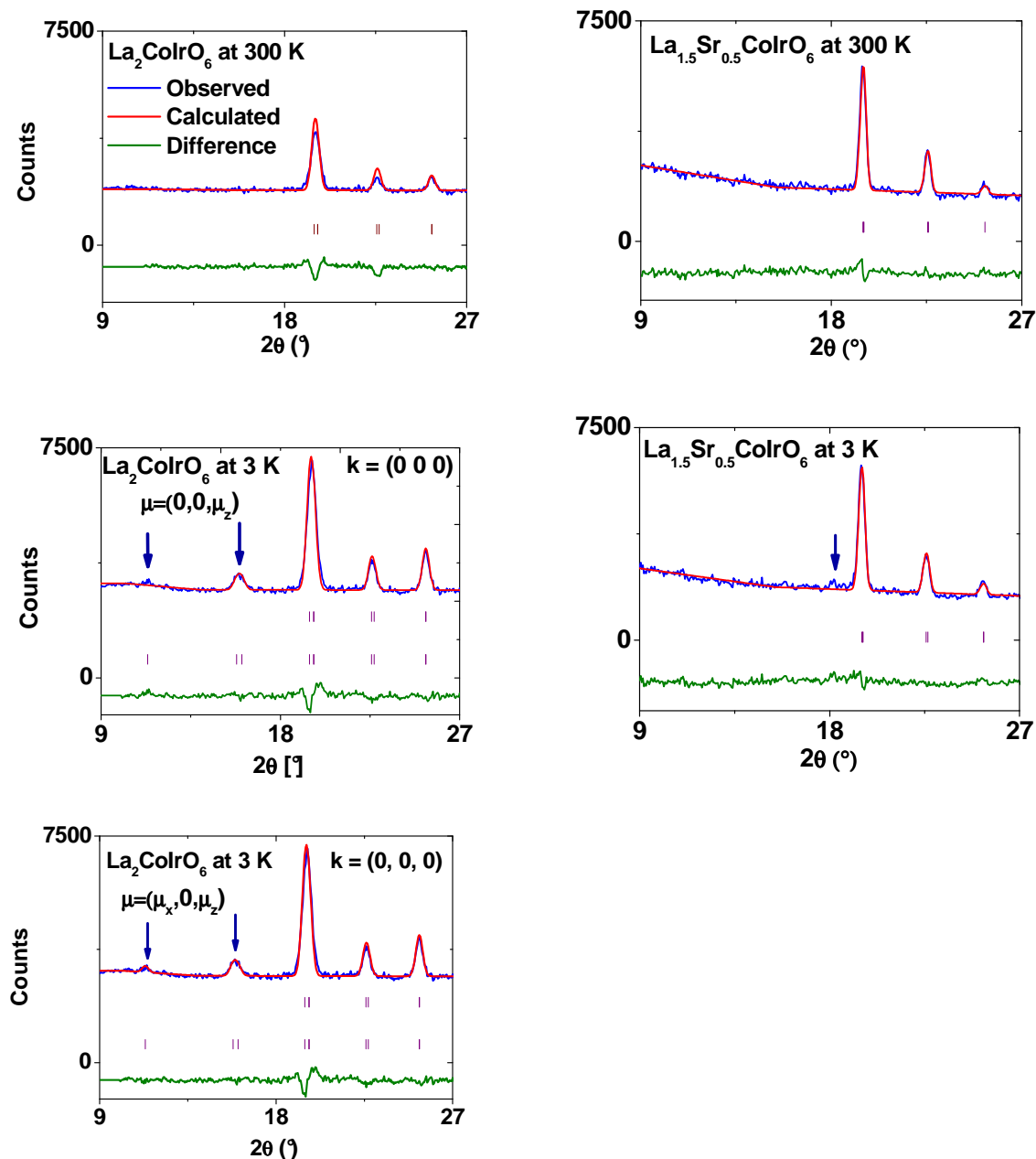


Fig. 5.12: Observed, calculated and difference low angle region Rietveld profiles for $\text{La}_2\text{CoIrO}_6$ and $\text{La}_{1.5}\text{Sr}_{0.5}\text{CoIrO}_6$ at 3 K, where prominent magnetic superstructure Bragg reflections were present. Reflection markers correspond to the positions of Bragg reflections of structural (top) and magnetic (bottom) contributions. As a comparison the same region is shown for 300 K also.

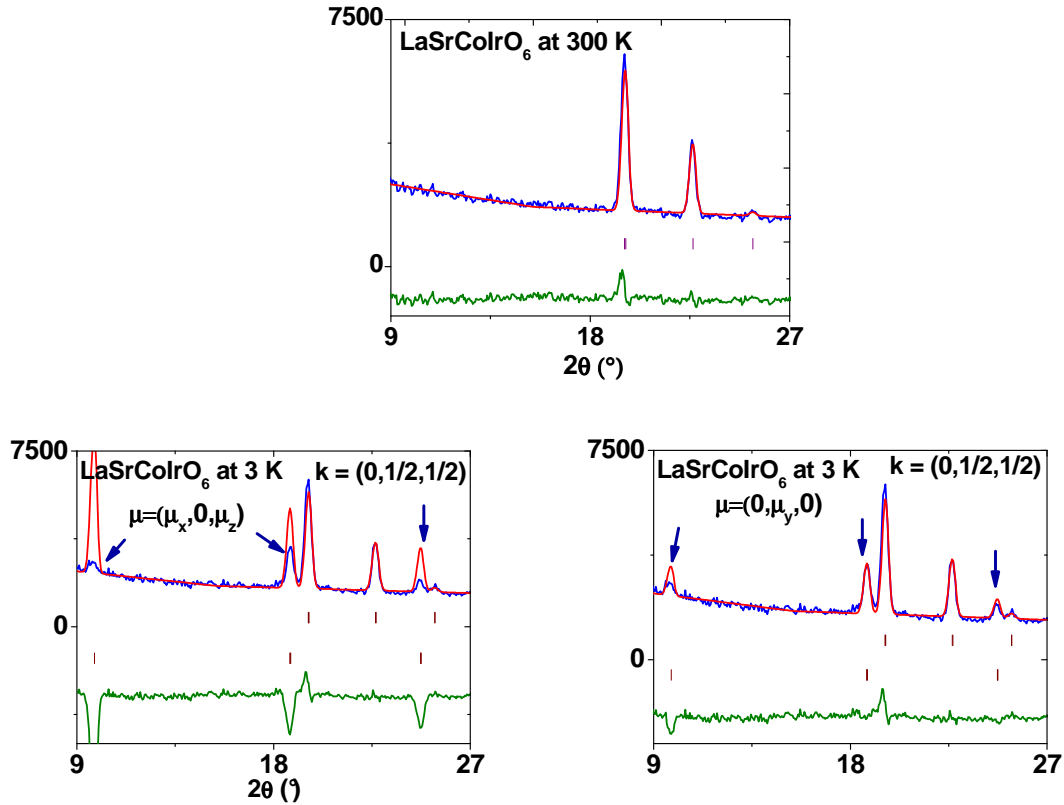


Fig. 5.13: Observed, calculated and difference low angle region Rietveld profiles for LaSrCoIrO_6 at 3 K, where prominent magnetic superstructure Bragg reflections are present. Shown are the calculated profiles for $k=(0,1/2,1/2)$ AFM structure with two different orientations of the AFM component. Reflection markers correspond to the positions of Bragg reflections of structural (top) and magnetic (bottom) contributions. As a comparison the same region is shown for 300 K also.

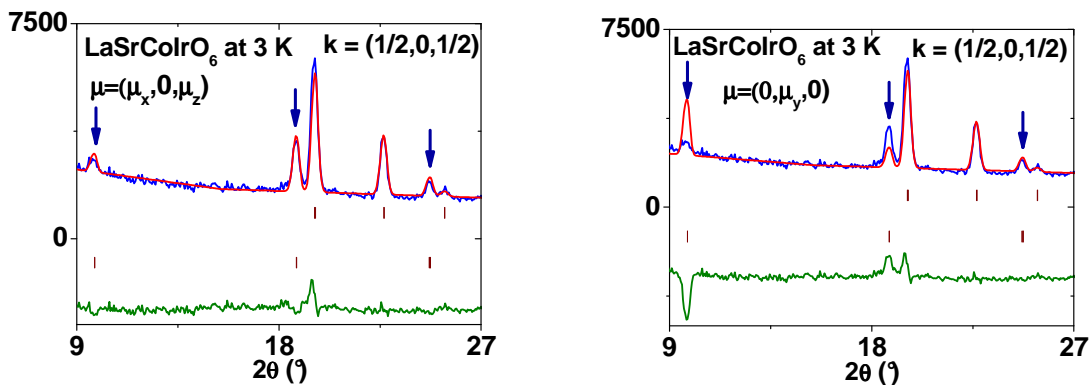


Fig. 5.14: Observed, calculated and difference low angle region Rietveld profiles for LaSrCoIrO_6 at 3 K, where prominent magnetic superstructure Bragg reflections were present. Shown are the calculated profiles for $k=(1/2,0,1/2)$ AFM structure with two different orientations of the AFM component. Reflection markers correspond to the positions of Bragg reflections of structural (top) and magnetic (bottom) contributions.

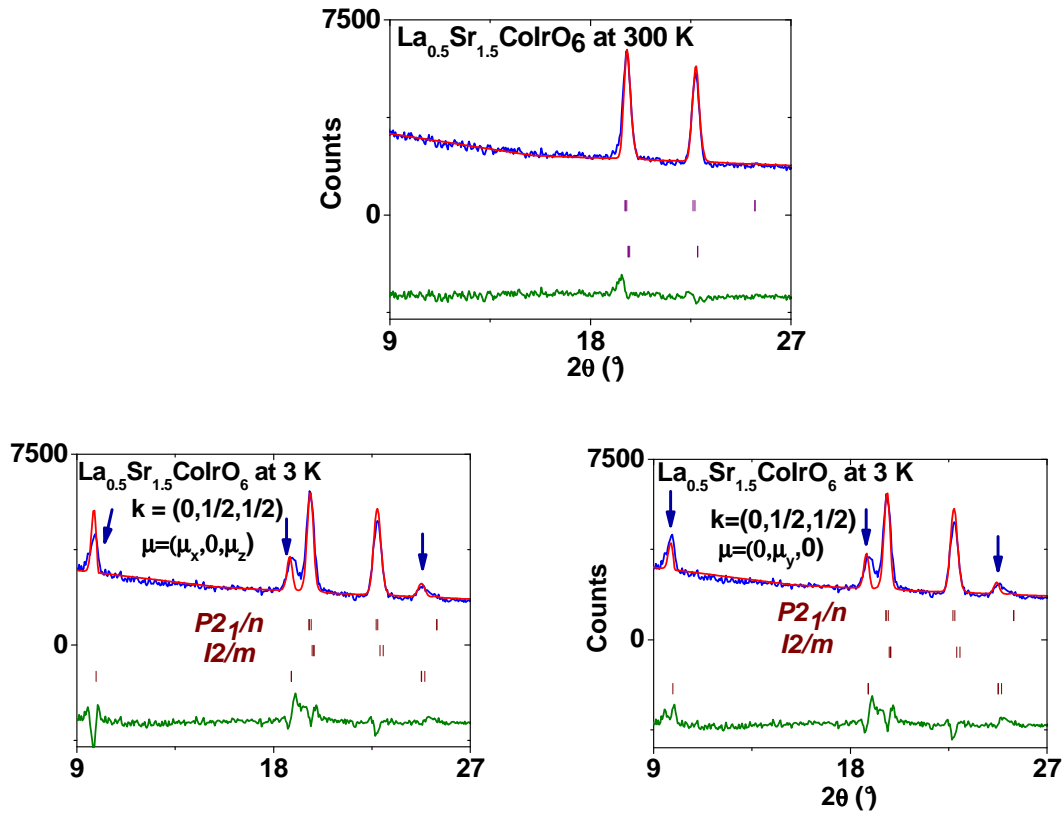


Fig. 5.15: Observed, calculated and difference low angle region Rietveld profiles for $\text{La}_{0.5}\text{Sr}_{1.5}\text{CoIrO}_6$ at 3 K, where prominent magnetic superstructure Bragg reflections were present. Shown are the calculated profiles for $k=(0,1/2,1/2)$ AFM structure with two different orientations of the AFM component. Reflection markers correspond to the positions of Bragg reflections of structural (top) and magnetic (bottom) contributions. As a comparison the same region is shown for 300 K also.

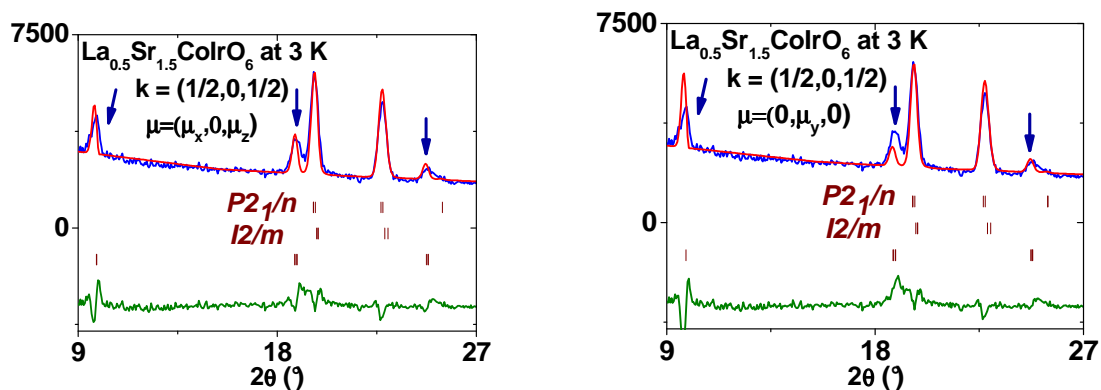


Fig. 5.16: Observed, calculated and difference low angle region Rietveld profiles for $\text{La}_{0.5}\text{Sr}_{1.5}\text{CoIrO}_6$ at 3 K, where prominent magnetic superstructure Bragg reflections were present. Shown are the calculated profiles for $k=(1/2,0,1/2)$ AFM structure with two different orientations of the AFM component. Reflection markers correspond to the positions of Bragg reflections of structural (top) and magnetic (bottom) contributions.

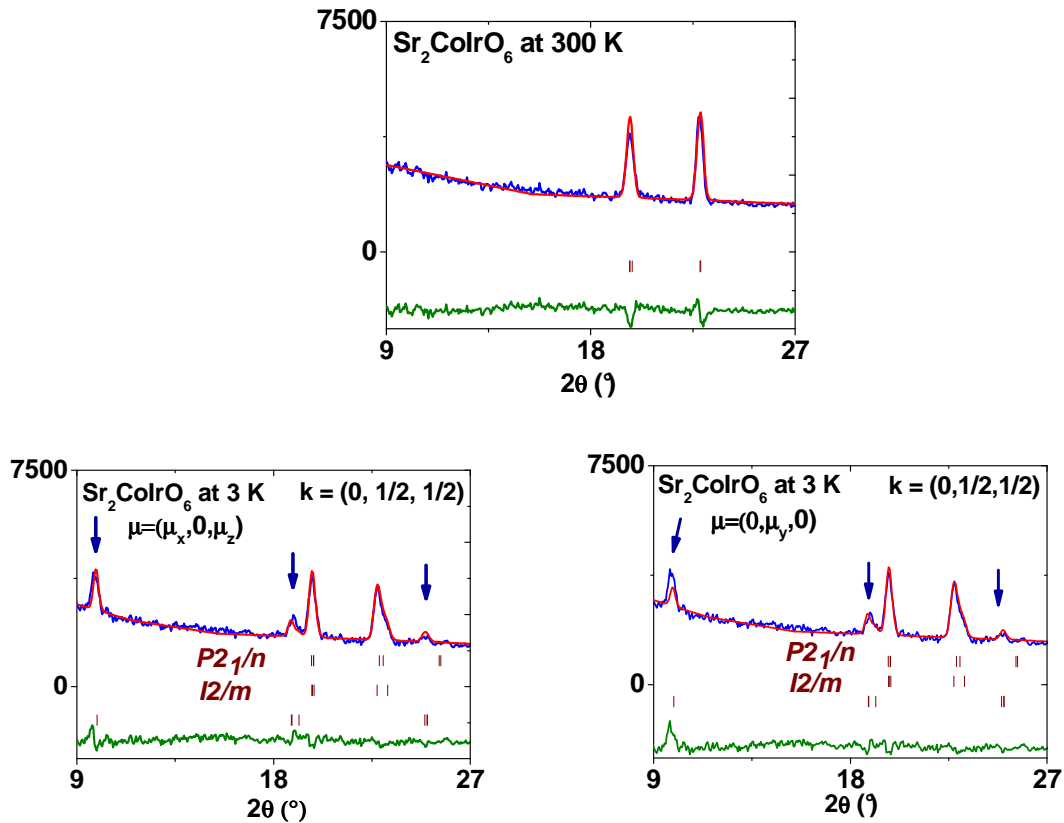


Fig. 5.17: Observed, calculated and difference low angle region Rietveld profiles for $\text{Sr}_2\text{CoIrO}_6$ at 3 K, where prominent magnetic superstructure Bragg reflections were present. Shown are the calculated profiles for $k=(0,1/2,1/2)$ AFM structure with two different orientations of the AFM component. Reflection markers correspond to the positions of Bragg reflections of structural (top) and magnetic (bottom) contributions. As a comparison the same region is shown for 300 K also.

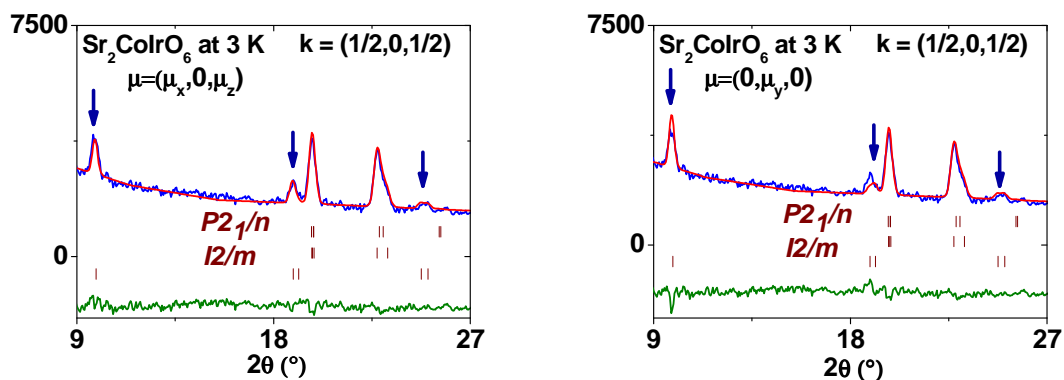


Fig. 5.18: Observed, calculated and difference low angle region Rietveld profiles for $\text{Sr}_2\text{CoIrO}_6$ at 3 K, where prominent magnetic superstructure Bragg reflections were present. Shown are the calculated profiles for $k=(1/2,0,1/2)$ AFM structure with two different orientations of the AFM component. Reflection markers correspond to the positions of Bragg reflections of structural (top) and magnetic (bottom) contributions.

This reveals long-range antiferromagnetic order in $\text{La}_{2-x}\text{Sr}_x\text{CoIrO}_6$. But the positions of the magnetic reflections depend on composition and were indexed as explained in the following. Four ambiguities remain in the derivation procedure of the magnetic structures from NPD: 1. The ferromagnetic component (FM) could not be extracted quantitatively from NPD, because the corresponding intensities are too low in comparison with the dominant nuclear contributions. Nevertheless, the direction of the FM component is determined by the analysis of magnetic symmetries in this section. 2. Any contribution from ordered magnetic moments on the Ir-site is too small to be detected. The magnetic moments were therefore refined only at Co-sites. 3. As the Co-sublattices are almost identical in the coexisting primitive and I-centered monoclinic modifications, the magnetic contributions for $x=1.5$ and $x=2$ cannot be assigned to one of these phases distinctly, but the magnetic arrangement (see Fig. 5.20 and fig. 5.21) is unambiguous. 4. A further ambiguity related to the propagation vector k is discussed in the next paragraphs.

The magnetic Bragg reflections are indexed by the choice of different magnetic translation vectors or the propagation vectors k depending on the composition. Furthermore in order to obtain a good agreement with the diffraction pattern in terms of the intensity (of the magnetic Bragg reflections), the direction of the AFM component (or generally the direction of the magnetic moment) is necessary or in other words the magnetic space group is needed. There are six magnetic space groups that can be derived from the crystallographic space group $P12_1/n1$ [123108]. In order to short list them, the behaviour of a magnetic moment $\mu=(\mu_x, \mu_y, \mu_z)$ under the symmetry operations of the magnetic space groups are investigated and compared with the (crystallographically) equivalent positions of Co under the symmetry operations in the conventional unit cell. They are shown in table 5.6. Note that the positions of the symmetry elements are selected in agreement with the “cell choice 2” in the international tables for crystallography, whereas the “cell choice 1” is used in [123].

Table 5.6: Magnetic symmetry operations on a magnetic moment within the six possible magnetic space groups.

Symmetry operations	1	$2_1(1/4,y,1/4)$	-1	$n(x,1/4,z)$
General position	x,y,z	-x+1/2,y+1/2,-z+1/2	-x,-y,-z	x+1/2,-y+1/2,z+1/2
Position of Co	0,1/2,0	1/2,0,1/2	0,1/2,0	1/2,0,1/2
$P2_1/n$	(μ_x, μ_y, μ_z)	$(-\mu_x, \mu_y, -\mu_z)$	(μ_x, μ_y, μ_z)	$(-\mu_x, \mu_y, -\mu_z)$
	AFM component in the xz plane and FM component in the y direction			
$P2_1/n I'$	$(-\mu_x, -\mu_y, -\mu_z)$	$(\mu_x, -\mu_y, \mu_z)$	$(-\mu_x, -\mu_y, -\mu_z)$	$(\mu_x, -\mu_y, \mu_z)$
	AFM component in the xz plane and FM component in the y direction			
$P2_1/n$	(μ_x, μ_y, μ_z)	$(\mu_x, -\mu_y, \mu_z)$	$(-\mu_x, -\mu_y, -\mu_z)$	$(-\mu_x, \mu_y, -\mu_z)$
$P2_1/n'$	(μ_x, μ_y, μ_z)	$(-\mu_x, \mu_y, -\mu_z)$	$(-\mu_x, -\mu_y, -\mu_z)$	$(\mu_x, -\mu_y, \mu_z)$
$P2_1/n'$	(μ_x, μ_y, μ_z)	$(\mu_x, -\mu_y, \mu_z)$	(μ_x, μ_y, μ_z)	$(\mu_x, -\mu_y, \mu_z)$
	AFM component in the y direction and FM component in the xz plane			
$P_{2a}2_1/n$	$(-\mu_x, -\mu_y, -\mu_z)$	$(\mu_x, -\mu_y, \mu_z)$	$(-\mu_x, -\mu_y, -\mu_z)$	$(\mu_x, -\mu_y, \mu_z)$
	AFM component in the xz plane and FM component in the y direction			

It is evident from table 5.6, that there are two types of orientation of the magnetic moments that are possible for the AFM and FM components of Co. In the first type, the AFM component is in the xz plane and the FM component is in the y direction, whereas in the second type, the AFM component is in the y direction and the FM component is on the xz plane. For the underlying magnetic Bragg reflections of the different compositions, this means that for any propagation vector k , two different orientations of the AFM components should be tested to find the best agreement with the diffraction pattern. They are $(\mu_x, 0, \mu_z)$ and $(0, \mu_y, 0)$. The different types of the magnetic structures are discussed in the following.

For $\text{La}_2\text{CoIrO}_6$ ($x=0$) the magnetic superstructure Bragg reflections are indexed with the propagation vectors $k=(0, 0, 0)$. As shown in fig. 5.12, Only the z component of the magnetic moment is not enough to reproduce the intensity of the magnetic Bragg reflections (although the positions are correctly predicted), therefore the x component is also additionally refined, thus reproducing the intensity successfully. For $x=1, 1.5$ and 2 the magnetic Bragg reflections should be described by a propagation vector other than $k=(0,0,0)$. For $x=1$ the magnetic Bragg reflections are indexed with the propagation vector $k=(0, 1/2, 1/2)$. But refining only the z

component does not reproduce the intensity of the magnetic Bragg reflections. Additionally refining the x component does not improve the fitting, but refining only the y component improves the fitting better than the previous cases. Alternatively an indexing with the propagation vector $k=(1/2,0,1/2)$ is also done. In that case refining the x and z components give the best agreement even better than $k=(0,1/2,1/2)$ with refined y component. Therefore the $k=(1/2,0,1/2)$ magnetic structure with AFM components in the xz plane is preferred against the other three models. For $x=1.5$ the better agreement with the intensity is reached for $k=(1/2,0,1/2)$ with the refinement of the xz component of the magnetic moment or for $k=(0,1/2,1/2)$ with the refinement of the y component only. In both cases the width of the magnetic reflections are not reproduced exactly by the refinement, indicating smaller magnetic domains. Note that this is the stoichiometry, where the phase transition between the two monoclinic phases first appears with a sudden change in the oxidation state of Co. For $x=2$ the best agreement with the magnetic Bragg reflections are obtained for either indexing with the propagation vector $k=(0,1/2,1/2)$ with the refinement of the x and z components or indexing with $k=(1/2,0,1/2)$ with the refinement of the x and z components. From the above discussion it could be concluded for $x=1$ the $k=(1/2,0,1/2)$ magnetic structure can be preferred against the $k=(0,1/2,1/2)$ one, whereas for $x=1.5$ and 2 there is no clear preference can be made between $k=(0,1/2,1/2)$ and $k=(1/2,0,1/2)$ magnetic structures thus resulting in a further ambiguity. For $x=0.5$ only very weak magnetic reflections (especially the one around 18°) are observed that could not be indexed unambiguously. This composition lies in the middle of the transition between the $k=(0,0,0)$ and $k=(1/2,0,1/2)/k=(0,1/2,1/2)$ magnetic structures. The refined anti-ferromagnetic moments at the Co-sites are listed in table 5.7.

Table 5.7: Refined magnetic moments of Co in $\text{La}_{2-x}\text{Sr}_x\text{CoIrO}_6$.

x	Propagation vector k	Magnetic moment of Co $\mu_{\text{Co}}=(\mu_x,\mu_y,\mu_z)$ (μ_B)	$ \mu_{\text{Co}} $ (μ_B)
0	(0,0,0)	(-0.7(1),0,1.5(1))	1.7(1)
0.5	-	-	-
1.0	(1/2,0,1/2)*	(1.2(1),0,2.3(1))	2.6(1)
	(0,1/2,1/2)	(0,2.6(1),0)	2.6(1)
1.5	(0,1/2,1/2)	(0,2.5(1),0)	2.5(1)
	(1/2,0,1/2)	(2.8(1),0,0)	2.8(1)
2.0	(0,1/2,1/2)	(1.6(1),0,2.1(1))	2.6(1)
	(1/2,0,1/2)	(0,0,2.6(1))	2.6(1)

*preferred magnetic structure for $x=1$

It is evident from table 5.7 that for $x=1$ and 2 both the k vectors give the same absolute value for $|\mu_{\text{Co}}|$, the only difference being the different AFM components, whereas there is a difference of $0.3 \mu_{\text{B}}$ between both the propagation vectors for $x=1.5$. But as already mentioned, the width of the magnetic reflections could not be fitted perfectly for this particular composition. The derived three types of anti-ferromagnetic structures are shown in fig. 5.19 – fig. 5.21 in different perspectives.

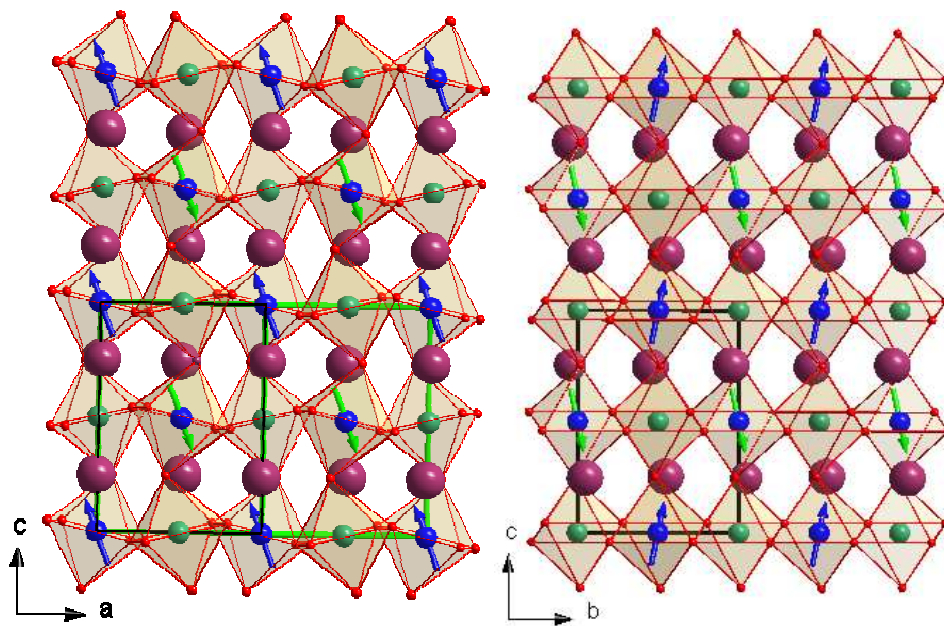


Fig. 5.19: Magnetic structure with $k=(0, 0, 0)$ for $x=0$ viewed along the b axis (left) and along the a axis in order to show the ferromagnetic component (shown exaggeratedly) in the b direction (right). Magnetic unit cell (black) and the distorted face-centered lattice of Co (green) are also shown.

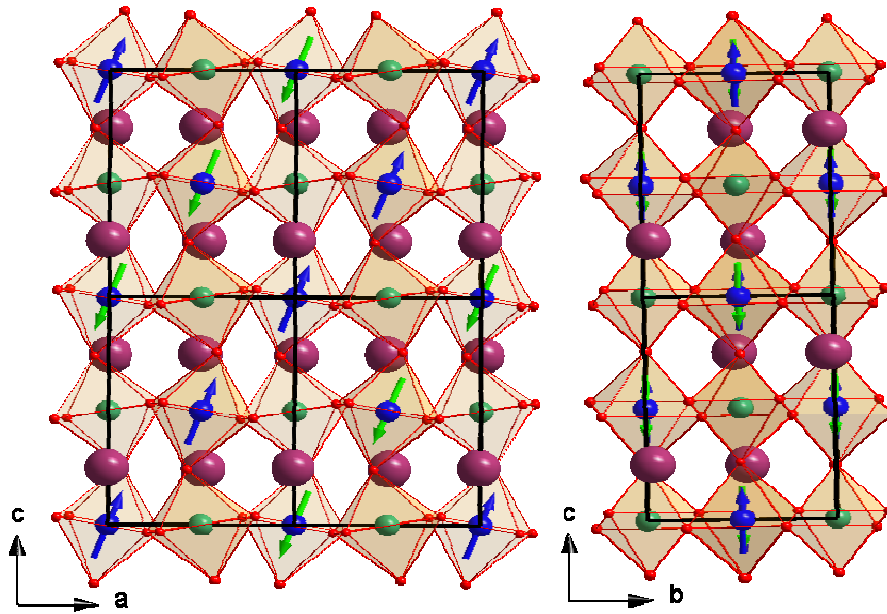


Fig. 5.20: Magnetic structure with $k=(1/2,0,1/2)$ for $x=1$ viewed along the b axis (left) and along the a axis. The magnetic unit cell is shown in black colour.

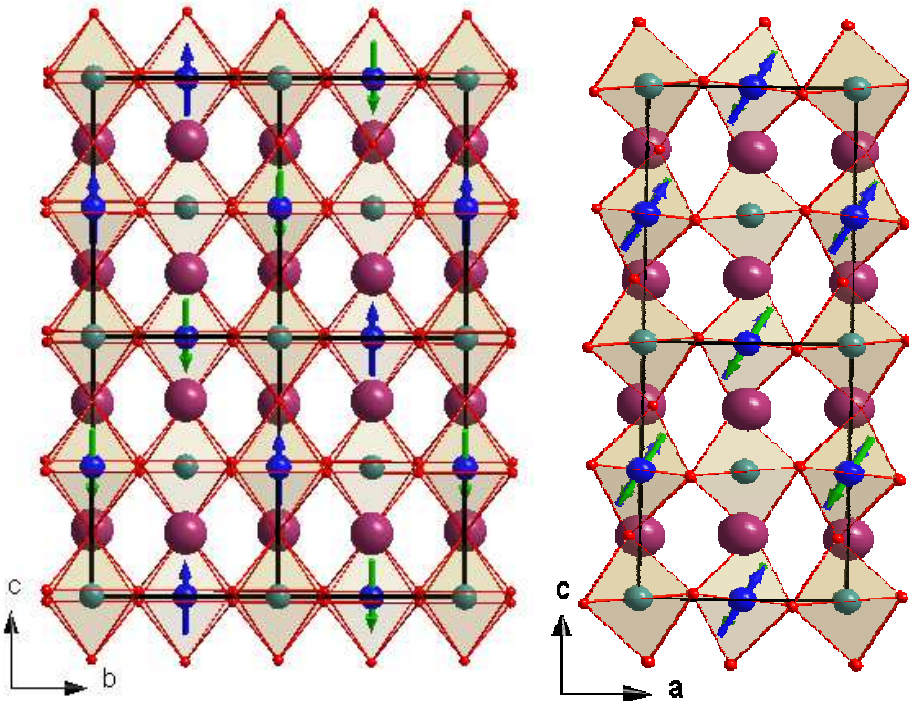


Fig. 5.21: The magnetic structure with $k=(0,1/2,1/2)$ for $x=2$ viewed along the a axis (left) and along the b axis. Magnetic unit cell is shown in black colour.

In both magnetic structures alternating ferromagnetic planes exist, but they are different in both structures. A qualitative explanation is based on the magnetic superexchange interactions. The geometries of the underlying exchange paths deviate from those in idealized

intersecting fcc sublattices of the Co and Ir ions due to the monoclinic distortions. The corresponding face-centered pseudo-cell for Co is shown in Fig. 5.19. As mentioned in section 2.5, the $k=(0,0,0)$ magnetic structure results from a strong nearest neighbour (NN) antiferromagnetic Co-O-O-Co interaction within the Co sublattice in competition with the 180° antiferromagnetic next nearest neighbour (NNN) σ Co-O-Ir-O-Co interaction between the Co sublattices through the vacant e_g orbitals of Ir. However, in this case, the Co-O-Ir angle is only 152.5° due to the distorted crystal structure and, therefore, the 180° interaction is weaker. This scenario is almost realized in $\text{La}_2\text{CoIrO}_6$, except for the small ferromagnetic component along the b-direction, resulting from the 180° (152.5° in this case) Co-O-Ir ferromagnetic interaction (Ir has 5 t_{2g} electrons) [87] between the Co and Ir sublattices, which is frustrated and probably responsible for a Dzyaloshinski-Moriya interaction. Similar interactions are proposed for $\text{La}_{1+x}\text{Ca}_{1-x}\text{CoRuO}_6$, where both B- and B'-sites are occupied with magnetic ions [81]. The nature of this above discussed NN Co-O-O-Co interaction is in most cases of π type and the ordering temperatures are also quite low. But for $\text{La}_2\text{CoIrO}_6$ apart from the π type interaction, due to the distorted bond angles, also contributions from σ type interactions are expected and a quite high ordering temperature of around 100 K can be explained with this scenario. For increasing x the Co-O-Ir bond angle along the 180° σ Co-O-Ir-O-Co path increases up to 166.3° for $P2_1/n$ and 167.5° for $I2/m$ for $x=2$, and this coupling becomes dominant for $x=1$ and $x=2$, resulting in the $k=(0, \frac{1}{2}, \frac{1}{2})/k=(1/2, 0, 1/2)$ type magnetic structures. The difference between $k=(0, 1/2, 1/2)$ and $k=(1/2, 0, 1/2)$ on the other hand depends as mentioned in section 2.5 on the secondary exchange paths of 90° Co-O-Ir-O-Co. Considering the symmetry operations apart from the doubling of the magnetic unit cell in the c direction for both $k=(0, 1/2, 1/2)$ and $k=(1/2, 0, 1/2)$, for the former a doubling of the magnetic unit cell takes place in the b direction parallel to the 2_1 screw axis and for the latter the doubling takes place in the a direction perpendicular to the 2_1 screw axis. The magnetic behaviour of $x=0.5$ can be explained as follows: In $x=0.5$, strongly competing NN Co-O-O-Co and NNN 180° Co-O-Ir-O-Co interactions are active (or transition zone of the weights of the strengths of the NN and NNN interactions) and as a consequence this composition is frustrated. Finally the phase diagram containing the different magnetic phases is shown in fig. 5.22.

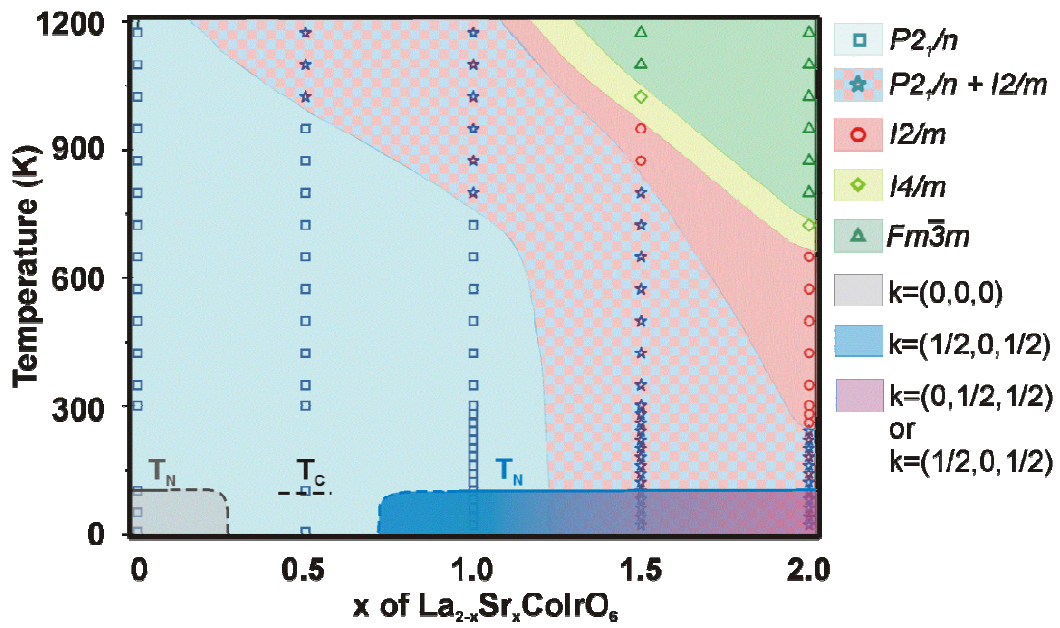


Fig. 5.22: Composition and temperature dependence in the phase diagram of $\text{La}_{2-x}\text{Sr}_x\text{CoIrO}_6$ together with the three different types of magnetic structures at low temperature. The symbols denote the experimentally obtained data.

5.4 Specific heat capacity

Changes in the physical degrees of freedom such as magnetic ordering should be reflected in the measured specific heat capacity. The temperature dependence of the specific heat capacity is shown in fig. 5.23 for three different compositions, $x=0$ (top left), which undergoes the $k=(0,0,0)$ AFM structure, 0.5 (bottom left), which is frustrated and 1.5 (bottom right), which undergoes the $k=(0,1/2,1/2)$ or $k=(1/2,0,1/2)$ AFM structure.

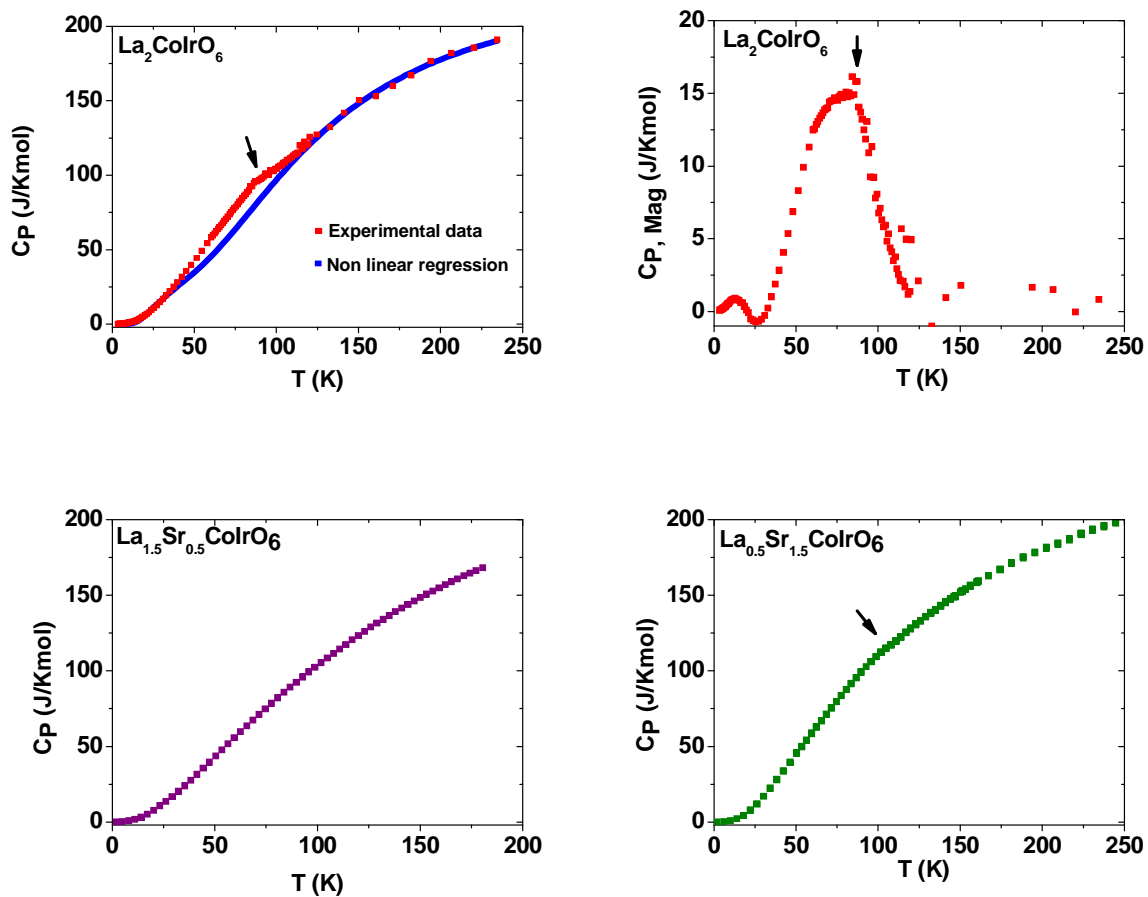


Fig. 5.23: Specific heat capacity of $x=0$ (top left), of $x=0.5$ (bottom left) and of $x=1.5$ (bottom right). On the top right side the magnetic contribution of $x=0$ is shown, which is extracted from the total specific heat capacity by subtracting the phononic contribution.

Anomalies can be seen around 90 K for $x=0$ and 100 K for $x=1.5$, where the most pronounced is for $x=0$. These are in good agreement with NPD and magnetization measurement results, regarding the ordering temperature. However the anomalies are very weak, as at 100 K the contributions from phonons are already quite dominant. For $x=0$, for which the anomaly is quite pronounced, the magnetic contribution $C_{P, Mag}$ is extracted from the total C_P by

subtracting the phononic contribution. As no iso-structural nonmagnetic compound related to the present series could be found, the phononic contribution is approximated by a theoretical model. For this purpose the Debye model is employed and the Debye integral is approximated by the Simpsons method with $n=4$. For a simple Debye model with single phonon spectrum, a large discrepancy between the experimental data and the theoretical values is observed. This is attributed to the fact that in the unit cell of $x=0$ there are both heavier atoms such as La, Co and Ir as well as lighter oxygen atoms. This may pave way for more than one phonon spectrum. Therefore a two phonon Debye model is employed and a reasonable fit is obtained. This is shown in fig.5.23 (top right) and has a maximum around 90 K. But the contribution is actually a broad cusp, indicating the concurrence of critical region short range order in this compound. From the magnetic contribution $C_{P,Mag}$ the thermal evolution of the magnetic entropy $S_{Mag}(T)$ is calculated by using the following integral and it is shown in fig. 5.24.

$$S_{Mag}(T) = \int_0^T \frac{C_{Mag}(T')}{T'} dT' \quad (5.1)$$

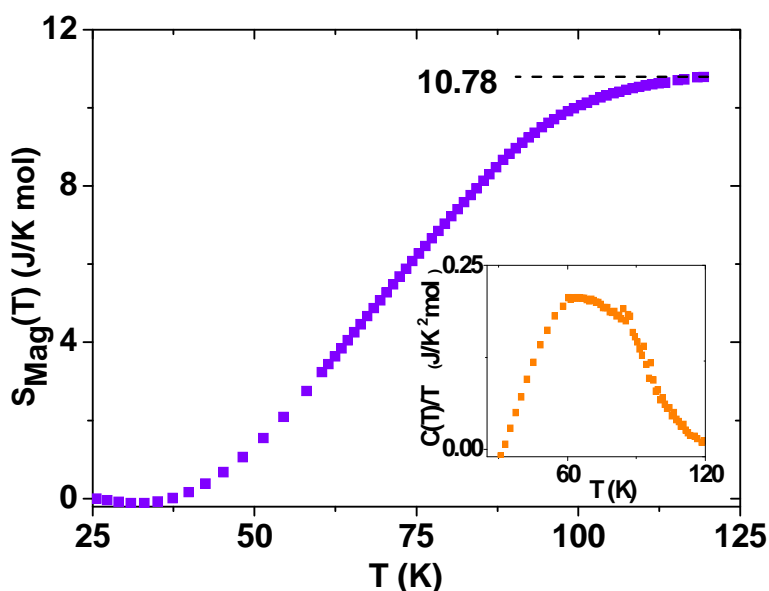


Fig. 5.24: Thermal evolution of the magnetic entropy calculated for $x=0$ from the magnetic contribution on the specific heat capacity. In the inset the integrand of (5.1) is shown.

These values are compared with the theoretical value obtained by the following expression for different spin systems and they are shown in table 5.8.

$$S_{\text{Mag}} = R \ln(2S + 1) \quad (5.2)$$

Table 5.8: Comparison of the magnetic entropy obtained for different spin systems from eq 5.2 with the one obtained from the magnetic contribution of the specific heat capacity.

System	S_{Mag} (J/K mol)
S=1 ($S_{\text{Co}}=1$)	9.13
S=3/2 ($S_{\text{Co}}=3/2$ HS or $S_{\text{Co}}=1, S_{\text{Ir}}=1/2$)	11.52
S=2 ($S_{\text{Co}}=3/2$ HS, $S_{\text{Ir}}=1/2$)	13.38
Experimental (at 120 K)	10.78

The best agreement between the theoretical value and the experimental value of 10.78 J/K mol at 120 K is achieved for S=3/2 system with 11.52 J/K mol. The cobalt ion may be either in Co^{2+} HS state or in a Co^{2+} intermediate state with a S=1/2 LS contribution from Ir^{4+} . For x=0.5 no anomaly is found over the whole measured temperature range, indicating the frustrated nature of the magnetic interaction in that particular composition. The values of specific heat capacity C_p of the compositions are comparable to the values found in other double perovskite systems containing cobalt, for example all three compounds have a C_p around 40 J/K mol at 50 K comparable with other double perovskites, which contain cobalt such as $\text{Sr}_2\text{CoTeO}_6$ [124] or Ba_2CoUO_6 [125], which has a value in the range of 40-50 J/K mol.

5.5 Transport properties of $\text{La}_{2-x}\text{Sr}_x\text{CoIrO}_6$

Resistivity measurements reveal a non-metal like behaviour for the whole series of samples, but the resistivity is reduced by up to three orders of magnitude at room temperature when La is replaced by Sr on the A-site. Three different representations of the temperature dependences of resistivity are shown in fig. 5.25 (a)-(c) to discuss the underlying transport mechanism.

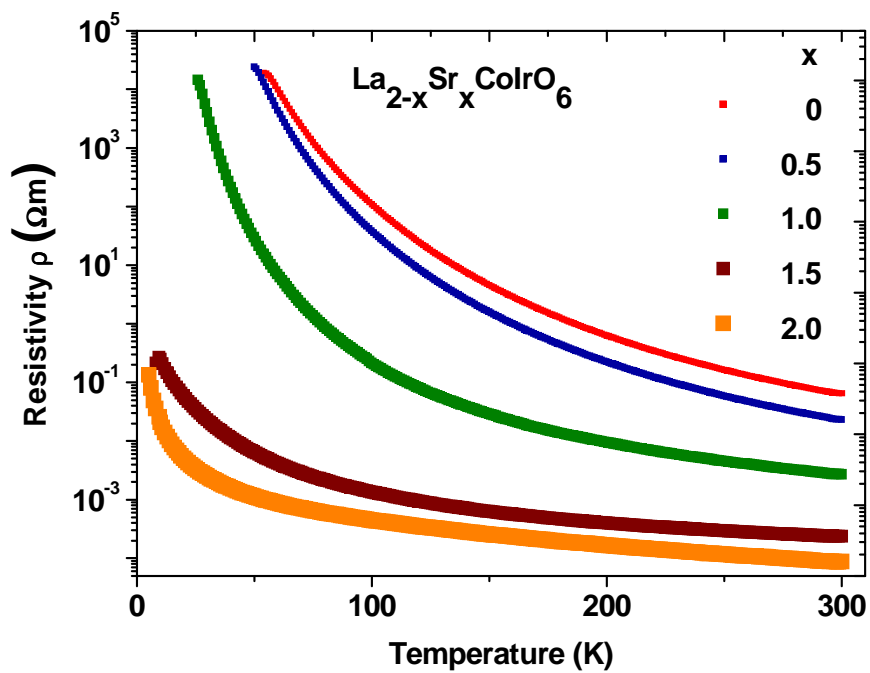


Fig. 5.25 (a): Temperature dependence of resistivity for $x=0, 0.5$ and 1 in logarithmic scale.

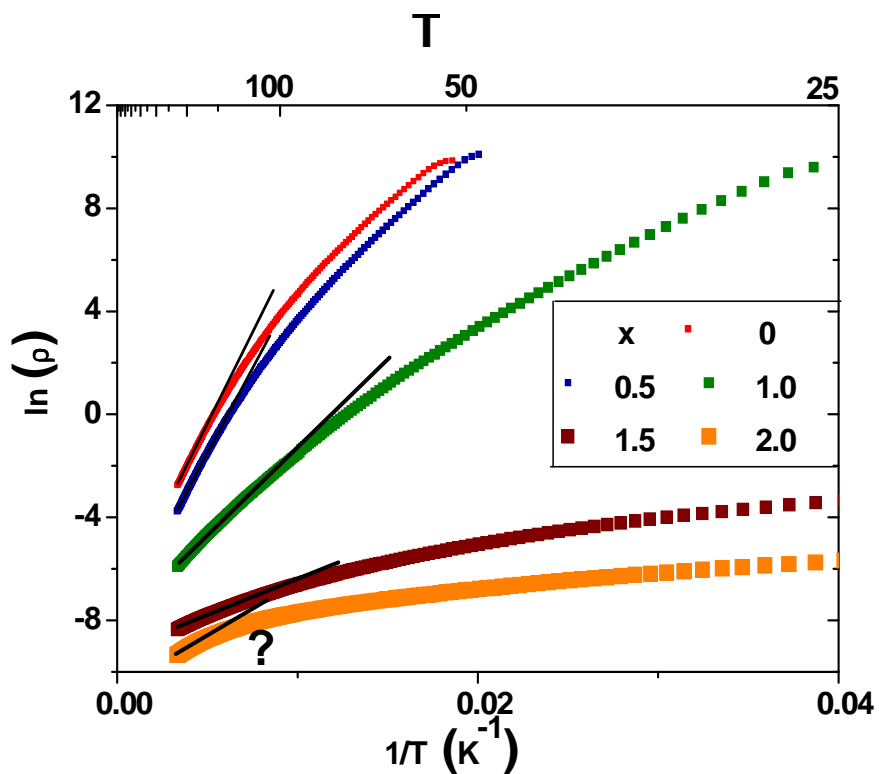


Fig. 5.25 (b): $\ln(\rho)$ vs $1/T$. A linear fit describes the high-temperature behaviour for $x \leq 1.5$, but fails for $x=2$.

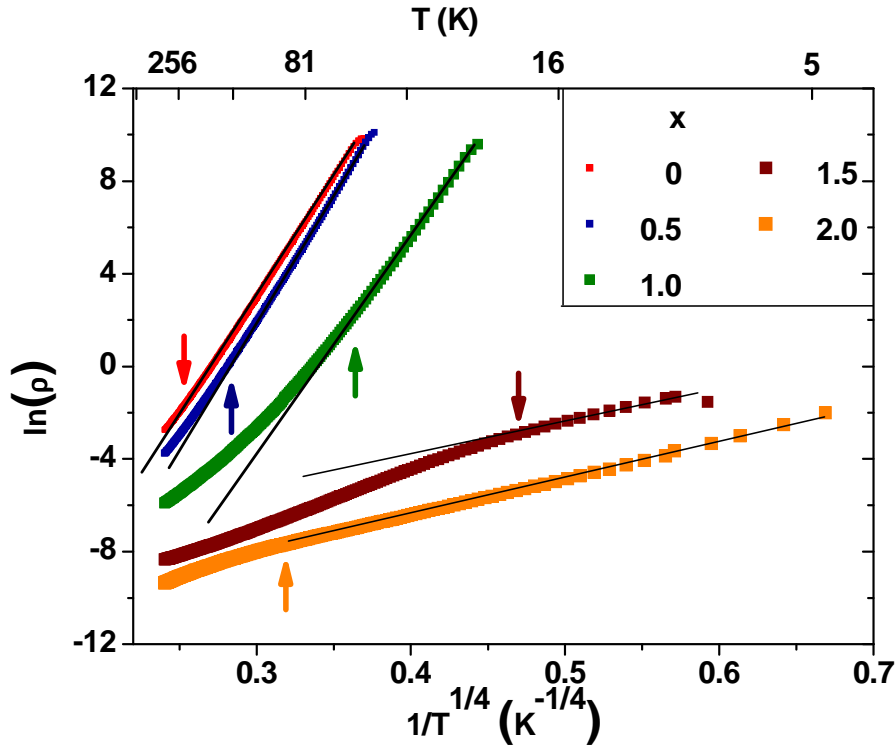


Fig. 5.25 (c): $\ln(\rho)$ vs $1/T^{0.25}$. The arrows mark the maximum temperature, up to which a linear dependence is well obeyed.

A linear dependence of $\ln \rho$ vs. $1/T$ indicates a simple thermal activation of electronic transport in contrast to a characteristic linear dependence of $\ln \rho$ vs. $1/T^{0.25}$ for a variable-range hopping (VRH) model ($d=3$ case) as introduced by Mott for disordered systems [33] and the mechanisms are explained in section 2.4. Both models are inadequate to describe the temperature dependence over the whole investigated temperature range, but appear suitable either in the lower or higher temperature regime. Therefore, a combination of both behaviours was applied to describe the experimental data over the whole temperature range:

$$\frac{1}{\rho} = \frac{1}{\rho_{01}} e^{-\left(\frac{E_G}{2k_B T}\right)} + \frac{1}{\rho_{02}} e^{-\left(\frac{T_0}{T}\right)^{\frac{1}{4}}}$$

The non-linear regression curves for $x=0$ - $x=2.0$ are shown together with the experimental data in fig. 5.26.

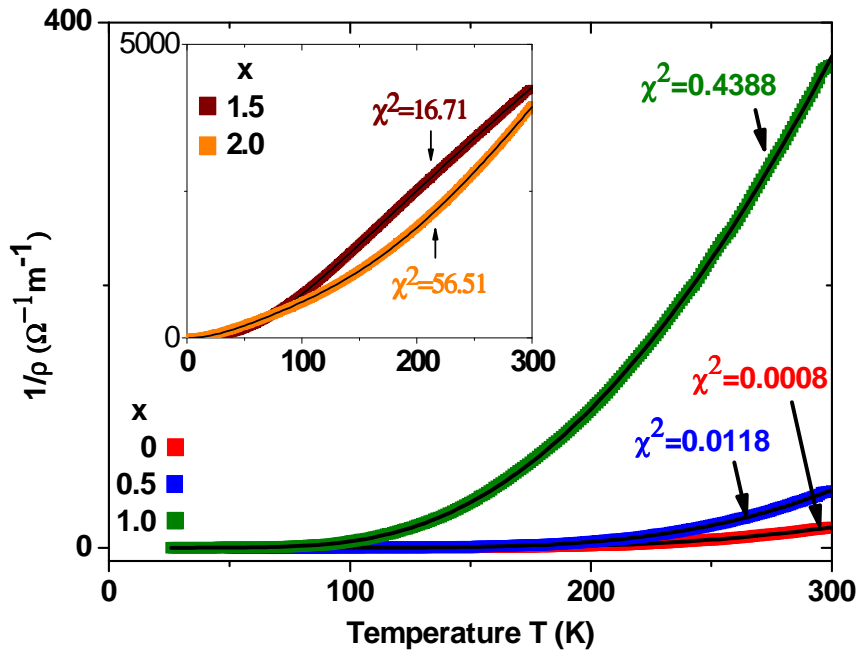


Fig. 5.26: The non-linear regression curves for $x=0-x=2.0$ together with the experimental data. χ^2 describes the goodness of a fit. Larger values for χ^2 mean larger discrepancy between the non-linear regression and the experimental data.

Accordingly, the activated (band) gaps E_G in the low-temperature regions vary from 0.26 eV for $x=0$ and $x=0.5$ over 0.12 eV for $x=1$ to 0.05 eV for $x=1.5$ (Table 5.9). For $x=2$ the VRH-mechanism dominates up to about 100 K, but the thermal activation model does not give a proper fit at higher temperatures. This peculiar situation might be caused by the high degree of B/B'-site cation disorder of 15% for $\text{Sr}_2\text{CoIrO}_6$. Assuming a band gap in accordance with the trend of this system, $E_G \leq 0.05$ eV is expected for $x=2$ and means that the distribution width of localized states within the gap approaches the band gap and this will result in a different mechanism for electron activation [126]. Either the room temperature modification $I2/m$ in case of an ideal charge ordering of the B and B' sites (zero site disorder) is metallic with a "V" shaped quasi gap, from which due to the high site disorder localized states are created or it has a very narrow band gap in which the localized states due to site disorder exist. In both of the cases the thermal activation of the carriers are strongly coupled with the hopping between the localized states and result in a non-simple activation like dependence.

The substitution of La by Sr has mainly two effects on the transport properties, which are closely related to the two degrees of freedom mentioned in the introduction: On one hand the

number of electrons at the B-site is reduced (hole doping) which affects the band filling and reduces the electron-electron Coulomb repulsion. In the $P2_1/n$ space group ($x \leq 1.5$), in agreement with the bond valence analysis, the holes are introduced predominantly in the t_{2g} bands of Ir ($\text{Ir}^{4+}: 5t_{2g} \rightarrow \text{Ir}^{5+}: 4t_{2g}$), whereas in the $I2/m$ space group ($x \geq 1.5$) they are predominantly introduced in the 3d bands of Co. On the other hand the average Co-O-Ir bond angle, determined from Rietveld refinements, increases from 152.5° for $x = 0$ to 166.3° ($P2_1/n$) for $x=2$ at 3K (Table 5.9) and means a broadening of the bandwidth. The same trend can also be observed at RT (Table 5.9). Both effects result in an increase of the electronic conductivity as observed. The temperature dependence of resistivity was also measured in an external magnetic field of $B=1$ T. No significant magnetoresistance effect was detected nor any anomalies at the magnetic ordering temperatures. Similar systematic investigations of the influence of the A-site cation on the transport properties of double perovskites are reported for $\text{La}_{1+x}\text{Sr}_{1-x}\text{CoRuO}_6$ ($-0.5 \leq x \leq 0.25$) [128] ($\text{La}_{2-x}\text{Sr}_x\text{CoRuO}_6$ ($0 \leq x \leq 2$) [127]) and $\text{La}_{1+x}\text{Ca}_{1-x}\text{CoRuO}_6$ ($-0.25 \leq x \leq 0.25$) [81]. But in contrast to an increase in the conductivity throughout the series as in the present case by Sr substitution, the conductivity is increased first by the hole doping into Ru $4t_{2g}$. However beyond a critical ratio as the ratio of Ru $3t_{2g}$ increases, the conductivity decreases and has a minimum for LaSrCoRuO_6 (or LaCaCoRuO_6) with Ru $3t_{2g}$ configuration. Note that this minimum of the conductivity is independent of the size degree of freedom of the A-site cation (La^{3+} and Ca^{2+} have almost the same ionic radius). Further doping introduces holes into t_{2g} bands of Co and the conductivity increases once again. Note that below RT the introduction of holes to the 3d bands of Co, changing its oxidation state does not induce a phase transition (phase separation) as in the case of $\text{La}_{2-x}\text{Sr}_x\text{CoIrO}_6$.

Table 5.9: Band gaps together with the average Co-O-Ir bond angles at 3 K and at room temperature.

x		Average bond angle at 3 K ($^\circ$)	Average bond angle at RT ($^\circ$)	Band gap E_g (eV)
0		152.46	152.74	0.26
0.5		154.69	158.65	0.26
1.0		157.54	158.64	0.12
1.5	$P2_1/n$	159.10	159.54	0.05
	$I2/m$	166.12	166.48	
2.0	$P2_1/n$	166.29	---	---
	$I2/m$	167.47	167.96	

5.6 Characterization of $\text{La}_2\text{CoIrO}_6$ single crystals

Compared to polycrystalline samples, single crystals have many advantages such as no inter-grain effects or most importantly anisotropic properties can be investigated on a single crystal. As already assumed in the introduction and confirmed by magnetization measurements, $\text{La}_2\text{CoIrO}_6$ undergoes NCM ordering and shows spin reorientation transition in an external magnetic field. Therefore it is interesting to find out how does the magnetic moment react to an external magnetic field applied in different directions or to investigate anisotropies in the spin reorientation transition. Note that the spin reorientation transition need not be a spin flip transition. Moreover it may land on a local energy minimum and such transitions are known as metamagnetic transitions.

In order to investigate such features, magnetization and heat capacity measurements are carried out for a single crystal with a mass of 4.33 mg. The experimental procedure is discussed in sections 3.2 and 3.3. The heat capacity measurement is only used to confirm the ordering temperature.

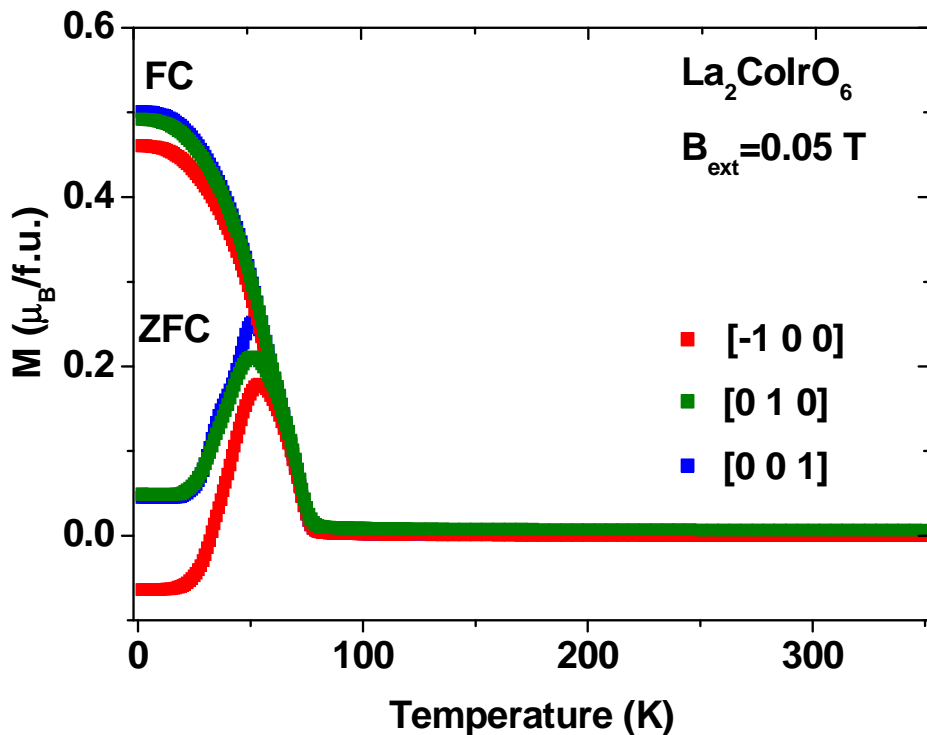


Fig. 5.27: Temperature dependence of magnetization for $\text{La}_2\text{CoIrO}_6$ in $[-1\ 0\ 0]$, $[0\ 1\ 0]$ and in $[0\ 0\ 1]$ directions.

In fig. 5.27 the temperature dependence of the magnetization (measured at 0.05 T) at the range 1.8-350 K is shown for the field directions $[-1\ 0\ 0]$, $[0\ 1\ 0]$ and $[0\ 0\ 1]$. The ordering temperatures T_C are obtained using the linear extrapolation method. They are 77.2 K, 77.6 K and 76.8 K for $[-1\ 0\ 0]$, $[0\ 1\ 0]$ and $[0\ 0\ 1]$ directions, respectively, and therefore they are almost identical. Furthermore this ordering temperature is also confirmed by the anomaly in the temperature dependence of the specific heat capacity, which is shown in fig. 5.28. The temperature dependence of the specific heat capacity shows also another weak anomaly around 30 K, The origin of this anomaly is unknown.

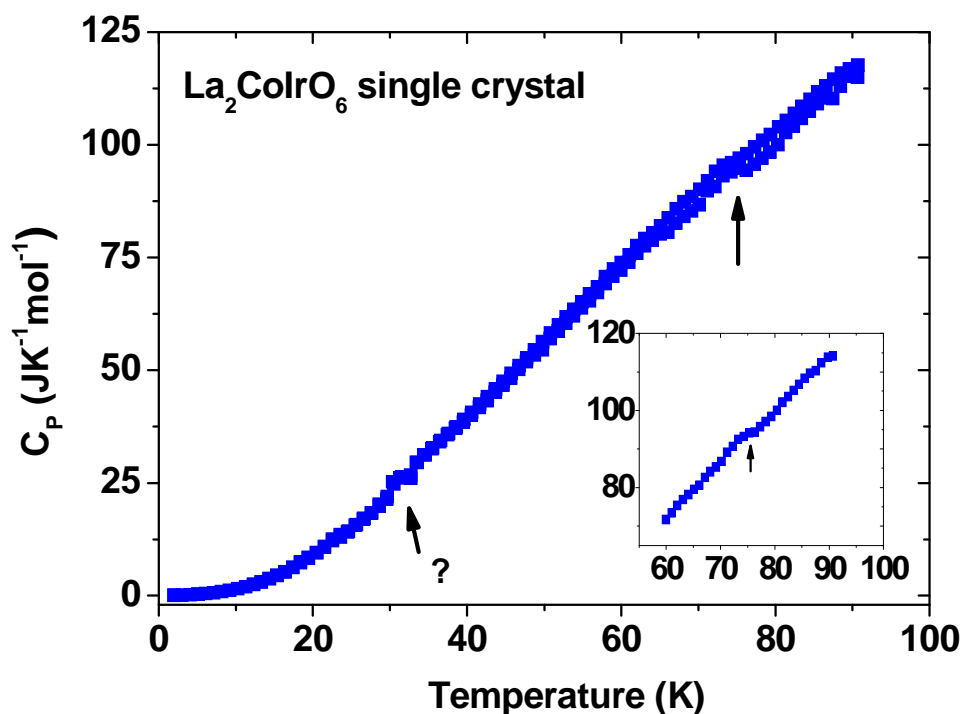


Fig. 5.28: Specific heat capacity of $\text{La}_2\text{CoIrO}_6$ single crystal.

But discrepancy between the ordering temperature of 95 K obtained for the polycrystalline sample and for the single crystal by means of magnetization measurements is quite large, almost 20 K. Other than that, the FC and ZFC in the $[-1\ 0\ 0]$ differ from the other two and especially the ZFC of $[-1\ 0\ 0]$ has a negative value at lower temperatures. This may be due to the fact, that the ferromagnetic component, which is in the $[0\ 1\ 0]$ (b) direction according to magnetic symmetry analysis has to overcome barriers in the angle dependence of the energy surfaces, which may differ in the $[-1\ 0\ 0]$ and $[1\ 0\ 0]$ directions (a measurement in the $[1,0,0]$ direction may look similar to $[0\ 1\ 0]$ and $[0\ 0\ 1]$ cases). In fig. 5.29 the field dependence of the magnetizations for the same field directions are shown and additionally in fig. 5.30 only

the virgin curves are shown. In all three directions hysteresis loops are obtained and as in the case of the polycrystalline sample, which are not saturated even at 7 T. Shape anomalies could be seen as in the case of polycrystalline sample, but they only exist in measurements in the $[-1\ 0\ 0]$ and $[0\ 1\ 0]$ directions and no anomalies could be seen in the $[0\ 0\ 1]$ direction. For the measurement in the $[0\ 1\ 0]$ direction anomalies in the hysteresis could be seen at 0 Tesla and 3 Tesla, whereas for the $[-1,0,0]$ case it is only seen at 3 Tesla. Another striking difference between the hysteresis of the single crystal and the polycrystalline sample is the value of the coercitivity field. Whereas for the polycrystalline sample it is around 2 T, it is 3 T for the single crystal in all three measured directions. In order to obtain more information of the anomalies in the field dependence of the magnetization, the virgin curves are enlarged and shown in fig. 5.30. In all three directions sudden jumps in the magnetization values could be seen. These are usually attributed to field induced spin reorientation transitions, due to the barriers in the energy surface. This is already discussed in section 5.2 together with examples in the class of double perovskites. This is further discussed in section 5.7.2, where results of the calculations based on the non collinear arrangement of the magnetic moments are addressed. The spin reorientation jumps in the virgin curves could be categorized into two types. For the $[-1\ 0\ 0]$ and $[0\ 1\ 0]$ directions, the jump starts at around 2 T and its magnitude is around $0.25\ \mu_B$, whereas for the $[0\ 0\ 1]$ direction it starts at around 2.5 T and has a magnitude around $0.6\ \mu_B$. Apart from small differences the evolution of the magnetization for $[-1\ 0\ 0]$ and $[0\ 1\ 0]$ are similar. This may be attributed to the fact that the topologies are similar for the magnetization in a and b directions. Note that the upper part of the virgin curve for $[-1\ 0\ 0]$ and $[0\ 1\ 0]$ is characteristic for domain wall dynamics, consisting of wall movement and rotation. In fig. 5.31 the virgin curves at different temperatures are shown for $[-1\ 0\ 0]$ and $[0\ 0\ 1]$. With increasing temperature at first the spin reorientation is eased by thermal energy, however for higher temperatures the magnetization decreases due to the destruction of the domains by the thermal energy.

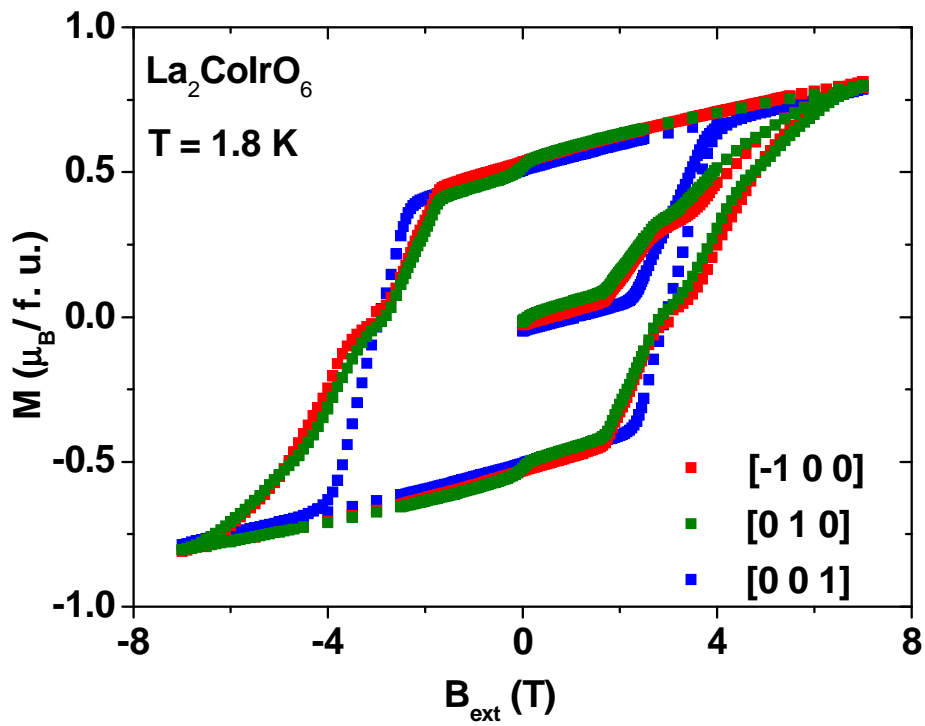


Fig. 5.29: Field dependence of magnetization for $\text{La}_2\text{CoIrO}_6$ in $[-1\ 0\ 0]$, $[0\ 1\ 0]$ and in $[0\ 0\ 1]$ directions.

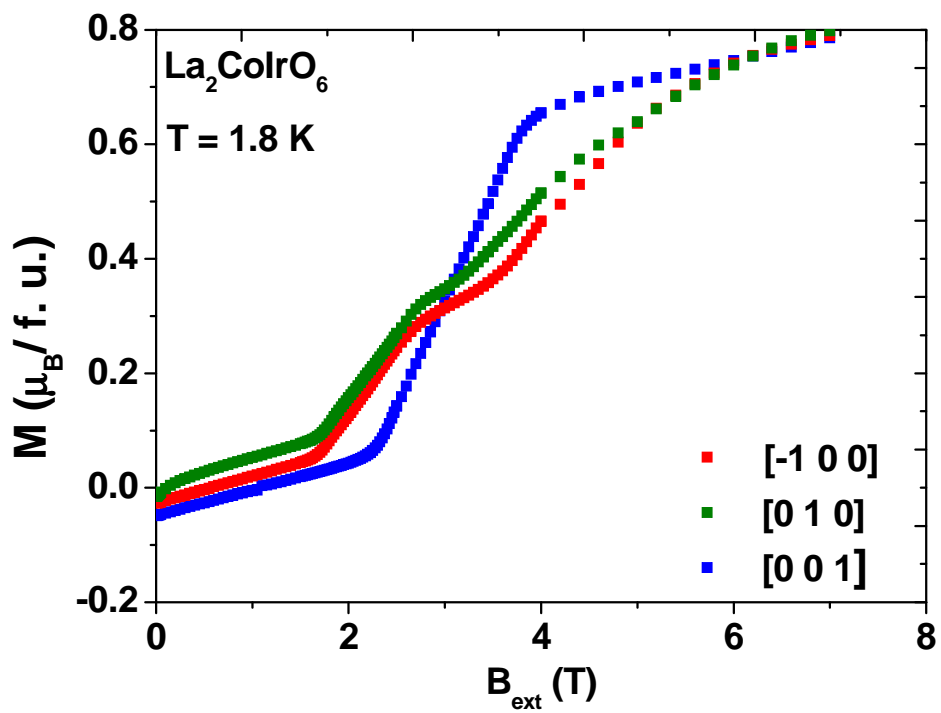


Fig. 5.30: Virgin curves of $\text{La}_2\text{CoIrO}_6$ in $[-1\ 0\ 0]$, $[0\ 1\ 0]$ and in $[0\ 0\ 1]$ directions.

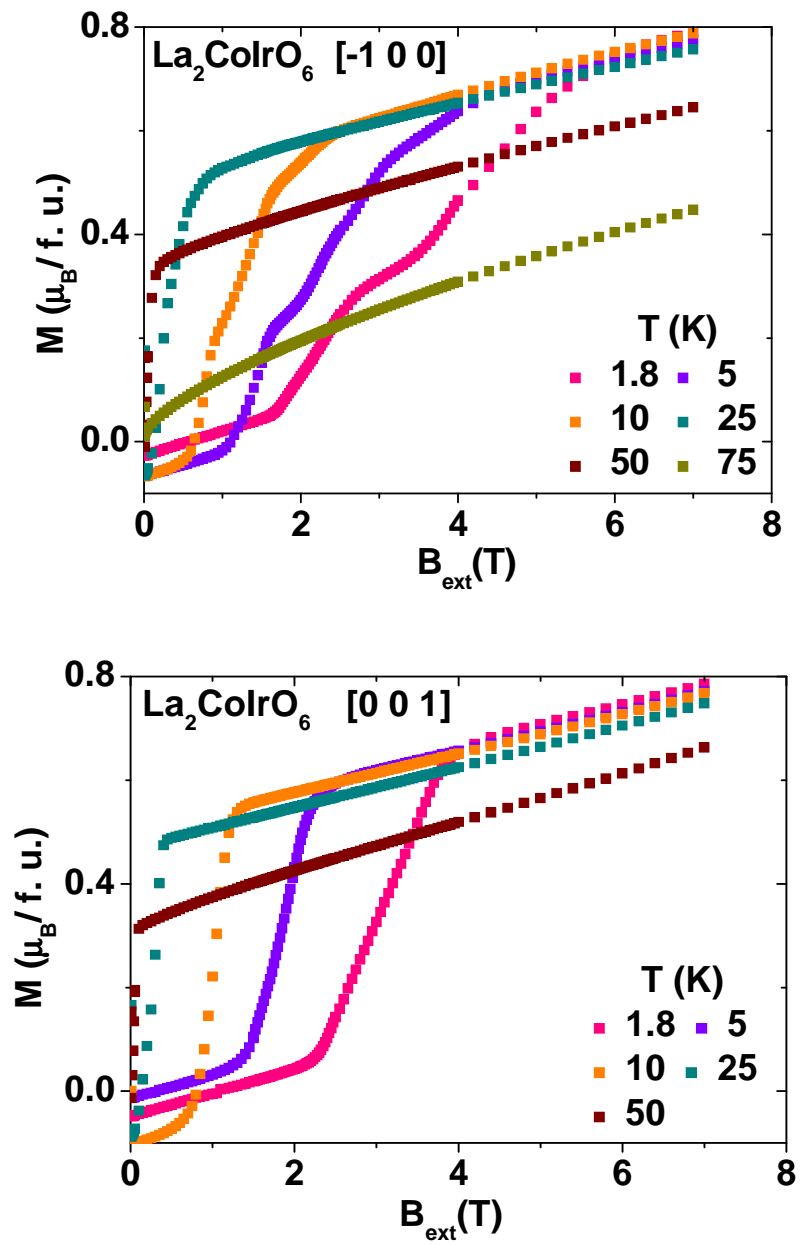


Fig. 5.31: Virgin curves of $\text{La}_2\text{CoIrO}_6$ in $[-1\ 0\ 0]$ and in $[0\ 0\ 1]$ directions for different temperatures.

5.7 Electronic structures

5.7.1 Collinear calculations

The electronic structure calculations for collinear arrangement of the magnetic moments are discussed in four parts, addressing (i) the density of states (DOS), (ii) a comparison of total energies for different configurations of $x=0$, (iii) the oxidation state of Co and Ir and (iv) the magnetic moments.

(i) The calculated DOS for $x=0$ of the experimentally found $k=(0,0,0)$ AFM structure is shown in fig. 5.32 for the GGA case. It is evident from the total DOS and the calculated occupancies of the d-bands, that $x=0$ has a metallic ground state with predominant HS-Co²⁺ and LS-Ir⁴⁺ in contrast to the experimental finding of an insulator with a band gap of 0.26 eV. Additionally the l-decomposed partial DOS of Co 3d (Co2) and Ir 5d (Ir2) for $x=0$, projected on the local coordinate system along the B/B'-O bond direction in the oxygen octahedra are also shown in fig. 5.32(b) – 5.32(c). From the partial DOS of Co 3d and Ir 5d it is evident that the three t_{2g} bands of Co-3d are similarly occupied (neglecting the additional break down of the t_{2g} degeneracy due to the monoclinic distortion: d_{xy} , d_{yz} and d_{xz}) by the two spin-down electrons per Co-atom and the three t_{2g} bands of Ir-5d are filled by 2.5 spin-up/down electrons per Ir-atom and thus a metallic state is obtained. The experimental non-metal behaviour with a band gap should be attributed to strong electron-electron onsite Coulomb repulsion that is badly described within the LDA/GGA approximation. A comparison of band width W with typical onsite Coulomb energies U is necessary to take this effect adequately into account. The approximate width W of the d bands could be estimated to 1.5 eV for Co t_{2g} , 0.7 eV for Co e_g , 2 eV for Ir t_{2g} and 2.7 eV for Ir e_g (from the partial DOS). Therefore, the bandwidth W of both Co- and Ir-d bands are small compared to (or in the case of Ir e_g at most equal with) the typical onsite Coulomb repulsion energies U , which are around 5.44 eV (0.4 Ry) and 2.72 eV (0.2) Ry for Co and Ir, respectively [129]. Therefore, an onsite Coulomb repulsion U has been included for the d bands together with exchange parameters $J(\text{Co})=0.918$ eV and $J(\text{Ir})=0.544$ eV via the fully localized limit (FLL) method as implemented in WIEN2k and described in [64] and [65].

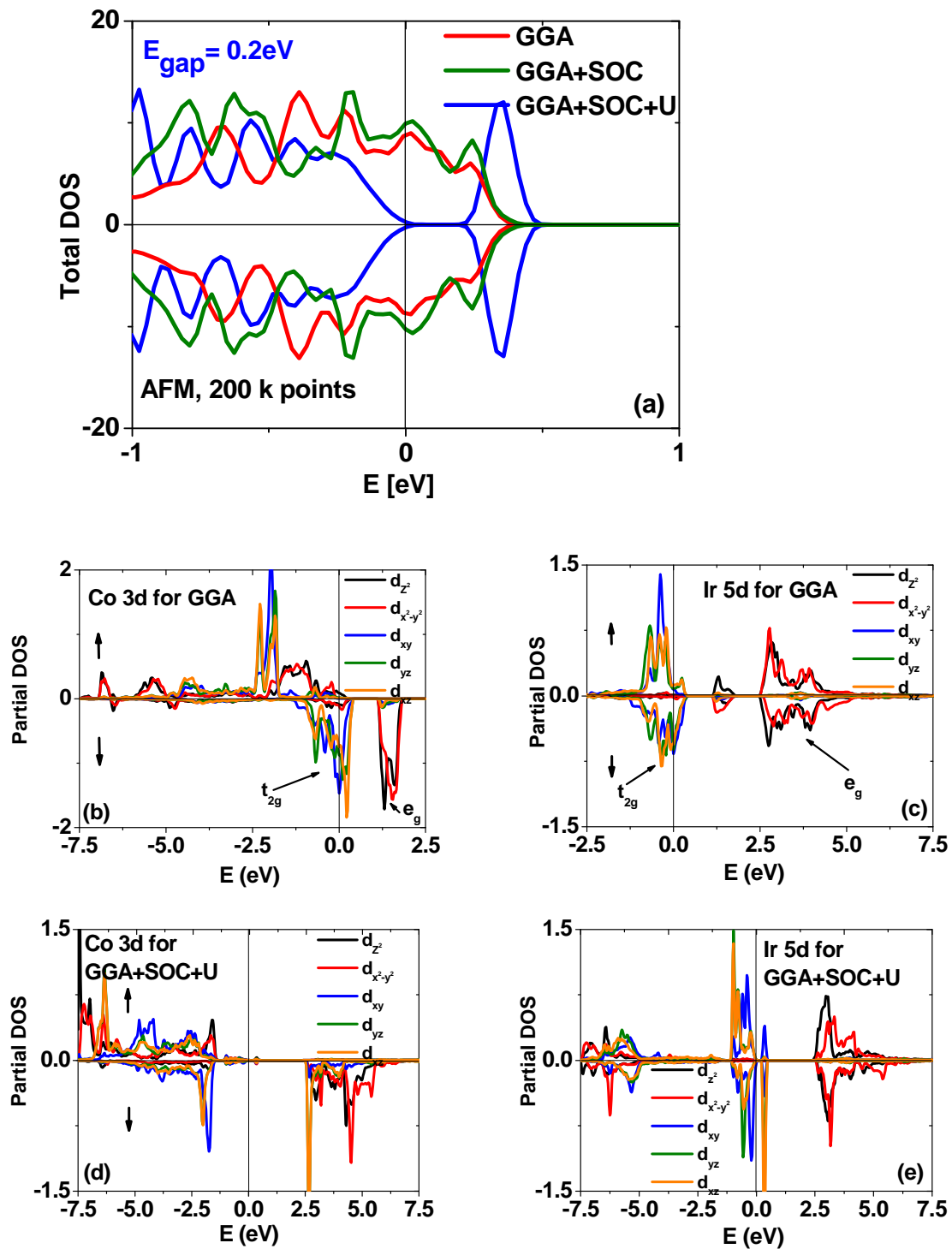


Fig. 5.32: (a) Total DOS of AFM for $x=0$ within GGA, GGA+SOC and GGA+SOC+U (top). (b) Partial DOS of Co 3d bands and (c) Ir 5d bands for GGA (middle). (d) Partial DOS of Co 3d bands and (e) Ir 5d bands for GGA+SOC+U (bottom). Note that for $x=0$ there are two independent sites for Co and Ir, each with opposite magnetic moments. Partial DOS in (b), (d) and (c), (e) correspond to only one Co (Co 2) and one Ir (Ir 2).

The total DOS $x=0$ AFM for GGA+SOC and GGA+SOC+U (Co and Ir) are also shown in fig. 5.32(a). It can be seen that there is not much difference in the total DOS between GGA and GGA+SOC. But as soon as U for both Co and Ir were added, a band gap opens up at the Fermi level which is around 0.2 eV in fairly good agreement with the experimental finding. This is also valid for the total DOS of the FM configuration (not shown). The inclusion of U shifts the two occupied spin-down “ t_{2g} ” orbitals around $-(U-J)/2$ and the one unoccupied “ t_{2g} ” orbital around $+(U-J)/2$ in case of 3d of a Co. In case of 5d of an Ir a fairly empty spin-down “ t_{2g} ” orbital is obtained by the $+(U-J)/2$ shift with an additional enhancement of the spin polarization are obtained for the above reason. This splitting in the “ t_{2g} ” bands of Co 3d and Ir 5d results in a band gap at the Fermi-level. However fractional occupancies were obtained for all the mentioned “ t_{2g} ” bands as a result of the competing hybridization and SOC as shown in fig. 5.32(d)-(e). The “ e_g ” (d_{z^2} , $d_{x^2-y^2}$) bands also undergo the above mentioned shifts but they are not relevant to the changes of the electronic structure at the Fermi-level.

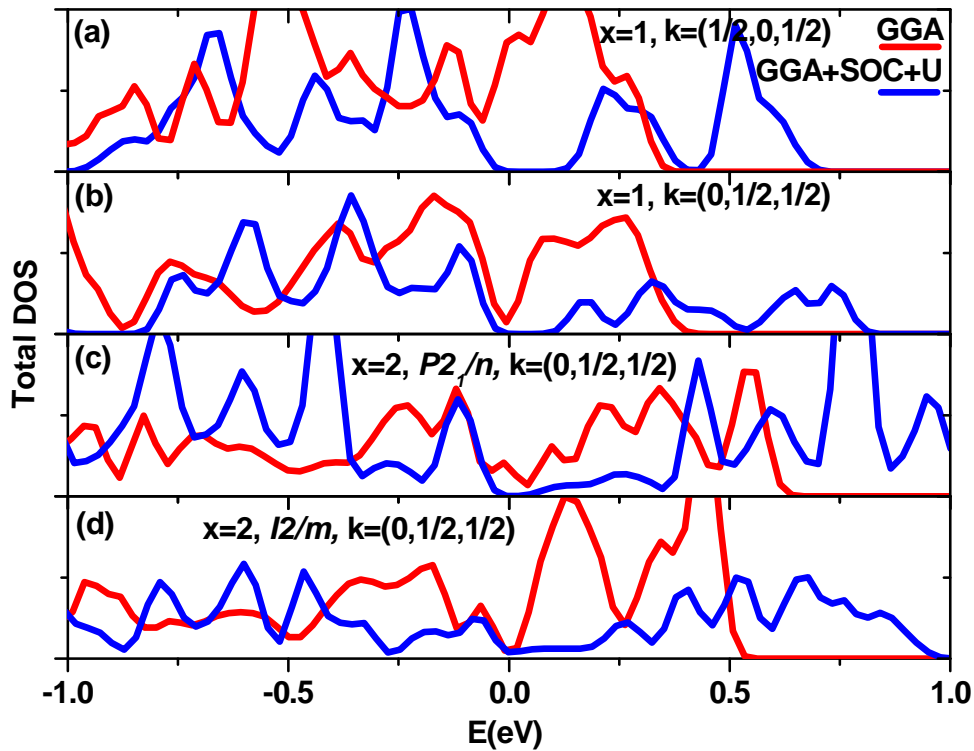


Fig. 5.33: Total (spin up) DOS of (a) $x=1$ $k=(1/2,0,1/2)$, (b) $k=(0,1/2,1/2)$, (c) $x=2$ ($P2_1/n$) $k=(0,1/2,1/2)$ and (d) $x=2$ ($I2/m$) $k=(0,1/2,1/2)$ AFM configurations for the GGA (red) and GGA+SOC+U(Co)=0.4Ry+U(Ir)=0.2Ry (blue) cases. Only minor differences between GGA and GGA+SOC with respect to the DOS around the Fermi level and thus the latter are not shown for $x=1$ and $x=2$.

The total DOS for $x=1$ and $x=2$ with the experimentally found $k=(1/2,0,1/2)$ and $k=(0,1/2,1/2)$ AFM structures are shown in fig. 5.33. As a comparison the DOS for $x=1$ with the $k=(0,1/2,1/2)$ AFM structure is also shown in fig. 5.33. For $x=1$ a band gap of around 0.1 eV can be seen from fig. 5.33 as soon as U was included in the calculation, almost independent of the experimentally found $k=(1/2,0,1/2)$ and the not preferred $k=(0,1/2,1/2)$ AFM structure. For $x=2$ the total DOS is shown for the two modifications coexisting at temperatures below 220 K. Whereas the low temperature modification $P2_1/n$ is a non-metal with a band gap around 0.05 eV, the high temperature modification $I2/m$ is metallic with a rather small DOS at the Fermi level even after the inclusion of U . In contrast to theory, resistivity measurements reveal $x=2$ to be non-metallic over the whole measured temperature range. However, the investigated $\text{Sr}_2\text{CoIrO}_6$ sample has a high degree of B/B'-site disorder and is better described as $\text{Sr}_2(\text{Co}_{0.85}\text{Ir}_{0.15})(\text{Ir}_{0.85}\text{Co}_{0.15})\text{O}_6$. The non-activation like temperature dependence of resistivity and the apparent band gap instead of a continuous band could result from localized states at the Fermi level due to this site disorder [130, 131]. For the $P2_1/n$ phase the calculated band gaps decrease from 0.2 eV for $x=0$ to 0.05 eV for $x=2$ in agreement with the observed reduction of E_g at least for $0 \leq x \leq 1.5$.

(ii) As the magnitude of FM (from the magnetization measurement) and the $k=(0,0,0)$ AFM components are similar for $x=0$, the total energies of these magnetic structures together with the $k=(0,1/2,1/2)$ AFM are compared for the GGA+SOC+ U case as shown in the second column of Table 5.10. All the atomic positions are taken from the structure model, refined based on NPD (experiment). For the $k=(0,1/2,1/2)$ AFM configuration the same atomic positions are taken and supercells have been built. The FM configuration has a total energy 0.25 mRy/ f.u. lower than the observed $k=(0,0,0)$ AFM configuration, whereas for the GGA case (not shown) the total energy of the AFM configuration is lower than the FM configuration. As the inclusion of U resulted in anisotropic occupancies of the d orbitals, this increases the total forces (certain components of oxygen are around 100 mRy/a.u. (a.u.: atomic unit)) acting on atoms and such occupations would couple to the lattice and move atoms in general positions (especially oxygen). Therefore for all three configurations, the internal atomic positions are relaxed till the forces are below 5 mRy/ a.u., and these total energies are compared (Table 5.10, third column). The $k=(0,0,0)$ AFM configuration is energetically more favoured than the FM (+3.1 mRy/f.u.) one. This small difference in the total energies of the two configurations is an indication for a strong competition between

ferromagnetic and antiferromagnetic interactions, and spin-orbit coupling together with electron correlations play the key role for the observed non-collinear magnetism for $x=0$. Note that in both cases the $k=(0,1/2,1/2)$ AFM configuration is energetically clearly unfavourable.

Table 5.10: Total energy differences ΔE , relatively to the experimentally (NPD) observed $k=(0,0,0)$ AFM, in mRy/f.u. for FM, $k=(0,0,0)$ AFM and $k=(0,1/2,1/2)$ AFM configurations for the GGA+SOC+U case. The total energy differences for the relaxed structure calculations are shown in the third column, again relatively to the total energy of the relaxed $k=(0,0,0)$ AFM structure.

$x=0$	ΔE (Experimental internal positions)	ΔE (Relaxed internal positions)
FM	-0.25	+3.10
AFM $k=(0,0,0)$	0.00	0.00
AFM $k=(0,1/2,1/2)$	+36.07	+40.70

(iii) Table 5.11 shows the occupation of the d bands of Co 2 and Ir 2 for the GGA and GGA+U+SOC cases. The striking difference between the two is that for GGA+SOC+U the difference between the occupations of $x=0$ and $x=2$ is larger than in GGA. The GGA+SOC+U results are interpreted as follows: For $x=0$, see Fig. 5.32(d)-(e), it is evident that the spin-up d-bands for Co 3d are almost fully occupied, while the spin-down DOS for the e_g (d_{z^2} , $d_{x^2-y^2}$) bands are almost completely unoccupied. This is in good agreement with the assumed high-spin state of Co^{2+} and the low-spin state for Ir^{4+} in the simple ionic picture, neglecting hybridization effects and residual electron densities at interstitials. The proposed tendency towards HS- $\text{Co}^{3+}/\text{Ir}^{5+}$ with increasing Sr-content is also supported by the calculated occupation of the d bands for $x=1$ and $x=2$. The occupation of the Co 3d bands changes significantly only for $x>1$, whereas changes in the occupation of the Ir 5d bands are only significant for $x\leq 1$. This is in good agreement with the successive changes of the Co-O and Ir-O bond lengths, see fig. 5.5.

Table 5.11: Calculated occupations of the Co 3d and Ir 5d bands for the experimentally found AFM structures in units of d-electrons per atom.

x	Co GGA			Co GGA+SOC+U			Ir GGA			Ir GGA+SOC+U		
	up	down	total	up	down	total	up	down	total	up	down	total
0	4.63	2.11	6.74	4.69	2.03	6.72	2.64	2.11	4.75	2.70	2.26	4.96
1	4.61	2.05	6.66	4.67	2.02	6.69	2.73	2.11	4.84	2.77	2.00	4.77
2 ($P2_1/n$)	4.56	1.89	6.45	4.68	1.65	6.33	2.75	1.89	4.64	2.72	1.91	4.63
2 ($I2/m$)	4.58	1.91	6.49	4.67	1.68	6.35	2.73	1.93	4.66	2.76	1.92	4.68

(iv) The calculated magnetic moment contributions from spin and orbital momentum are compared for Co and Ir in Table 5.12 within GGA+SOC+U. The calculated spin moment of Co for $x=0$ is $2.68 \mu_B$ per Co-ion ($2.53 \mu_B$ per Co-ion for GGA) and much larger than the observed magnetic moment of $|\mu|=1.7 \mu_B$ per Co-ion (NPD). As different 3d orbital occupancies for Co are possible within the same oxidation state and lattice parameters in LDA/GGA+U [17], such an orbital occupancy for 3d Co in the vicinity of the desired AFM moment of $1.7 \mu_B/\text{Co}$ was forced with the FLL method. Apart from the HS state discussed above another LS state (also Co^{2+}) with zero magnetic moment could be stabilized but a solution for the desired occupation did not converge. Therefore, another variant of the GGA+U approximation was used, namely the “around mean field” method (AMF) [64], known to reduce the magnetic moment of the respective ion in certain cases [132]. With this method a convergent solution could be found with an AFM moment of $1.84 \mu_B/\text{Co}$ (orbital moment: $0.17 \mu_B/\text{Co}$) with $U(\text{Ir})=2.72 \text{ eV}$ as above, but with a reduced U for Co of 3.4 eV (0.25 Ry). However, the magnetic moments of Ir are aligned antiparallel in contrast to the FLL results, where the alignment of the magnetic moments of Co and Ir become parallel, independent on the initial spin configuration (Table 5.12). Higher U values with the AMF method resulted either in larger magnetic moments (for initial spin moments of Co larger than $2.6 \mu_B$) or in smaller magnetic moments below $1 \mu_B/\text{Co}$ (for initial spin moments of Co smaller than $2.6 \mu_B$ with a small stability window for IS). In all cases the oxidation state of Co tends to be +2. The dependence of the spin state on the $U(\text{Co})$ is shown in fig. 5.34.

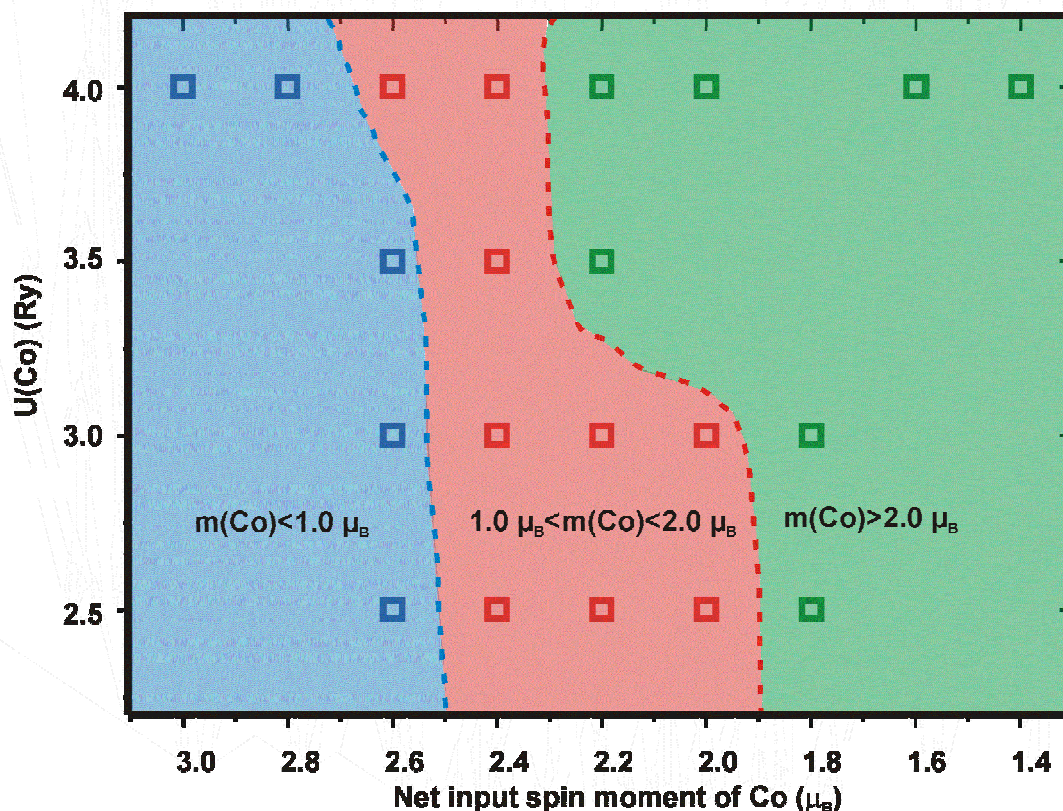


Fig. 5.34: Spin moment (state) of Co within GGA+SOC+U(AMF) depending on the input spin moment and $U(\text{Co})$.

For $x=1$ and $x=2$ the calculated magnetic moments (HS) of Co with the FLL method agree well with the NPD results, taking the effect of finite temperature (3K) and the site disorder [133] on the B/B'-sites into account. In case of $x=0$ the non-collinearity could also contribute to a further reduction of the magnetic moments. With an increasing degree of La substitution by Sr also a possible transition between the intermediate and high spin state takes place for Co, in addition to the obvious increase of the Co oxidation state. Note that spin and orbital contributions to the magnetic moments have always the same sign for both Co- and Ir-ions along the whole series. This is a remarkable difference to double perovskites with ferromagnetic ordering having high Curie-temperatures (above room temperature) like the Re-based compounds $A_2B\text{ReO}_6$ with $A=\text{Ca}, \text{Sr}$ or Ba and $B=\text{Fe}$ or Cr , where spin and orbital contributions on the Re-site have always different signs [134].

Table 5.12: Calculated spin (m_S) and orbital moments (m_L) for $x=0, 1$ and 2 for the experimentally found AFM structures within GGA+SOC+U.

x	0		1	2 ($P2_1/n$)	2 ($I2/m$)
	FLL	AMF			
$m_S(\text{Co})$ (μ_B/atom)	2.68	1.84	2.67	3.05	2.99
$m_L(\text{Co})$ (μ_B/atom)	0.17	0.17	0.16	0.11	0.10
$m_S(\text{Ir})$ (μ_B/atom)	0.44	-0.10	0.77	0.80	0.85
$m_L(\text{Ir})$ (μ_B/atom)	0.43	-0.01	0.29	0.16	0.17

5.7.2 Non collinear calculations (NCM calculations)

As already mentioned, non-collinear calculations are performed for $\text{La}_2\text{CoIrO}_6$ with the FM component of Co being in the b direction and only for the $U(\text{Co})=0.4$ Ry/0.3 Ry and $U(\text{Ir})=0.2$ Ry cases in FLL limit (with SOC). At first the AFM component of Co is aligned in the c direction and tilted towards the b direction, creating a FM component. The results are shown in fig. 5.35 and fig. 5.36 for the above configurations for the $U(\text{Co})=0.4$ Ry, $U(\text{Ir})=0.2$ Ry and $U(\text{Co})=0.3$ Ry, $U(\text{Ir})=0.2$ Ry cases. In both cases local minima are found below 10° , which indicates that the canting of the Co moments lies within this range. Further tilting of the Co moments towards the b axis needs to overcome energy barriers, which is somewhat different for different $U(\text{Co})$ values. Overcoming such energy barriers may reflect the spin reorientation transitions, observed in virgin curves of the $\text{La}_2\text{CoIrO}_6$ single crystals.

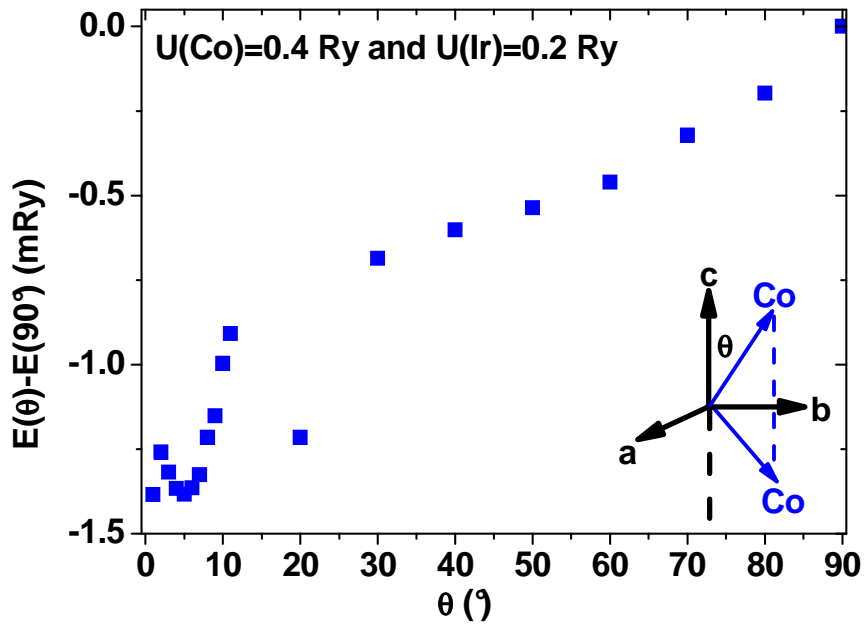


Fig. 5.35: Angular dependence of the total energies for the $U(\text{Co})=0.4 \text{ Ry}$, $U(\text{Ir})=0.2 \text{ Ry}$ case. The Co moments are tilted from $[0,0,1]$ and $[0,0,-1]$ towards the b axis.

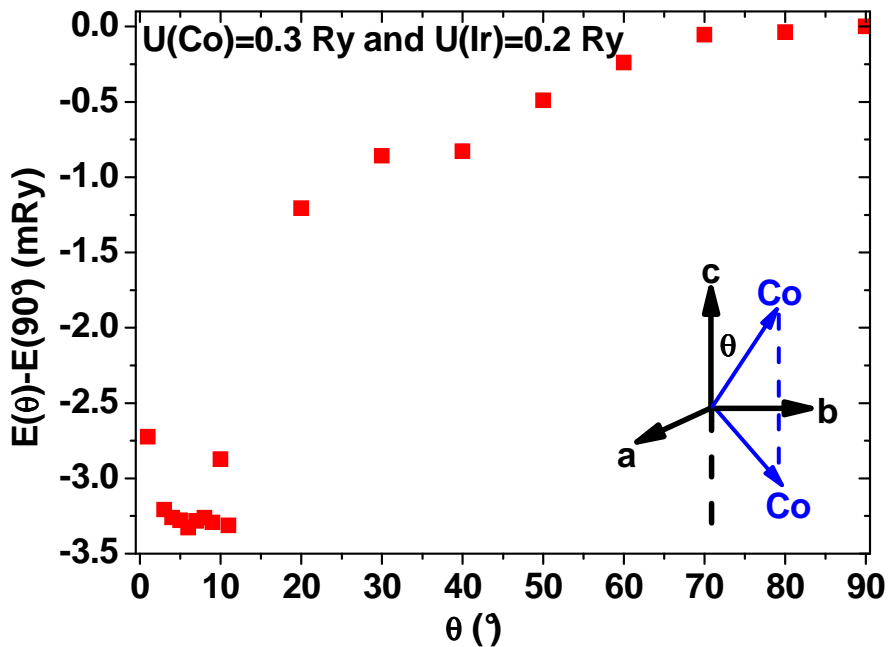


Fig. 5.36: Angular dependence of the total energies for the $U(\text{Co})=0.3 \text{ Ry}$, $U(\text{Ir})=0.2 \text{ Ry}$ case. The Co moments are tilted from $[0\ 0\ 1]$ and $[0\ 0\ -1]$ towards the b axis.

In order to find even more information on this phenomenon, NCM calculations are performed for the experimentally found AFM arrangement of Co in the $[-1\ 0\ 2]$ direction (AFM component of Co from the NPD is in the ac plane with $\mu=(-0.7,0,1.5)\ \mu_B$). From this direction the magnetic moment of Co is slowly tilted towards the b axis and calculations are performed for different angles. The total energies are shown in fig. 5.37 (a) and (b) for the $U(\text{Co})=0.4\ \text{Ry}$, $U(\text{Ir})=0.2\ \text{Ry}$ and $U(\text{Co})=0.3\ \text{Ry}$, $U(\text{Ir})=0.2\ \text{Ry}$ cases.

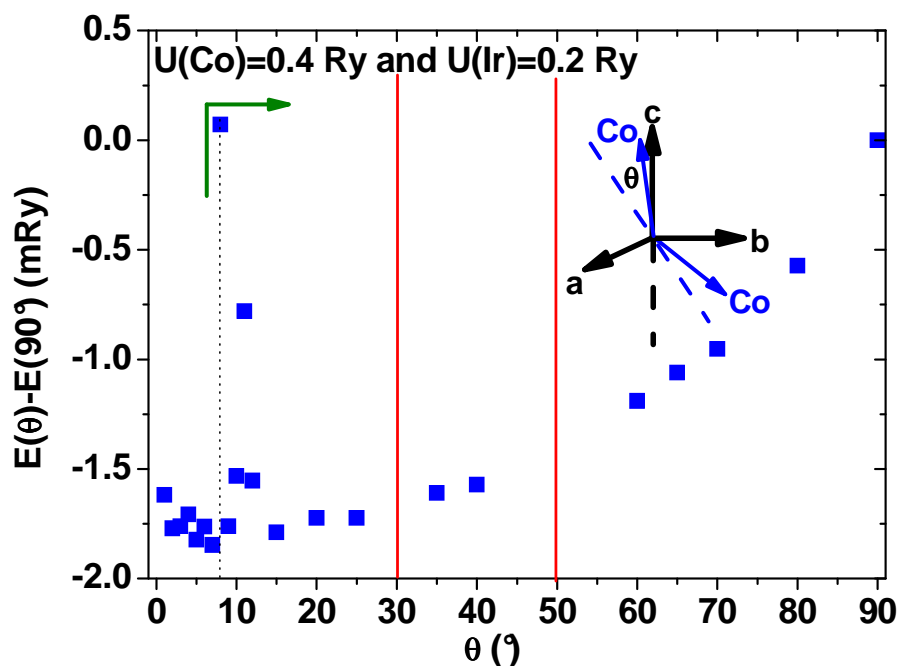


Fig. 5.37 (a): Angular dependence of the total energies for the $U(\text{Co})=0.4\ \text{Ry}$, $U(\text{Ir})=0.2\ \text{Ry}$ case. The Co moments are tilted from the experimentally found $[-1\ 0\ 2]$ towards the b axis.

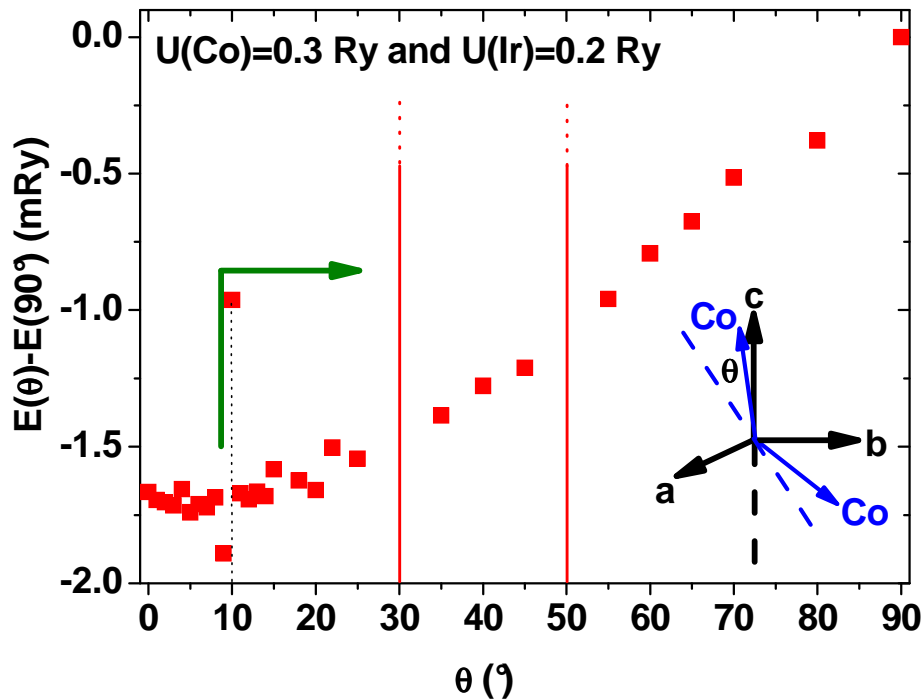


Fig. 5.37 (b): Angular dependence of the total energies for the $U(\text{Co})=0.3$ Ry, $U(\text{Ir})=0.2$ Ry case. The Co moments are tilted from the experimentally found $[-1\ 0\ 2]$ towards the b axis.

For both $U(\text{Co})$ values there is an energy barrier at the low angle region, which follows an energy minimum. In the following any calculation output values corresponding to the $U(\text{Co})=0.3$ Ry case will be given within brackets. For the $U(\text{Co})=0.4$ Ry (0.3Ry) case the energy barrier is at 8° (10°), which follows an energy minimum at 7° (9°). This barrier is more pronounced than in the other cases discussed above for the $[0\ 0\ 1]$ AFM orientation of Co and it has a magnitude of 2 mRy (1mRy). Overcoming this barrier may shift the tilting from 8° (10°) directly to 90° (55°) as one may expect from the angle dependence of the energy. But at 30° and at 50° there are two lines drawn vertically. These correspond to angles where the Ir moments flip their relative orientation to Co and they are further 1.6 mRy (1.6mRy) and 1.2 mRy (1.1mRy) energetically higher than the energy value at 90° , therefore not shown in fig. 5.37 (a) and (b). The barrier may not be overcome by laboratory magnetic fields and it can be assumed that as soon as the barrier at 8° (10°) is crossed, the ferromagnetic component of Co would reach a value close to the one at 25° . This may explain the sudden increase during the spin reorientation transition in the virgin curves especially in the b direction. In this context an energy barrier of 1mRy at 10° for $U(\text{Co})=0.3$ Ry seems to be more reasonable value from an experimental point of view than 2 mRy at 8° for $U(\text{Co})=0.4$ Ry. But as already mentioned the GGA+U in the FLL limit produces the HS state of Co (spin

moment of $2.7 \mu_B$ in average), in contrary to the NPD result of $1.7 \mu_B$. The possible IS of Co could not be stabilized with the AMF method as in the case of collinear calculations. But still the relative change in the total ferromagnetic component between the transitions can be analysed. The total ferromagnetic component for the important angles is shown in table 5.13.

Table 5.13: Total ferromagnetic component for some important tilt angles.

θ ($^\circ$)	0	0	7	9	8	10	25	25
U(Co) (Ry)	0.4	0.3	0.4	0.3	0.4	0.3	0.4	0.3
Net m_s (total) (μ_B)	0.64	0.63	0.81	0.71	0.83	0.88	1.12	1.24
Net m_L (total) (μ_B)	0.38	0.37	0.39	0.38	0.40	0.40	0.40	0.40
Net m (total) (μ_B)	1.02	1.00	1.20	1.09	1.23	1.28	1.52	1.64

According to the angular dependence of the energy in the b direction, the magnetic moment of Co would be at 7° (9°) without any external magnetic field. This corresponds to a total ferromagnetic component of $1.02 \mu_B$ ($1.00 \mu_B$) which is not far away from the spontaneous magnetization of $0.7 \mu_B$ determined from the hysteresis of $\text{La}_2\text{CoIrO}_6$ at 1.8 K. Considering the finite temperature and the site disorder this is even a reasonable agreement. For further discussion, fig. 5 30 is considered. The change of the magnetic moment of Co from 7° to 8° (from 9° to 10°) invokes a change in the total ferromagnetic component of $0.02 \mu_B$ ($0.19 \mu_B$), whereas in the virgin curve this corresponds to a change of slightly larger than $0.1 \mu_B$. Now overcoming the barrier at 8° (10°) changes the total ferromagnetic component around $0.29 \mu_B$ ($0.36 \mu_B$), whereas the spin reorientation transition changes the magnetization around $0.25 \mu_B$ in the virgin curve. Therefore the changes in the virgin curve are in fairly good agreement with the calculations. Nevertheless, to further elucidate the dynamics of the spin reorientation completely, at least additional calculations for other directions are necessary. Finally the band gaps for different angles are compared and they are shown in fig. 5.38 for 30° and 80° tilting for $U(\text{Co})=0.3$ Ry and $U(\text{Co})=0.4$ Ry (in both cases $U(\text{Ir})=0.2$ Ry).

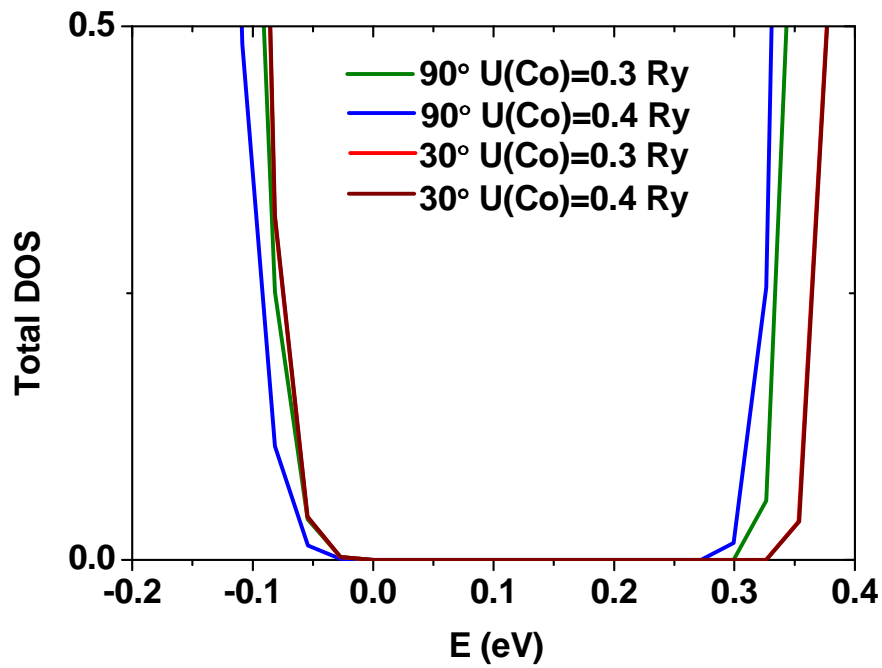


Fig. 5.38: Calculated band gaps for different tilting.

The band gaps differ slightly from one another (0.28 eV-0.32 eV) and are larger than for the collinear case with the same $U(\text{Co})$ value. Nevertheless they are comparable with the experimentally obtained band gap of around 0.26 eV.

5.8 The $\text{La}_{2-x}\text{Ca}_x\text{CoIrO}_6$ ($0 \leq x \leq 0.75$) system

As already mentioned the size degree of freedom is eliminated in this system, leaving only the band filling degree of freedom. Therefore, this system serves to the investigation of the effects of hole doping into Co and Ir sites. The results will be compared with $\text{La}_{2-x}\text{Sr}_x\text{CoIrO}_6$, where apart from the hole doping the effects of the size degree of freedom also exist. In the present work the crystal structure, magnetic properties, transport properties and electronic structure are investigated for $x=0.5$ and 0.75 .

5.8.1 Crystal structures at room temperature and at 4K

Rietveld refinements of structural parameters are performed, based on x-ray and neutron diffraction data simultaneously, using the program FullProf [92]. As an example the diffraction patterns of $\text{La}_{1.5}\text{Ca}_{0.5}\text{CoIrO}_6$ obtained from neutron diffraction and x-ray diffraction together with the calculated ones are shown in fig. 5.39 and fig. 5.40. It is evident that single phase samples are obtained for the mentioned compositions. The diffraction patterns with the calculated intensities of $\text{La}_{1.25}\text{Ca}_{0.75}\text{CoIrO}_6$ are shown in appendix 1.

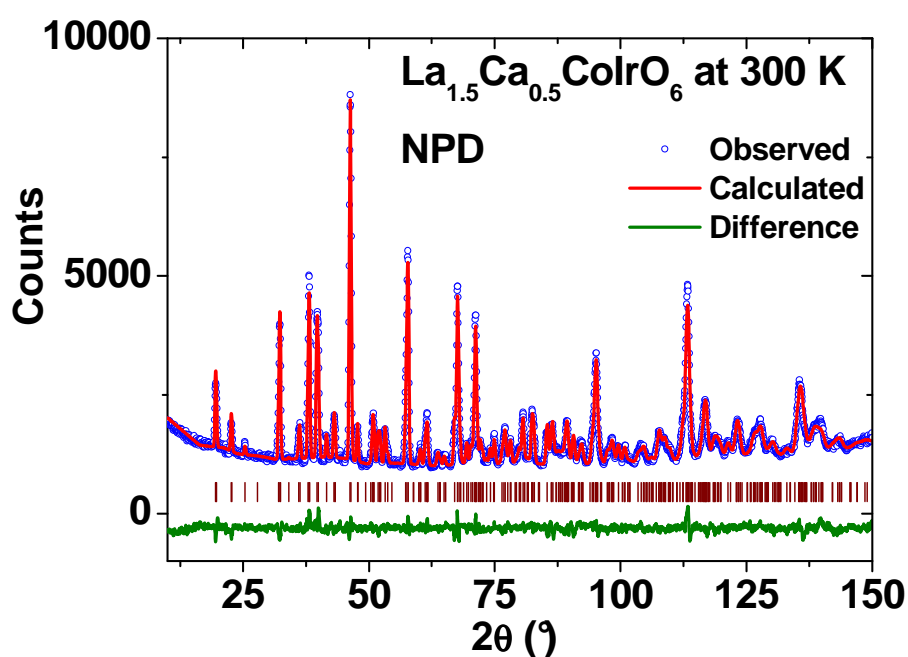


Fig. 5.39: Room temperature neutron powder diffraction (NPD) pattern of $\text{La}_{1.5}\text{Ca}_{0.5}\text{CoIrO}_6$ with the calculated pattern.

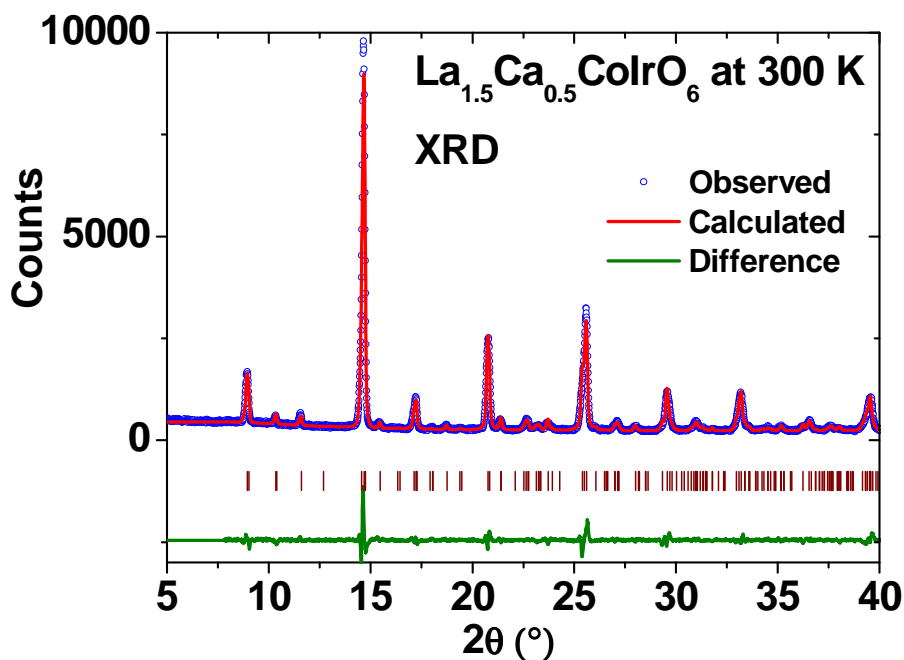


Fig. 5.40: Room temperature x-ray diffraction (XRD) pattern of $\text{La}_{1.5}\text{Ca}_{0.5}\text{CoIrO}_6$ with the calculated pattern.

Both of the compounds $x=0.5$ and $x=0.75$ crystallize with a monoclinic symmetry at room temperature and at 4K in the space group $P2_1/n$ as in the case of $x=0$ ($\text{La}_2\text{CoIrO}_6$). No phase transition takes place up to $x \leq 0.75$. For both $x=0.5$ and 0.75 the tolerance factor f is clearly less than 0.97 and thus fulfils this empirical rule for monoclinic symmetry. The structural parameters together with the space groups and tolerance factors are listed in Table 5.14. The atomic coordinates of the two different compositions are given in appendix 2. In contrast to the $\text{La}_{2-x}\text{Sr}_x\text{CoIrO}_6$ system a clear trend of monotonic decreasing lattice parameters is seen with increasing Ca substitution. This is most probably due to the fact that this system has only the band filling degree of freedom due to hole doping in contrast to the LaSr system, which has an additional degree of freedom through the size effect (A site), thus the resulting lattice parameters are a consequence of the two correlated degrees of freedom in the LaSr system.

Table 5.14: Space groups and structural parameters of $\text{La}_{2-x}\text{Ca}_x\text{CoIrO}_6$ at room temperature.

x	Space group	f	a (Å)	b (Å)	c (Å)	β (°)
0	$P2_1/n$	0.8682	5.5819(1)	5.6576(1)	7.9078(2)	89.98(1)
0.5	$P2_1/n$	0.8748	5.5459(1)	5.6108(1)	7.8580(1)	89.987(9)
0.75	$P2_1/n$	0.8781	5.5330(1)	5.5872(1)	7.8374(2)	89.99(1)

In fig. 5.41 the average bond lengths of Co-O and Ir-O are shown, which were calculated using the software Diamond [113]. As a comparison the bond lengths of the LaSr system are also shown. From fig. 5.41 it is evident that both systems differ in their behaviour upon doping. Whereas as already seen in section 5.1.1, the holes are predominantly introduced to the d bands of Ir upon Sr substitution up to $x \leq 1.5$ in the $P2_1/n$ phase, for the LaCa case up to $x \leq 0.5$ holes are introduced to the d bands of Ir, but further Ca substitution introduces holes predominantly to the d bands of Co^{2+} . This partial oxidation of Co^{2+} is reflected in the sudden decrease of the Co-O bond length for $x=0.75$. This can also be seen from the calculated bond valence sums (BVS) for the LaCa system shown in table. 5.15, where a significant change to the BVS of Ir can be seen for $x=0 \rightarrow x=0.5$ but for $x=0.5 \rightarrow x=0.75$ only the BVS of Co changes significantly.

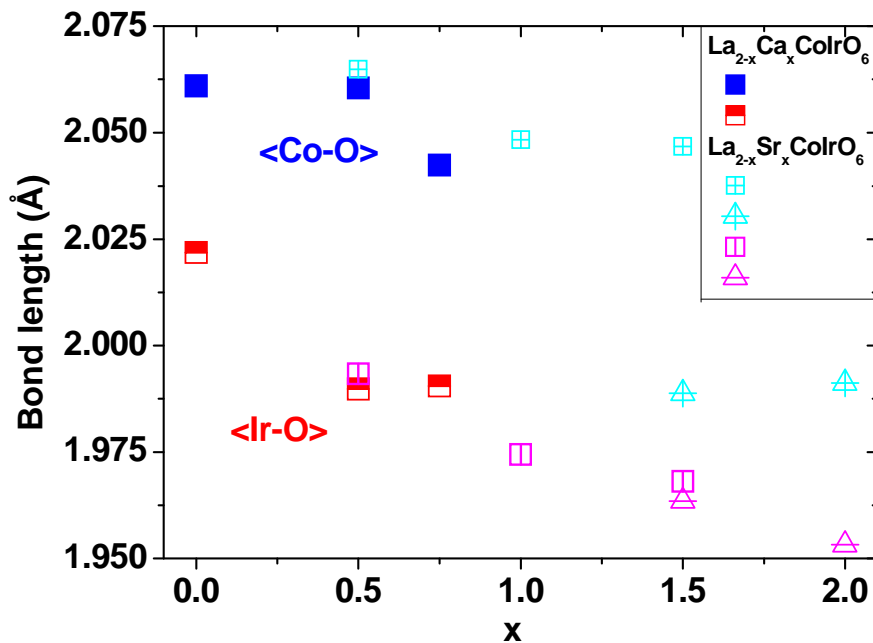


Fig 5.41: Composition dependence of Co-O and Ir-O bond lengths of $\text{La}_{2-x}\text{Ca}_x\text{CoIrO}_6$. As a comparison the bond lengths of $\text{La}_{2-x}\text{Sr}_x\text{CoIrO}_6$ are also shown.

Table 5.15: Bond valence sums calculated from Co-O and Ir-O at room temperature for $\text{La}_{2-x}\text{Ca}_x\text{CoIrO}_6$.

x	BVS [$r_0(\text{Co}^{2+}-\text{O}^{2-})$]	BVS [$r_0(\text{Co}^{3+}-\text{O}^{2-})$]	BVS [$r_0(\text{Ir}^{4+}-\text{O}^{2-})$]	BVS [$r_0(\text{Ir}^{5+}-\text{O}^{2-})$]
0	2.22	2.26	3.98	4.52
0.5	2.22	2.26	4.34	4.92
0.75	2.34	2.39	4.35	4.93

5.8.2 Magnetic properties of $\text{La}_{2-x}\text{Ca}_x\text{CoIrO}_6$

The temperature dependence of magnetization of $\text{La}_{2-x}\text{Ca}_x\text{CoIrO}_6$ in an external field of 0.05 T reveals that the magnetic ordering temperature decreases from around 100K for $x=0$ (polycrystalline sample) to a value around 50 K for $x=0.5$ and 0.75, as shown in fig. 5.42. The specific magnetization is reduced more than one order of magnitude with increasing substitution of La by Ca. Differences between magnetizations in field-cooled (FC) and zero-field cooled mode (ZFC) are also observed for $x=0.5$ and 0.75, indicating the presence of ferromagnetic components, confirmed by the hysteresis loops in fig. 5.43, obtained at 5 K in external magnetic fields up to 6 T. The spontaneous magnetization, determined by linear extrapolation of the high-field dependence of magnetization to zero field (Table 5.5), is also reduced more than one order of magnitude with increasing substitution of La by Ca. Nevertheless, the spontaneous magnetization of $x=0.5$ is of the same magnitude as $x=0$.

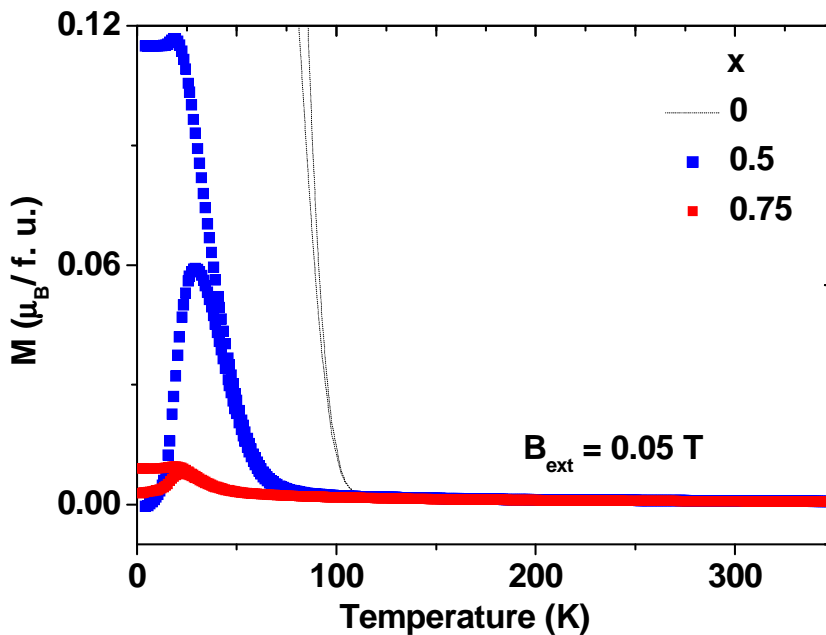


Fig. 5.42: Temperature dependence of magnetization for $\text{La}_{2-x}\text{Ca}_x\text{CoIrO}_6$. The dotted curve belongs to $\text{La}_2\text{CoIrO}_6$.

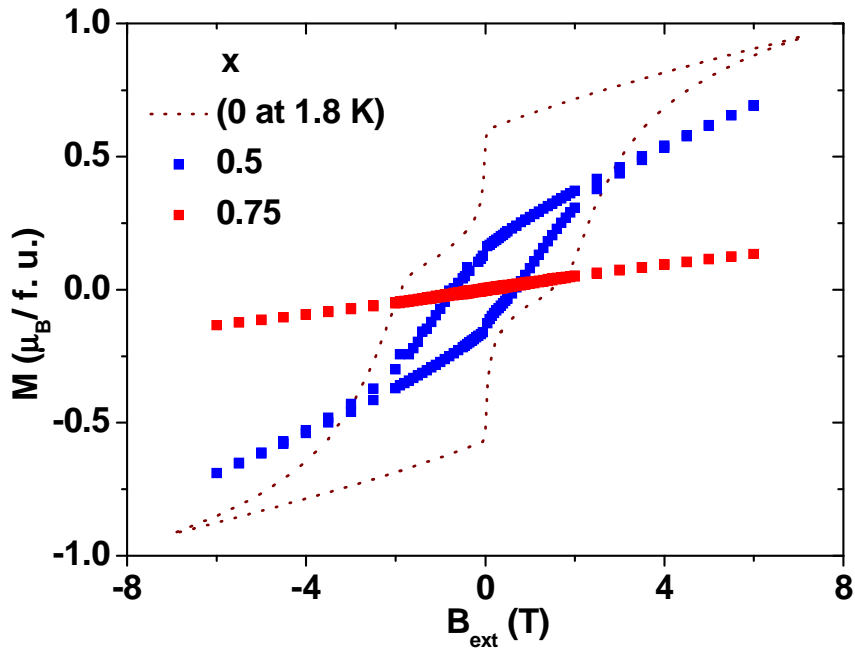


Fig. 5.43: Field dependence of magnetization for $\text{La}_{2-x}\text{Ca}_x\text{CoIrO}_6$. The dotted hysteresis belongs to $\text{La}_2\text{CoIrO}_6$.

Curie-temperatures are determined using the linear extrapolation method and they decrease from 95 K for $x=0$ (polycrystalline) to 70 K for $x=0.5$ and 61 K for $x=0.75$ with increasing Ca substitution (table 5.16). The Ca substituted compounds have somewhat smaller Curie-temperatures than the Sr substituted ones. The size degree of freedom that controls the bandwidth through the bond angles, which is additionally varied in the Sr substituted compounds, may be the reason for this difference. The paramagnetic Curie-Weiss temperatures θ , determined from the Curie-Weiss fits, are negative for $x=0.5$ and 0.75 , indicating dominant antiferromagnetic interactions, which does not change significantly between $x=0.5$ and 0.75 (table 5.16). The low values for the ferromagnetic components and the strong antiferromagnetic interactions are an indication for non-collinear magnetism (NCM). Magnetizations are not saturated at 6 T, further supporting the proposed NCM. The compound with $x=0.5$ also shows the typical form of the hysteresis, which is attributed to spin reorientation transition as in the case of $\text{La}_2\text{CoIrO}_6$, although the effect is less significant. The compound with $x=0.75$ does not show this behaviour. The effective magnetic moments μ_{eff} of $x=0.5$ and 0.75 were calculated from the Curie constants and are compared with the value obtained for $x=0$. With increasing Ca substitution, μ_{eff} increases from $4.7 \mu_B / \text{f. u.}$ for $x=0$ to $5.3 \mu_B / \text{f. u.}$ for $x=0.5$ and to $5.1 \mu_B / \text{f. u.}$ for $x=0.75$. As in the case of $\text{La}_{2-x}\text{Sr}_x\text{CoIrO}_6$, the

experimentally determined values for μ_{eff} are larger than the calculated spin-only values (table. 5.16), indicating significant contributions to the paramagnetic moments from Ir and/or orbital momentum.

Table 5.16: Ferromagnetic Curie-temperature T_C , paramagnetic Curie-Weiss temperature θ , spontaneous magnetization M_S , experimentally determined and calculated effective magnetic moments μ_{eff} and $\mu_{\text{eff}}(\text{Co-spin only})$

x	μ_{eff} (μ_B / f. u.)	$\mu_{\text{eff}}(\text{Co-spin only})$ (μ_B / f. u.)	Θ (K)	M_S (μ_B / f. u.)	T_C (K) (linear extrapolation)
0	4.7(1)	3.88 (Co^{2+})	-13.8(6)	0.70	95
0.5	5.3(1)		-70.2(1)	0.23	70
0.75	5.1(0)		-76.5(1)	0.01	61

In order to investigate the underlying magnetic ordering, neutron powder diffraction patterns are recorded for $x=0.5$ and 0.75 at 4 K and at room temperature. They are shown in fig. 5.44 (a)-(d). It should be mentioned that the first two ambiguities discussed in section 5.3 are valid in the present system too.

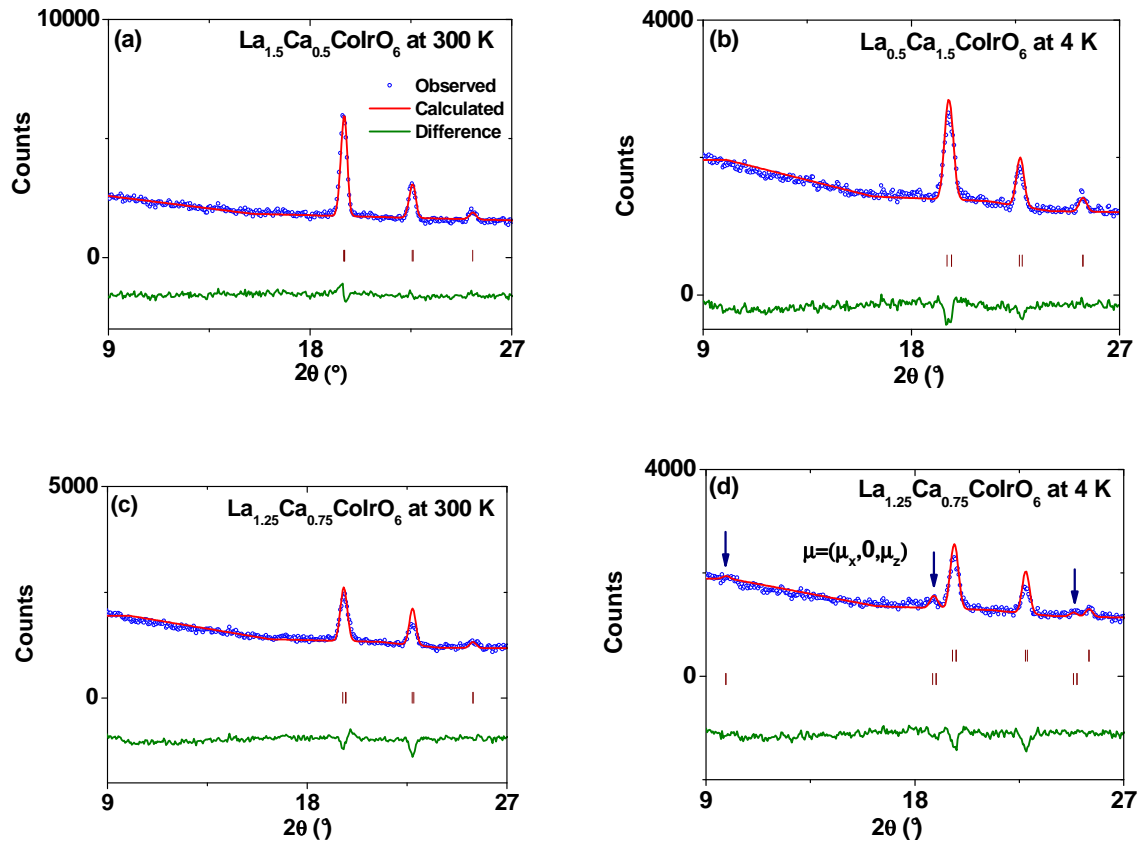


Fig. 5.44: Observed, calculated and difference low angle region Rietveld profiles for $x=0.5$ and 0.75 at room temperature (a), (c) and at 4 K (b), (d), where prominent magnetic superstructure Bragg reflections were present. Reflection markers correspond to the positions of Bragg reflections of structural (top) and magnetic (bottom) contributions.

For the $x=0.5$ case no magnetic Bragg reflections are found at 4 K, whereas for $x=0.75$ weak magnetic Bragg reflections are found, that could be indexed by the propagation vector $k=(1/2,0,1/2)$. Furthermore, the best agreement with the diffraction pattern in terms of the intensity (of the magnetic Bragg reflections) is obtained for the refinement of x and z components of the AFM moment of Co. The (AFM) moment of Co is $\mu=(1.5(1),0,0.5(1)) \mu_B/\text{Co}$ with $|\mu|=1.6(1) \mu_B$ for $x=0.75$. As in the case of $\text{La}_{2-x}\text{Sr}_x\text{CoIrO}_6$, there is a magnetic phase transition from the $k=(0,0,0)$ AFM structure of $x=0$ to the $k=(1/2,0,1/2)$ AFM structure of $x=0.75$. In the compound $x=0.5$ competing NN and NNN interactions lead to a frustration, thus no magnetic Bragg reflections are found. Even for the $x=0.75$ case, assuming a partially oxidated Co^{2+} state (see fig. 5.41), there should be three unpaired electrons resulting in a magnetic moment of $3 \mu_B$. Even considering hybridization effects, the magnetic moment at the Co site should be larger than $2 \mu_B$. Therefore, the obtained AFM moment of 1.6μ for $x=0.75$ is also due to a frustration. The composition dependent magnetic phase transition from

the $k=(0,0,0)$ AFM structure to the $k=(1/2,0,1/2)$ AFM structure with a totally frustrated transition zone ($x=0.5$ in both cases) seems to be a common feature of both $\text{La}_{2-x}\text{Sr}_x\text{CoIrO}_6$ and $\text{La}_{2-x}\text{Ca}_x\text{CoIrO}_6$ systems. As the band filling degree of freedom is active in both systems, this can be attributed to the hole doping.

5. 8. 3. Transport properties of $\text{La}_{2-x}\text{Ca}_x\text{CoIrO}_6$

It is evident from fig. 5.45 (a) that all samples in this system show a non-metal like behaviour similar to the $\text{La}_{2-x}\text{Sr}_x\text{CoIrO}_6$ system. But the resistivity is reduced by almost two orders of magnitude at room temperature, when La is substituted by Ca on the A-site in contrast to the Sr substitution. In order to understand the underlying transport mechanism, $\ln \rho$ vs $1/T^{1/4}$ and $\ln \rho$ vs $1/T$ plots are made and they are shown in fig. 5.45 (b).

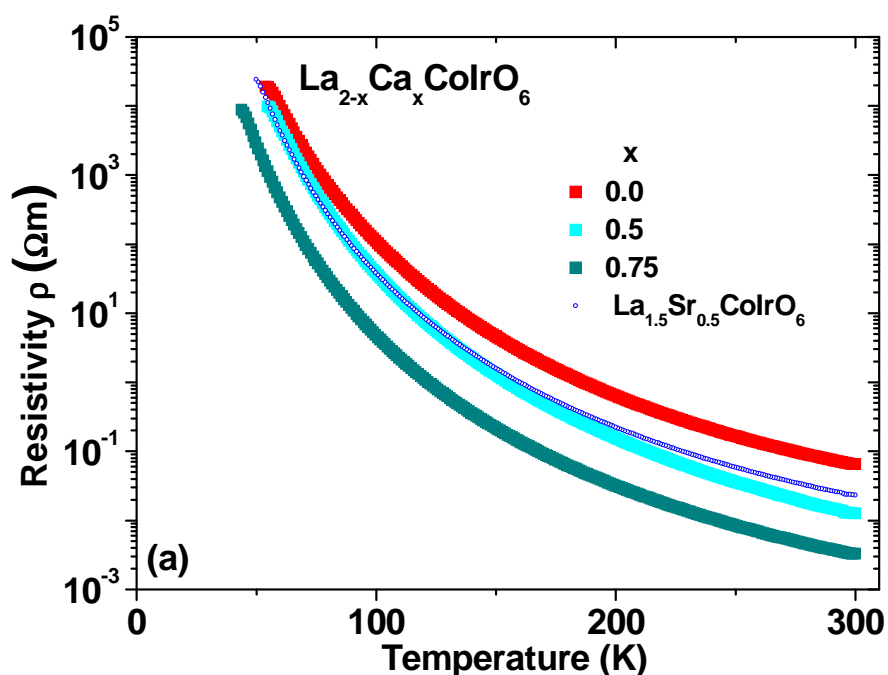


Fig. 5.45(a): Temperature dependence of resistivity for $x=0, 0.5$ and 0.75 in logarithmic scale ($x=0.5$ of the LaSr system is also shown).

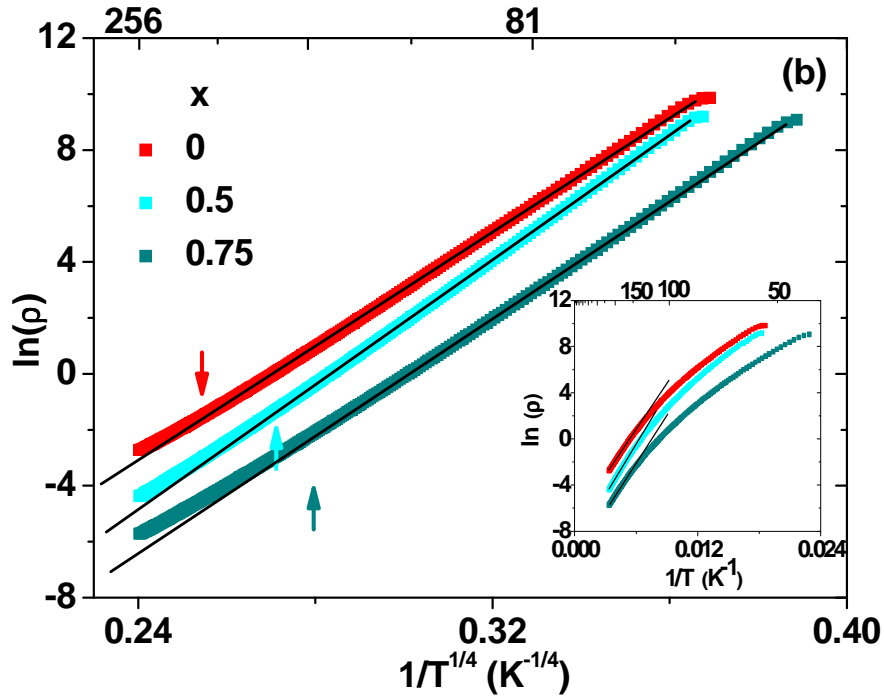


Fig. 5.45(b): A linear fit of $\ln(\rho)$ vs $1/T^{1/4}$ and $\ln(\rho)$ vs $1/T$ describes the low-temperature and high temperature behaviour, respectively. The arrows mark the maximum temperature, up to which a linear dependence is well obeyed.

Similar to the $\text{La}_{2-x}\text{Sr}_x\text{CoIrO}_6$ system, a combination of the thermal activation and VRH behaviour is needed to describe the experimental data over the whole temperature range, where the high temperature range is better described by the former and the low temperature range is better described by the latter. The activated (band) gaps E_G , which were determined by the non-linear regression and the average bond angles, are shown in table 5.17.

Table 5.17: Band gaps together with the average Co-O-Ir bond angles at 4 (3 K for $x=0$) K and at room temperature.

x	Average bond angle		Band gap E_g (eV)
	at 4 (3) K ($^\circ$)	at RT ($^\circ$)	
0	152.46	152.74	0.26
0.5	152.75	153.15	0.29
0.75	153.66	154.03	0.27

As the size degree of freedom is eliminated in the $\text{La}_{2-x}\text{Ca}_x\text{CoIrO}_6$ system, a change in the averaged Co-O-Ir bond angles is negligible with increasing Ca substitution and accounts for

only around 1° for $x=0 \rightarrow x=0.75$ (table 5.17). In the $\text{La}_{2-x}\text{Sr}_x\text{CoIrO}_6$ system such an amount of substitution results in an increase of around 6° in the Co-O-Ir bond angle (table 5.9). But the interesting aspect concerns the substitution dependency of the band gap. Although holes are introduced to the B sites with increasing Ca substitution, the band gap, which in this system is a consequence of electron-electron repulsion, is almost constant or even increases slightly from 0.26 eV for $x=0$ to 0.27 eV for $x=0.75$. This is in contrast to the Sr substitution, where the band gap has decreased from 0.26 eV for $x=0$ to 0.12 eV for $x=1$. The reason for this difference lies within the additional size degree of freedom in $\text{La}_{2-x}\text{Sr}_x\text{CoIrO}_6$, which influences the bond angles, which in turn determine the band width of Co and Ir. With increasing Sr substitution the deviation of the bond angles from 180° becomes smaller, thus it favours delocalization, which is manifested in the band width. Although the hole doping would reduce the electron-electron repulsion especially at lower (hole) doping levels, provided that the size degree of freedom with significant effects exists, this would dominate over the band filling degree of freedom. At lower level of hole doping in $\text{La}_{2-x}\text{Ca}_x\text{CoIrO}_6$, although the number of electrons are reduced, the constant distortion of the bond angles (especially in lower symmetry crystal structures as in the present case) will limit the size of the band width, which in turn would enhance the electron-electron repulsion and the splitting of the bands.

6. Summary

The series $\text{La}_{2-x}\text{Sr}_x\text{CoIrO}_6$ is a suitable model system to investigate the effect of structural and chemical degrees of freedom on the resulting physical properties of double perovskites. Depending on the temperature and composition the following sequence of phase transitions is observed in this series: $P2_1/n \leftrightarrow P2_1/n + I2/m \leftrightarrow I2/m \leftrightarrow I4/m \leftrightarrow Fm-3m$. Whereas the phase transition between the monoclinic phases is of first order, the phase transitions between monoclinic ($I2/m$) and tetragonal and between tetragonal and cubic phases are of second order in nature. Changes in the oxidation states of both Co from Co^{2+} to Co^{3+} and Ir from Ir^{4+} to Ir^{5+} are concluded from the variation of the Co-O and Ir-O bond lengths, trends within the Bader charges, bond valence sums (BVS) and atomic sphere integration. Whereas $\text{Ir}^{4+} \rightarrow \text{Ir}^{5+}$ takes place gradually within the $P2_1/n$ phase and does not change significantly in the $I2/m$ phase, the $\text{Co}^{2+} \rightarrow \text{Co}^{3+}$ takes place abruptly in the $I2/m$ phase at the phase boundary of $P2_1/n/I2/m$ at $x=1.5$. Concerning the magnetic structures, three different types of them are discussed with respect to electronic structure calculations. With increasing Sr substitution, there is a transition from a stronger nearest neighbour (NN) AFM exchange interaction for $x=1$ to a stronger next nearest neighbour (NNN) AFM exchange interaction for $x \geq 1$. Competing interactions lead to NCM, most pronounced in $\text{La}_2\text{CoIrO}_6$. With increasing Sr-content, however, the ferromagnetic components are considerably reduced, so that the collinear approximations become more and more appropriate with increasing x . A reduction of the band gap is established with increasing Sr-content from 0.26 eV for $x=0$ to 0.05 for $x=1.5$, and a significant influence of B/B'-site cation disorder on the electronic transport properties is proposed based on the results for $\text{Sr}_2(\text{Co}_{0.85}\text{Ir}_{0.15})(\text{Ir}_{0.85}\text{Co}_{0.15})\text{O}_6$ ($x=2$). These gaps are the consequence of strongly correlated motion of the electrons due to strong onsite electron-electron Coulomb repulsion, which is confirmed by the fact that the band gap in the DOS could only be realized by applying an additional orbital dependent potential term U for the correlated 3d and 5d orbitals. Special attention is diverted towards $\text{La}_2\text{CoIrO}_6$. For this composition electronic structure calculations were performed for both AFM and FM configurations, which gave very similar total energies and thus support NCM by a sensitive preference of one of the possible states. Spin reorientation transition are found in single crystals of $\text{La}_2\text{CoIrO}_6$, which could be attributed to local minima in the angular dependence of the total energy, calculated from the non collinear arrangement of the magnetic moments of cobalt using the software code WIENNCM. The band gaps and d-band occupations are almost similar to the reported ones for collinear configurations. The above results are compared with

the system $\text{La}_{2-x}\text{Ca}_x\text{CoIrO}_6$, which has only the band filling degree of freedom due to similar ionic radii of La^{3+} and Ca^{2+} . But single phase samples were obtained only for $x \leq 0.75$. The most significant similarity between the systems is the magnetic phase transition from dominant NN AFM interaction to NNN AFM interaction. But they differ in the change of the oxidation states of Co and Ir upon Sr/Ca substitution. Especially the reduction of the band gap upon Sr substitution is attributed to the size degree of freedom, which influences the bandwidth of 3d Co and 5d Ir, whereas the band gap hardly changes through low level hole doping upon Ca substitution. The low level hole doping seems to be not enough to reduce the electron-electron repulsion significantly, as the bandwidth is limited by the eliminated size degree of freedom in the LaCa system (which is almost constant as the Co-O-Ir bond angles are almost constant) upon Ca substitution.

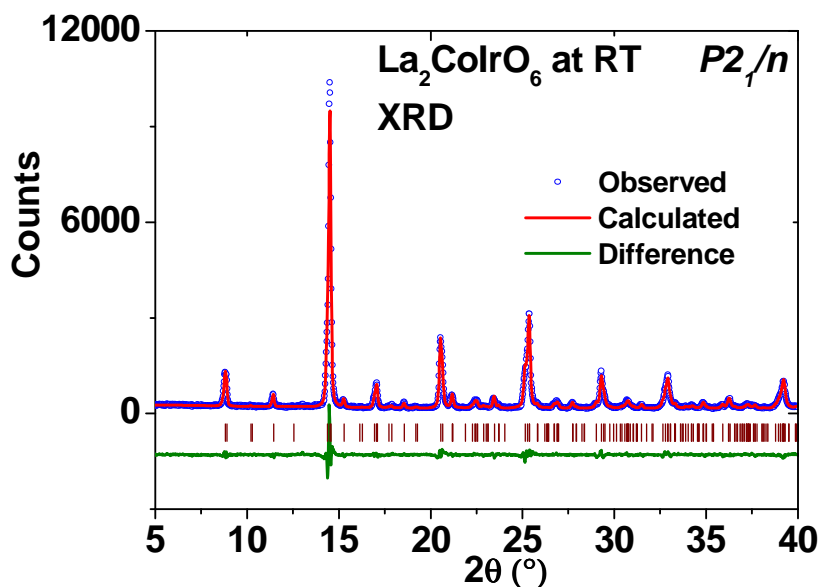
In another work the oxygen deficiency of $\text{Sr}_2\text{CoIrO}_{6-\delta}$ is varied in argon flow. These results can be compared with the results of the most related oxygen deficiency system $\text{Sr}_2\text{CoMoO}_{6-\delta}$. On one hand $\text{Sr}_2\text{CoIrO}_{6-\delta}$ undergoes a structural phase transition from $I2/m \rightarrow I4/m$ upon oxygen removal at room temperature (as prepared $\text{Sr}_2\text{CoMoO}_6$ crystallizes in $I4/m$) and on the other hand electrons are pumped into the B sites upon oxygen removal. For $\text{Sr}_2\text{CoMoO}_{6-\delta}$ this would slowly fill the empty d bands of Mo^{6+} . This leads to a delocalized ferromagnetic interaction. For $\text{Sr}_2\text{CoIrO}_{6-\delta}$ however there are already four 5d electrons before the oxygen removal and more electrons through this removal would increase the electron-electron interaction, thus the AFM structure is retained.

7. Outlook

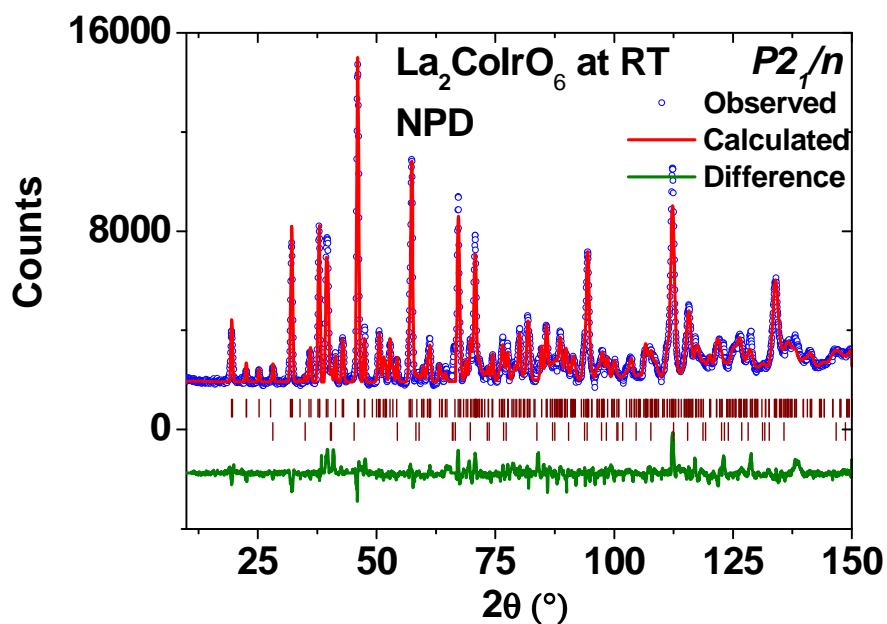
Even after the thorough experimental and theoretical investigation of the system, a few open questions remain: The most important one is about the spin state of Co in $\text{La}_2\text{CoIrO}_6$. Whereas a magnetic moment of $1.7 \mu_{\text{B}}$ is obtained from NPD, the GGA and GGA+U(FLL) tend to prefer a HS state for Co. In collinear calculations, a IS state for Co could be stabilized with the AMF flavour of GGA+U, whereas in NCM calculations this IS state could not be realized. Even the derivation of the spin state of Co from magnetic entropy contribution, which is in turn determined from the magnetic contribution to the specific heat capacity, gives two options: IS or HS state for Co. Neutron diffraction on single crystals should be carried out in order to compare the AFM component with the results from NPD. Furthermore, spectroscopic methods such as XES should also be applied to obtain more information on the spin state of Co. Another challenge encountered is the magnitude of the magnetic moment of Ir, which is too small to be detected from NPD. Methods such as XMCD should be therefore applied to determine the magnetic moment of Ir, which could be compared with the magnetic moments predicted by DFT calculations.

8. Appendix

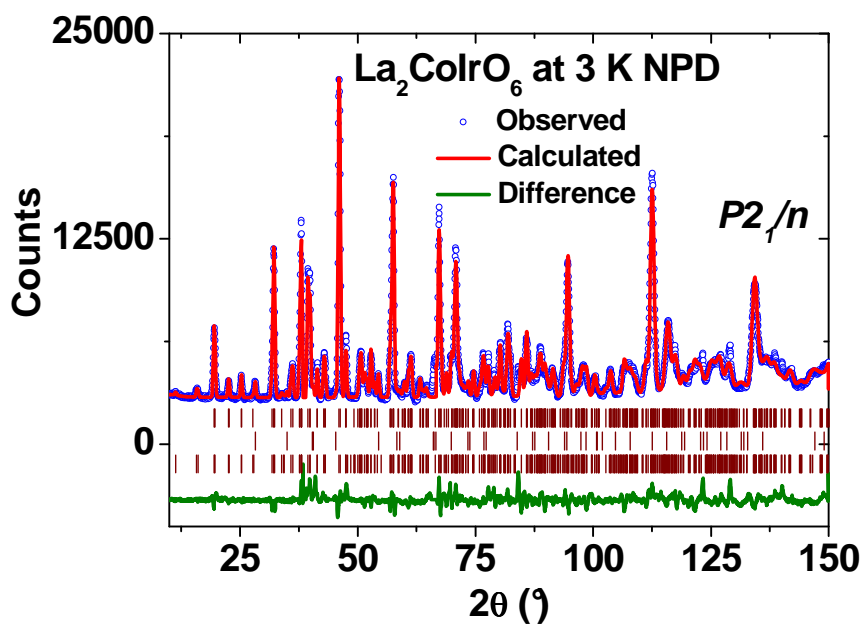
Appendix 1: X-ray and neutron diffraction patterns with calculated intensities



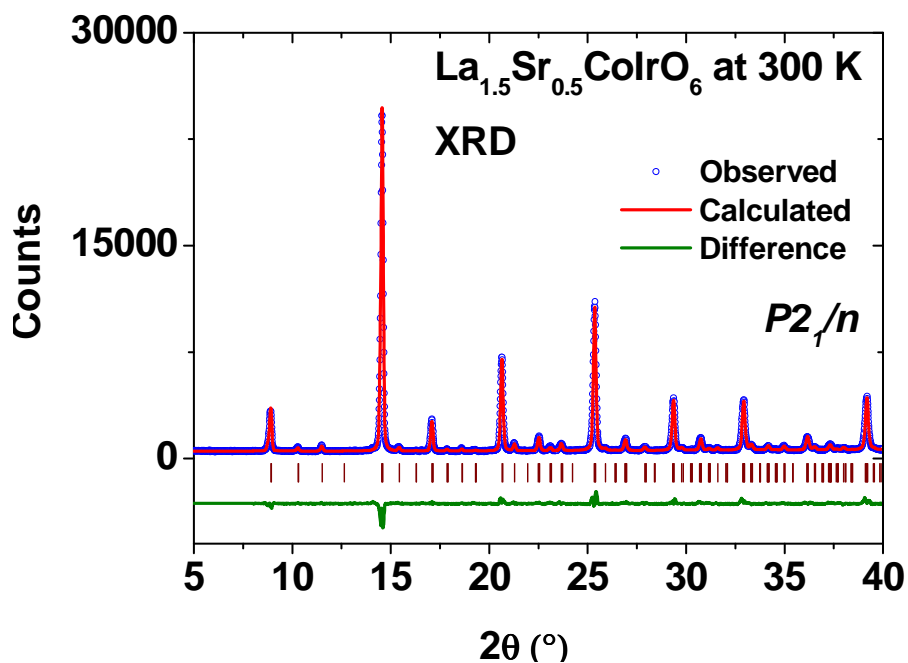
A 1.1: X-ray Diffraction pattern of La₂CoIrO₆ at room temperature.



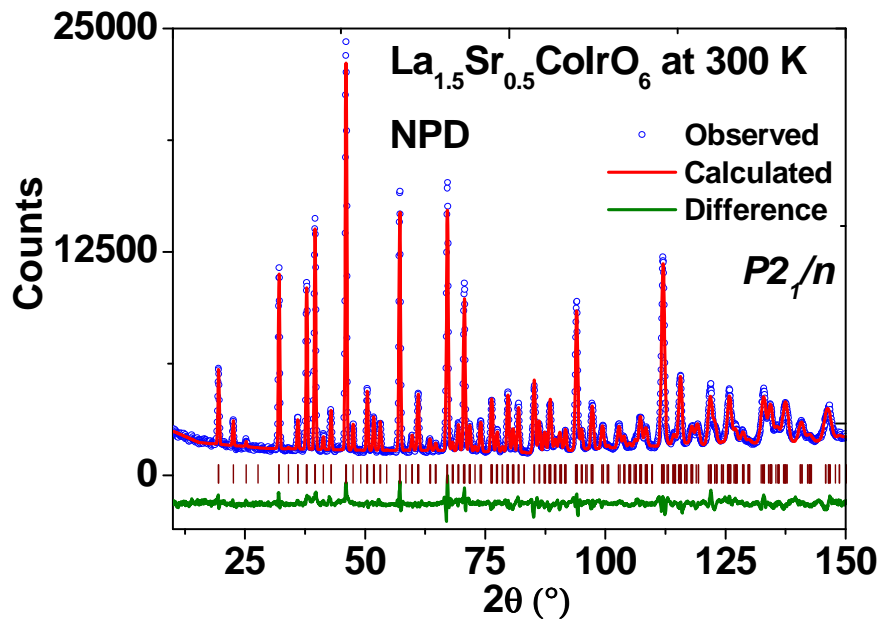
A 1.2: Neutron diffraction pattern of La₂CoIrO₆ at room temperature. Reflection markers correspond to the positions of Bragg reflections of the compound (top) and IrO₂ impurity (bottom) contributions



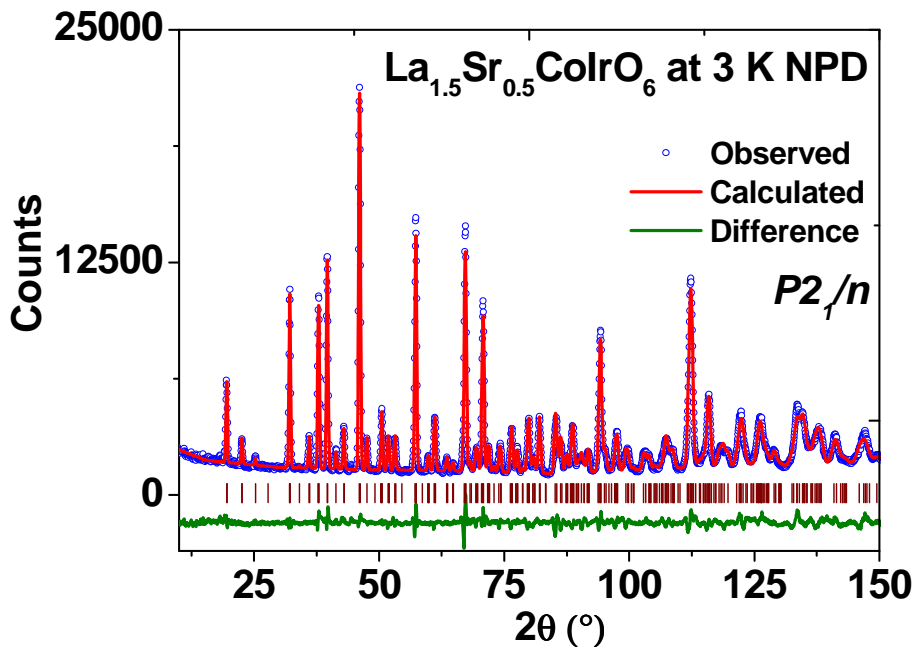
A 1.3: Neutron diffraction pattern of La₂CoIrO₆ at 3K. Reflection markers correspond to the positions of Bragg reflections of the compound (top), IrO₂ impurity (middle) and the magnetic (bottom) contributions.



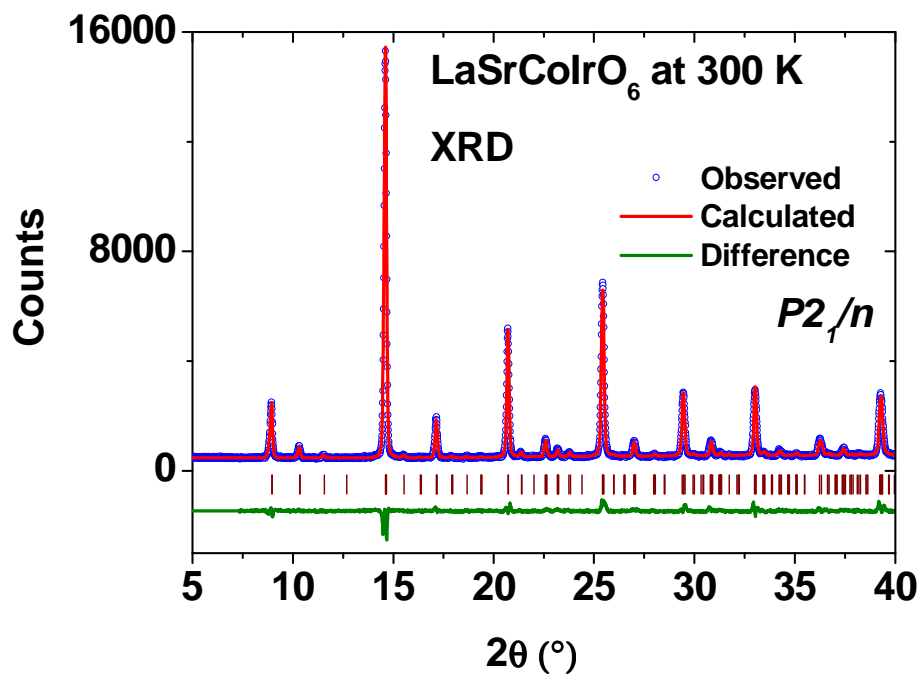
A 1.4: X-ray Diffraction pattern of La_{1.5}Sr_{0.5}CoIrO₆ at room temperature.



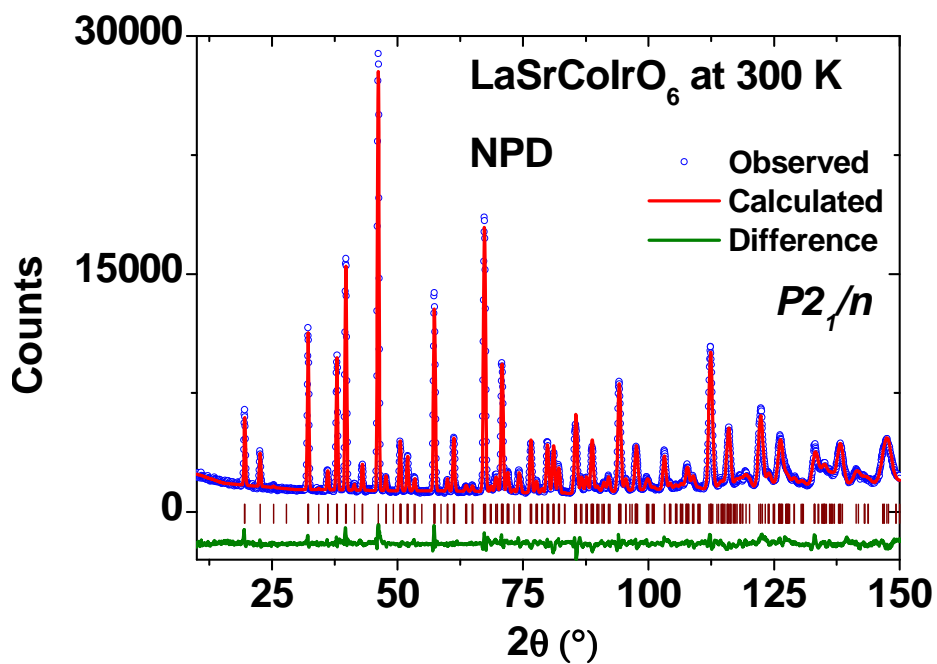
A 1.5: Neutron diffraction pattern of $\text{La}_{1.5}\text{Sr}_{0.5}\text{CoIrO}_6$ at room temperature.



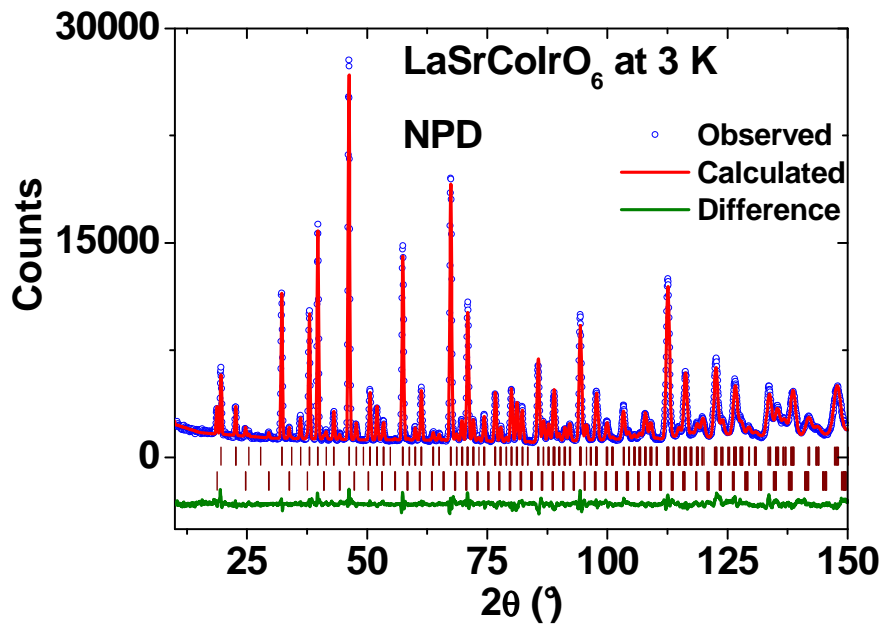
A 1.6: Neutron diffraction pattern of $\text{La}_{1.5}\text{Sr}_{0.5}\text{CoIrO}_6$ at 3K.



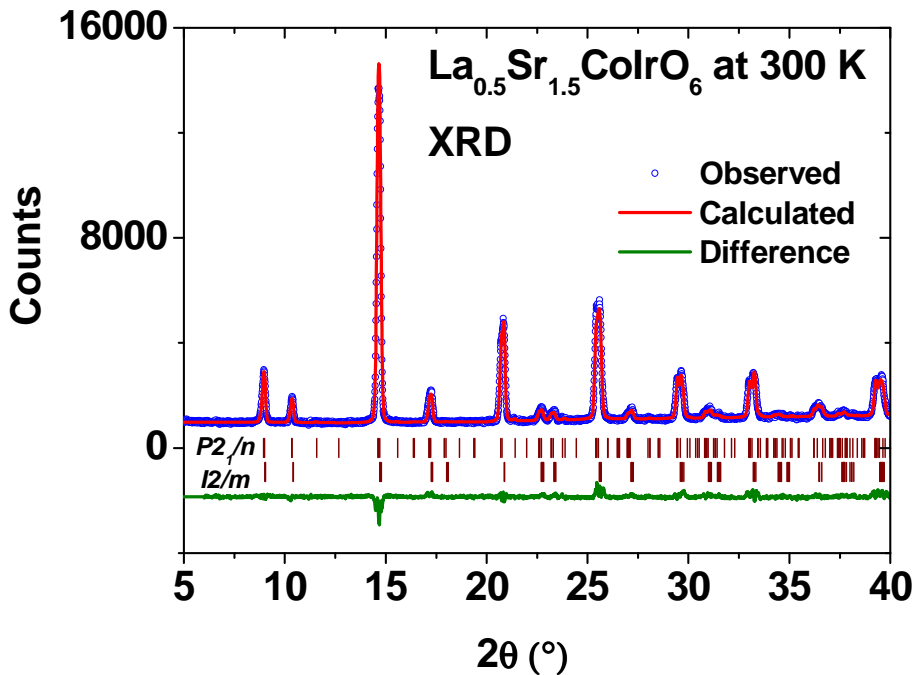
A 1.7: X-ray Diffraction pattern of LaSrCoIrO₆ at room temperature.



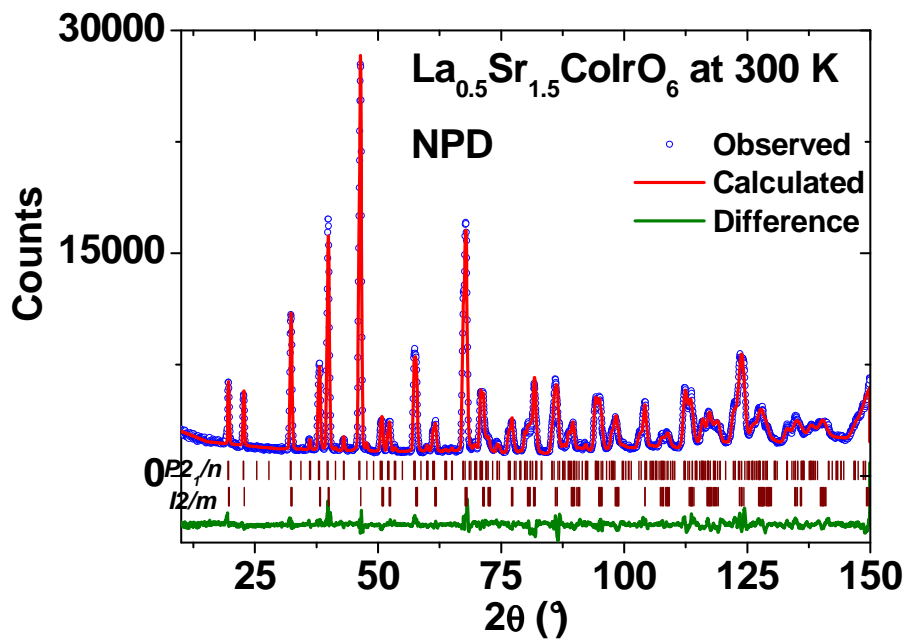
A 1.8: Neutron diffraction pattern of LaSrCoIrO₆ at room temperature.



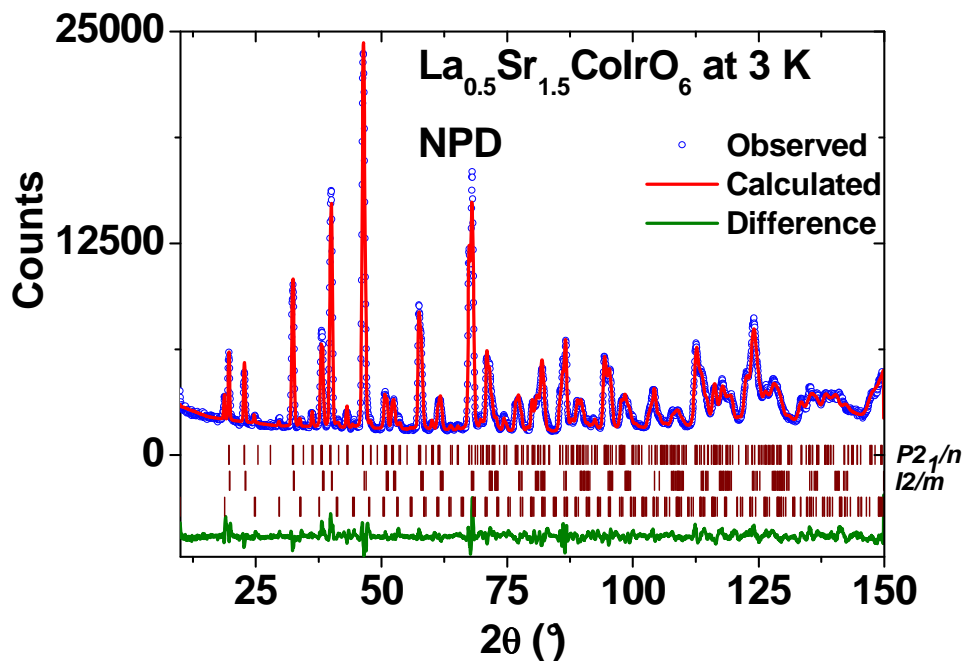
A 1.9: Neutron diffraction pattern of LaSrCoIrO₆ at 3K. Reflection markers correspond to the positions of Bragg reflections of the structural (top) and the magnetic (bottom) contributions.



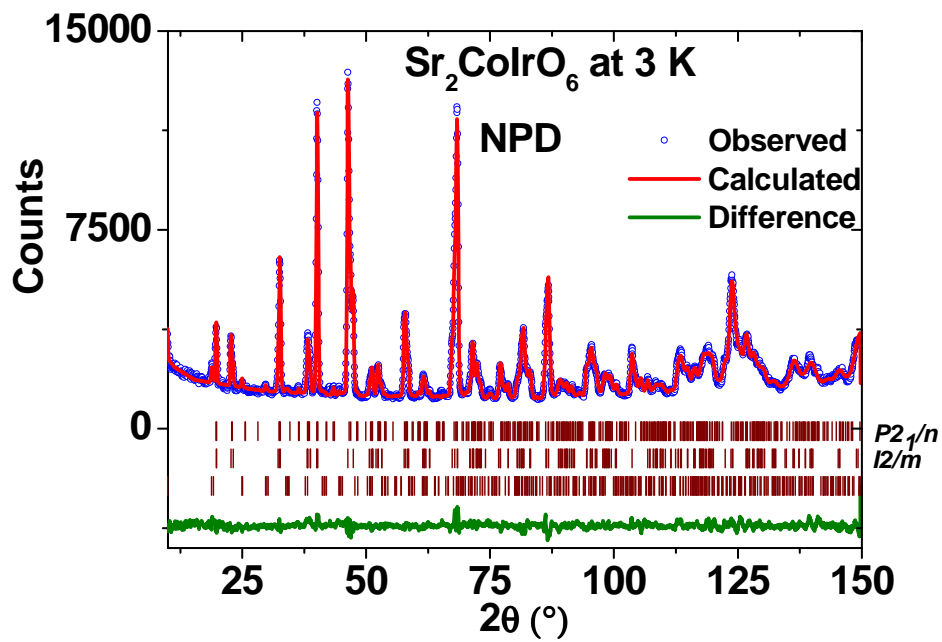
A 1.10: X-ray Diffraction pattern of La_{0.5}Sr_{1.5}CoIrO₆ at room temperature. Reflection markers correspond to the positions of Bragg reflections of the *P*2₁/*n* (top) and the *I*2/*m* (bottom) phases.



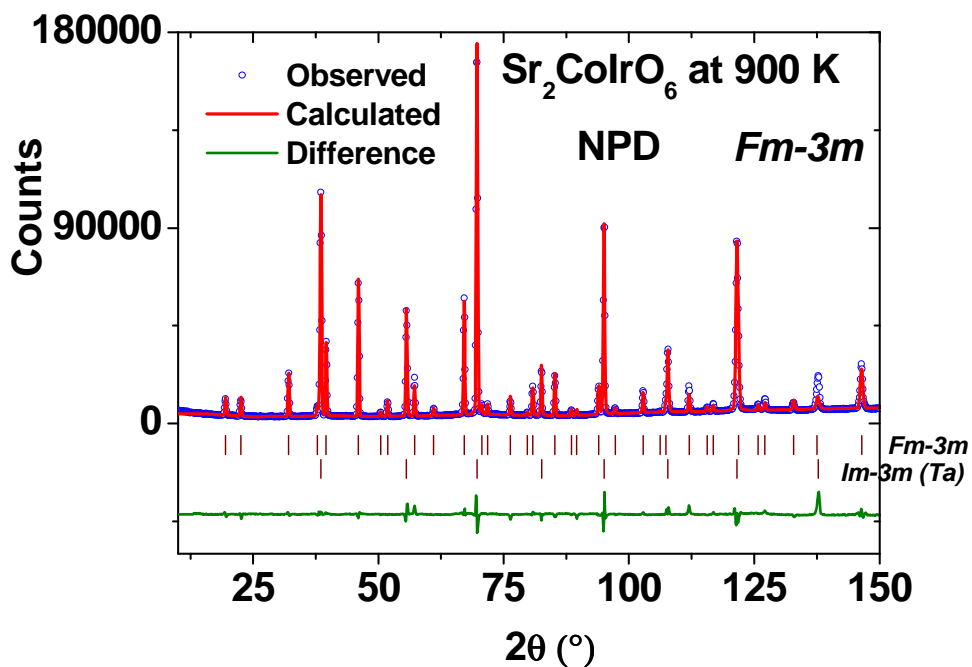
A 1.11: Neutron diffraction pattern of $\text{La}_{0.5}\text{Sr}_{1.5}\text{CoIrO}_6$ at room temperature. Reflection markers correspond to the positions of Bragg reflections of the $P2_1/n$ (top) and the $I2/m$ (bottom) phases.



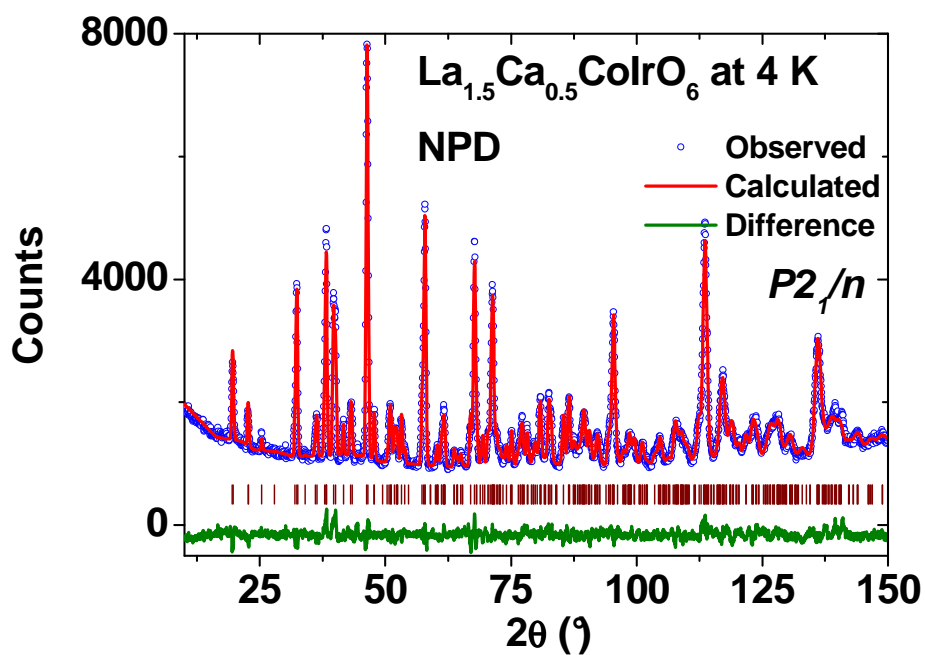
A 1.12: Neutron diffraction pattern of $\text{La}_{0.5}\text{Sr}_{1.5}\text{CoIrO}_6$ at 3K. Reflection markers correspond to the positions of Bragg reflections of the $P2_1/n$ (top) phase, the $I2/m$ (middle) phase and the magnetic contribution (bottom).



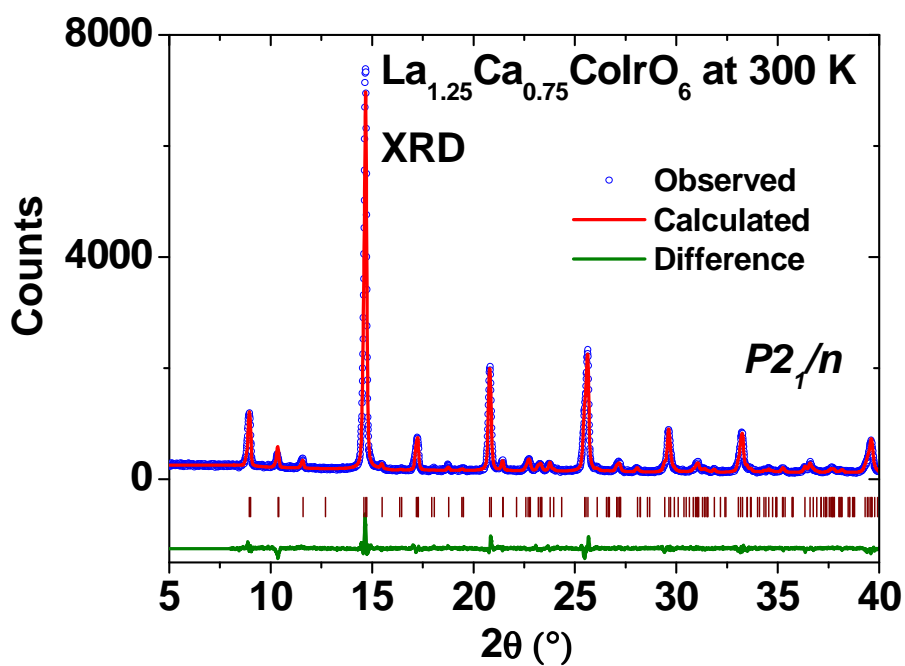
A 1.13: Neutron diffraction pattern of Sr₂CoIrO₆ at 3K. Reflection markers correspond to the positions of Bragg reflections of the *P2₁/n* (top) phase, the *I2/m* (middle) phase and the magnetic contribution (bottom).



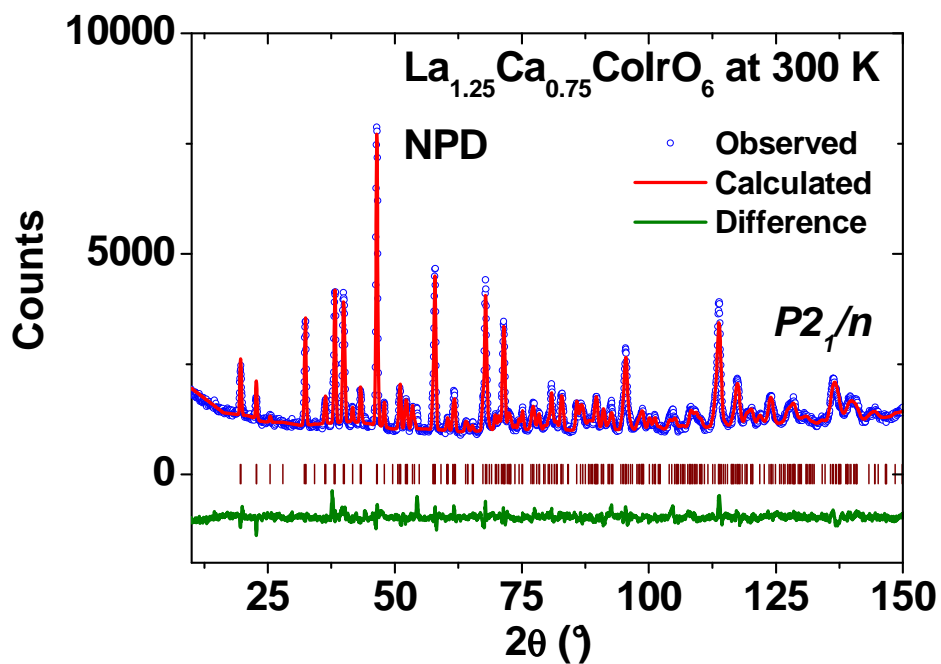
A 1.14: Neutron diffraction pattern of Sr₂CoIrO₆ at 900K. Reflection markers correspond to the positions of Bragg reflections of the structural (top) and Ta capsule (bottom) contributions.



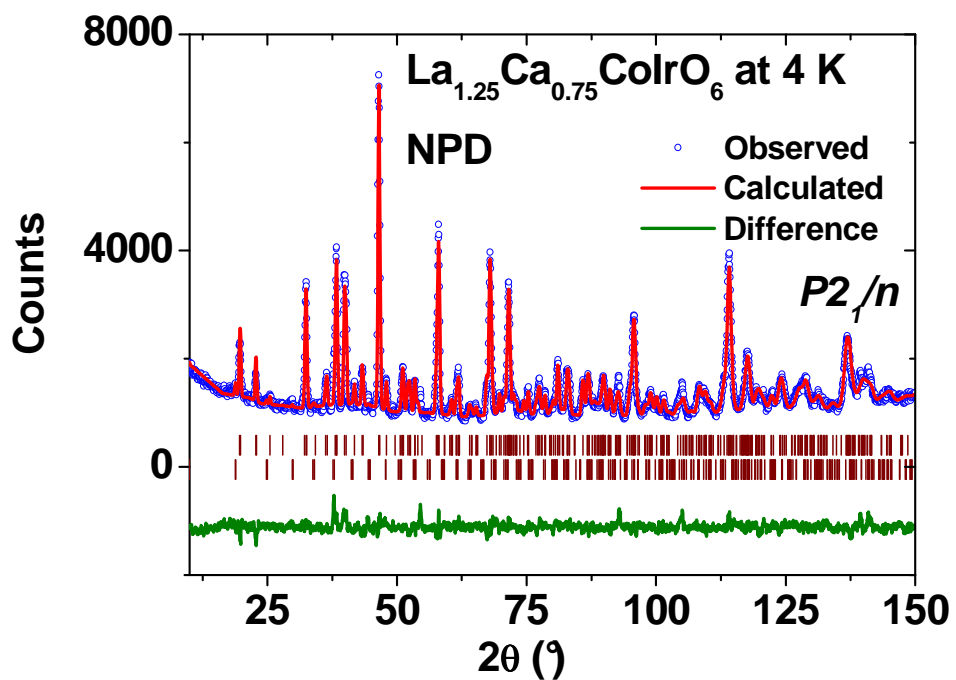
A 1.15: Neutron diffraction pattern of $\text{La}_{1.5}\text{Ca}_{0.5}\text{CoIrO}_6$ at 4K.



A 1.16: X-ray Diffraction pattern of $\text{La}_{1.5}\text{Ca}_{0.5}\text{CoIrO}_6$ at room temperature.



A 1.17: Neutron diffraction pattern of $\text{La}_{1.25}\text{Ca}_{0.75}\text{CoIrO}_6$ at room temperature..



A 1.18: Neutron diffraction pattern of $\text{La}_{1.25}\text{Ca}_{0.75}\text{CoIrO}_6$ at 4K. Reflection markers correspond to the positions of Bragg reflections of the structural (top) and the magnetic (bottom) contributions.

Appendix 2: Atomic positions at room temperature

A2.1: Atomic positions of $\text{La}_2\text{CoIrO}_6$ ($P2_1/n$) at room temperature.

Atom	x	y	Z
La	0.50984	0.54757	0.25341
Co	0	0.5	0
Ir	0.5	0	0
O1	0.19994	0.19929	0.95675
O2	0.29182	0.71525	0.95980
O3	0.41617	0.98396	0.24639

A2.2: Atomic positions of $\text{La}_{1.5}\text{Sr}_{0.5}\text{CoIrO}_6$ ($P2_1/n$) at room temperature.

Atom	x	y	Z
La/Sr	0.50873	0.53401	0.24889
Co	0	0.5	0
Ir	0.5	0	0
O1	0.20605	0.20074	0.96438
O2	0.27924	0.72427	0.95972
O3	0.41887	0.99127	0.24055

A2.3: Atomic positions of LaSrCoIrO_6 ($P2_1/n$) at room temperature.

Atom	x	y	Z
La/Sr	0.50511	0.52091	0.24830
Co	0	0.5	0
Ir	0.5	0	0
O1	0.21052	0.20794	0.96881
O2	0.27513	0.73782	0.97234
O3	0.42852	1.00594	0.24249

A2.4: Atomic positions of $\text{La}_{0.5}\text{Sr}_{1.5}\text{CoIrO}_6$ ($P2_1/n$) at room temperature.

Atom	x	y	Z
La/Sr	0.50835	0.52507	0.24646
Co	0	0.5	0
Ir	0.5	0	0
O1	0.21122	0.20718	0.96593
O2	0.27557	0.73573	0.97089
O3	0.42501	0.99948	0.24330

A2.5: Atomic positions of $\text{La}_{0.5}\text{Sr}_{1.5}\text{CoIrO}_6$ ($I2/m$) at room temperature.

Atom	x	y	Z
La/Sr	0.49829	0.00000	0.25516
Co	0	0	0.5
Ir	0	0	0
O1	0.25901	0.24105	0.02308
O2	-0.05553	0.00000	0.24461

A2.6: Atomic positions of $\text{Sr}_2\text{CoIrO}_6$ ($I2/m$) at room temperature.

Atom	x	y	Z
Sr	0.50336	0.00000	0.25000
Co	0	0	0.5
Ir	0	0	0
O1	0.23727	0.25899	0.03267
O2	0.01448	0.00000	0.24654

A2.8: Atomic positions of $\text{La}_{1.5}\text{Ca}_{0.5}\text{CoIrO}_6$ ($P2_1/n$) at room temperature.

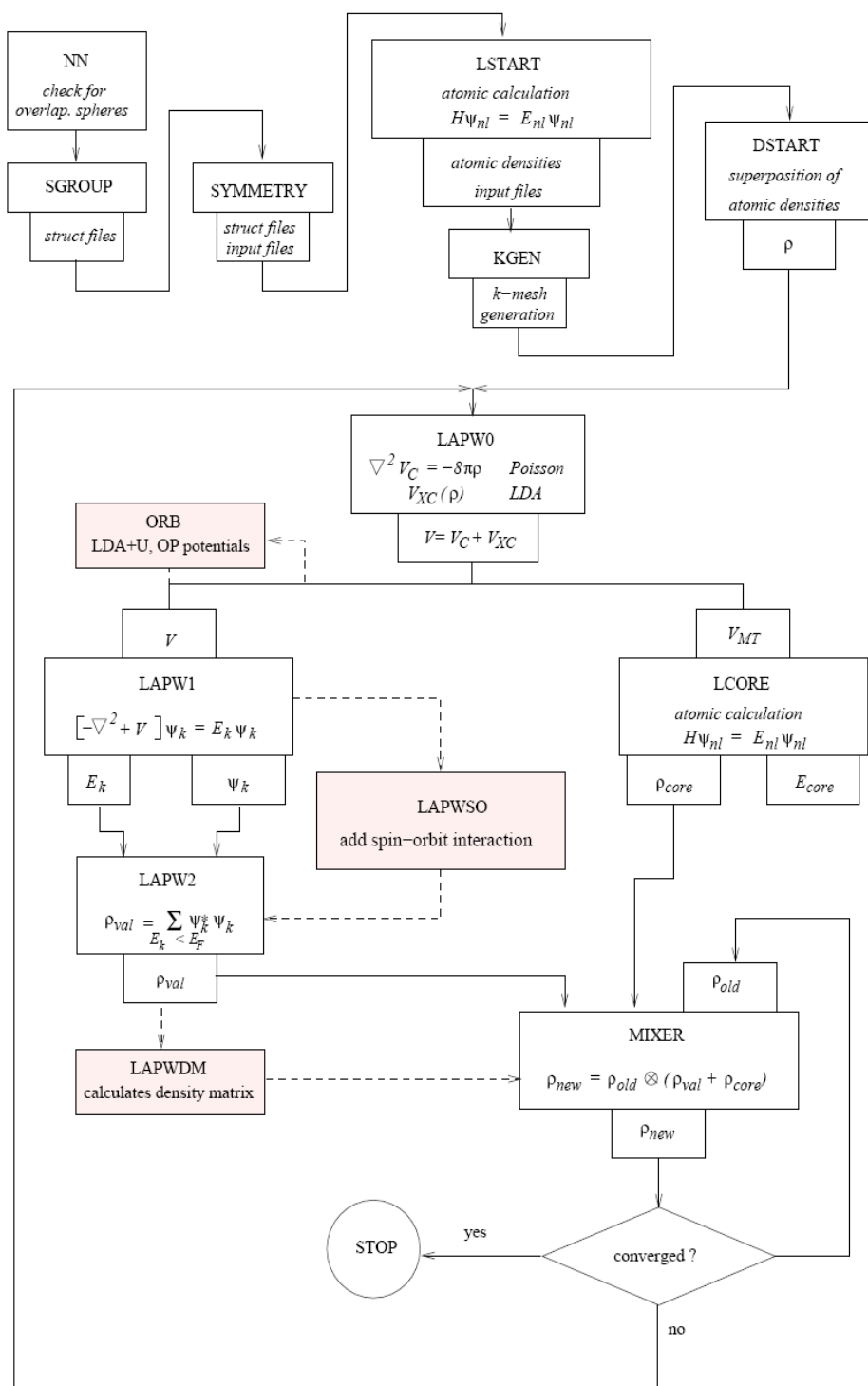
Atom	x	y	Z
La/Ca	0.50756	0.54319	0.25192
Co	0	0.5	0
Ir	0.5	0	0
O1	0.20480	0.19701	0.95963
O2	0.29070	0.71851	0.95794
O3	0.41585	0.98620	0.24477

A2.8: Atomic positions of $\text{La}_{1.25}\text{Ca}_{0.75}\text{CoIrO}_6$ ($P2_1/n$) at room temperature.

Atom	x	y	Z
La/Ca	0.50881	0.54248	0.24867
Co	0	0.5	0
Ir	0.5	0	0
O1	0.21683	0.19831	0.96368
O2	0.29794	0.71764	0.95389
O3	0.41927	0.98183	0.24864

Appendix 3: Self-consistent procedure (SCF) flow chart and important input files for WIEN2K and WIENNCM for $\text{La}_2\text{CoIrO}_6$

A3.1 A more sophisticated SCF flow chart of WIEN2K and WIENNCM



A. 3.2 Input for generating the potential: case.in0

```
TOT 13 (5...CA-LDA, 13...PBE-GGA, 11...WC-GGA)
NR2V IFFT (R2V)
45 45 60 2.00 min IFFT-parameters, enhancement factor
```

A. 3.3 Input for generating eigenvalues and eigenvectors: case.in1

```
WFFIL (WFPRI, SUPWF)
6.50 10 4 (R-MT*K-MAX; MAX L IN WF, V-NMT
0.30 5 0 (GLOBAL E-PARAMETER WITH n OTHER CHOICES, global
APW/LAPW)
0 -2.55 0.002 CONT 1
0 0.30 0.000 CONT 1
1 -1.29 0.002 CONT 1
1 0.30 0.000 CONT 1
2 0.30 0.005 CONT 1
0.30 5 0 (GLOBAL E-PARAMETER WITH n OTHER CHOICES, global
APW/LAPW)
0 -2.55 0.002 CONT 1
0 0.30 0.000 CONT 1
1 -1.29 0.002 CONT 1
1 0.30 0.000 CONT 1
2 0.30 0.005 CONT 1
0.30 4 0 (GLOBAL E-PARAMETER WITH n OTHER CHOICES, global
APW/LAPW)
1 0.30 0.000 CONT 1
1 -4.57 0.001 STOP 1
2 0.60 0.005 CONT 1
0 0.30 0.000 CONT 1
0.30 7 0 (GLOBAL E-PARAMETER WITH n OTHER CHOICES, global
APW/LAPW)
0 0.30 0.000 CONT 1
0 -6.88 0.001 STOP 1
1 0.30 0.000 CONT 1
1 -3.45 0.001 STOP 1
3 0.30 0.000 CONT 1
3 -4.14 0.001 STOP 1
2 0.30 0.005 CONT 1
0.30 3 0 (GLOBAL E-PARAMETER WITH n OTHER CHOICES, global
APW/LAPW)
0 -1.46 0.002 CONT 1
0 0.30 0.000 CONT 1
1 0.30 0.000 CONT 1
0.30 3 0 (GLOBAL E-PARAMETER WITH n OTHER CHOICES, global
APW/LAPW)
0 -1.46 0.002 CONT 1
0 0.30 0.000 CONT 1
1 0.30 0.000 CONT 1
0.30 3 0 (GLOBAL E-PARAMETER WITH n OTHER CHOICES, global
APW/LAPW)
0 -1.46 0.002 CONT 1
0 0.30 0.000 CONT 1
1 0.30 0.000 CONT 1
0.30 3 0 (GLOBAL E-PARAMETER WITH n OTHER CHOICES, global
APW/LAPW)
0 -1.46 0.002 CONT 1
0 0.30 0.000 CONT 1
1 0.30 0.000 CONT 1
0.30 3 0 (GLOBAL E-PARAMETER WITH n OTHER CHOICES, global
APW/LAPW)
0 -1.46 0.002 CONT 1
0 0.30 0.000 CONT 1
```

```

1 0.30 0.000 CONT 1
0.30 3 0 (GLOBAL E-PARAMETER WITH n OTHER CHOICES, global
APW/LAPW)
0 -1.46 0.002 CONT 1
0 0.30 0.000 CONT 1
1 0.30 0.000 CONT 1
0.30 4 0 (GLOBAL E-PARAMETER WITH n OTHER CHOICES, global
APW/LAPW)
1 0.30 0.000 CONT 1
1 -4.34 0.001 STOP 1
2 0.60 0.005 CONT 1
0 0.30 0.000 CONT 1
0.30 7 0 (GLOBAL E-PARAMETER WITH n OTHER CHOICES, global
APW/LAPW)
0 0.30 0.000 CONT 1
0 -6.85 0.001 STOP 1
1 0.30 0.000 CONT 1
1 -3.41 0.001 STOP 1
3 0.30 0.000 CONT 1
3 -4.13 0.001 STOP 1
2 0.30 0.005 CONT 1
K-VECTORS FROM UNIT:4 -10.2 2.0 244 emin/emax/nband

```

A. 3.4 Input for generating the valence charge density expansion: case.in2

```

TOT (TOT, FOR, QTL, EFG, FERMI)
-10.2 208.0 0.50 0.05 EMIN, NE, ESEPERMIN, ESEPERO
TETRA 0.000 (GAUSS, ROOT, TEMP, TETRA, ALL eval)
0 0 1 0 1 1 -1 1 2 0 2 1 -2 1 2 2 -2 2 3 0 3 1 -3 1 3 2 -3 2 3 3
-3 3 4 0 4 1 -4 1 4 2 -4 2 4 3 -4 3 4 4 -4 4 5 0 5 1 -5 1 5 2 -5 2
5 3 -5 3 5 4 -5 4 5 5 -5 5 6 0 6 1 -6 1 6 2 -6 2 6 3 -6 3 6 4 -6 4
6 5 -6 5 6 6 -6 6
0 0 1 0 1 1 -1 1 2 0 2 1 -2 1 2 2 -2 2 3 0 3 1 -3 1 3 2 -3 2 3 3
-3 3 4 0 4 1 -4 1 4 2 -4 2 4 3 -4 3 4 4 -4 4 5 0 5 1 -5 1 5 2 -5 2
5 3 -5 3 5 4 -5 4 5 5 -5 5 6 0 6 1 -6 1 6 2 -6 2 6 3 -6 3 6 4 -6 4
6 5 -6 5 6 6 -6 6
0 0 2 0 2 1 -2 1 2 2 -2 2 4 0 4 1 -4 1 4 2 -4 2 4 3 -4 3 4 4 -4 4
6 0 6 1 -6 1 6 2 -6 2 6 3 -6 3 6 4 -6 4 6 5 -6 5 6 6 -6 6
0 0 2 0 2 1 -2 1 2 2 -2 2 4 0 4 1 -4 1 4 2 -4 2 4 3 -4 3 4 4 -4 4
6 0 6 1 -6 1 6 2 -6 2 6 3 -6 3 6 4 -6 4 6 5 -6 5 6 6 -6 6
0 0 1 0 1 1 -1 1 2 0 2 1 -2 1 2 2 -2 2 3 0 3 1 -3 1 3 2 -3 2 3 3
-3 3 4 0 4 1 -4 1 4 2 -4 2 4 3 -4 3 4 4 -4 4 5 0 5 1 -5 1 5 2 -5 2
5 3 -5 3 5 4 -5 4 5 5 -5 5 6 0 6 1 -6 1 6 2 -6 2 6 3 -6 3 6 4 -6 4
6 5 -6 5 6 6 -6 6
0 0 1 0 1 1 -1 1 2 0 2 1 -2 1 2 2 -2 2 3 0 3 1 -3 1 3 2 -3 2 3 3
-3 3 4 0 4 1 -4 1 4 2 -4 2 4 3 -4 3 4 4 -4 4 5 0 5 1 -5 1 5 2 -5 2
5 3 -5 3 5 4 -5 4 5 5 -5 5 6 0 6 1 -6 1 6 2 -6 2 6 3 -6 3 6 4 -6 4
6 5 -6 5 6 6 -6 6
0 0 1 0 1 1 -1 1 2 0 2 1 -2 1 2 2 -2 2 3 0 3 1 -3 1 3 2 -3 2 3 3
-3 3 4 0 4 1 -4 1 4 2 -4 2 4 3 -4 3 4 4 -4 4 5 0 5 1 -5 1 5 2 -5 2
5 3 -5 3 5 4 -5 4 5 5 -5 5 6 0 6 1 -6 1 6 2 -6 2 6 3 -6 3 6 4 -6 4
6 5 -6 5 6 6 -6 6
0 0 1 0 1 1 -1 1 2 0 2 1 -2 1 2 2 -2 2 3 0 3 1 -3 1 3 2 -3 2 3 3
-3 3 4 0 4 1 -4 1 4 2 -4 2 4 3 -4 3 4 4 -4 4 5 0 5 1 -5 1 5 2 -5 2
5 3 -5 3 5 4 -5 4 5 5 -5 5 6 0 6 1 -6 1 6 2 -6 2 6 3 -6 3 6 4 -6 4
6 5 -6 5 6 6 -6 6

```

```

5 3 -5 3 5 4 -5 4 5 5 -5 5 6 0 6 1 -6 1 6 2 -6 2 6 3 -6 3 6 4 -6 4
6 5 -6 5 6 6 -6 6
0 0 2 0 2 1 -2 1 2 2 -2 2 4 0 4 1 -4 1 4 2 -4 2 4 3 -4 3 4 4 -4 4
6 0 6 1 -6 1 6 2 -6 2 6 3 -6 3 6 4 -6 4 6 5 -6 5 6 6 -6 6
0 0 2 0 2 1 -2 1 2 2 -2 2 4 0 4 1 -4 1 4 2 -4 2 4 3 -4 3 4 4 -4 4
6 0 6 1 -6 1 6 2 -6 2 6 3 -6 3 6 4 -6 4 6 5 -6 5 6 6 -6 6
12.00 GMAX
NOFILE FILE/NOFILE write recprlist

```

A. 3. 5 Input for calculating the density matrix: case.indm

```

-9. Emin cutoff energy
4 number of atoms for which density matrix is calculated
3 1 2 index of 1st atom, number of L's, L1
4 1 2 index of 1st atom, number of L's, L1
11 1 2 index of 1st atom, number of L's, L1
12 1 2 index of 1st atom, number of L's, L1
0 0 r-index, (l,s)-index

```

A. 3. 6 Input for calculating the orbital dependent potential: case.inorb

```

1 4 0 nmod, natorb, ipr
PRATT, 1.0 mixmod, amix
3 1 2 iatom nlorb, lorb
4 1 2 iatom nlorb, lorb
11 1 2 iatom nlorb, lorb
12 1 2 iatom nlorb, lorb
1 nsic (LDA+U(SIC) used)
0.4 0.0675 U J
0.2 0.04 U J
0.4 0.0675 U J
0.2 0.04 U J

```

A. 3. 7 Input for calculating spin-orbit coupling: case.inso

```

WFFIL
5 1 0 llmax, ipr, kpot
-10.0000 1.50000 emin, emax (output energy window)
0. 0. 1. direction of magnetization (lattice vectors)
0 number of atoms for which RLO is added
6 5 6 7 8 9 10 number of atoms for which SO is switch
off; atoms

```

A. 3. 8 Master input file with the structural information: case.struct

```

P s-o calc. M|| 0.00 0.00 1.00
12
RELA
10.522755 10.696610 14.920528 90.000000 89.961200 90.000000
ATOM -1: X=0.50980000 Y=0.54750000 Z=0.25340000
MULT= 2 ISPLIT= 8
-1: X=0.49020000 Y=0.45250000 Z=0.74660000
La1 NPT= 781 R0=.000010000 RMT= 2.38000 Z: 57.00000
LOCAL ROT MATRIX: 1.0000000 0.0000000 0.0000000
0.0000000 1.0000000 0.0000000
0.0000000 0.0000000 1.0000000
ATOM -2: X=0.99020000 Y=0.04750000 Z=0.24660000
MULT= 2 ISPLIT= 8
-2: X=0.00980000 Y=0.95250000 Z=0.75340000
La2 NPT= 781 R0=.000010000 RMT= 2.38000 Z: 57.00000

```

```

LOCAL ROT MATRIX:   1.0000000  0.0000000  0.0000000
                    0.0000000  1.0000000  0.0000000
                    0.0000000  0.0000000  1.0000000
ATOM  -3: X=0.50000000 Y=0.00000000 Z=0.50000000
      MULT= 1          ISPLIT= 8
Co3      NPT= 781  R0=.000050000 RMT= 2.04000  Z: 27.00000
LOCAL ROT MATRIX:   1.0000000  0.0000000  0.0000000
                    0.0000000  1.0000000  0.0000000
                    0.0000000  0.0000000  1.0000000
ATOM  -4: X=0.00000000 Y=0.50000000 Z=0.50000000
      MULT= 1          ISPLIT= 8
Ir4      NPT= 781  R0=.000005000 RMT= 1.98000  Z: 77.00000
LOCAL ROT MATRIX:   1.0000000  0.0000000  0.0000000
                    0.0000000  1.0000000  0.0000000
                    0.0000000  0.0000000  1.0000000
ATOM  -5: X=0.20820000 Y=0.19840000 Z=0.95650000
      MULT= 2          ISPLIT= 8
-5: X=0.79180000 Y=0.80160000 Z=0.04350000
O 5      NPT= 781  R0=.000100000 RMT= 1.76000  Z: 8.00000
LOCAL ROT MATRIX:   1.0000000  0.0000000  0.0000000
                    0.0000000  1.0000000  0.0000000
                    0.0000000  0.0000000  1.0000000
ATOM  -6: X=0.29180000 Y=0.69840000 Z=0.54350000
      MULT= 2          ISPLIT= 8
-6: X=0.70820000 Y=0.30160000 Z=0.45650000
O 6      NPT= 781  R0=.000100000 RMT= 1.76000  Z: 8.00000
LOCAL ROT MATRIX:   1.0000000  0.0000000  0.0000000
                    0.0000000  1.0000000  0.0000000
                    0.0000000  0.0000000  1.0000000
ATOM  -7: X=0.29740000 Y=0.71630000 Z=0.95660000
      MULT= 2          ISPLIT= 8
-7: X=0.70260000 Y=0.28370000 Z=0.04340000
O 7      NPT= 781  R0=.000100000 RMT= 1.76000  Z: 8.00000
LOCAL ROT MATRIX:   1.0000000  0.0000000  0.0000000
                    0.0000000  1.0000000  0.0000000
                    0.0000000  0.0000000  1.0000000
ATOM  -8: X=0.20260000 Y=0.21630000 Z=0.54340000
      MULT= 2          ISPLIT= 8
-8: X=0.79740000 Y=0.78370000 Z=0.45660000
O 8      NPT= 781  R0=.000100000 RMT= 1.76000  Z: 8.00000
LOCAL ROT MATRIX:   1.0000000  0.0000000  0.0000000
                    0.0000000  1.0000000  0.0000000
                    0.0000000  0.0000000  1.0000000
ATOM  -9: X=0.41540000 Y=0.98260000 Z=0.24770000
      MULT= 2          ISPLIT= 8
-9: X=0.58460000 Y=0.01740000 Z=0.75230000
O 9      NPT= 781  R0=.000100000 RMT= 1.76000  Z: 8.00000
LOCAL ROT MATRIX:   1.0000000  0.0000000  0.0000000
                    0.0000000  1.0000000  0.0000000
                    0.0000000  0.0000000  1.0000000
ATOM -10: X=0.08460000 Y=0.48260000 Z=0.25230000
      MULT= 2          ISPLIT= 8
-10: X=0.91540000 Y=0.51740000 Z=0.74770000
O 10     NPT= 781  R0=.000100000 RMT= 1.76000  Z: 8.00000
LOCAL ROT MATRIX:   1.0000000  0.0000000  0.0000000
                    0.0000000  1.0000000  0.0000000
                    0.0000000  0.0000000  1.0000000
ATOM -11: X=0.00000000 Y=0.50000000 Z=0.00000000
      MULT= 1          ISPLIT= 5
Co11     NPT= 781  R0=.000050000 RMT= 2.04000  Z: 27.00000
LOCAL ROT MATRIX:   0.5604300  0.8189400  0.2735100
                    -0.820860  0.5658700 -0.068991
                    -0.110060 -0.095588  0.9593900

```

```

ATOM -12: X=0.50000000 Y=0.00000000 Z=0.00000000
          MULT= 1           ISPLIT= 5
Ir12      NPT= 781  R0=.000005000 RMT= 1.98000  Z: 77.00000
LOCAL ROT MATRIX:  0.7955600 0.5872400 0.3053900
                  -0.596740 0.7999800 0.0682800
                  0.1048200 0.1232200 -0.949780
          2      NUMBER OF SYMMETRY OPERATIONS
          1 0 0 0.0000000
          0 1 0 0.0000000
          0 0 1 0.0000000
          1  A  1 so. oper. type orig. index
-1 0 0 0.0000000
 0-1 0 0.0000000
 0 0-1 0.0000000
          2  A  2

```

A. 3.9 Input for the direction of the magnetic moments in WIENNCM: case.inncm

```

FULL
0.000000 0.000000 0.000000
176.00000 26.87600 0
 3.99850 153.12000 0
 74.25768 72.65000 1  0.077355 0.269959 0.062784
105.74232 107.35000 1 -0.077355 0.269959 -0.062784
 73.28599 90.29727 1  0.000808 0.002646 -0.000011
 73.28599 90.29727 1  0.000808 0.002646 -0.000011
106.71401 89.70273 1 -0.000808 0.002646 0.000011
106.71401 89.70273 1 -0.000808 0.002646 0.000011
121.01861 44.01606 1 -0.010386 0.016992 0.014716
121.01861 44.01606 1 -0.010386 0.016992 0.014716
 58.98139 135.98394 1  0.010386 0.016992 -0.014716
 58.98139 135.98394 1  0.010386 0.016992 -0.014716
 79.38998 53.86080 1  0.006678 0.035067 0.018675
 79.38998 53.86080 1  0.006678 0.035067 0.018675
100.61002 126.13920 1 -0.006678 0.035067 -0.018675
100.61002 126.13920 1 -0.006678 0.035067 -0.018675
 46.17174 127.12790 1  0.012127 0.012428 -0.009356
 46.17174 127.12790 1  0.012127 0.012428 -0.009356
133.82826 52.87210 1 -0.012127 0.012428 0.009356
133.82826 52.87210 1 -0.012127 0.012428 0.009356
 0.50000

```

9. Bibliography

- [1] K.-I. Kobayashi, T. Kimura, H. Sawada, K. Terakura, and Y. Tokura, *Nature* **395**, 677 (1998).
- [2] H. Kato, T. Okuda, Y. Okimoto, Y. Tomioka, Y. Takenoya, A. Ohkubo, M. Kawasaki, and Y. Tokura, *Appl. Phys. Lett.* **81**, 328 (2002).
- [3] H. Kato, T. Okuda, Y. Okimoto, Y. Tomioka, K. Oikawa, T. Kamiyama, and Y. Tokura, *Phys. Rev. B* **65**, 144404 (2002).
- [4] Q. Zhou, B. J. Kennedy, and M. M. Elcombe, *J. Solid State Chem.* **180**, 541 (2007).
- [5] Y. Krockenberger, K. Mogare, M. Reehuis, M. Tovar, M. Jansen, G. Vaitheeswaran, V. Kanchana, F. Bultmark, A. Delin, F. Wilhelm, A. Rogalev, A. Winkler, and L. Alff, *Phys. Rev. B* **75**, 020404 (2007).
- [6] Z. H. Han, H. E. Mohottala, J. I. Budnick, W. A. Hines, P. W. Klamut, B. Dabrowski, and M. Maxwell, *J. Phys: Condens. Matter* **18**, 2273 (2006).
- [7] F. Galasso and W. Darby, *Inorg. Chem.* **4**, 71 (1965).
- [8] G. Blasse, *J. Inorg. Nucl. Chem.* **27**, 993 (1965).
- [9] A. V. Powell, J. G. Gore, and P. D. Battle, *J. Alloys Compounds* **201**, 73 (1993).
- [10] M. Uhl, S. Matar, and B. Siberchicot, *J. Magn. Magn. Mater.* **187**, 201 (1998).
- [11] R. C. Currie, J. F. Vente, E. Frikkee, and D. J. W. Ijdo, *J. Solid State Chem.* **116**, 199 (1995).
- [12] L. Bufaiçal, L. Mendonça Ferreira, R. Lora-Serrano, O. Agüero, I. Torriani, E. Granado, P. G. Pagliuso, A. Caytuero, and E. Baggio-Saitovich, *J. Appl. Phys.* **103**, 07F716 (2008).
- [13] G. Demazeau, B. Siberchicot, S. Matar, C. Gayet, and A. Largeteau, *J. Appl. Phys.* **75**, 4617 (1994).
- [14] K. Okuda, S. Kawamata, K. Nakahigashi, I. Ishibashi, M. Hayashi, H. Ohta, H. Nojiri and
- [15] M. T. Czyzyk, R. Potze, and G. A. Sawatzky, *Phys. Rev. B* **46**, 3729 (1992).
- [16] R. H. Potze, G. A. Sawatzky, and M. Abbate, *Phys. Rev. B* **51**, 11501 (1995).
- M. Motokawa, *J. Magn. Magn. Mater.* **177-181**, 1375 (1998).
- [17] H. Wu and T. Burnus, *Phys. Rev. B* **80**, 081105(R) (2009).
- [18] G. Maris, Y. Ren, V. Volotchaev, C. Zobel, T. Lorenz, and T. T. M. Palstra, *Phys. Rev. B* **67**, 224423 (2003).
- [19] J.-W. G. Bos and J. P. Attfield, *Phys. Rev. B* **70**, 174434 (2004).
- [20] M. C. Viola, M. J. Martinez-Lope, J. A. Alonso, P. Velasco, J. L. Martinez, J. C. Pedregosa, R. E. Carbonio, and M. T. Fernandez-Diaz, *Chem. Mater.* **14**, 812 (2002).

- [21] J. W. G. Bos and J. P. Attfield, *J. Mater. Chem.* **15**, 715 (2005).
- [22] M. C. Viola, M. J. Martinez-Lope, J. A. Alonso, J. L. Martinez, J. M. De Paoli, S. agola, J. C. Pedregosa, M. T. Fernandez-Diaz, and R. E. Carbonio, *Chem. Mater.* **15**, 1655 (2003).
- [23] H. Kato, T. Okuda, Y. Okimoto, Y. Tomioka, K. Oikawa, T. Kamiyama, and Y. Tokura, *Phys. Rev. B* **69**, 184412 (2004).
- [24] J. B. Philipp, P. Majewski, L. Alff, A. Erb, R. Gross, T. Graf, M. S. Brandt, J. Simon, T. Walther, W. Mader, D. Topwal, and D. D. Sarma, *Phys. Rev. B* **68**, 144431 (2003).
- [25] M. Baer, *Beyond Born-Oppenheimer* (Wiley, 2006).
- [26] N. D. Lang and W. Kohn, *Phys. Rev. B* **1**, 4555 (1970).
- [27] D. R. Hartree, *Proc. Cambridge Phil. Soc.*, 89 (1928).
- [28] F. Fock. *Zs. f. Phys.*, 126 (1930).
- [29] J. C. Slater, *Phys. Rev.* **81 Nr. 3**, 385 (1951).
- [30] C. Coulson, *Rev. Mod. Phys.* **32 Nr.2**, 170 (1960).
- [31] E. Fermi, *Rend. Accad. Naz. Lincei.* 6, 602 (1927).
- [32] L. H. Thomas, *Proc. Camb. Phil. Soc.* **23**, 542 (1927).
- [33] P. Dirac, *Proc. Camb. Phil. Soc.* **26**, 376 (1930).
- [34] W. Kohn, *Rev. Mod. Phys.* **71**, 1253 (1999).
- [35] P. Hohenberg and W. Kohn, *Phys. Rev.* **136(3B)**, 864 (1964).
- [36] W. Kohn and L. J. Sham, *Phys. Rev.* **140(4A)**, 1133 (1965).
- [37] J. F. Janak, *Phys. Rev. B* **18**, 7165 (1978).
- [38] J. P. Perdew, K. Burke, and M. Ernzerhof, *Phys. Rev. Lett.* **77**, 3865 (1996).
- [39] P. E. Blöchl, O. Jepsen, and O. K. Andersen, *Phys. Rev. B* **49**, 16223 (1994).
- [40] M. Methfessel, C. O. Rodriguez, and O. K. Andersen, *Phys. Rev. B* **40**, 2009 (1989).
- [41] N. Papanikolaou, R. Zeller, and P. H. Dederichs, *J Phys.; Condens. Matter* **14**, 2799 (2002).
- [42] W. E. Pickett, *Pseudopotential Methods in Condensed Matter Applications* (North-Holland, 1989).
- [43] K. Koepnik and H. Eschrig, *Phys. Rev. B* **59**, 1743 (1999).
- [44] J. C. Slater, *Phys. Rev.* **51**, 846 (1937).
- [45] K. H. Schwarz, P. Blaha, and G. K. H. Madsen, *Comput. Phys. Commun.* **147**, 71 (2002).
- [46] O. K. Andersen, *Phys. Rev. B* **12**, 3060 (1975).
- [47] D. J. Singh, *Phys. Rev. B* **43**, 6388 (1991).
- [48] E. Sjöstedt, L. Nordström, and D. J. Singh, *Solid State Comm.* **114**, 15 (2000).
- [49] J. J. Sakurai, *Advanced Quantum Mechanics* (Addison-Wesley, 1967).

- [50] A. H. McDonald, W. E. Pickett, and D. D. Koelling, *J. Phys. C: Solid State Phys.* **13**, 2675 (1980).
- [51] F. Tran, P. Blaha, and K. Schwarz, *Phys. Rev.* **B 74**, 155108 (2006).
- [52] N. Mott, *Rev. Mod. Phys.* **40**, 677 (1968).
- [53] W. Kohn, *Phys. Rev. Lett.* **19**, 789 (1967).
- [54] J. Hubbard, *Proc. Roy. Soc. A* **281**, 401 (1964).
- [55] P. W. Anderson, *Phys. Rev.* **115**, 2 (1959).
- [56] S. Chadov, J. Minar, M. I. Katsnelson, H. Ebert, D. Ködderitzsch, and A. I. Lichtenstein, *Europhys. Lett.* **82**, 37001 (2008).
- [57] J. Perdew, R. Parr, M. Levy, and J. Balduz, *Phys. Rev. Lett.* **49**, 1691 (1982).
- [58] J. Perdew and M. Levy, *Phys. Rev. Lett.* **51**, 1884 (1983).
- [59] M. Cococcioni and S. de Gironcoli, *Phys. Rev.* **B 71**, 035105 (2005).
- [60] O. Gunnarsson and K. Schönhammer, *Phys. Rev. Lett.* **56**, 1968 (1986).
- [61] A. I. Liechtenstein, V. I. Anisimov, and J. Zaanen, *Phys. Rev.* **B 52**, R5467 (1995).
- [62] I. V. Solovyev, P. H. Dederichs, and V. I. Anisimov, *Phys. Rev.* **B 50**, 16861 (1994).
- [63] V. I. Anisimov, J. Zaanen, and O. K. Andersen, *Phys. Rev.* **B 44**, 943 (1991).
- [64] M. T. Czyzyk and G. A. Sawatzky, *Phys. Rev.* **B 49**, 14211 (1994).
- [65] V. I. Anisimov, I. V. Solovyev, M. A. Korotin, M. T. Czyzyk, and G. A. Sawatzky, *Phys. Rev.* **B 48**, 16929 (1993).
- [66] V.M. Goldschmidt, *Naturwissenschaften* **14**, 477 (1926).
- [67] A. M. Glazer, *Acta Crystallogr., Sect. B: Struct. Crystallogr. Cryst. Chem.* **28**, 3384 (1972).
- [68] M. T. Anderson, K. B. Greenwood, G. A. Taylor, and K. R. Poeppelmeier, *Prog. Solid State Chem.* **22**, 197 (1993).
- [69] C.J. Howard, H.T. Stokes, *Acta Cryst.* **B 54**, 782 (1998).
- [70] M. Gatashki, J. M. Igartua, and E. Hernandez-Bocanegra, *J. Phys. Condens. Mater.* **15**, 6199 (2003).
- [71] G. Popov, M. Greenblatt, and M. Croft, *Phys. Rev.* **B 67**, 024406 (2003).
- [72] D. Serrate, J. M. De Teresa, and M. R. Ibarra, *J. Phys.: Condens. Matter* **19**, 023201 (2007).
- [73] I. D. Brown, and D. Altermatt, *Acta Cryst.* **B 41**, 244 (1985).
- [74] R. F. W. Bader, *Atoms in Molecules - A Quantum Theory* (Clarendon Press, Oxford, U.K., 1990).

- [75] R. Vidya, P. Ravindran, K. Knizek, A. Kjekshus, and H. Fjellvag, *Inorg. Chem.* **47**, 6608 (2008).
- [76] M. Kaveh and N. Wiser, *J. Phys. F: Metal Phys.* **11**, 1749 (1981).
- [77] E. Abrahams, *Phys. Rev.* **95**, 839 (1954).
- [78] E. M. Ramos, I. Alvarez, M. L. Viega, and C. Pico, *J. Mater. Sci. Lett.* **14**, 1577 (1995).
- [79] S. J. Moon, H. Jin, K. W. Kim, W. S. Choi, Y. S. Lee, J. Yu, G. Cao, A. Sumi, H. Funakubo, C. Bernhard, and T. W. Noh, *Phys. Rev. Lett* **101**, 226402 (2008).
- [80] N. F. Mott, *Phil. Mag.* **19:160**, 835 (1969).
- [81] J.-W. G. Bos, and J. P. Attfield, *Phys. Rev.* **B 69**, 094434 (2004).
- [82] R. Saez-Puche, E. Climent-Pascual, R. Ruiz-Bustos, M. A. Alario-Franco, and M. T. Fernandez-Diaz, *Prog. Solid State Chem.* **35**, 211 (2007).
- [83] J. B. Phillip, P. Majewski, D. Reisinger, S. Geprägs, M. Opel, A. Erb, L. Alff, and R. Gross, *Acta Phys. Pol.* **A 105**, 7 (2004).
- [84] P. Sanyal, H. Das, and T. Saha-Dasgupta, *Phys. Rev.* **B 80**, 224412 (2009).
- [85] T. Aharen, J. E. Greedan, C. A. Bridges, A. A. Aczel, J. Rodriguez, G. MacDougall, G. M. Luke, V. K. Michaelis, S. Kroeker, C. R. Wiebe, H. Zhou, and L. M. D. Cranswick, *Phys. Rev.* **B 81**, 064436 (2010).
- [86] S. Di Matteo, G. Jackeli, and N. B. Perkins, *Phys. Rev.* **B 67**, 184427 (2003).
- [87] J. B. Goodenough, *Magnetism and the Chemical Bond* (John Wiley, New York-London, 1963), p. 177, Table XII.
- [88] P. D. Battle, J. B. Goodenough, and R. Price, *J. Solid State Chem.* **46**, 234 (1983).
- [89] M. Knapp, C. Baetz, H. Ehrenberg, and H. Fuess, *J. Synchrotron Rad.* **11**, 328 (2004).
- [90] M. Knapp, V. Joco, C. Baetz, H. H. Brecht, A. Berghaeuser, H. Ehrenberg, H. von Seggern, and H. Fuess, *Nucl. Instrum. Methods Phys. Res. A* **521**, 565 (2004).
- [91] J. Ihringer and A. Küster, *J. Appl. Cryst.* **26**, 135 (1993).
- [92] J. Rodriguez-Carvajal, *Physica* **B 192**, 55 (1993).
- [93] M. Hölzel, A. Senyshyn, R. Gilles, H. Boysen, and H. Fuess, *Neutron News* **18**, 23 (2007).
- [94] R. A. Young, *The Rietveld Method* (Oxford Univ. Press, 1995).
- [95] S. Riesner: private communication.
- [96] N. Narayanan, *Diplomarbeit*, TU Darmstadt (2007).
- [97] J. Diederichs, S. Spagna, and R. E. Sager, *Czechoslovak J. Phys.* **46**, 2803 (Suppl. S5) (1996).
- [98] Quantum Design, MPMS: Hardware Reference Manual.

- [99] PPMS, Quantum Design brochure.
- [100] Quantum Design, PPMS: Resistivity Option User's Manual, Part Number 1076-100A (1999).
- [101] L. J. van der Pauw, Philips Tech. Rev. **20**, 220 (1958).
- [102] Quantum Design, Application Note 1076-304.
- [103] Quantum Design, PPMS: Heat Capacity Option User's Manual, Part Number 1085-150,J0 (2007).
- [104] Quantum Design, Application Note 1085-152.
- Seggern, and H. Fuess, Nucl. Instrum. Meth. **A 521**, 565 (2004).
- [105] P. Blaha, K. H. Schwarz, G. Madsen, D. Kvasnicka, and J. Luitz, WIEN2k, An Augmented Plane wave plus Local Orbitals Program for Calculating Crystal Properties (TU Wien Austria, 2001).
- [106] J. Kuneš, P. Novák, M. Diviš, and P. M. Oppeneer, Phys. Rev. **B 63**, 205111 (2001).
- [107] R. Laskowski, G. K. H. Madsen, P. Blaha, and K. H. Schwarz, Phys. Rev. **B 69**, 140408(R) (2004).
- [108] D. J. Singh, *Plane waves, pseudopotentials and the LAPW method* (Kluwer Academic, Dordrecht, 1994).
- [109] F. Galasso and W. Darby, Inorg. Chem. **4**, 71 (1965).
- [110] J. W. Nielsen, J. Appl. Phys. **31** (Supl), 51S (1960).
- [111] J. P. Remeika, J. Am. Chem. Soc. **78**, 4259 (1956).
- [112] P. M. Woodward, Acta Crystallogr., Sect. **B 25**, 32 (1997).
- [113] W. T. Pennington, DIAMOND - Visual Crystal Structure Information System, J. Appl. Cryst. **32**, 1028 (1999).
- [114] I. D. Brown, Accumulated table of bond valence parameters, bvparm2006.cif (2006)
- [115] R. D. Shannon, Acta. Cryst. **A 32**, 751 (1976).
- [116] K. Yamamura, M. Wakeshima, and Y. Hinatsu, J. Solid State Chem. **179**, 605 (2006).
- [117] L. Ortega-SanMartin, J. P. Chapman, E. Hernandez-Bocanegra, M. Insausti, M. I. Arriortua, and T. Rojo, J. Phys.: Condens. Matter **16**, 3879 (2004).
- [118] D Serrate, J. M. De Teresa, P. A. Algarabel, J. Galibert, C. Ritter, J. Blasco, and M R Ibarra, Phys. Rev. B **75**, 165109 (2007).
- [119] M. Sikora, O. Mathon, P. Van der Linden, J. M. Michalik, J. M. De Teresa, Cz. Kapusta, and S. Pascarelli, Phys. Rev. **B 79**, 220402(R) (2009).
- [120] V. Y. Irkhin, J. Magn. Magn. Mater. **258-259**, 228 (2003).

- [121] M. Retuerto, M. J. Martinez-Lope, M. Garcia-Hernandez, M. T. Fernandez-Diaz, and J. A. Alonso, *Eur. J. Inorg. Chem* **2008**, 588 (2008).
- [122] K. Oikawa, T. Kamiyama, H. Kato, and Y. Tokura, *J. Phys. Soc. Jpn* **72**, 1411 (2003).
- [123] D. B. Litvin, *Magnetic Space Group Types* (Penn State Berks, 2010).
- [124] L. Ortega-San Martin, J. P. Chapman, L. Lezama, J. Sanchez-Marcos, J. Rodriguez-Fernandez, M. I. Arriortua, and T. Rojo, *J. Mater. Chem.* **15**, 183 (2005).
- [125] Y. Hinatsu and Y. Doi, *J. Solid State Chem.* **179**, 2079 (2006).
- [126] C. Michel, S. D. Baranovskii, P. J. Klar, and P. Thomas, *Appl. Phys. Lett.* **89**, 112116 (2006).
- [127] P. Tomes, J. Hejtmanek, and K. Knizek, *Solid State Sci.* **10**, 486 (2008).
- [128] J.-W. G. Bos and J. P. Attfield, *Chem. Mater.* **16**, 1822 (2004).
- [129] I. V. Solovyev, P. H. Dederichs, and V. I. Anisimov, *Phys. Rev.* **B 50**, 16861 (1994).
- [130] C. Michel, S. D. Baranovskii, P. J. Klar, and P. Thomas, *Appl. Phys. Lett.* **89**, 112116 (2006).
- [131] D. Niebieskikwiat, R. D. Sanchez, A. Caneiro, L. Morales, M. Vasques-Mansilla, F. Rivadulla, and L. E. Hueso, *Phys. Rev.* **B 62**, 3340 (2000).
- [132] E. R. Ylvisaker, W. E. Pickett, and K. Koepf, *Phys. Rev.* **B 79**, 035103 (2009).
- [133] L. Balcells, J. Navarro, M. Bibes, A. Roig, B. Martinez, and J. Fontcuberta, *Appl. Phys. Lett.* **78**, 781 (2001).
- [134] A. Winkler, N. Narayanan, D. Mikhailova, K. G. Bramnik, H. Ehrenberg, H. Fuess, G. Vaitheeswaran, V. Kanchana, F. Wilhelm, A. Rogalev, A. Kolchinskaya, and L. Alff, *New Journal of Physics* **11**, 073047 (2009).

Physikalische Eigenschaften der Doppelperowskite $\text{La}_{2-x}\text{Sr}_x\text{CoIrO}_6$ ($0 \leq x \leq 2$)

Zusammenfassung

Im letzten Jahrzehnt wurden Doppelperowskite $\text{A}_2\text{BB}'\text{O}_6$ mit Übergangsmetallen am BB' -Platz aufgrund interessanter physikalischer Eigenschaften wie Metall-Isolator-Übergang, kolossaler Magnetowiderstand und strukturelle und magnetische Phasenübergänge intensiv untersucht. Während sich die meisten Untersuchungen bezüglich der 3d/5d Übergangsmetall-Kombination auf W, Re und Os basierte Systeme richteten, wurden die Ir basierten Doppelperowskite kaum untersucht. In diesem System verspricht der Einfluss einer großen Spin-Orbit-Kopplung in Kombination mit der Elektronenkorrelation auf die ausgedehnte Wellenfunktion (verglichen mit 3d) interessante Effekte. Andererseits kann Co in einer bestimmten Oxidationsstufe abhängig von der Verbindung, in verschiedenen Spin-Zuständen vorliegen. Daher wird bei einem Doppelperowskit mit Co und Ir am B bzw. B' Platz interessante physikalische Eigenschaften erwartet.

Im Rahmen dieser Arbeit wurde die Verbindung $\text{La}_2\text{CoIrO}_6$ hinsichtlich ihrer Kristallstruktur, magnetischen Eigenschaften und elektronischen Struktur untersucht. Diese Verbindung weist nicht-kollinearen Magnetismus und im externen Magnetfeld einen Spin-Reorientierungsübergang auf. Darüber hinaus wurde die elektronische Struktur am BB' -Platz durch die Substitution des A-Kations beeinflusst und die dadurch ändernden physikalischen Eigenschaften untersucht. Während in $\text{La}_{2-x}\text{Sr}_x\text{CoIrO}_6$ sowohl der Freiheitsgrad der A-Kationengröße als auch der Freiheitsgrad der Bandfüllung vorhanden sind, ist der Freiheitsgrad der A-Kationengröße in $\text{La}_{2-x}\text{Ca}_x\text{CoIrO}_6$ ausgeschaltet (gleiche Kationenradien von La und Ca). Abhängig von der Temperatur und Zusammensetzung, weist das $\text{La}_{2-x}\text{Sr}_x\text{CoIrO}_6$ System die folgenden strukturellen Phasenübergänge auf: $P2_1/n \leftrightarrow P2_1/n + I2/m \leftrightarrow I2/m \leftrightarrow I4/m \leftrightarrow Fm-3m$. Die mit Ca substituierten Zusammensetzungen hingegen zeigen keine strukturellen Phasenübergänge. Bezüglich der magnetischen Ordnung weisen sowohl das $\text{La}_{2-x}\text{Sr}_x\text{CoIrO}_6$ System als auch das $\text{La}_{2-x}\text{Ca}_x\text{CoIrO}_6$ System den folgenden magnetischen Phasenübergang auf, was auf einen Übergang vom dominanten Nächstnachbar-Wechselwirkung zum dominanten Übernächstnachbar-Wechselwirkung schließen lässt: $\text{AFM } k=(0,0,0) \rightarrow k=(1/2,0,1/2)$. Widerstandsmessungen ergaben, dass $\text{La}_2\text{CoIrO}_6$ ein Isolator ist, und die Bandlücke durch die Sr-Substitution kleiner wird. Diese Ergebnisse wurden auch durch theoretische Berechnungen im Rahmen der Dichtefunktionaltheorie (DFT) mit GGA+U (mit Ausnahme von $\text{Sr}_2\text{CoIrO}_6$) bestätigt. Darüber hinaus liefern sie als Erklärungsmodell eine stärkere Elektronen-Elektronen-Wechselwirkung. Bei $\text{Sr}_2\text{CoIrO}_6$ ist eine

Bandlückenbestimmung (aus Widerstandsmessungen) aufgrund der starken Kopplung zwischen der thermischen Aktivierung und dem Variable-Range-Hopping nicht möglich. Bei der Ca-Substitution konnte keine Änderung der Bandlücke festgestellt werden, was auf den nahezu konstanten Co-O-Ir Bindungswinkel zurückzuführen ist.

Lebenslauf

Persönliche Daten

Name	Narayanan
Vorname	Narendirakumar
Nationalität	Deutsch
Geburtsdatum	28. November 1978
Geburtsort	Colombo, Sri Lanka
Familienstand	ledig

Schulbildung

1985-1997	Primary-, Middle- und Upper-School im St. Joseph's College in Colombo, Sri Lanka
1997-1998	Eingliederung in die Berufs- und Arbeitswelt (EBA) an der Beruflichen Schule in Bensheim
1998-2001	Oberstufe an der Geschwister-Scholl-Schule in Bensheim
2001	Erlangung der allgemeinen Hochschulreife (Abitur)

Hochschulausbildung

2001-2007	Studium der Materialwissenschaften an der Technischen Universität Darmstadt
2006/07	Diplomarbeit im Fachgebiet Dünne Schichten unter der Betreuung von Prof. Dr. Lambert Alff
2007	Abschluss: Diplom-Ingenieur

Promotion

2007-2010	Wissenschaftlicher Mitarbeiter an der Technischen Universität
-----------	---

Darmstadt im Fachbereich Material- und Geowissenschaften,
Fachgebiet Strukturforschung

2007-2010 Promotion im Fachgebiet Strukturforschung unter der Leitung von
Priv.-Doz. Dr. Helmut Ehrenberg
Physical properties of double perovskites $La_{2-x}Sr_xCoIrO_6$ ($0 \leq x \leq 2$)

10-12/2008 Forschungsaufenthalt an der TU Wien

Praktische Tätigkeiten

11-12/2005 Industriepraktikum bei der Vacuumschmelze GmbH & Co. KG,
Hanau

Eidesstattliche Erklärung

Hiermit erkläre ich an Eides Statt, dass ich meine Dissertation selbstständig und nur mit den angegebenen Hilfsmitteln angefertigt habe.

Narendirakumar Narayanan